

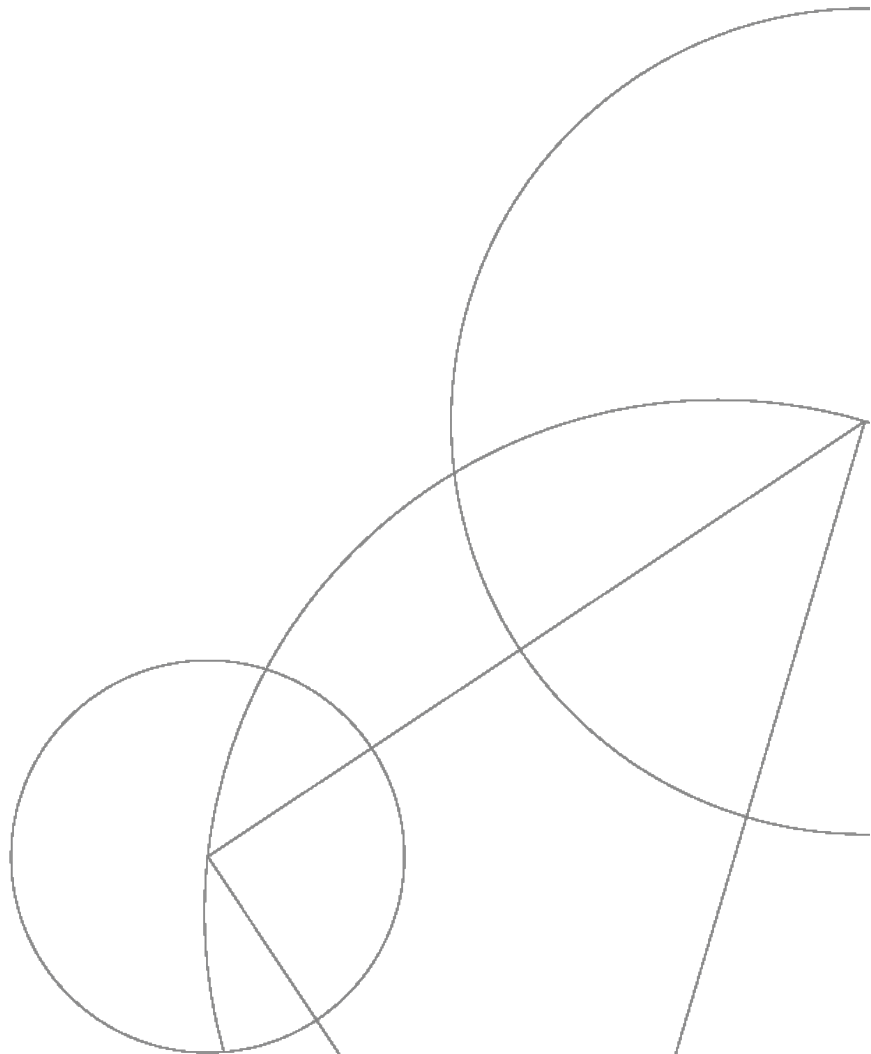


Master's Thesis in Solid State Physics

Phonon-Magnon Coupling in Frustrated and Multiferroic h -YMnO₃

Author: Turi K. SCHÄFFER
Supervisor: Kim LEFMANN

June 30, 2014



”

For there are, for example, people who are interested in solid state physics, and they are doing the right thing, for one cannot imagine what great possibilities will open up in this field.

Niels Bohr, 12 May 1934

Preface

This thesis, written so that all physics master's students with knowledge of basic solid state physics can understand its contents, culminates my MSc in physics at the Niels Bohr Institute, University of Copenhagen.

Written as a resource for continuing researchers in the field, as well as a report of the results and conclusions from recent experiments, the thesis includes a complete and thorough introduction to previous investigations, relevant theory, the most ground-breaking previous experiments, and ideas for future experiments. The organization of the report should facilitate location of information relevant to any and all aspects of the project. The lengthy bibliography is reasonably comprehensive.

The result sections of the thesis are based on three experiments which were performed in 2012 and 2013 at the instruments EIGER and RITA II at Paul Scherrer Institut in Switzerland prior to my involvement in the project and one experiment executed in 2014 at C5 at Chalk River National Laboratories in Canada in which I have participated.

Enjoy yourself!



Acknowledgements

Firstly, I would like to thank my supervisor, Kim Lefmann, who is the most positive person in the world. Secondly I am thankful for all the help Sonja Lindahl Holm has provided during the project and for her good company on the beam times. Deep thanks should be given to Pascale Deen for support on the theory of polarized neutron scattering, but also general good scientific advice. Thank you to my office mate Ursula Bengaard for calming conversations and coffee breaks. Thank you to Jacob Larsen and Roxy Wilson for fruitful discussions and proofreading.

Many thanks should be given to Amy Poole (collaborator and instrument scientist at RITA II), Uwe Stuhr (instrument scientist at EIGER), Thomas Keller (instrument scientist at TRISP) and Zahra Yamani (instrument scientist at C5) for experimental support and scientific advice.

Thank you to my mother, father and fiancé for great support and warm hugs.

Lastly I would also like to thank the Siemens Student Foundation and DANSCATT for supporting my travel expenses.

Without all of you, this project would not have seen the light of day.



Abstract

The frustrated and multiferroic system $h\text{-YMnO}_3$ has been investigated with elastic neutron scattering, revealing the antiferromagnetic ordering temperature $T_N = 72.0$ K and the associated critical exponent $\beta = 0.196$. The two critical exponents $\gamma = 1.55$ and $\nu = 0.614$ associated with diffuse scattering around the (100) magnetic Bragg peak were also determined.

Inelastic neutron scattering experiments revealed the magnon dispersions around the (100) magnetic Bragg peak in agreement with previous experiments. Transverse energy scans in the ab -plane, from the (030) zone center to the zone boundary, showed a clear transverse phonon. Below the magnetic ordering temperature at $T = 40$ K at the zone boundary, a crossing of a phonon and a magnon dispersion was observed, and polarized neutron scattering experiments, separating the magnetic and structural signal, revealed that the modes were mixed at the crossing point and changed nature beyond the zone boundary. These mixed modes, *i.e.* excitations associated with multiferroic systems, is the first example of mixed modes observed at the zone boundary in $h\text{-YMnO}_3$.

A magnetic signal observed at $T = 100$ K, well above the magnetic ordering temperature, that seems to be part of a dispersion, may be the reason for the spin fluctuations suppressing the thermal conductivity in the system at high temperatures.

Contents

List of Figures	vi
List of Tables	ix
1 Introduction	1
1.1 Motivation	1
1.2 Magnetoelectric effect	2
1.3 Symmetry	3
1.4 Neutron scattering	3
2 Theoretical background	4
2.1 Crystals and reciprocal space	4
2.2 Magnetism	6
2.3 Geometrical frustration	9
2.4 Ferroelectricity	10
2.4.1 Proper ferroelectrics	10
2.4.2 Improper ferroelectrics	12
2.5 Multiferroics	12
2.5.1 Type I multiferroics	14
2.5.2 Type II multiferroics	15
2.5.3 The $RMnO_3$ multiferroics	16
2.6 Elementary excitations	16
2.6.1 Lattice vibrations	17
2.6.2 Spin waves	19
2.7 Macroscopic properties of crystals	21
2.7.1 Magnetic susceptibility	21
2.7.2 Heat capacity	21
2.7.3 Thermal conductivity	22
2.7.4 Electric susceptibility	22
3 Neutron scattering	23
3.1 Why neutrons?	23
3.2 The neutron scattering cross section	24
3.3 Coherent and incoherent scattering	27
3.4 Scattering theory	27
3.5 Elastic neutron scattering	29
3.5.1 Nuclear scattering	29
3.5.2 Magnetic scattering	30
3.6 Inelastic neutron scattering	32
3.6.1 Phonons	33
3.6.2 Magnons	33
3.7 The three-axis spectrometer	34
3.8 Polarized Neutron Scattering	36
3.8.1 Nuclear scattering	38
3.8.2 Magnetic scattering	39
3.8.3 Coherent and incoherent scattering	39
3.8.4 Experimental setup	40
3.8.5 Examples of polarization analysis	43

4	YMnO₃	45
4.1	Crystal structure and magnetism of Mn ³⁺	45
4.2	The structural and magnetic phase transitions	45
4.3	Bulk Measurements	48
4.4	The magnetic structure and space group	51
4.5	Ferromagnetic signal	52
4.6	The magnetoelastic coupling	53
4.7	Diffuse magnetic scattering	56
4.8	Excitations in YMnO ₃	56
4.9	Coupling of the order parameters	60
5	Instruments	64
5.1	RITA II - cold instrument	64
5.2	EIGER - thermal instrument	65
5.3	C5 - thermal polarized instrument	66
6	Non-polarized data	70
6.1	Orientation in reciprocal space	70
6.2	Experimental practice and data analysis	70
6.3	The magnetic phase transition	73
6.4	Diffuse scattering around (0 $\bar{1}$ 0)	74
6.5	Magnon dispersions around (0 $\bar{1}$ 0)	77
6.6	Spin wave gaps around (1 0 0)	78
6.7	Magnon and transverse phonon around (0 3 0)	80
6.7.1	Temperature dependence of the transverse phonon	81
7	Polarized data	84
7.1	Strategy	84
7.2	Flipping ratio	85
7.3	Measurements above T_N	86
7.4	Measurements below T_N	89
7.4.1	Horizontal vs vertical field measurements	90
8	Discussion	93
8.1	Critical phenomena	93
8.2	The magnetoelastic coupling	94
8.3	Magnetic signal above T_N	97
9	Conclusion	101
10	Outlook	102
10.1	Completion of present data	102
10.1.1	Color maps at $T = 40$ K and $T = 100$ K	102
10.1.2	Temperature dependence	102
10.1.3	Other directions in reciprocal space	102
10.1.4	Line-widths with spin-echo	103
10.2	Theoretical calculations	103
10.3	Pressure experiments	103
10.4	Magnetic field experiments	105
10.5	Electric field experiments	106

CONTENTS

References	107
A Space Group $P6_3/mmc$	114
B Space Group $P6_3cm$	117
C Space Group $P6_3$	119
D Periodic table	121
E Conversion Tables	122
F Sample holder for C5	123
G Plots	124
G.1 Diffuse scattering around $(0\bar{1}0)$	124
G.2 Energy scans around the (100) magnon dispersions	127
G.3 Energy scans around (300) at $T = 40$ K and $T = 100$ K	128
G.4 Q-scans of transverse phonon around (300)	130
G.5 Longitudinal phonon measured at $k = 3.25$ and $k = 3.35$	131
G.6 Measurements above T_N	132
G.7 Measurements below T_N	134
G.7.1 Horizontal field versus vertical field at $T = 40$ K	136

List of Figures

1.1	The advance of articles about multiferroics	1
1.2	Illustration of the magnetoelectric effect	2
1.3	Multiferroics and their symmetries	3
2.1	Miller indices	5
2.2	Two examples of crystal structures in real and reciprocal space	5
2.3	The hexagonal unit cell	6
2.4	Symmetry points in the reciprocal hexagonal lattice	6
2.5	The magnetic moment	7
2.6	Ferromagnetic and antiferromagnetic order	8
2.7	Illustration of the superexchange interaction	9
2.8	Illustration of the Dzyaloshinskii-Moriya interaction	9
2.9	Antiferromagnetically coupled triangular lattice	10
2.10	Molecular orbitals between d and p -orbitals	11
2.11	Illustration of lone pair induced ferroelectricity	12
2.12	Mechanisms for improper ferroelectrics	13
2.13	Diagram explaining multiferroism	14
2.14	Time and space inversion	15
2.15	Longitudinal and transverse phonons	17
2.16	Acoustic and optical phonon dispersion	18
2.17	Visualization of a spin wave	19
2.18	Magnon dispersion	20
2.19	Susceptibility and ordering temperatures	21
3.1	Neutron energy transfer	23
3.2	Selected neutron and X-ray cross sections	25
3.3	Geometry illustrating the scattering cross section	26
3.4	Illustration of the scattering vector \mathbf{Q}	26
3.5	Illustration of Bragg's Law	29
3.6	The geometry of magnetic scattering	31
3.7	The inelastic scattering process	32
3.8	Tree-axis spectrometer	35
3.9	The geometry behind a constant \mathbf{Q} -scan	37
3.10	Polarization direction \mathbf{P} , scattering vector \mathbf{Q} and magnetic moment \mathbf{S}	39
3.11	Polarization direction \mathbf{P} , scattering vector \mathbf{Q} and magnetic moment \mathbf{S}	40
3.12	Polarized three-axis experimental setup	42
3.13	Flipper conditions for the four polarized scattering cross sections	43
3.14	Examples of polarized neutron data	44
4.1	The room temperature crystal structure of YMnO_3	46
4.2	A trigonal bipyramide environment	46
4.3	Trimerization of the trigonal bipyramids	47
4.4	Magnetic phase transition of YMnO_3 determined by Chatterji <i>et al.</i> and Roessli <i>et al.</i>	48
4.5	Curie-Weiss temperature of YMnO_3	48
4.6	Heat capacity and magnetic entropy as a function of temperature of YMnO_3	49
4.7	Thermal conductivity of YMnO_3 as a function of temperature	50
4.8	Thermal conductivity of YMnO_3 compared with models	50
4.9	The dielectric constant as a function of temperature of YMnO_3	51
4.10	Non-linear coupling of the polarization and the magnetization	52

LIST OF FIGURES

4.11	Two magnetic structures in the space group $P6'_3$	53
4.12	Ferromagnetic peak $(2\bar{1}0)$ and the DM interaction	53
4.13	Contraction of manganese ions at the magnetic transition	54
4.14	Atom positions as a function of temperature	55
4.15	The correlation length of YMnO_3	56
4.16	Phonon dispersions for different directions in the Brillouin Zone	57
4.17	Spin wave dispersions for different directions in the Brillouin Zone	57
4.18	Spin wave dispersions along $(q\ 0\ 0)$	58
4.19	Spin wave dispersions for different directions in the Brillouin zone measured with inelastic neutron scattering	58
4.20	Phonons around the zone center measured with inelastic neutron scattering	59
4.21	Phonons and magnon dispersions along $(q\ 0\ 0)$	59
4.22	Hybrid excitation measured with polarized neutrons	60
4.23	Dispersion relation of the hybrid mode	61
4.24	Magnetic structures belonging to the Γ_4 representation of $P6'_3$	62
5.1	RITA II	64
5.2	Picture of the crystal on the sample holder for the RITA II and EIGER experiments	65
5.3	$(\mathbf{Q}, \hbar\omega)$ -range at RITA II, EIGER and C5	66
5.4	EIGER	67
5.5	Picture of the sample and sample holder at C5	68
5.6	Picture of the final sample mount at C5	68
5.7	Sketch of C5	68
5.8	The scattering plane spanned by the perpendicular axes ζ and η	69
6.1	Overview of reciprocal space	71
6.2	Gaussian and Lorentzian distribution	72
6.3	Intensity of the $(0\bar{1}0)$ magnetic Bragg peak	73
6.4	Color maps of diffuse scattering around $(0\bar{1}0)$	75
6.5	Diffuse scattering around $(0\bar{1}0)$	76
6.6	Lorentzian peak width and amplitude as a function of temperature	76
6.7	Lorentzian peak width and amplitude as a function of reduced temperature	77
6.8	Magnon dispersions at $(0\bar{1}0)$	77
6.9	Line width of magnon at $(0\bar{1}180)$	78
6.10	Energy scans around (100) at different temperatures	79
6.11	Energy scans at (100) at selected temperatures	79
6.12	Peak position, amplitude and width at (100)	80
6.13	Color plots at $T = 100$ K and $T = 40$ K	81
6.14	Energy scans of the transverse phonon at different temperatures	82
6.15	Phonon width in Q and energy as a function of temperature	83
7.1	Four selected non-polarized constant- Q -cuts	84
7.2	Color plot at $T = 100$ K and $T = 40$ K with scans done at C5	85
7.3	Bragg peak scans determining the flipping ratio	86
7.4	Polarized neutron data taken at $T = 100$ K	87
7.5	Polarized and non-polarized neutron data taken at $T = 100$ K	88
7.6	Polarized neutron data taken at $T = 40$ K	90
7.7	Polarized and non-polarized neutron data taken at $T = 40$ K	91
7.8	Horizontal and vertical field measurements scaled	92
8.1	Color plots at $T = 100$ K with labels	95
8.2	Color plots at $T = 100$ K with different scaling	95
8.3	Color plots at $T = 40$ K with labels	96

LIST OF FIGURES

8.4	Color plots at $T = 40$ K different scaling	96
8.5	Generic plot of a magneto-elastic coupling	97
8.6	Energy scan at $h = -1$ at $T = 100$ K	98
8.7	Color plots at $T = 100$ K with magnetic dispersion	98
8.8	Persistent spin waves in the (110) direction iron observed by Lynn <i>et al.</i>	99
8.9	Thermal conductivity of YMnO_3 compared with models	100
10.1	The angle of the Mn-spins and the effective magnetic moment under pressure . .	104
10.2	Ordering temperature under pressure	104
10.3	Unit cell volume and lattice constants as a function of pressure	105
A.1	Space group $P6_3mmc$ (No. 194)	114
A.2	Space group $P6_3mmc$ (No. 194)	115
A.3	Space group $P6_3mmc$ (No. 194)	116
B.1	Space group $P6_3cm$ (No. 185)	117
B.2	Space group $P6_3cm$ (No. 185)	118
C.1	Space group $P6'_3$ (No. 173)	119
C.2	Space group $P6'_3$ (No. 173)	120
D.1	Periodic table	121
F.1	Picture of the final sample mount at C5	123
G.1	Diffuse scattering around $(0\bar{1}0)$ at $T = 71$ K, $T = 72.5$ K, $T = 74$ K and $T = 76$ K.	124
G.2	Diffuse scattering around $(0\bar{1}0)$ at $T = 78$ K, $T = 80$ K, $T = 85$ K and $T = 90$ K	125
G.3	Diffuse scattering around $(0\bar{1}0)$ at $T = 100$ K	126
G.4	Energy scan at (100)	127
G.5	Four selected non-polarized constant-Q-cuts	128
G.6	Four selected non-polarized constant-Q-cuts	129
G.7	Q-scans of the transverse phonon at different temperatures	130
G.8	Longitudinal phonon	131
G.9	Polarized data above T_N	132
G.10	Polarized data plotted together with non-polarized data above T_N	133
G.11	Polarized data below T_N	134
G.12	Polarized data plotted together with non-polarized data below T_N	135
G.13	Horizontal and vertical field measurements at $T = 40$ K	136

List of Tables

2.1	Examples of ferroelectrics	10
2.2	The properties of broken symmetry phases	16
3.1	Cross sections of relevant elements	28
3.2	Horizontal field and vertical field cross sections	41
5.1	Settings at the RITA II experiments	65
5.2	Settings at the EIGER experiments	66
5.3	Settings at the C5 experiment	67
8.1	Critical exponents for various models and experiments	94
E.1	Conversion table for neutron scattering	122
E.2	Conversion table for relevant quantities	122

1 Introduction

The introduction section is a short motivation where the key concepts and the structure of the thesis are explained. A justification for the selection of topics from the huge field of multiferroics is included here.

1.1 Motivation

In recent years combining different physical properties in the same chemical compound in order to create new exotic phenomena has become popular. These materials will, hopefully, become the building block for future electronic devices, revolutionizing the data storage industry.

One group of materials that contains different physical properties in the same phase are the so-called multiferroics. A multiferroic material orders in more than one way in the same phase, which is rare because the different orderings, in general, compete as they originate from completely different physical phenomena. A thorough introduction to multiferroic systems will be presented in Sec. 2.5.

The multiferroic system on which this report is based, yttrium manganate (YMnO_3), is magnetically and electrically ordered in the same phase. YMnO_3 is a model system for what is known as a type I multiferroic, where the two phases are entered at different temperatures. It is simple because it contains only one magnetic ion, Mn^{3+} . Unfortunately, YMnO_3 does not become multiferroic until cooled to below 70 K and it is therefore not a viable component of hard disks or other room temperature electronic devices. The known properties of YMnO_3 and previous measurements are presented in Sec. 4.

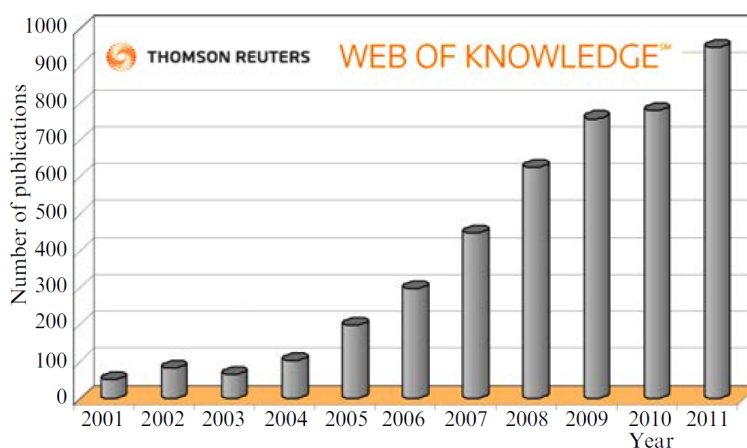


Figure 1.1: The last decade the research field of multiferroics and magnetoelectrics has dramatically increased. From [64]. The numbers for 2012 and 2013 are 1188 and 1176, respectively [93].

The implications and potential applications of the magnetoelectric effect have led to the recent explosion of scientific interest in the field of multiferroics, Fig. 1.1. The magnetoelectric effect is the coupling between magnetic and electric order parameters. This effect makes it possible to switch the electric polarization with a magnetic field and to switch the magnetization with an electric field. In the context of hard disks this effect might be useful. In standard hard disks one writes and reads with magnetic fields, which is difficult, and therefore expensive. With a hard

disk made of multiferroic materials using electric fields, as well as magnetic fields, in the process would be possible, reducing the cost.

For this goal to be realized, understanding a multiferroic system like YMnO_3 at an atomic level is necessary; this thesis is one of many steps toward that goal.

1.2 Magnetoelectric effect

The magnetoelectric effect, the coupling between polarization and magnetization in a material, is the driving force in the field of multiferroics due to the mentioned applications. In Fig. 1.2 the coupling, where it is possible to drive the polarization with a magnetic field and the magnetization with an electric field, is illustrated.

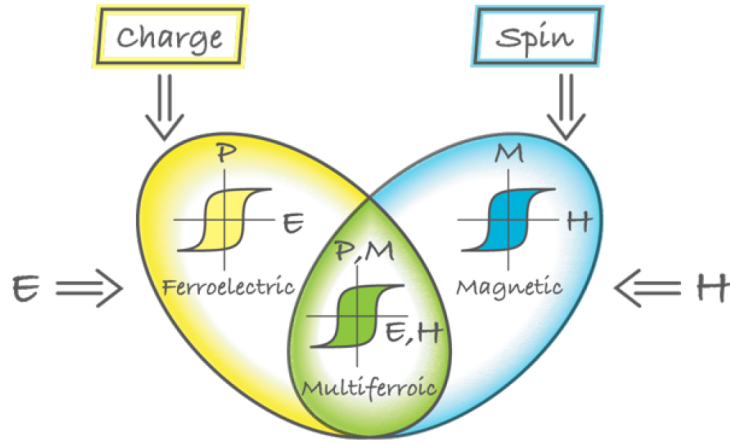


Figure 1.2: The ordering of charges results in a spontaneous polarization and the ordering of spins gives the system a spontaneous magnetization. The polarization can be switched by an electric field and the magnetization can be switched by a magnetic field. When both orderings are present in the same material simultaneously, the dream is to exploit the coupling in the function of hard disks. From [36].

The linear magnetoelectric effect can be revealed by examining the free energy F equation [50]:

$$F(\mathbf{E}, \mathbf{H}) = F_0 - P_i^S E_i - M_i^S H_i - \frac{1}{2} \epsilon_0 \epsilon_{ij} E_i E_j - \frac{1}{2} \mu_0 \mu_{ij} H_i H_j - \frac{1}{2} \beta_{ijk} E_i H_j H_k - \frac{1}{2} \gamma_{ijk} H_i E_j E_k - \dots \quad (1.1)$$

where P is the electric polarization, M is the magnetization, \mathbf{H} is the magnetic field and \mathbf{E} is the electric field. By differentiating the free energy with the electric field E and the magnetic field H , the following expressions for the polarization and magnetization are obtained:

$$P_i(\mathbf{E}, \mathbf{H}) = -\frac{\partial F}{\partial E_i} = P_i^S + \epsilon_0 \epsilon_{ij} E_j + \alpha_{ij} H_j + \frac{1}{2} \beta_{ijk} H_j H_k + \gamma_{ijk} H_i E_j + \dots \quad (1.2)$$

$$M_i(\mathbf{E}, \mathbf{H}) = -\frac{\partial F}{\partial H_i} = M_i^S + \epsilon_0 \epsilon_{ij} H_j + \alpha_{ij} E_j + \beta_{ijk} E_i H_j + \frac{1}{2} \gamma_{ijk} E_j E_k + \dots \quad (1.3)$$

where ϵ and μ are the electric and magnetic susceptibilities, respectively. α is the linear magnetoelectric coupling constant. The higher order couplings, β and γ are much smaller than the first order coupling α .

The magnetoelectric effect is not the only possible coupling in multiferroic materials. Sometimes the coupling is very weak and driven by a mechanism other than the ones creating the polarization or the magnetization. In YMnO_3 , the linear coupling is symmetry forbidden and only higher order magnetoelectric couplings are present. Therefore the magnetoelectric effect is weaker in YMnO_3 than in compounds where the coupling is of first order.

1.3 Symmetry

Symmetry considerations are important when working with multiferroics and one of the reasons why they are rare. In Fig. 1.3 the different types of "ferroic" orderings and their space and time symmetry properties are shown. Only ferroelectrics and (anti)ferromagnets are described in this thesis in Sec. 2.4 and Sec. 2.2, respectively.

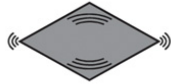
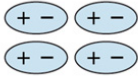
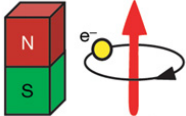
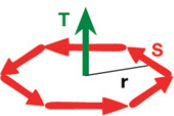
Time \ Space	Invariant	Change
	Invariant	Change
Invariant	Ferroelastic 	Ferroelectric 
Change	Ferromagnetic 	Ferrotoroidic 

Figure 1.3: Ferroelastics are both time and space invariant. Ferroelectrics are time invariant but break space inversion symmetry. Ferromagnetics are space invariant but break time inversion symmetry and ferrotoroidics break both symmetries. From [89].

The ferrotoroidic order, combining both symmetry breakings in one property, is the newest research field in the multiferroics community, but it will not be discussed further in this thesis, and is merely shown here to give the entire picture of the field.

1.4 Neutron scattering

When determining where atoms are and what they do, neutron scattering is the ultimate experimental method. Neutrons can interact with both the nucleus of an atom, determining crystal structures and lattice vibrations, and with the unpaired electron spins revealing magnetic properties. Many different neutron scattering techniques were utilized for examining YMnO_3 ; the theory behind neutron scattering is given in Sec. 3.1.

2 Theoretical background

In this section the relevant theory for understanding the project will be presented, including an introduction to magnetism, the relevant crystal structures, and exotic concepts such as multiferroism and frustration. The section concludes with a presentation about the macroscopic properties of materials, how they are measured and what can be learned about microscopic properties from bulk measurements.

2.1 Crystals and reciprocal space

A material is characterized as a crystal if it has a unit of atoms, called the unit cell, that, if repeated by translation, creates the crystal structure. All crystals belong to a lattice system and a space group.

There are seven lattice systems: triclinic, monoclinic, orthorhombic, tetragonal, trigonal, hexagonal and cubic [51]. There are 14 Bravais lattices (1 triclinic, 2 monoclinic, 4 orthorhombic, 2 tetragonal, 1 trigonal, 1 hexagonal and 3 cubic), and 230 space groups. The space group determines the symmetry operations of a crystal. The space group notation is $Xdef$ where $X = P$ (primitive), I (body-centered), F (face-centered), C (side-centered) or R (rhombohedral) describes the lattice type and def are the three most important symmetry operations of the system, with glide planes and screw axes included [51]. In appendix A-C, examples of three primitive space groups and their symmetry operations are listed. When the space group is known, all symmetry operations and therefore reflections in reciprocal space can be calculated. The space group coupled with lattice dimensions predicts systematic absences and diffraction patterns.

When examining the properties of crystals with X-ray, neutron or electron diffraction techniques, the data received gives information about the Fourier transform of the crystal structure and dynamics. This Fourier transform¹ of real space is called the reciprocal space (or \mathbf{k} -space or momentum space). All crystal structures have a crystal lattice in real space defined by real space lattice vectors [45]:

$$\mathbf{r} = n_a \mathbf{a} + n_b \mathbf{b} + n_c \mathbf{c} \quad (2.1)$$

and the reciprocal lattice is spanned by reciprocal lattice vectors:

$$\mathbf{G}_{hkl} = h\mathbf{a}^* + k\mathbf{b}^* + l\mathbf{c}^* \quad (2.2)$$

defined by:

$$\mathbf{a}^* = 2\pi \frac{\mathbf{b} \times \mathbf{c}}{\mathbf{a} \cdot \mathbf{b} \times \mathbf{c}} \quad \mathbf{b}^* = 2\pi \frac{\mathbf{c} \times \mathbf{a}}{\mathbf{a} \cdot \mathbf{b} \times \mathbf{c}} \quad \mathbf{c}^* = 2\pi \frac{\mathbf{a} \times \mathbf{b}}{\mathbf{a} \cdot \mathbf{b} \times \mathbf{c}} \quad (2.3)$$

\mathbf{G}_{hkl} is normal to the family of (hkl) planes in the real lattice. The connection between the reciprocal lattice vectors and real space lattice spacings is given by:

$$d_{hkl} = \frac{2\pi}{|\mathbf{G}_{hkl}|} \quad (2.4)$$

where d_{hkl} is the spacing between the (hkl) layers, see Fig. 2.1.

¹The Fourier transform is given by $F(\mathbf{k}) = \int_{-\infty}^{\infty} f(\mathbf{r}) \exp(-i\mathbf{k} \cdot \mathbf{r}) d^3r$, where \mathbf{k} is the momentum and \mathbf{r} is the real space lattice vector.

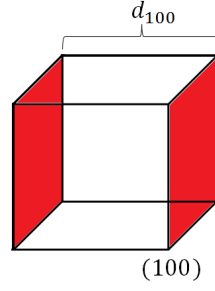


Figure 2.1: The lattice spacing and the lattice planes in a cubic structure. d_{100} is the distance between the (100) lattice planes, which are colored red.

For a simple cubic crystal the real and reciprocal lattices are identical except for the lattice dimensions as can be seen in Fig. 2.2. The hexagonal structure, which is the relevant structure in this thesis, has almost the same real and reciprocal lattice. The only difference is the side lengths and a 30° rotation around the hexagonal axis (the z -axis), Fig. 2.3 .

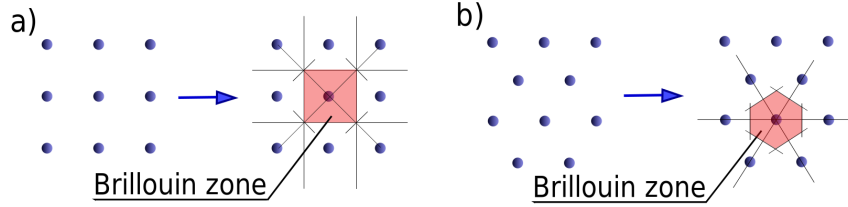


Figure 2.2: The first Brillouin zone contains all information about the lattice vibrations in the solid. Each \mathbf{k} -vector outside the Brillouin Zone is mathematically equivalent to one \mathbf{k} -vector inside the zone. **a)** The relation between the crystal structure in real and reciprocal space for a primitive cubic structure. The Brillouin zone is marked with pink. **b)** The real and reciprocal lattice points for a primitive hexagonal lattice. The Brillouin Zone is marked with pink. Adapted from [94].

For the hexagonal structure the translation vectors in real space are given by:

$$\mathbf{a} = a\hat{\mathbf{x}} \quad \mathbf{b} = \frac{a}{2}(\hat{\mathbf{x}} + \sqrt{3}\hat{\mathbf{y}}) \quad \mathbf{c} = c\hat{\mathbf{z}} \quad (2.5)$$

where the side lengths $a = b \neq c$. Inserting this into Eq. (2.3) the reciprocal lattice vectors for the hexagonal system is obtained:

$$\mathbf{a}^* = \frac{2\pi}{a\sqrt{3}}(\sqrt{3}\hat{\mathbf{x}} + \hat{\mathbf{y}}) \quad \mathbf{b}^* = \frac{4\pi}{a\sqrt{3}}\hat{\mathbf{y}} \quad \mathbf{c}^* = \frac{2\pi}{c}\hat{\mathbf{z}} \quad (2.6)$$

and the unit cell volume V_c is given by:

$$V_c = a^2 c \sin(60^\circ) = \frac{\sqrt{3}}{2} a^2 c \quad (2.7)$$

Not all of reciprocal space needs to be mapped out when examining a crystal. For example, when looking at crystal vibrations (see Sec. 2.6) it is only necessary to look at one Brillouin zone (a volume surrounding one reciprocal lattice point) because the properties of lattice vibrations are periodic in reciprocal space. The Brillouin zone is constructed by drawing lines from one reciprocal lattice point to another and thereafter constructing lines that are perpendicular to the first ones at their midpoints. The primitive cubic and hexagonal Brillouin zones in two dimensions can be seen in Fig. 2.2 and the three dimensional hexagonal Brillouin zone is depicted in Fig. 2.4.

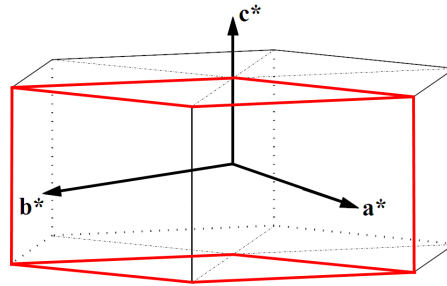


Figure 2.3: The hexagonal unit cell is spanned by the reciprocal lattice vectors \mathbf{a}^* , \mathbf{b}^* and \mathbf{c}^* . The unit cell contour is marked with red. Adapted from [70].

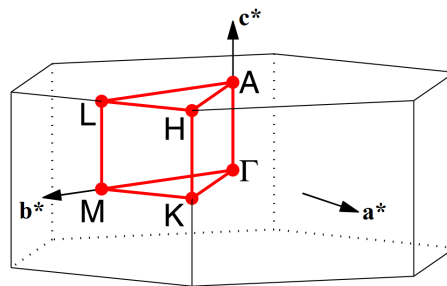


Figure 2.4: The symmetry points spanning the Brillouin zone are conventionally named with capital letters. The zone center, for example, is always called Γ . The notation is used when plotting dispersion relations in different directions of reciprocal space, providing a convention for plotting multiple high symmetry directions in a single two-dimensional plot. Adapted from [70].

2.2 Magnetism

Refrigerator magnets and compass needles are the most well-known type of magnets because their macroscopic magnetization is easily observed. But there are many other types of magnetism – some of which do not arise until the material is cooled close to the absolute zero temperature. But what is the origin of magnetism?

In short, magnetism arises due to unpaired electrons. Electrons have an electric charge and when they orbit the atomic nucleus they form a closed circuit, and induce a magnetic moment [4], see Fig. 2.5.

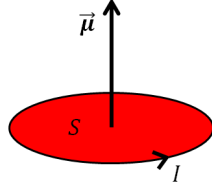


Figure 2.5: The magnetic moment μ points perpendicular to the plane S which is encircled by a current loop I . The magnetic moment could, for example, be induced by the orbital motion of an electron.

When determining the magnetic properties of a material, the orbital angular momentum \mathbf{L} of the electron and the intrinsic angular momentum, called spin \mathbf{S} , as well as the coupling between the two, needs to be considered. The total angular momentum is given by $\mathbf{J} = \mathbf{L} + \mathbf{S}$. In some cases \mathbf{J} is a good quantum number – in some cases it is not. The ground state for a particular ion can be determined by Hund’s empirical rules:

1. Maximize S : This minimizes the Coulomb repulsion energy because the spins are placed as far away from each other as possible, in different orbitals. The spacial part of the wave function has to be antisymmetric.
2. Maximize L : This also minimizes the Coulomb repulsion because the spins move in phase.
3. $J = |L - S|$ if the shell is less than half full or $J = |L + S|$ if the shell is more than half full, which is related to minimizing the spin-orbit coupling energy.

According to Hund’s rules the estimated ground state magnetic moment is given by $\mu_{\text{effective}}/\mu_B = g_J \sqrt{J(J+1)}$ where g_J is the Landé g -factor [38]:

$$g_J = 1 + \frac{J(J+1) + S(S+1) - L(L+1)}{2J(J+1)} \quad (2.8)$$

Hund’s rules work well for rare earth metal ions because their unfilled $4f$ -orbitals are low-lying and screened by the $5s$ and $5p$ -orbitals and the orbitals of the ligands will not change the energy of the $4f$ -orbitals. It is a different matter with transition metal ions where Hund’s third rule is partially overruled by both the crystal field² and Jahn-Teller distortions³ because the d -orbitals overlap with the p -orbitals from the ligands. The crystal field will lower the energy of some orbitals and increase the energy of other orbitals, and the electrons will occupy the orbitals with the lowest energy.

For the transition metal ion Mn^{3+} , applying Hund’s rules gives the ground state quantum number $S = 2$, $L = 2$ and $J = 0$ and the magnetic moment $\mu_{\text{effective}}/\mu_B = 0$. This is not true and the reason is orbital quenching [45]. For transition metal ions the predicted moment is much closer to the experimental value if $\mathbf{L} = 0$ so that $\mathbf{J} = \mathbf{S}$ and $g_J = 2$ and the ground state magnetic moment given by:

$$\mu_{\text{effective}}/\mu_B = 2\sqrt{S(S+1)} \quad (2.9)$$

For the Mn^{3+} ions, Eq. (2.9) gives $\mu_{\text{effective}}/\mu_B = 4.9$ whereas the experimental value is $\mu_{\text{experimental}}/\mu_B = 4.82$ [4]. The spin-orbit coupling can be included as a perturbation which results in a ground state that is quenched, but with a g -value that differs slightly from the spin-only g -value of 2. The deviation from 2 gives an idea of the size of the spin-orbit coupling. The

²When a transition metal ion is free, it has spherical symmetry and the d -orbitals are degenerate, but when the ion is surrounded by ions in a crystal lattice, the spherical symmetry is broken and the atomic orbitals are no longer degenerate. This is called the crystal field splitting.

³In some crystal environments an elongation of one of the crystal axes can lower the symmetry and also the energy of the system. This is called a Jahn-Teller distortion.

ordering of magnetic moments, and thereby the origin of magnetism, is mediated by the quantum mechanical exchange interaction. The simplest mathematical expression for the exchange energy is the Heisenberg Hamiltonian, which describes the interaction between spins \mathbf{S}_i and \mathbf{S}_j .

$$\mathbf{H} = - \sum_{ij} J_{ij} \mathbf{S}_i \cdot \mathbf{S}_j \quad (2.10)$$

where J_{ij} is the exchange interaction. $J_{ij} > 0$ favors a parallel spin arrangement to minimize the energy and $J_{ij} < 0$ favors an anti-parallel spin arrangement to minimize the energy.

When a magnetic material is cooled down below some critical temperature T_c , time-reversal symmetry (and sometimes rotational and translational symmetry) breaks spontaneously and the magnetic moments arrange themselves relative to each other. If all the spins are parallel, the system is ferromagnetically ordered. If the spins are anti-parallel the order is antiferromagnetic. These two types of magnetic orderings are depicted in Fig. 2.6. For a ferromagnet the critical temperature is called the Curie temperature T_C and the order parameter is the magnetization \mathbf{M} , defined as the sum over all the magnetic moments $\boldsymbol{\mu}$:

$$\mathbf{M} = \sum_i \boldsymbol{\mu}_i \quad (2.11)$$

The order parameter is a parameter that is zero above the critical temperature and non-zero below the critical temperature. The Néel temperature T_N is the critical temperature for an antiferromagnet. Because the magnetization is zero, the order parameter of the phase transition is the staggered magnetization *i.e.* the sum of the magnetizations of the individual lattices with spin up and spin down: $\mathbf{M}_A - \mathbf{M}_B$.

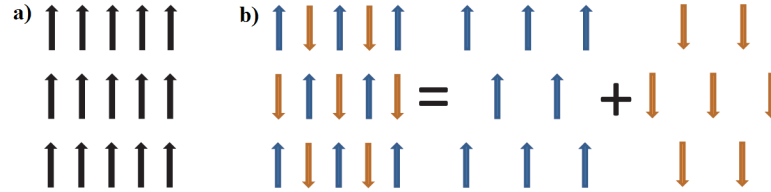


Figure 2.6: a) The black arrows indicate a ferromagnetically ordered spin configuration. b) One can think of the antiferromagnetic spin configuration as two combined lattices where half the spins point up (blue arrows) and the other half point down (brown arrows).

There are many exchange interactions which couple the spins to each other. Two of them will be presented below: the superexchange interaction and the Dzyaloliskii-Moriya interaction (or just DM-interaction).

The "super" in superexchange interaction means that the coupling is not directly between the magnetic ions, but mediated by a non-magnetic ion. The size of the interaction depends on the size of the overlap between the orbitals so the angle between the magnetic ions and the ligand is important. The superexchange interaction lowers the kinetic energy by delocalizing electrons throughout the crystal structure. The superexchange interaction favors antiferromagnetic ordering as depicted in Fig. 2.7. A ferromagnetic coupling would prevent the delocalization because of Pauli's exclusion principle.

The DM-interaction is a relativistic correction to the superexchange interaction. It arises due to spin-orbit coupling, and the strength of the interaction is proportional to the spin-orbit

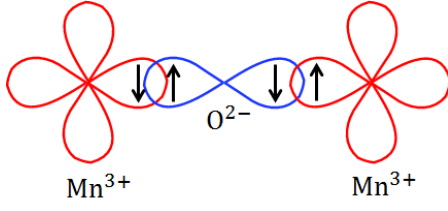


Figure 2.7: The superexchange interaction is mediated by the bridging ion (in this case oxygen). The spins creating the magnetism in the magnetic ion (in this case Mn^{3+}) can move, via the p -orbitals of oxygen and thereby become delocalized. Adapted from [81].

coupling. In materials with transition metal ions, the DM-interaction is small because of orbital quenching. The DM-interaction is a ferromagnetic interaction with the Hamiltonian:

$$H_{DM} = \mathbf{D}_{12} \cdot (\mathbf{S}_1 \times \mathbf{S}_2) \quad (2.12)$$

where the coupling constant \mathbf{D}_{12} depends on the vector between the two magnetic sites \mathbf{r}_{12} and the displacement vector of the ligand out of the plane \mathbf{x} , Fig. 2.8:

$$\mathbf{D}_{12} \propto (\mathbf{x} \times \mathbf{r}_{12}) \quad (2.13)$$

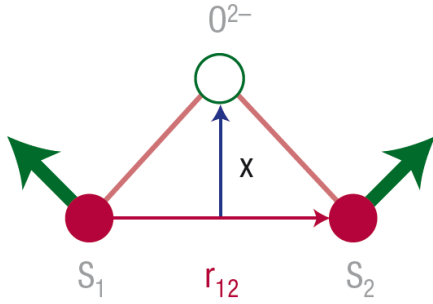


Figure 2.8: The Dzyaloshinskii-Moriya interaction induces a small net magnetic moment perpendicular to plane of which the spins have ordered. From [13].

To determine the magnetic structure of a crystal, one needs to know the direction and magnitude of all the magnetic moments on all of the magnetic ions. Those can be found with neutron scattering (see Sec. 3.5.2).

2.3 Geometrical frustration

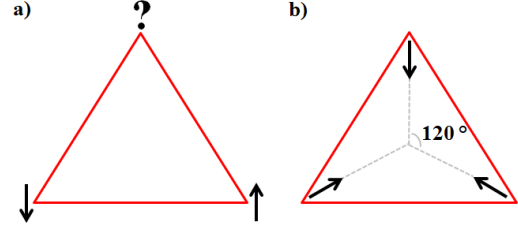
The antiferromagnetic exchange interaction can make things complicated if the system, for geometrical reasons, cannot fulfill the antiferromagnetic interactions [4]; this is the case for a triangular lattice. An illustration of the problem with three spins can be seen in Fig. 2.9. In this case only one spin is frustrated because it cannot be antiparallel to both its neighbors, but if the structure is expanded to include more spins the system will contain many frustrated spins that will fluctuate. It is not possible to satisfy all the interactions in the system to find a ground state, which creates both a degeneration of the ground state energy and a larger entropy.

The entropy S is given by:

$$S = k_B \ln(\# \text{ of states}) \quad (2.14)$$

For N spins that can either point up or down, resulting in 2^N possible states, Eq. (2.15) gives the maximal value of the entropy:

Figure 2.9: In an antiferromagnetically coupled triangular lattice, one of the spins is frustrated. **a)** $S = 1/2$ case, the first two spins are antiparallel, but the third spin can not pick a satisfactory direction. No matter what the third spin chooses one of the neighbors in the triangle will not have the energy minimized. **b)** In the classical magnet the spins tend to turn and point in a 120° angle with respect to each other minimizing the frustration.



$$S_{\max} = Nk_B \ln(2) \quad (2.15)$$

For the three spins in Fig. 2.9 the number of states is 2^3 i.e. $S = 3k_B \ln(2)$.

2.4 Ferroelectricity

Ferroelectricity was first discovered in Rochelle salt ($\text{KNaC}_4\text{H}_4\text{O}_6 \cdot 4\text{H}_2\text{O}$) in 1921 [86], where the first polarization hysteresis loop was measured. Since then many other compounds have been discovered and ferroelectric materials are used in many electronic devices today.

A ferroelectric material attains a stable and switchable electric polarization at a critical temperature T_c where it goes from a paraelectric phase to a ferroelectric phase. It is a structural phase transition where atomic displacement changes break inversion symmetry and thereby create a permanent polarization, inducing a surface charge.

The Landau Theory is accurate for systems with long range order and thereby ferroelectrics. All ferroelectrics are insulators. If they were not, an applied electric field would create a current flow instead of a permanent polarization. There are two groups of ferroelectrics: proper ferroelectrics and improper ferroelectrics [92]. The difference between the two types is the mechanism that breaks the inversion symmetry and thereby induces a polarization in the system. Examples of proper and improper ferroelectrics can be found in Table 2.1.

Some proper ferroelectrics and some improper ferroelectrics are type I multiferroics, while a few of the improper ferroelectrics are type II multiferroics, which will be discussed further in Sec. 2.5.

Type	Mechanism creating ferroelectricity	Compound
Proper	Covalent bonding between d^0 -orbital and ligand	BaTiO_3 , PbTiO_3 , PbZrO_3
Proper	Polarization of lone pair	BiMnO_3^* , BiFeO_3^* , PbVO_3^*
Improper	Charge ordering	$\text{LuFe}_2\text{O}_4^*$, $\text{Ca}_3\text{CoMnO}_6^*$, $\text{TbMn}_2\text{O}_5^{**}$
Improper	Magnetic (collinear) ordering	$\alpha\text{-RMnO}_3^{**}$, $R = \text{Y, Ho}$
Improper	Magnetic (spiral) ordering	$\text{Ni}_3\text{V}_2\text{O}_6^{**}$, MnWO_4^{**} , $\alpha\text{-RMnO}_3^{**}$, $R = \text{Tb, Dy, Gd}$
Improper	Structural transition	$h\text{-RMnO}_3^*$, $R = \text{Y, Yb, Ho, In}$

Table 2.1: Examples of proper and improper ferroelectrics. The compounds marked with * are type I multiferroics and the compounds marked with ** are type II multiferroics. From [13], [36] and [92].

2.4.1 Proper ferroelectrics

The primary order parameter in a proper ferroelectric is the ferroelectric distortion. The size of the spontaneous polarization P for a proper ferroelectric is around $100\mu\text{C}/\text{cm}^2$ [92]. In a

proper ferroelectric, an ionic displacement breaks inversion symmetry. There are two different ways of inducing ferroelectricity in a proper ferroelectric: by creating a covalent bond between a d^0 -orbital (an empty d -orbital) and a p -orbital and by the polarization of a s^2 lone pair; both are explained below.

The mechanism using a d^0 -orbital works by displacing a non-magnetic ion away from the center of its surrounding anions and thereby creating an electric dipole moment in the material. This off-center displacement stabilizes the system because the non-magnetic ion is positive and the ligands are negative and the displacement creates a strong covalent bond with the surrounding ions, see Fig. 2.10. Examples are BaTiO_3 and PbZrO_3 ; these compounds contain the d^0 -ions Ti^{4+} and Zr^{4+} , respectively, that form a covalent bond with oxygen ions. Ferroelectrics created by the d^0 -orbital mechanism can never be magnetic.

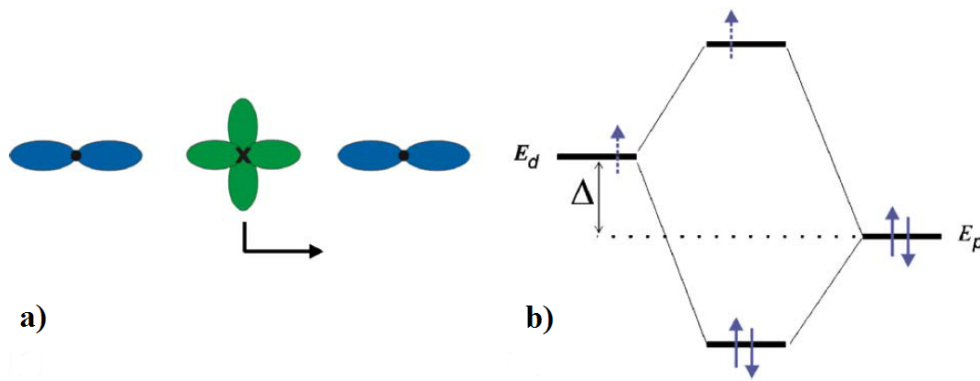
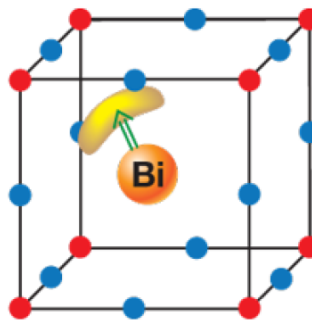


Figure 2.10: a) Visualization of the angular part of the (green) d -orbitals being shifted towards the angular part of the (blue) p -orbital of one of the surrounding oxygen atoms. b) If the d -orbital is empty no electrons will occupy the anti-bonding molecular orbital and the overall energy is lowered by the creation of a covalent bond. On the other hand if the transition metal has a magnetic moment i.e has unpaired electrons in the d -orbital, the anti-bonding molecular orbital will be occupied (illustrated with a dashed arrow) and the shift is not favourable for the system. E_d is the energy of the d -orbital, E_p is the energy of the p -orbital and Δ indicates the energy difference between E_d and E_p . From [35].

The other mechanism that can create a proper ferroelectric is the polarization of a lone pair, which makes it possible for a compound with d -electrons to be ferroelectric, Fig. 2.11. For example, the two compounds BiMnO_3 and BiFeO_3 contain magnetic Mn^{3+} and Fe^{4+} ions, respectively. This makes it unfavorable to create a covalent bond with the ligands as shown in Fig. 2.10 b) because the anti-bonding molecular orbital is occupied. Instead, the materials create a polarization with the lone pair on the Bi^{3+} -ions. The polarization is created because the lone pair shifts away from its centrosymmetric position compared to the surrounding ligands, creating hybridized sp^2 or sp^3 states with the low-lying p -orbitals [92]. The lone pair induced ferroelectrics can be magnetic if they contain a magnetic ion in the B-site (ABO_3) and are therefore interesting in relation to multiferroics.

Figure 2.11: Illustration of a lone pair induced polarization. If all the $6s^2$ -lone pairs on Bi^{3+} (marked with yellow) order, a polarization is induced in the direction of the green arrow. The red spheres are the transition metal ions (Mn^{3+} or Fe^{4+}) and the blue spheres represent oxygen. From [36].



2.4.2 Improper ferroelectrics

An improper ferroelectric is a material where the ferroelectricity is a byproduct of some other mechanism. For example, it could be the creation of magnetic ordering that induces a polarization [36]. Ferroelectrics of this kind are called "magnetic ferroelectrics"⁴. Another mechanism could be a structural transition that creates a "geometrical ferroelectric" or it could be induced by charge ordering creating "electronic ferroelectrics". Illustrations of the different mechanisms inducing ferroelectricity can be seen in Fig. 2.12. The polarization size for improper ferroelectrics is typically two to three orders of magnitude smaller than for proper ferroelectrics [13].

2.5 Multiferroics

Multiferroic materials combine the different orderings (anti)ferromagnetism, ferroelectricity and ferroelasticity in the same structural phase. A ferromagnet shows hysteresis in the magnetization \mathbf{M} , a ferroelectric shows hysteresis in the polarization \mathbf{P} and a ferroelastic shows hysteresis in strain σ . As illustrated in Fig. 2.13, multiferroic systems show hysteresis loops in all their order parameters. Because the different order parameters are present in the same phase they are coupled to each other. However, the amount of coupling differs greatly from compound to compound.

The most desired effect, which has been studied extensively, is the magnetoelectric coupling, where it is possible to control magnetization with an electric field and control polarization with a magnetic field. To a first approximation, the magnetoelectric coupling is at first glance possible in systems with any type of magnetic long range ordering and a spontaneous electric polarization, hence many different compounds have been studied.

The multiferroic properties are attractive because they may have practical applications, but multiferroic systems are rare. This is because ferroelectricity and ferromagnetism in most cases are incompatible [26]. The first problem is symmetry. Magnetism breaks time reversal and ferroelectrics break inversion symmetry, as illustrated in Fig. 2.14. In multiferroics time and space inversion symmetry needs to be broken simultaneously, which restricts the abundance of multiferroic materials.

Out of the 122 Shubnikov magnetic groups (crystallographic space groups combined with time inversion symmetry) [26] only 31 allow a spontaneous polarization and 31 allow a spontaneous magnetization. The only 13 groups that are found in both groups and thereby allow for simultaneous polarization and magnetization. These are: 1, 2, $2'$, m , m' , 3, $3m'$, 4, $4m'm'$, $m'm2'$, $m'm'2'$, 6 and $6m'm'$ [92], where 1, 2, 3, 4 and 6 are pure 1-fold, 2-fold, 3-fold, 4-fold and

⁴Magnetic ferroelectrics are always multiferroics and have created a new class of multiferroics called type II multiferroics. This will be discussed further in Sec. 2.5

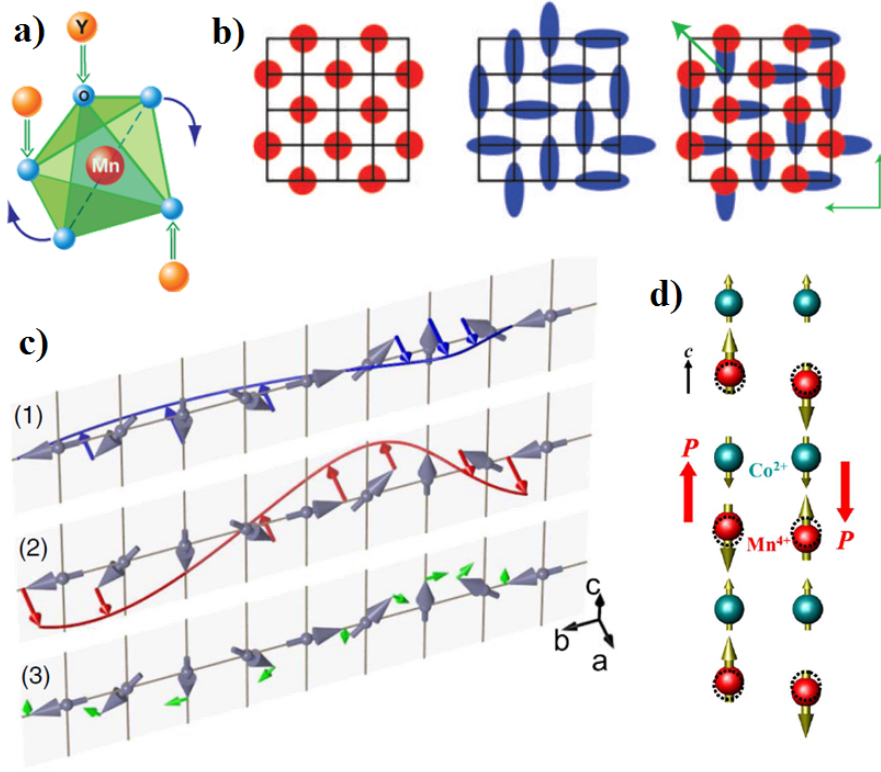


Figure 2.12: a) Illustration of a geometrically induced polarization. The tilting of the Mn-polyhedra indicated with the blue arrows moves the oxygen ions (blue spheres) closer to the yttrium-ions (orange spheres) and thereby induce a polarization. The Mn-ions are stationary in the process. This is the mechanism for h -YMnO₃, which is the focus of this thesis. From [36]. b) Illustration of three different types of charge ordering. The leftmost picture illustrates site-centered charge order. The middle picture shows bond-centered charge orderings which breaks inversion symmetry and thereby creates a polarization indicated with the green arrows. From [19]. c) Illustration of a magnetic spiral induced polarization. From [69]. d) Illustration of a magnetic collinear induced polarization in Ca₃CoMnO₆. The red spheres are the Mn⁴⁺-ions and turquoise spheres are Co²⁺-ions, which order in a $\uparrow\uparrow\downarrow\downarrow$ (two spins pointing up followed by two pointing down) inducing different directions of the polarization shown with a red arrow. From [14].

6-fold rotation axis, respectively, m is a mirror plane and $'$ represents time inversion. In the 1 group both the spins and the polarization can point in arbitrary directions. In the $2'$ and $m'2'$ groups the spins must point perpendicular to the 2-fold axis and in the m' group the spins can point in any direction in the plane. In the m group the spins must point perpendicular to the plane. In the 2 and $m'2'$ group the spins must point along the axis. For the rest of the groups, 3 , $3m'$, 4 , $4m'2'$, $m'2'$, 6 and $6m'2'$, the spins must point along the axis of higher order. Furthermore, very few of the materials belonging to these 13 groups are in fact multiferroics.

This is due to the competing origins of the different orderings. As shown in Table 2.1 most systems that are ferroelectric contain a non-magnetic transition metal ion and for systems to order

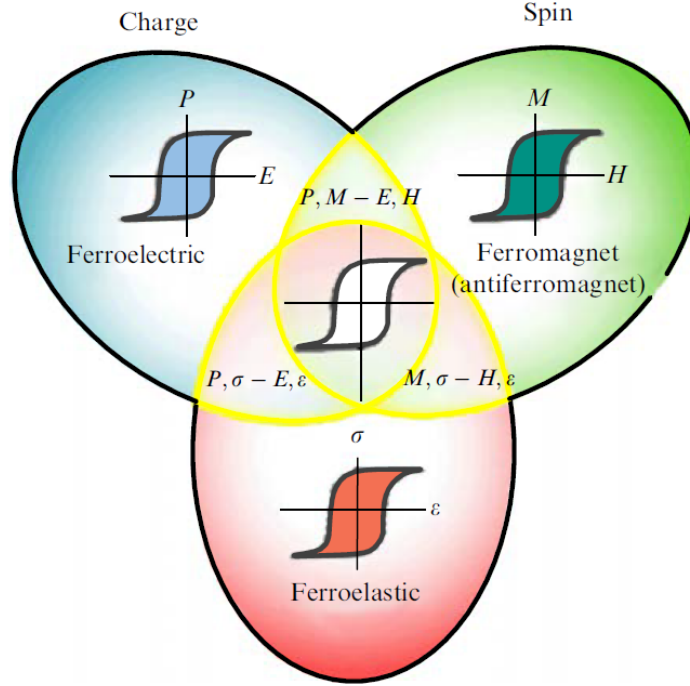


Figure 2.13: A multiferroic material possesses two or all of the following properties: (anti)ferromagnetism, ferroelectricity, and ferroelastisity. The magnetization (polarization or strain) can be switched by a magnetic (electric or stress) field. If a sample is ferroelectric and ferromagnetic simultaneously the coupling between the two order parameters may make it possible to switch the magnetization with an electric field and vice versa. From [64].

(anti)ferromagnetically they need to contain a ion with unpaired spins. In addition, materials that contain magnetic ions tend to be metallic and not insulators which makes it impossible to be ferroelectric [26].

2.5.1 Type I multiferroics

In type I multiferroics the ferroelectric phase transition often occurs at higher temperatures than the magnetic ordering temperature, $T_c > T_N$, since the two orderings originate from different sources. The spontaneous polarization is quite large for these multiferroics, but the coupling is weak due to the different origins.

Of the proper ferroelectrics only the lone pair induced can be multiferroics, see Table 2.1. BiFeO_3 attains a polarization of $P = 75 \mu\text{C}/\text{cm}^2$ below $T_c = 1103 \text{ K}$ and orders magnetically below $T_N = 643 \text{ K}$ [92]. It is the only known room temperature multiferroic. Another multiferroic in this class is BiMnO_3 , which is special because both the magnetization and polarization are quite large. It enters the ferroelectric phase below $T_c = 800 \text{ K}$ with a polarization of $P = 20 \mu\text{C}/\text{cm}^2$ and orders magnetically below $T_N = 100 \text{ K}$.

Of the improper ferroelectrics, the ones induced by charge ordering and geometric distortions

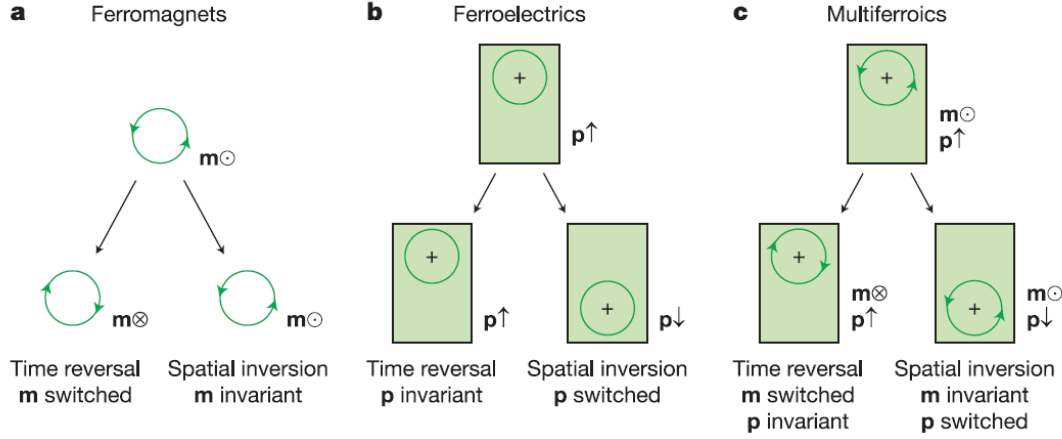


Figure 2.14: Multiferroics are rare because of symmetry restrictions. **a)** The magnetization in a ferromagnet changes sign under time-inversion, but is unchanged under space inversion. **b)** The ferroelectric polarization is invariant under time-inversion and changes sign under space inversion. **c)** A multiferroic system needs to break both time and space inversion simultaneously. Otherwise it is not possible for the two properties to coexist in the same phase. From [18].

are contained in this group. Hexagonal HoMnO_3 is one of the geometric ferroelectrics with a polarization $P = 5.6 \mu\text{C}/\text{cm}^2$ attained below $T_c = 950$ K and with a magnetic ordering of the Mn^{3+} -ions below $T_N = 76$ K and ordering of the Ho^{3+} -ions at $T_C = 5$ K. Hexagonal HoMnO_3 is closely related to the compound examined in this thesis, hexagonal YMnO_3 , except for the presence of the magnetic rare earth ions.

The problem with the type I multiferroics is that only a weak indirect coupling between the two order parameters can occur because the phase transitions are far apart in temperature, originating from the different mechanisms and for symmetry reasons.

2.5.2 Type II multiferroics

The magnetically induced ferroelectrics are called type II multiferroics. The ferroelectricity only exists in the magnetically ordered phase *i.e.* $T_c \leq T_N$ [36] and the ferroelectricity would not exist without the magnetic order and the coupling between the two order parameters is large.

Examples of type II multiferroics are TbMnO_3 , TbMn_2O_5 , $\text{Ni}_3\text{V}_2\text{O}_6$ and MnWO_3 [36]. They all have a spiral magnetic ordering due to spin-frustration that breaks inversion symmetry and thereby allows polarization. In the Tb-compounds, the influence of a magnetic field on the polarization is large [37].

The other group of systems that are type II multiferroics are the ones with collinear magnetic ordering. An example is $\text{Ca}_3\text{CoMnO}_6$ [14] where the different magnetic ions Mn^{4+} and Co^{2+} result in a one-dimensional frustration of the spins, called exchange striction, between ferromagnetic and antiferromagnetic couplings due to magnetic order of the form $\uparrow\uparrow\downarrow\downarrow$ (two spins pointing up is followed by two pointing down). The two spins in the middle are frustrated because they cannot fulfill being either ferromagnetically coupled or antiferromagnetically coupled to both neighbors. In the family of orthorhombic RMnO_2 , where R is a small rare earth ion like Y^{3+}

and Ho^{3+} , the ferroelectricity is also induced by the magnetic $\uparrow\uparrow\downarrow$ ordering of the Mn^{3+} -ions. The frustration pushes the oxygen ions in a direction perpendicular to the plane of the magnetic ordering [46].

2.5.3 The RMnO_3 multiferroics

Let us take a closer look at the multiferroics of the form RMnO_3 where R is a rare earth ion or the transition metal ions Sc, Y, In and Lu [58]. These transition metal ions all behave like the rare earth ions because they are positioned in group 3 and 13 and therefore have the preferred oxidation number 3+ like the rare earth metals. RMnO_3 can crystallize in two different forms: orthorhombic (perovskite) (o- RMnO_3) and hexagonal (h- RMnO_3). A periodic table where the relevant elements are marked can be found in appendix D.

In the orthorhombic form the Mn^{3+} -ions are surrounded by six oxygen atoms in an octahedral environment. All the mentioned R ions can form crystals of the orthorhombic form. Only the smallest R -ions (Ho, Er, Tm, Yb, Sc, Y and Lu) can form the hexagonal crystal form naturally⁵, whereas the Mn^{3+} -ions are surrounded by only five oxygen ions in a trigonal bipyramidal environment. The trigonal and orthorhombic metal ion environments give rise to different orbital splittings of the Mn-ion orbitals [4]. In both the orthorhombic and the hexagonal form the nature of the R -ions, whether if the ion is magnetic or not, influences the multiferroic properties.

All the orthorhombic forms are type II multiferroics with spiral or collinear magnetic ordering that induces the ferroelectricity.

The hexagonal forms are type I multiferroics with a magnetic transition temperature well below the ferroelectric ordering temperature. If they contain magnetic rare earth ions, these order below the Mn^{3+} ordering temperature.

In Sec. 4 the type I multiferroic hexagonal YMnO_3 where Mn^{3+} is the only magnetic ion, is investigated further.

2.6 Elementary excitations

In all ordered phases there are elementary excitations and studies of the excitations reveal dynamic properties, see Table 2.2.

Ordering	Broken Symmetry	High T Phase	Low T Phase	Order parameter	Excitations
Crystal	Translation & rotation	Liquid	Solid	$\rho\mathbf{G}$	Phonons
Ferromagnet	Rotation & time	Paramagnet	Ferromagnet	\mathbf{M}	Magnons
Antiferromagnet	Rotation & time	Paramagnet	Antiferromagnet	$\mathbf{M} = \mathbf{M}_\uparrow - \mathbf{M}_\downarrow$	Magnons
Ferroelectric	Inversion	Paraelectric	Ferroelectric	\mathbf{P}	Soft Modes
Ferroelastic		Paraelastic	Ferroelastic	$\boldsymbol{\sigma}$	
Multiferroic	Inversion & time	Paraelectric & paramagnet	Multiferroic	\mathbf{P} & \mathbf{M} & $\boldsymbol{\sigma}$	Electromagnons

Table 2.2: When a system enters the low T phase from the high T phase the symmetry is broken. The order is weakened by excitations in the order parameter.

There are two different types of phase transitions: first order phase transition where the change in the order parameter across the critical temperature is discontinuous and second order phase transitions with a continuous change in the order parameter across the critical temperature. An example of a first order phase transitions is the melting of ice. Most magnetic phase transitions are second order phase transition and are characterized by a divergent susceptibility, an infinite correlation length, and an exponential decay of correlations near criticality. The

⁵For the small R -ion compounds the perovskite structure is only metastable and the synthesis needs to be done under high-pressure conditions [46].

exponent of the power law decay is called a critical exponent and the critical exponent helps determine the nature of the system. The critical exponent for the decay of the magnetization M is called β and determined by a fit to [4]:

$$M \propto (T_C - T)^\beta \quad (2.16)$$

for $T < T_C$. Different magnetic models have their own β -value: the Mean-Field model ($\beta = 1/2$), the two-dimensional Ising model ($\beta = 0.125$), the three-dimensional Ising model ($\beta = 0.326$) and the 3-dimensional Heisenberg model ($\beta = 0.367$) [4]. The β -value for a given material contains information about which of the simple models best describes the system.

The β -value is determined by measuring the intensity of a magnetic Bragg peak around the transition temperature and then fitting the data to the power law in Eq. (2.16). The points used for fitting should be chosen with care, since the law is only valid for temperatures close to T_C . If critical scattering⁶ is present close to T_C those points should not be included either.

2.6.1 Lattice vibrations

In crystals the elementary excitations are vibrations in the lattice. The energy of the vibration depends on where in the Brillouin zone it is found. The energy of a lattice vibration is quantized and called a phonon. Every atom has three degrees of freedom and therefore three modes of vibration (along x , y and z): two transverse movements where the displacement of the atoms is perpendicular to the propagation direction \mathbf{q} and one longitudinal movement where the displacement of the atoms is parallel to the propagation direction of the vibration, Fig. 2.15.

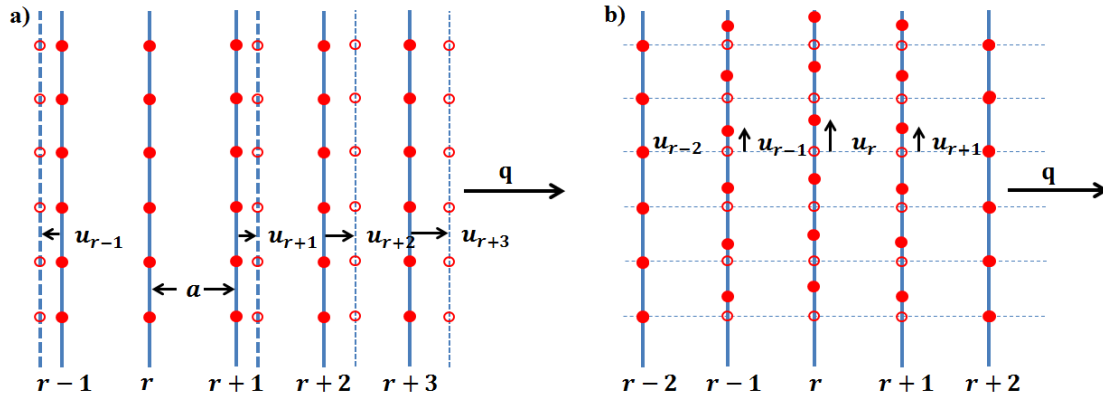


Figure 2.15: a) The displacement of the atoms is parallel to the propagation direction \mathbf{q} for longitudinal phonons. a is the lattice spacing between adjacent layers \mathbf{r} and $\mathbf{r} + 1$ and the displacements away from equilibrium is given by \mathbf{u} . b) For transverse phonons the displacement of the atoms is perpendicular to the propagation direction \mathbf{q} .

⁶When approaching a critical phase transition, for example going from a paramagnetic phase to a ferromagnetic phase, small regions of the ferromagnetic phase appear in the paramagnetic phase (approaching T_C from high temperatures) and small regions of the paramagnetic phase appear in the ferromagnetic phase when approaching T_C from low temperatures. These small regions are short-lived and fluctuate and give rise to critical scattering. When reaching the critical temperature, from both below and above, the regions increase in size and diverge at the critical point [15].

For a crystal with p atoms in the unit cell and N unit cells, there are in total pN atoms. In this crystal there are $3pN$ degrees of freedom. In the Brillouin zone the number of allowed \mathbf{q} -values is N , so the number of acoustic phonons is $3N$. The dispersion relation for a one-dimensional acoustic phonon branch can be seen in Fig. 2.16 b).

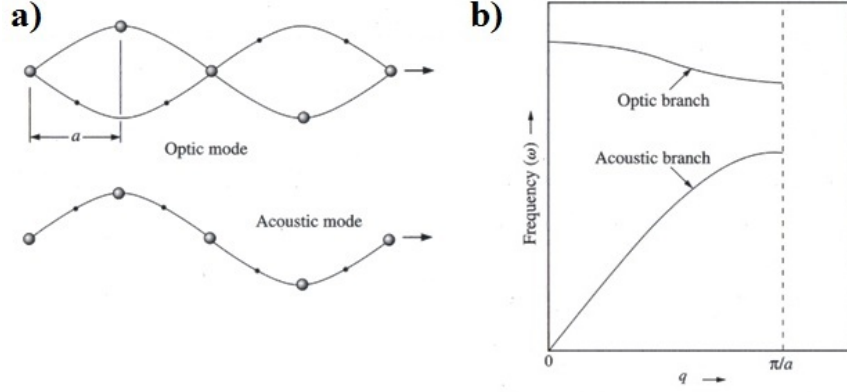


Figure 2.16: **a)** The movements of the atoms in both an acoustic phonon and an optical phonon in a one-dimensional chain with two different atoms. In an acoustic phonon the atoms are in phase and in the optical phonon the atoms are out of phase. **b)** The dispersion of an acoustic and optical phonon in a di-atomic chain with lattice spacing a in the first Brillouin zone. The amplitude at the zone boundary ($q = \pi/a$) is a measure of the spring constant. From [95].

The remaining $(3p - 3)N$ degrees of freedom belong to the optical phonons. The amplitudes of the phonons are given by the displacement of the atoms from equilibrium. For a chain with one kind of atoms of mass m in the unit cell the energy of the lattice vibrations can be described by the following Hamiltonian:

$$\mathbf{H} = \sum_{i=1}^N \frac{\mathbf{p}_i^2}{2m} + \frac{1}{2} m \omega^2 \sum_{\langle ij \rangle} (\mathbf{x}_i - \mathbf{x}_j)^2 \quad (2.17)$$

where the first term is the kinetic energy and the second term is the potential energy of a harmonic oscillator with spring constant $K = m\omega^2$ summed over nearest neighbors. The frequency ω for a chain with two different atoms m_1 and m_2 in the unit cell is given by [38]:

$$\omega_{\pm}^2(q) = K \left(\frac{1}{m_1} + \frac{1}{m_2} \right) \pm K \sqrt{\left(\frac{1}{m_1} + \frac{1}{m_2} \right)^2 - \frac{4 \sin^2\left(\frac{qa}{2}\right)}{m_1 m_2}} \quad (2.18)$$

For each q value there are two branches of ω . The plus sign $\omega_+(q)$ gives the frequency of the optical phonon branch. The dispersion for a one-dimensional optical phonon can be seen in Fig. 2.16 b). In the long wave length limit (for small qa) the frequency of the optical phonon is given by:

$$\omega^2 \approx 2K \left(\frac{1}{m_1} + \frac{1}{m_2} \right) \quad (2.19)$$

Optical phonons are lattice vibrations where the atoms inside one unit cell move in anti-phase – one atom moves to the left and the neighboring atom to the right, see Fig. 2.16 a). They do

not show a dispersion at the zone center as can be seen in Eq. (2.19). Optical phonons may be excited by infrared radiation because an electric field will move all positive ions in one direction and all the negative ions in the opposite direction. This is utilized in Raman spectroscopy.

The acoustic phonon frequency is obtained taking the minus sign in Eq. (2.18). In the long wavelength limit where qa is small the following dispersion is obtained:

$$\omega^2 \approx \frac{K/2}{m_1 + m_2} q^2 a^2 \quad (2.20)$$

which shows that even at low temperatures the acoustic phonons are important. The atoms move in the same direction (in phase) and they carry the speed of sound in the lattice, see Fig. 2.16 a). The slope of the dispersion is approximately linear at small \mathbf{q} (long wavelength).

Knowledge of the phonons in a crystal gives a lot of information about the system. The high velocity (large slope) phonons are responsible for the heat conductivity. If the phonon density of states (all the combined phonon dispersion relations) is known, it determines the heat capacity of a crystal. Phonons are bosons and the number of phonons is therefore given by the Bose factor [95]:

$$n_j(\mathbf{q}) = \frac{1}{\exp(\hbar\omega_j(\mathbf{q})/k_B T) - 1} \quad (2.21)$$

where $n_j(\mathbf{q})$ is the number of phonons with wave vector \mathbf{q} belonging to the j th branch of the dispersion relation. If the temperature is zero there are no phonons present.

2.6.2 Spin waves

In three-dimensional magnetically ordered systems the excitations are called spin waves. Since the spins are coupled to each other via the exchange interaction the movement of one spin will influence the neighboring spins and thereby initialize a wave of spins precessing around a given axis, Fig. 2.17. The energies of spin waves are quantized, like those of lattice vibrations and are called magnons.

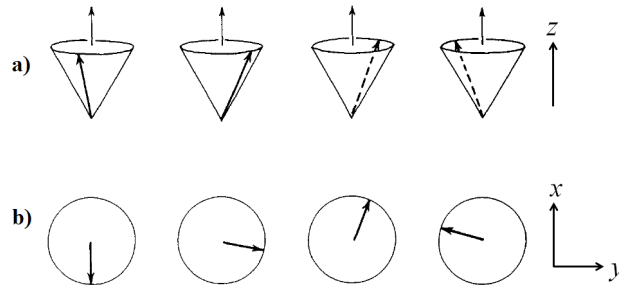


Figure 2.17: Visualization of a ferromagnetic spin wave. **a)** The spins all precess around the z -axis. **b)** Looking down the z -axis the component of the spins in the xy -plane show a wave motion. From [76].

Measurements of the dispersion relations of magnons gives a measure of the coupling constant J and the degree of long range order. For a ferromagnetically coupled linear chain the dispersion relation is given by:

$$\hbar\omega = 4JS(1 - \cos(qa)) \quad (2.22)$$

where $\hbar\omega$ is the spin wave energy, J is the exchange coupling, S is the magnitude of the spin, a is the distance between two adjacent atoms and q is the magnitude of the wave vector [9]. For small q , $\hbar\omega \propto q^2$. The spin wave dispersion relation for an antiferromagnetically coupled chain is given by:

$$\hbar\omega = 4|JS|\sin(qa) \quad (2.23)$$

In this case for small q , $\hbar\omega \propto q$. The typical dispersion relations for both the ferromagnetic and antiferromagnetic one-dimensional chain can be seen in Fig. 2.18.

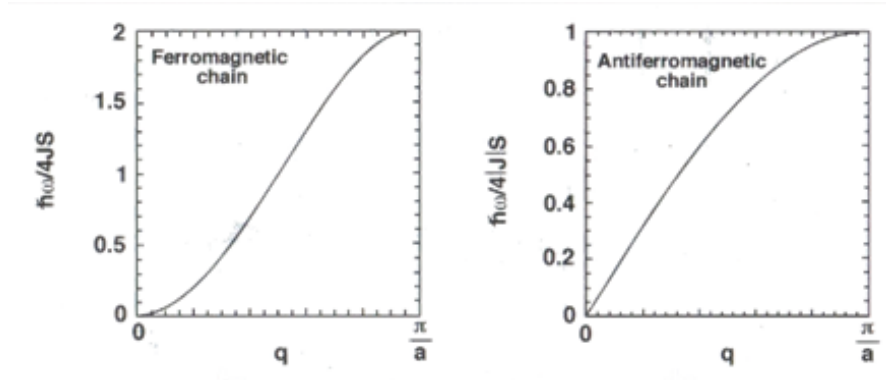


Figure 2.18: The dispersion of a ferromagnetic and an antiferromagnetic magnon in a one-dimensional lattice with lattice spacing a in the first Brillouin zone. The energy at the zone boundary ($q = \pi/a$) is a direct measure of the coupling constant J . From [9].

For both the ferromagnetic and the antiferromagnetic dispersion relation the energy $\hbar\omega$ is zero when $q = 0$. This is often not the case in real systems, where anisotropy in the crystal creates an energy gap. In general the dispersion relation can be written as [9]:

$$\hbar\omega = 2S[\mathcal{J}(0) - \mathcal{J}(\mathbf{q})] \quad (2.24)$$

where $\mathcal{J}(\mathbf{q})$ is the Fourier transformed exchange coupling given by:

$$\mathcal{J}(\mathbf{q}) = \sum_{l'} J_{ll'} \exp(i\mathbf{q}(\mathbf{R}_l - \mathbf{R}_{l'})) \quad (2.25)$$

where \mathbf{R}_l and $\mathbf{R}_{l'}$ are the coordinates of the l th and l' th unit cell [9].

The line-width of the magnon dispersion reveals the lifetime of the excitation. This is also the case for phonons. Heisenberg's uncertainty principle states [24]:

$$\Delta E \Delta t \geq \frac{\hbar}{2} \quad (2.26)$$

where ΔE is the uncertainty in energy and Δt is the uncertainty in time. A broad dispersion results in a short life time, whereas for a narrow dispersion *i.e.* a small uncertainty in energy, the uncertainty in time must be large, giving the excitation a long lifetime. The width of phonon and magnon dispersions can be measured with inelastic neutron scattering and is one of the experiments performed in this thesis. The inelastic neutron scattering technique is described in Sec. 3.6.

2.7 Macroscopic properties of crystals

Measurements of the magnetic and electric susceptibilities, heat capacity and thermal conductivity helps to understand the macroscopic nature of a sample. It is especially interesting to measure these properties around phase transitions because of anomalies occurring here. The first measurements performed on samples are often macroscopic measurements because they can reveal fundamental properties of the material, indicating whether the material is a good candidate for further measurements at large facilities, like neutron scattering facilities, Sec. 3.

2.7.1 Magnetic susceptibility

Magnetic susceptibility measurements can reveal if the system is ferromagnetic or antiferromagnetic. The magnetic susceptibility χ is a measure of how magnetizable the system is and for small magnetic fields it is given as [4]:

$$\chi = \frac{M}{H} \simeq \frac{\mu_0 M}{B} \quad (2.27)$$

The magnetic susceptibility is measured by applying a DC magnetic field and vibrating the sample or by applying an AC magnetic field while keeping the sample stationary. The electric response of the sample to the magnetic field⁷ is proportional to the magnetic susceptibility. The susceptibility is proportional to the Curie-Weiss law [4]:

$$\chi = \lim_{B \rightarrow 0} \frac{\mu_0 M}{B} \propto \frac{1}{T - \Theta_{CW}} \quad (2.28)$$

where $\Theta_{CW} = T_N$ for an antiferromagnet, $\Theta_{CW} = T_C$ for a ferromagnet and $\Theta_{CW} = 0$ for a paramagnet. Plotting the inverse susceptibility as a function of temperature directly reveals the ordering temperature as seen in Fig. 2.19.

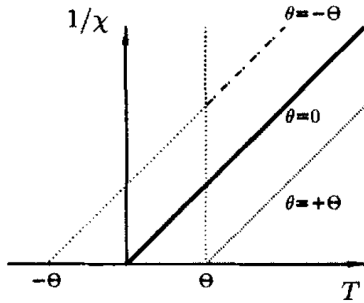


Figure 2.19: A plot of the inverse susceptibility as a function of temperature directly shows whether the system is ferromagnetic, paramagnetic or antiferromagnetic. If the Curie-Weiss temperature $\Theta_{CW} > 0$, the system orders ferromagnetically; if $\Theta_{CW} = 0$, it is a paramagnetic system; and if $\Theta_{CW} < 0$, the system is antiferromagnetically coupled. From [4].

2.7.2 Heat capacity

Heat capacity stems from lattice vibrations [45]. It is a measure of the amount of energy needed to change the temperature of a material by one degree and is given by [38]:

$$C_p = \left(\frac{\partial U}{\partial T} \right)_p \quad (2.29)$$

⁷Maxwell's third law gives the connection between a varying magnetic field and the induced electric field: $\nabla \times \mathbf{E} = -\frac{\partial \mathbf{B}}{\partial t}$.

The heat capacity usually decreases with decreasing temperature, which is in good agreement with the Bose factor, the number of phonons.

If the heat capacity has a strange behavior it should also be seen in the phonon spectrum of the material.

2.7.3 Thermal conductivity

The thermal conductivity κ is given by [38]:

$$j_U = -\kappa A \frac{dT}{dx} \quad (2.30)$$

where j_U is the heat current, A is the cross sectional area of the material and dT/dx is the temperature gradient. The minus sign shows that the heat always flows from high temperatures to lower temperatures. If κ is large, the material is a good conductor. The unit of thermal conductivity is W/(mK).

Like heat capacity, thermal conductivity stems from lattice vibrations [45]. Changes in the thermal conductivity at a given temperature should also be seen in the phonon spectrum of the material.

2.7.4 Electric susceptibility

The electric susceptibility χ_e is the proportionality constant between the electric field \mathbf{E} in a material and the polarization \mathbf{P} induced by it [23]:

$$\mathbf{P} = \epsilon_0 \chi_e \mathbf{E} \quad (2.31)$$

$\epsilon_0 \doteq 8.85 \cdot 10^{-12}$ F/m is the vacuum permittivity. The connection between the electric susceptibility and the dielectric constant, which is the quantity measured in an experiment. The relationship between the relative dielectric constant and the electric susceptibility of a material is:

$$\epsilon_r = 1 + \chi_e \quad (2.32)$$

The dielectric constant of a material is the ratio between the capacitance between two capacitor plates, when the material fills the space between the two capacitors C and the capacitance when the space between the plates is filled with vacuum C_0 :

$$\epsilon_r = \frac{C}{C_0} \quad (2.33)$$

3 Neutron scattering

Neutron scattering experiments can reveal the position and motion of atoms in a sample. Because neutrons have a magnetic moment that interacts with the magnetic ions in a sample, neutron scattering is an important tool in the understanding of all kinds of magnetic structures and properties. It is a complex experimental method and in this section the underlying theory, necessary to understand the experiments performed for this thesis, is presented. The practical details about the individual experiments are described in Sec. 5.

3.1 Why neutrons?

The neutron is an electrically neutral particle consisting of three quarks - one up quark with charge $q = +2/3$ and two down quarks with charge $q = -1/3$. It is a spin-1/2 particle with its magnetic moment anti-parallel to the spin. The magnetic moment μ_n is created by the internal motion of the quarks and is given by [9]:

$$\mu_n = -\gamma\mu_N\sigma = -1.913\mu_N\sigma = -\gamma\frac{e\hbar}{2m_n}\sigma \quad (3.1)$$

where μ_N is the nuclear magneton, m_n is the mass of the neutron, σ is the spin state of the neutron and γ is the gyromagnetic ratio. Neutrons interact with nuclei in a sample via the strong nuclear force and with the magnetic field created by unpaired electron spins inside a sample via the dipole-dipole interaction. Because of these two very different ways of interacting with matter, neutrons can be used to determine a wide range of properties. In Fig. 3.1, a generic neutron spectrum, showing intensity as a function of energy transfer is depicted. This spectrum shows that neutrons can be used for determining crystal and magnetic structures (elastic scattering), measuring phonon and magnon dispersions (coherent inelastic scattering), and, for larger energy transfers, the molecular vibrations can be investigated (incoherent inelastic scattering).

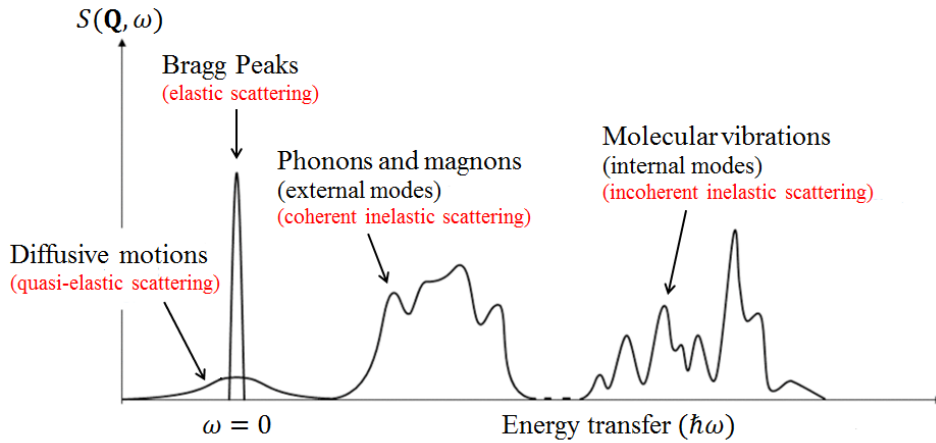


Figure 3.1: The energy transfer during a neutron scattering experiment determines which properties are measured. The intensity in this generic neutron spectrum is not to scale. The elastic scattering is much more intense than the inelastic scattering. Adapted from [95].

The most important examples of why and when neutrons are good probing particles are listed below.

- **Isotopes and light atoms**

Neutrons can often distinguish between different isotopes of the same element because the neutron cross section varies throughout the table of isotopes and depends only on the nucleus. Whereas X-rays are not able to distinguish between different isotopes because the number of electrons is similar, or locate hydrogen atoms because the electron cloud is too small, neutrons scatter differently from different isotopes and (too) efficiently from hydrogen⁸. Therefore it is possible to determine the position of hydrogen atoms in a sample with neutrons and to distinguish isotopes and elements placed near each other in the periodic table. See Fig. 3.2.

- **Crystal and magnetic structures**

Like X-rays, the wavelength of neutrons correspond to the distance between atoms in crystals ($\sim 2 \text{ \AA}$) and it is therefore possible to resolve crystal structures with neutrons. Because the neutron has a magnetic moment it interacts with unpaired electron spins and makes it possible to determine the magnetic structure of crystals and also the direction of the magnetic moments.

- **Excitations**

The energy of (cold and thermal) neutrons correspond to the energy range ($\sim 1 - 100 \text{ meV}$) of elementary excitations like phonons and magnons and it is possible to measure their dispersion relations (the relation between energy and momentum). X-rays on the other hand are not very suitable for studying these excitations because their energy is way too large ($\sim 100 \text{ keV}$).

- **Large penetration and small interaction**

Because neutrons are electrically neutral they do not significantly interact with matter. It is thus possible to do experiments where the sample is placed inside large cryostats or magnets. It is also possible to examine the bulk of a material rather than just the surface as with normal X-rays. The samples will (often) survive a neutron scattering experiment and can be used over and over again, whereas at large X-ray facilities the high energy of the X-rays can burn or evaporate the sample after a few minutes in the beam.

3.2 The neutron scattering cross section

The scattering cross section σ is a measure of how well a probe beam scatters off a sample. The cross section for X-rays scales with the number of electrons $\sigma \sim Z^2$ and hydrogen (H) and Deuterium (D or ${}^2_1\text{H}$) are therefore indistinguishable. With neutrons, on the other hand, there is a huge difference in the cross section as depicted in Fig. 3.2.

To establish an expression for the cross section a couple of terms need to be presented. First the neutron flux Ψ is given by [45]:

$$\Psi = \frac{\text{\# of neutrons hitting a surface per second}}{\text{Area of the surface perpendicular to the neutron beam}} \quad (3.2)$$

⁸If you are not interested in the location of the hydrogen atoms you need to deuterate your sample – exchange all the protons with deuterium ${}^2_1\text{H}$ – so the signal from the interesting part of the sample is not drowned by the incoherent scattering from hydrogen. Incoherent and coherent scattering will be explained further in Sec. 3.3.

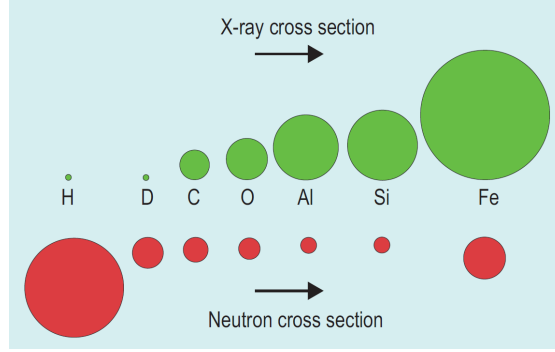


Figure 3.2: The neutron and X-ray cross section of selected elements. From [30].

The neutron flux is different at different neutron scattering facilities and when planning a neutron scattering experiment it is important to include the flux in the calculation of measuring times. A low flux will increase the required time for an experiment.

The total cross section σ is defined by:

$$\sigma = \frac{1}{\Psi} \cdot \# \text{ of neutrons scattered per second in all directions} \quad (3.3)$$

which is independent of the neutron flux and is therefore the same regardless of the experimental conditions. The cross section is solely a material property and is measured in units of area. In neutron scattering experiments it is not possible to measure the total scattering cross section, but only the scattering through a solid angle $d\Omega$ (the detector area, Fig. 3.3) which leads to the definition of the differential scattering cross section:

$$\frac{d\sigma}{d\Omega_f} = \frac{1}{\Psi} \frac{\# \text{ of neutrons scattered into solid angle } d\Omega_f \text{ per second}}{d\Omega_f} \quad (3.4)$$

When doing inelastic neutron scattering experiments the final energy E_f is also measured and the double differential scattering cross section is defined by:

$$\frac{d^2\sigma}{d\Omega_f dE_f} = \frac{1}{\Psi} \frac{\# \text{ of neutrons scattered into } d\Omega \text{ with energies } [E_f; E_f + dE_f] \text{ per second}}{d\Omega_f dE_f} \quad (3.5)$$

With the Van Hove [90] formalism the double differential cross section for a system of N atoms can be written as [72]:

$$\frac{d^2\sigma}{d\Omega_f dE_f} = b^2 \frac{k_f}{k_i} N S(\mathbf{Q}, \omega) \quad (3.6)$$

where b is the scattering length, k_i and k_f are the initial and final neutron wave vectors respectively and $S(\mathbf{Q}, \omega)$ is the scattering function as plotted on the y -axis in Fig. 3.1. In a neutron scattering experiment it is ultimately the scattering function that is measured. The scattering function is the time and spacial Fourier transform of the correlation function of the scattering system and it is a measure of the probability that the scattering changes the system by $\hbar\omega \equiv E_i - E_f$ and momentum $\hbar\mathbf{Q} \equiv \hbar\mathbf{k}_i - \hbar\mathbf{k}_f$, Fig. 3.4.

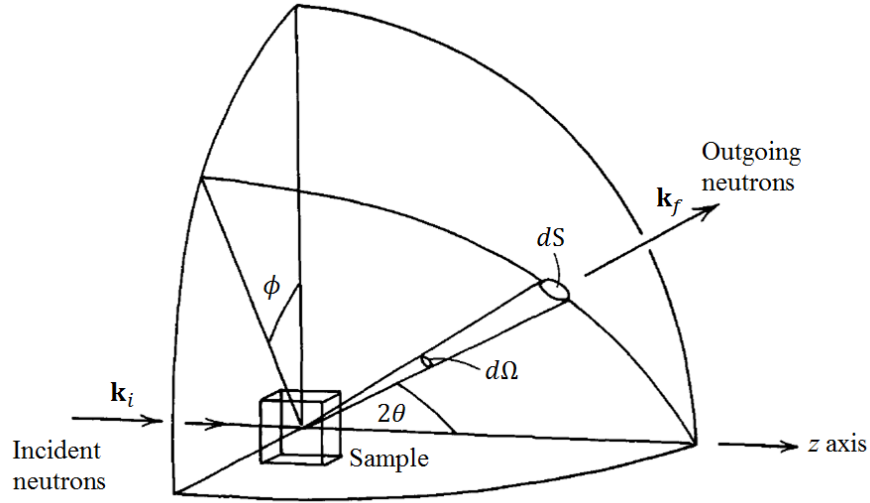


Figure 3.3: The geometry of a neutron scattering experiment. An incident neutron with wave vector \mathbf{k}_i hits the sample and scatters into a new state with wave vector \mathbf{k}_f into the solid angle $d\Omega$. $|\mathbf{k}| = k = 2\pi/\lambda$ and dS denotes the area of the detector and 2θ is the scattering angle. The differential cross section is given by the number of neutrons passing through a solid angle $d\Omega_f$ in the direction of 2θ and ϕ per second. θ and ϕ are polar coordinates. Adapted from [76].

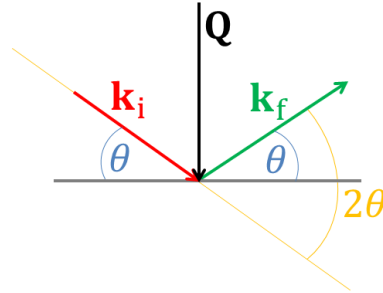


Figure 3.4: Illustration of the scattering vector defined as $\mathbf{Q} \equiv \mathbf{k}_i - \mathbf{k}_f$. 2θ is the scattering angle.

For elastic scattering the correlation function is time-independent and for inelastic scattering the correlation function is time-dependent. The scattering function will be discussed further in the following sections.

When a beam of neutrons is guided towards a sample in an experiment, it is far from all the neutrons that scatter off the sample, hit the detector, and thereby contribute to the signal the experimentalist is measuring. Most of the neutrons pass through the sample and are stopped by a beam stop. Other neutrons are simply absorbed by the nuclei in the sample and the remainder of the neutrons are scattered off the sample and contribute to the total cross section. A small

part of these neutrons contribute to what is actually measured: the differential scattering cross section and the double differential cross section.

The definition of the absorption cross section for thermal neutrons is similar to Eq. (3.3) and is inversely proportional to the neutron velocity. The absorption cross section for selected elements can be seen in Table 3.1.

3.3 Coherent and incoherent scattering

The double differential cross section has both a coherent and an incoherent part [95]:

$$\frac{d^2\sigma}{d\Omega_f dE_f} = \left(\frac{d^2\sigma}{d\Omega_f dE_f} \right)_{\text{coherent}} + \left(\frac{d^2\sigma}{d\Omega_f dE_f} \right)_{\text{incoherent}} \quad (3.7)$$

where both terms can be structural and magnetic and have both an elastic and an inelastic contribution. It is important to know the difference between coherent and incoherent scattering and the general rule is to minimize the incoherent scattering as much as possible. The coherent scattering depends on the relative positions of the atoms and their average scattering length $\langle b \rangle$ (also called the coherent scattering length b_{coh}) and is the one containing the desired information.

The incoherent scattering creates a uniform background and can therefore make it impossible to see the signal from the coherent scattering.

Incoherent scattering is the scattering of neutrons in all directions without interference and is a measure of the individual motion of the particles. Different isotopes of the same element will scatter neutrons differently *i.e.* the scattering lengths will vary from site to site. This is called isotope incoherent scattering. For isotopes with a non-zero nuclear spin I , the scattering length will take two different values because the neutron is a spin-1/2-particle; b_+ corresponds to when the spin of the nucleus and the incoming neutron are parallel ($I + 1/2$) and b_- corresponds to when the spins are anti-parallel ($I - 1/2$). Differences in the orientation of the nuclear spins will contribute to the incoherent scattering. This is called spin incoherent scattering.

The only situation where incoherent scattering does not occur is when a sample is composed of a single isotope that has nuclear spin $I = 0$. Some isotopes are far worse sources of incoherent scattering than others. As previously mentioned, hydrogen creates a huge incoherent scattering because of the strong spin dependent interaction between the neutron and the proton.

It is not always easy to separate the coherent and the incoherent signal, but with polarized neutrons it is possible, as we will see in Sec. 3.8. Sometimes it is possible to take advantage of strong incoherent scattering. When calibrating detectors at neutron scattering experiments vanadium is often used because of its large and uniform incoherent scattering cross section.

3.4 Scattering theory

When describing the interaction between the neutron beam and the sample one needs to take advantage of the fact that the neutron has both particle (moves with a speed v) and wave-like properties (has a wavelength λ or wave number k) [95]:

$$\lambda = \frac{2\pi\hbar}{m_n v} \quad \text{and} \quad k = \frac{2\pi}{\lambda} \quad (3.8)$$

where $m_n = 1.67495 \cdot 10^{-27}$ kg is the mass of the neutron. Instead of the neutron velocity \mathbf{v} the wave vector \mathbf{k} , which is a vector with the same direction as the velocity and magnitude as the wave number k can be used to describe the neutron:

Element	σ_{coh}	σ_{inc}	σ_{abs}
Hydrogen	1.7568	80.27	0.33326
Deuterium	5.592	2.05	0.00052
Oxygen	4.232	0	0.00019
Manganese	1.75	0.40	13.3
Yttrium	7.55	0.15	1.28
Vanadium	0.133	5.08	5.08
Aluminum	1.495	0.0082	0.231
Carbon	5.550	0.001	0.00350
Boron	3.54	1.7	767.0
Nitrogen	11.01	0.49	1.9

Table 3.1: The coherent σ_{coh} , incoherent σ_{inc} and absorption σ_{abs} cross sections for selected elements. The incoherent cross section σ_{inc} is the sum of spin-incoherent scattering and isotope incoherent scattering [72]. All numbers correspond to the natural abundances of elements (except hydrogen and deuterium) and are in barns ($= 10^{-28} \text{ m}^2$). σ_{abs} is given as the value of neutrons with $v = 2200 \text{ m/s}$.

$$\mathbf{k} = \frac{m_n \mathbf{v}}{\hbar} \quad (3.9)$$

After interacting with a single nucleus the neutron beam can be described by a spherical wave since the neutron wavelength is much larger than the size of the nucleus, thereby causing S-wave scattering. When the solid angle $d\Omega$ is small the spherical wave can be approximated by a plane wave .

It is practical to look at the quantum mechanical description of the interaction between the neutron and the sample. The Born approximation⁹ can be applied because the interaction is weak and both the incoming $|\mathbf{k}_i\rangle$ and outgoing $|\mathbf{k}_f\rangle$ wave of neutrons can be approximated by the following complex plane waves:

$$|\mathbf{k}_i\rangle = \frac{1}{\sqrt{Y}} \exp(i\mathbf{k}_i \cdot \mathbf{r}) \quad \text{and} \quad |\mathbf{k}_f\rangle = \frac{1}{\sqrt{Y}} \exp(i\mathbf{k}_f \cdot \mathbf{r}) \quad (3.10)$$

where the normalization factor $Y = L^3$ is a large (compared to the experimental setup) Cartesian volume with side lengths L . The spin part of the neutron is ignored until Sec. 3.8 on polarized neutron scattering.

The neutron causes a small perturbation of the scattering system and makes the system transfer from one quantum state to another without changing the nature of the states in the process. Therefore the scattering cross section can be obtained by applying Fermi's Golden Rule:

$$\left(\frac{d^2\sigma}{d\Omega_f dE_f} \right)_{\lambda_i \rightarrow \lambda_f} = \frac{k_f}{k_i} \left(\frac{m_n}{2\pi\hbar^2} \right)^2 |\langle \mathbf{k}_f \lambda_f | V | \mathbf{k}_i \lambda_i \rangle|^2 \delta(\hbar\omega + E_i - E_f) \quad (3.11)$$

where $\langle \mathbf{k}_f \lambda_f | V | \mathbf{k}_i \lambda_i \rangle$ is the interaction matrix element. V is the interaction Hamiltonian for a given interaction.

⁹The Born approximation utilizes first order perturbation theory because the nuclear scattering is short range only S-wave scattering is possible. Magnetic scattering is long range, but weak, so it still applies.

3.5 Elastic neutron scattering

Elastic neutron scattering is used for measuring the nuclear and magnetic Bragg peaks. During elastic neutron scattering experiments there is no energy $\hbar\omega = 0$ ($E_i = E_f$) or momentum $\hbar\mathbf{Q} = 0$ ($\mathbf{k}_i = \mathbf{k}_f = \mathbf{k}$) transfer between the neutron and the scattering system.

Like X-rays, the neutrons scatter off the (hkl) lattice planes in the crystal and the scattering fulfills Bragg's Law [51]:

$$n\lambda = 2d_{hkl} \sin \theta_{hkl} \quad (3.12)$$

where n is the order, θ_{hkl} is the angle between the neutron beam and the family of (hkl) lattice planes with lattice spacing d_{hkl} . The scattering angle is the double angle $2\theta_{hkl}$, Fig. 3.5.

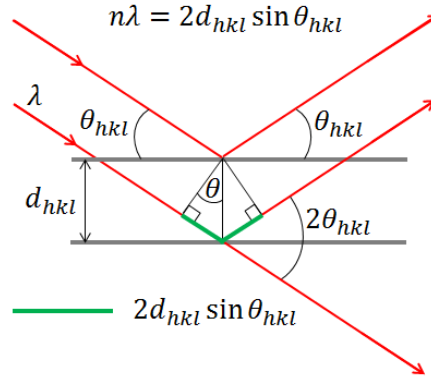


Figure 3.5: Illustration of Bragg's law. λ is the wavelength of the radiation incident on the crystal with the angle θ_{hkl} to the (hkl) lattice planes and d_{hkl} is the distance between lattice planes. The green line is the extra distance traveled by the wave scattering off the lower lattice plane. Constructive interference is obtained when the extra distance traveled is an integer number n of wavelengths. The angle $2\theta_{hkl}$ is called the scattering angle.

3.5.1 Nuclear scattering

Van Hove expressed the scattering function by using the definition of the time dependent atomic density operator [72]:

$$\rho_{\mathbf{Q}}(t) = \sum_l \exp(i\mathbf{Q} \cdot \mathbf{r}_l(t)) \quad (3.13)$$

which gives an expression for the scattering function:

$$S(\mathbf{Q}, \omega) = \frac{1}{2\pi\hbar N} \int_{-\infty}^{\infty} dt \langle \rho_{\mathbf{Q}}(0) \rho_{\mathbf{Q}}(t) \rangle \exp(-i\omega t) \quad (3.14)$$

For elastic nuclear scattering the time average of the density function that is considered, which gives the scattering function the following form [72]:

$$S(\mathbf{Q}, \omega) = \delta(\hbar\omega) \frac{1}{N} \left\langle \sum_{ll'} \exp(-i\mathbf{Q} \cdot (\mathbf{r}_l - \mathbf{r}_{l'})) \right\rangle \quad (3.15)$$

The differential scattering cross section for coherent elastic scattering is then given by [72]:

$$\frac{d\sigma}{d\Omega} = N \frac{(2\pi)^3}{V_0} \sum_{\mathbf{G}} \delta(\mathbf{Q} - \mathbf{G}_{hkl}) |F_N(\mathbf{G}_{hkl})|^2 \quad (3.16)$$

where V_0 is the volume of the unit cell and $F_N(\mathbf{G}_{hkl})$ is the static nuclear structure factor which describes the amplitude of the wave scattered into the (hkl) Bragg reflection by the atomic nuclei in one unit cell. It is given by [95]:

$$F_N(\mathbf{G}_{hkl}) = \sum_j b_j \exp(i\mathbf{G}_{hkl} \cdot \mathbf{r}_j) \exp(-W(\mathbf{Q})) \quad (3.17)$$

where \mathbf{r}_j is the vector of the j th atom in the unit cell, and $\exp(-W(\mathbf{Q}))$ is the Debye-Waller factor. It accounts for the reduction in scattering amplitude due to the motion of the atoms away from their equilibrium position. F_{hkl} is a complex quantity, and can be expressed as a product between its magnitude and its phase factor $F_{hkl} = |F_{hkl}| \exp(i\phi_{hkl})$. The (relative) nuclear structure factor for different reflections can be determined by comparing the intensities of multiple Bragg peaks. $I_{hkl} \propto |F_{hkl}|^2$, so the amplitude is directly measured while the phase is not.

3.5.2 Magnetic scattering

The interaction between the neutron and a magnetic ion is given by the dipole-dipole interaction and the scattering potential has the form [9]:

$$\mathbf{V}(\mathbf{r}) = -\gamma\mu_N 2\mu_B \boldsymbol{\sigma} \cdot \left[\nabla \left(\frac{\mathbf{S} \times \hat{\mathbf{R}}}{R^2} \right) + \frac{1}{\hbar} \left(\frac{\mathbf{p} \times \hat{\mathbf{R}}}{R^2} \right) \right] \quad (3.18)$$

where the first term is the spin interaction with the electron and the second term is the orbital interaction with the electron.

When evaluating the matrix element $\langle \mathbf{k}_f | V | \mathbf{k}_i \rangle$ in Eq. (3.11) the following expression for double differential scattering cross section is obtained:

$$\frac{d^2\sigma}{d\omega_f dE_f} = \frac{N}{\hbar} \frac{k_f}{k_i} p^2 \exp(-2W(\mathbf{Q})) \sum_{\alpha, \beta} (\delta_{\alpha, \beta} - \hat{\mathbf{Q}}_\alpha \hat{\mathbf{Q}}_\beta) S^{\alpha\beta}(\mathbf{Q}, \omega) \quad (3.19)$$

where the magnetic scattering length p (when the orbital component is quenched) is given by:

$$p = \left(\frac{\mu_0}{4\pi} \right) \left(\frac{e^2}{m_e} \right) \gamma S f(\mathbf{Q}), \quad (3.20)$$

where S is the atomic spin. $f(\mathbf{Q})$ is the magnetic form factor which is unity when $\mathbf{Q} = 0$ and is given by:

$$f(\mathbf{Q}) = \int \rho_s(\mathbf{r}) \exp(i\mathbf{Q} \cdot \mathbf{r}) d\mathbf{r} \quad (3.21)$$

where $\rho_s(\mathbf{r})$ is the spin density. The form factor is the Fourier transform of the electron spin density around the atomic center. The size of the scattering depends on the form factor. The form factor for nuclear scattering $f(\mathbf{Q})$ is constant for all \mathbf{Q} . The scattering function has the form:

$$S^{\alpha\beta}(\mathbf{Q}, \omega) = \frac{1}{2\pi} \int_{-\infty}^{\infty} dt \exp(-i\omega t) \sum_l \exp(i\mathbf{Q} \cdot \mathbf{r}_l) \langle S_0^\alpha(0) S_l^\beta(t) \rangle \quad (3.22)$$

The differential scattering cross section can be written as [72]:

$$\frac{d\sigma}{d\Omega} = N \frac{(2\pi)^3}{V_0} \sum_{\mathbf{G}} \delta(\mathbf{Q} - \mathbf{G}_{hkl}) |F_M(\mathbf{G}_{hkl})|^2 \quad (3.23)$$

where the static magnetic structure factor $F_M(\mathbf{G}_{hkl})$ is given by [95]:

$$F_M(\mathbf{Q}) = \sum_j f_j(\mathbf{Q}) p_j \mathbf{S}_\perp \exp(i\mathbf{Q} \cdot \mathbf{r}_j) \exp(-W_j(\mathbf{Q})) \quad (3.24)$$

Notice that the magnetic form factor is contained in p_j . The geometry of magnetic scattering can be found in Fig. 3.6. The scattering is largest when \mathbf{Q} is perpendicular to the magnetic moments $\boldsymbol{\mu}$ and no magnetic scattering when $\mathbf{Q} \parallel \boldsymbol{\mu}$.

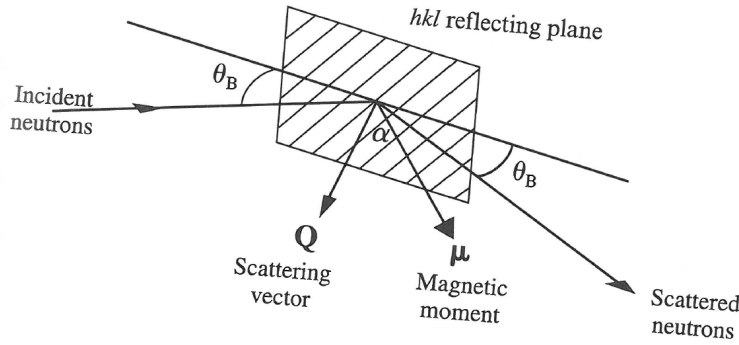


Figure 3.6: The geometry of elastic magnetic scattering. The intensity of the scattered beam is proportional to $\sin^2 \alpha$ and the intensity is therefore zero if the magnetic moment $\boldsymbol{\mu}$ and the scattering vector \mathbf{Q} are parallel. From [95].

The magnetic interaction vector \mathbf{S}_\perp is given by:

$$\mathbf{S}_\perp = \hat{\mathbf{Q}} \times (\mathbf{S} \times \hat{\mathbf{Q}}) \quad (3.25)$$

which leads to:

$$|\mathbf{S}_\perp|^2 = \sum_{\alpha, \beta} (\delta_{\alpha, \beta} - \hat{Q}_\alpha \hat{Q}_\beta) S_\alpha^* S_\beta \quad (3.26)$$

This expression is the selection rule for magnetic neutron scattering and is therefore included in the double differential scattering cross section in Eq. (3.19). It is clearly seen that the magnetic scattering is zero if the magnetic moments are parallel to the scattering vector.

3.6 Inelastic neutron scattering

Other methods for measuring the dynamics of crystals, like Raman scattering and infrared spectroscopy, have selection rules and limited \mathbf{Q} -range. Inelastic neutron scattering is therefore, in some cases, the only available tool for measuring phonon and magnon dispersions. Inelastic neutron scattering is a direct measurement of the vibrational frequency and amplitude of the nuclei. During an inelastic experiment the neutron either gives energy to the sample or receives energy from the sample so $\mathbf{k}_i \neq \mathbf{k}_f$. When the neutron loses energy to the sample and thereby creates an excitation, it is called down scattering and when the neutron annihilates an excitation, and thereby gains energy, it is called up scattering. Down scattering $E_i > E_f$ is most common and the sign of the energy conservation is defined so the energy loss of the neutron gives a positive energy $\hbar\omega$. One quantum of vibrational energy (or spin wave energy) is exchanged between the neutron and the crystal:

$$\Delta E = \hbar\omega = E_i - E_f \equiv \frac{\hbar^2(k_i^2 - k_f^2)}{2m_n} = \pm \hbar\omega_j(\mathbf{q}) \quad (3.27)$$

where $\omega_j(\mathbf{q})$ is the angular frequency of the j th branch of the dispersion relation. Conservation of momentum in the scattering process gives the following condition:

$$\mathbf{Q} \equiv \mathbf{k}_i - \mathbf{k}_f = \mathbf{G}_{hkl} \pm \mathbf{q} \quad (3.28)$$

where \mathbf{Q} is the scattering vector, \mathbf{G}_{hkl} is the reciprocal lattice vector and \mathbf{q} is the phonon or magnon wave vector (the reduced momentum transfer from the lattice point (hkl)). A visualization of the scattering conditions in real and reciprocal space can be seen in Fig. 3.7.

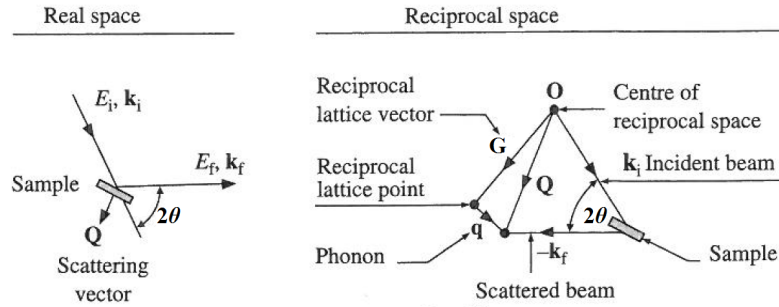


Figure 3.7: The connection between the incoming wave vector \mathbf{k}_i , the outgoing (final) wave vector \mathbf{k}_f and the scattering vector \mathbf{Q} in both real space and reciprocal space for an inelastic scattering process. \mathbf{G} is the reciprocal lattice vector and 2θ is the scattering vector. Adapted from [95].

From the energy and momentum conservation equations it is possible to determine the physical limit of the (\mathbf{Q}, ω) range that is accessible with a final fixed energy of E_f :

$$\frac{\hbar^2 Q^2}{2m_n} = 2E_i - \hbar\omega - 2\sqrt{E_i(E_i - \hbar\omega)} \cos(2\theta) \quad (3.29)$$

This range has been calculated for all the instrumental setups used in this thesis and are depicted in Sec. 5.

3.6.1 Phonons

The integrated intensity for a constant- \mathbf{Q} scan¹⁰ is proportional to the dynamical structure factor squared $|F_j(\mathbf{q}, \mathbf{Q})|^2$ which is given by [95]:

$$F_j(\mathbf{q}, \mathbf{Q}) = \sum_l \left(\frac{1}{2m_l \omega_j(\mathbf{q})} \right)^{1/2} b_l [\mathbf{Q} \cdot \hat{\mathbf{e}}_j(\mathbf{q})] \times \exp(i\mathbf{Q} \cdot \mathbf{r}_l) \exp[-2W(\mathbf{Q})] \quad (3.30)$$

where m_l , b_l and \mathbf{r}_l is the mass, the scattering length and the position vector of the l th atom, respectively. $\omega_j(\mathbf{Q})$ is the angular frequency and $\hat{\mathbf{e}}_j(\mathbf{q})$ is the polarization of the j th branch. The double differential scattering cross section for coherent one-phonon-scattering is given by:

$$\begin{aligned} \frac{d^2\sigma}{d\Omega_f dE_f} &= \frac{k_f}{k_i} \frac{(2\pi)^3}{V_0} \sum_{j\mathbf{q}, \mathbf{G}} |F_j(\mathbf{q}, \mathbf{Q})|^2 \\ &\times [n_j(\mathbf{q})\delta(\omega + \omega_j(\mathbf{q}))\delta(\mathbf{Q} + \mathbf{q} - \mathbf{G}) + (n_j(\mathbf{q}) + 1)\delta(\omega - \omega_j(\mathbf{q}))\delta(\mathbf{Q} - \mathbf{q} - \mathbf{G})] \end{aligned} \quad (3.31)$$

where $n_j(\mathbf{q})$ is the Bose factor giving the number of phonons with wave vector \mathbf{q} from Eq. (2.21). The term $n_j(\mathbf{q})\delta(\omega + \omega_j(\mathbf{q}))\delta(\mathbf{Q} + \mathbf{q} - \mathbf{G})$ denotes phonon annihilation and $(n_j(\mathbf{q}) + 1)\delta(\omega - \omega_j(\mathbf{q}))\delta(\mathbf{Q} - \mathbf{q} - \mathbf{G})$ denotes phonon creation. When $T \rightarrow 0$ the Bose factor (see Sec. 2.6) goes to zero, $n_j(\mathbf{q}) = 0$, i.e there are no phonons in the system. It is therefore not possible to annihilate a phonon when $T = 0$, but it is always possible to create a phonon because of the +1 term in the pre-factor.

Inserting Eq. (3.30) into Eq. (3.31) a final expression for the double differential cross section is found:

$$\begin{aligned} \frac{d^2\sigma}{d\Omega_f dE_f} &= \frac{k_f}{k_i} \frac{b^2(2\pi)^3}{2MV_0} \exp(-2W(\mathbf{Q})) \sum_{\mathbf{Q}, p, \mathbf{G}} \frac{(\mathbf{Q} \cdot \mathbf{e}_j(\mathbf{q}))^2}{\omega_j(\mathbf{q})} \\ &\times [(n_j(\mathbf{q}) + 1)\delta(\omega - \omega_j(\mathbf{q}))\delta(\mathbf{Q} - \mathbf{q} + \mathbf{G}) + n_j(\mathbf{q})\delta(\omega + \omega_j(\mathbf{q}))\delta(\mathbf{Q} + \mathbf{q} + \mathbf{G})] \end{aligned} \quad (3.32)$$

The term $\mathbf{Q} \cdot \mathbf{e}_j(\mathbf{q})$ shows an important result when measuring phonon dispersions: neutrons only scatter from vibrations that are parallel to the scattering vector.

3.6.2 Magnons

Magnons are approximately bosons; like phonons they obey Bose-Einstein statistics. Measurements on magnetic materials are often done at low temperatures, so magnon creation (down scattering) is most common. The biggest difference between measuring phonons and magnons is that the intensity of phonons increases with larger \mathbf{Q} -values, whereas the magnetic scattering decreases since the magnetic form factor in Eq. (3.21) decreases with large \mathbf{Q} 's.

Another big difference between phonon and magnon scattering is the scattering condition. The neutrons only scatter from the component of the magnetization that is perpendicular to the scattering vector.

The double differential cross section is the sum of the cross sections for creating and annihilating a magnon and is given by [9]:

¹⁰The conditions for a constant- \mathbf{Q} scan is explained in detail in Sec. 3.7

$$\begin{aligned} \left(\frac{d^2\sigma}{d\Omega_f dE_f} \right)_{\text{creation}} &= (\gamma r_0)^2 \frac{k_f}{k_i} \left[\frac{g}{2} f(\mathbf{q}) \right]^2 \exp(-2W(\mathbf{Q})) \frac{(2\pi)^3}{2NV_0} (1 + \hat{\mathbf{Q}}_z^2) \\ &\times \sum_{\mathbf{G}, \mathbf{q}} (n_j(\mathbf{q}) + 1) \delta(\omega - \omega_j(\mathbf{q})) \delta(\mathbf{Q} - \mathbf{q} - \mathbf{G}) \end{aligned} \quad (3.33)$$

$$\begin{aligned} \left(\frac{d^2\sigma}{d\Omega_f dE_f} \right)_{\text{annihilation}} &= (\gamma r_0)^2 \frac{k_f}{k_i} \left[\frac{g}{2} f(\mathbf{q}) \right]^2 \exp(-2W(\mathbf{Q})) \frac{(2\pi)^3}{2NV_0} (1 + \hat{\mathbf{Q}}_z^2) \\ &\times \sum_{\mathbf{G}, \mathbf{q}} n_j(\mathbf{q}) \delta(\omega - \omega_j(\mathbf{q})) \delta(\mathbf{Q} - \mathbf{q} - \mathbf{G}) \end{aligned} \quad (3.34)$$

3.7 The three-axis spectrometer

Before introducing polarized neutron scattering the conventional three-axis instrument which has been used for all the experiments in this thesis will be presented. The three-axis spectrometer was invented and developed by Bertram Brockhouse at the Chalk River National Laboratories in Canada in the 1950s and he, together with Clifford Shull, received the Nobel Prize in 1994 for their pioneering work [55]. He had created the only experimental technique that could show the dynamics of crystals.

A sketch of a typical three-axis spectrometer can be seen in Fig. 3.8. The instrument is called a "three-axis" spectrometer because the neutrons are scattered around three axes on the way to the detector. The first axis selects the initial wave vector \mathbf{k}_i , the second axis is the sample and the third axis is the analyzing crystal which determines the final wave vector \mathbf{k}_f ¹¹.

The components of a three-axis spectrometer are briefly described below:

Neutron Source: Neutrons can be produced by nuclear fission or by spallation. Fission sources are (often) continuous while spallation sources are (often) pulsed¹². Spallation works by bombarding a heavy target with protons and thereby release neutrons.

Moderator: When the neutrons are released from the heavy target or from the reactor their energy is too high for doing experiments on the order of MeV. Their energy is reduced by sending them through a moderating material, such as water (300 K), to slow them down. The neutrons attain the temperature of the moderating material with the Maxwell-Boltzmann distribution of velocities given by [95]:

$$n(v) = \frac{4n_0 v^2}{\sqrt{\pi} v_T^3} \exp\left(-\frac{v^2}{v_T^2}\right) \quad (3.35)$$

where $n(v)dv$ is the number of neutrons per unit volume with velocities between v and $v + dv$, n_0 is the total number of neutrons in a unit volume and v_T is given by:

$$v_T = \left(\frac{2k_B T_{\text{effective}}}{m_n} \right)^{1/2} \quad (3.36)$$

¹¹It is often \mathbf{k}_f that is held fixed while \mathbf{k}_i is varied. This is an experimental trick because the intensities then are directly comparable with the dynamical structure factor $|F_j(\mathbf{q}, \mathbf{Q})|^2$, see Eq. (3.30) [95].

¹²The spallation source SINQ at the Paul Scherrer Institute is a continuous spallation source.

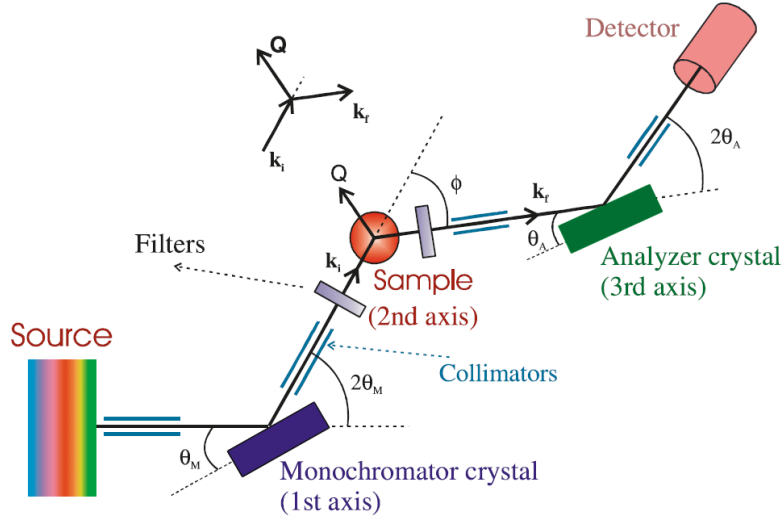


Figure 3.8: A sketch of a three-axis spectrometer. The source sends out neutrons with all wavelengths. A monochromator crystal positioned at the first axis selects one wave vector \mathbf{k}_i . The selected neutrons scatter off the sample which is positioned at the second axis. The scattered neutrons then reach the third axis of the three-axis spectrometer with an analyzer crystal (which is often the same type of crystal as the monochromator crystal) and it selects the neutrons with one outgoing wave vector \mathbf{k}_f . Finally the neutrons are detected in a detector. Filters are positioned on both sides of the sample and prevents unwanted neutrons from passing. Collimators positioned between the axes also help the selection of collinear neutrons. From [96].

where $T_{\text{effective}}$ is the effective temperature of the moderator. If cold neutrons are needed one uses liquid hydrogen (25 K). If hot neutrons are needed one uses molten graphite (2000 K).

Guide: When the neutrons have the right energy they need to be guided to the experiment with minimal intensity loss. This is done by sending the neutrons through rectangular tubes with layers of super mirrors [45] on the inside called guides. By total reflection the neutrons proceed through the guide which can be up to 100 m long without much loss of intensity.

Monochromator (1st axis) and analyzer (3rd axis): The monochromator and analyzer are crystals that select the initial wave vector \mathbf{k}_i and final wave vector \mathbf{k}_f , respectively, by Bragg diffraction as explained in Sec. 3.5. It is important that the crystal has a small absorption cross section. A too high mosaicity gives a bad resolution. Pyrolytic graphite crystals are often used as monochromating crystals, referred to as PG-crystals.

Collimators: Collimation controls the divergence of the beam. The soller collimation consist of parallel blades of a neutron absorbing material that reduce the divergence of the beam. The

degree of collimation is given by:

$$\alpha = \frac{w}{L} \quad (3.37)$$

where w is the width between the blades and L is the length of the blades. In pinhole collimation vertical and horizontal slits determine the size of the beam. The collimation plays a big role in the \mathbf{Q} -resolution of the instrument.

Filters: Filters are placed to remove higher order wavelengths, see Eq. (3.12), from the monochromator. Filters also reduces the risk of spurious signals from the sample environment. Spurious signals are signals in the data, that are not from the sample. A spurious signal can come from higher order neutrons or from Bragg scattering from the sample environment. Normally spurious signals are very intense and sharp - even sharper than the resolution. Pyrolytic graphite filters work well because the transmission of 2nd and 3rd order scattering is low. Pyrolytic graphite works most efficiently at 2.37 Å and 1.55 Å, while other filters like Be-filters work for wavelengths larger than 4 Å. Cooled Sapphire filters work for wavelength smaller than 0.8 Å.

Sample environment and sample (2nd axis): The sample environment can be changed between each experiment, but often consists of a cryostat for cooling down the sample. Other equipment could be magnets or pressure cells.

Detector: The detector determines the energy of the neutrons. A ^3He gas detector measures the ionizing energy that is released when neutrons are absorbed by the gas. The nuclear reaction is given by: $^3\text{He} + n \rightarrow ^3\text{H} + p + 0.8 \text{ MeV}$, where n is a neutron and p is a proton.

One of the problems with three-axis spectrometer experiments¹³ is that it is a point by point measurement¹⁴, that is one (Q, ω) -point is measured at a time and it is necessary to change to geometry of the instrument at every data point. During three-axis experiments it is common to do energy scans (where \mathbf{Q} is fixed) and \mathbf{Q} -scans (where E_f is fixed). The geometry in reciprocal space of a constant- \mathbf{Q} energy scan, which is the one mainly utilized in this thesis, can be seen in Fig. 3.9. In real space the sample and analyzer must rotate around the monochromator assembly together.

A constant energy scan, where \mathbf{Q} is varied is usually used when dispersions are very steep, which is the case for magnon dispersions in transition metals [49].

3.8 Polarized Neutron Scattering

Until now the spin state of the neutron has been completely ignored and it is only the change from one momentum state to another that has been considered. With polarized neutron scattering, both the momentum state and the spin state of the neutron is taken into account. The change (or not change) in the spin state of the neutron provides new information about the scattering system. The polarization of neutrons is defined as the expectation value of the neutron spins divided by the maximal length of the spins:

¹³At a time-of-flight experiment it is possible to measure a large area in (Q, ω) and thereby directly measure the dispersion of phonons and magnons.

¹⁴At RITA II at SINQ at PSI there are nine analyzer blades and it is therefore possible to measure nine (Q, ω) -points in a single measurement.

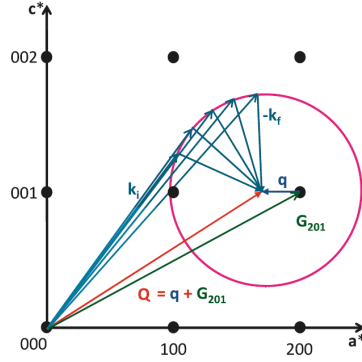


Figure 3.9: The geometry in reciprocal space behind a constant \mathbf{Q} -scan where the neutron intensity is measured as a function of energy. The momentum transfer \mathbf{Q} is kept constant and the energy is changed by varying the initial wavevector \mathbf{k}_i . \mathbf{G}_{201} is the reciprocal lattice vector of the (201) Bragg peak. This type of scan is often used when determining the dispersion relations of phonons and magnons and was used intensively in this thesis. From [96].

$$\mathbf{P} = \langle \hat{\mathbf{s}} \rangle / (1/2) = 2\langle \hat{\mathbf{s}} \rangle = \langle \boldsymbol{\sigma} \rangle \quad (3.38)$$

where $\boldsymbol{\sigma}$ are the Pauli spin matrices:

$$\sigma_x = \begin{bmatrix} 0 & 1 \\ 1 & 0 \end{bmatrix}, \sigma_y = \begin{bmatrix} 0 & -i \\ i & 0 \end{bmatrix}, \sigma_z = \begin{bmatrix} 1 & 0 \\ 0 & -1 \end{bmatrix} \quad (3.39)$$

The polarization \mathbf{P}_0 of the beam is defined by [72]:

$$\mathbf{P}_0 = \frac{1}{N} \sum_j \mathbf{P}_j \quad (3.40)$$

where N is the number of spins and \mathbf{P}_j is the polarization of the j th spin. When neutrons are polarized all the spins point in the same direction along an axis determined by a magnetic field. The spin of the neutron can either be parallel or antiparallel to the magnetic field because it is a spin-1/2 particle and the magnetic field divides the neutron into its two Zeeman states. The polarization of the beam is then defined as a scalar by [77]:

$$P_0 = \frac{N_+ - N_-}{N_+ + N_-} = n_+ - n_- \quad (3.41)$$

where N_+ is the number of neutrons parallel to the z -axis and N_- is the number of neutrons antiparallel to the z -axis. $n_+ = \frac{1}{2}(1 + P_0)$ and $n_- = \frac{1}{2}(1 - P_0)$ are the probabilities of finding a neutron with spin up and spin down, respectively. If all the spins of the neutrons point up $P = 1$ and if all the spins point down $P = -1$. For a completely non-polarized beam $P = 0$.

When polarization is taken into account, the double differential cross section, Eq. (3.19), consists of four cross-sections:

$$\frac{d^2\sigma}{d\Omega_f dE_f} = \frac{1}{2} (\text{sum of the four spin state cross sections}) \quad (3.42)$$

The $\frac{1}{2}$ indicates that the probability of the up and down state of the neutron is the same [76]. The four cross sections are the spin up to up, $\sigma_{\uparrow\uparrow}$, down to down, $\sigma_{\downarrow\downarrow}$, up to down, $\sigma_{\uparrow\downarrow}$, and down to up, $\sigma_{\downarrow\uparrow}$, transitions.

For all experiments, it is important to measure the flipping ratio R , given by [72]:

$$R = \left(\frac{F_N + F_M}{F_N - F_M} \right)^2 \quad (3.43)$$

which is the ratio between the cross sections $\sigma^{\uparrow\uparrow}$ and $\sigma^{\downarrow\downarrow}$, *i.e.* the polarization parallel to the scattering vector and the polarization anti-parallel to the scattering vector¹⁵. R depends on the neutron energy, the size of the beam and its collimation. A flipping ratio of $R = 30$ is difficult to obtain when the beam is of the size 3 mm².

The double differential scattering cross section, where the initial and final spin states, σ_i and σ_f , are taken into account, becomes [72]:

$$\left(\frac{d^2\sigma}{d\Omega_f dE_f} \right)_{\sigma_i, \sigma_f} = \frac{k_f}{k_i} \sum_{i, f} P(i) |\langle f | \sum_l \exp(i\mathbf{Q} \cdot \mathbf{r}_l) U_l^{\sigma_i \sigma_f} | i \rangle|^2 \delta(\hbar\omega + E_i - E_f) \quad (3.44)$$

where $P(i)$ is the probability of being in the initial state $|i\rangle$. The scattering amplitude $U_l^{\sigma_i \sigma_f}$ is given by:

$$U_l^{\sigma_i \sigma_f} = \langle \sigma_f | b_l - p_l \mathbf{S}_{\perp l} \cdot \boldsymbol{\sigma} + B_l \mathbf{I}_l \cdot \boldsymbol{\sigma} | \sigma_i \rangle \quad (3.45)$$

When evaluating the matrix element in Eq. (3.11), it is clearer to look at the nuclear and the magnetic contributions separately.

3.8.1 Nuclear scattering

First the nuclear part is considered. The scattering length operator is given by [76]:

$$\hat{\mathbf{b}} = A + B \boldsymbol{\sigma} \cdot \mathbf{I} \quad (3.46)$$

where $A = \frac{(I+1)b_+ + Ib_-}{2I+1}$ and $B = \frac{b_+ - b_-}{2I+1}$. Evaluating the matrix elements for nuclear scattering produces the following results:

$$\begin{aligned} U_{\uparrow\uparrow}^{\text{nuclear}} &= \langle \uparrow | \mathbf{b} | \uparrow \rangle = A + BI_z \\ U_{\downarrow\downarrow}^{\text{nuclear}} &= \langle \downarrow | \mathbf{b} | \downarrow \rangle = A - BI_z \\ U_{\uparrow\downarrow}^{\text{nuclear}} &= \langle \downarrow | \mathbf{b} | \uparrow \rangle = B(I_x + iI_y) \\ U_{\downarrow\uparrow}^{\text{nuclear}} &= \langle \uparrow | \mathbf{b} | \downarrow \rangle = B(I_x - iI_y) \end{aligned} \quad (3.47)$$

For coherent scattering, $B = 0$, and all coherent scattering appears in the non-spinflip channels. For incoherent scattering, if $I = 0$, there is no spinflip scattering.

¹⁵In practice the flipping ratio is determined by measuring a Bragg Peak with the flipper off and then with the flipper on, see Fig. 3.13.

3.8.2 Magnetic scattering

The magnetic scattering potential, when the orbital part is omitted, is given by [77]:

$$V_m(\mathbf{Q}) = -(\gamma r_0/2) \boldsymbol{\sigma} \cdot \mathbf{S}_\perp(\mathbf{Q}) \quad (3.48)$$

where $\mathbf{S}_\perp(\mathbf{Q})$ is the magnetic interaction vector presented in Sec. 3.5.2. A visualization of \mathbf{S}_\perp can be found in Fig. 3.10. The matrix elements for magnetic scattering are:

$$\begin{aligned} U_{\uparrow\uparrow}^{\text{magnetic}} &= \langle \uparrow | V_m(\mathbf{Q}) | \uparrow \rangle = S_{z\perp}(\mathbf{Q}) \\ U_{\downarrow\downarrow}^{\text{magnetic}} &= \langle \downarrow | V_m(\mathbf{Q}) | \downarrow \rangle = -S_{z\perp}(\mathbf{Q}) \\ U_{\uparrow\downarrow}^{\text{magnetic}} &= \langle \downarrow | V_m(\mathbf{Q}) | \uparrow \rangle = S_{x\perp}(\mathbf{Q}) + iS_{y\perp}(\mathbf{Q}) \\ U_{\downarrow\uparrow}^{\text{magnetic}} &= \langle \uparrow | V_m(\mathbf{Q}) | \downarrow \rangle = S_{x\perp}(\mathbf{Q}) - iS_{y\perp}(\mathbf{Q}) \end{aligned} \quad (3.49)$$

The only components of the magnetization that contribute to the non-spinflip scattering are the ones that are parallel to the neutron spin *i.e.* the polarization and the spinflip scattering are only sensitive to the spin components perpendicular to the beam polarization.

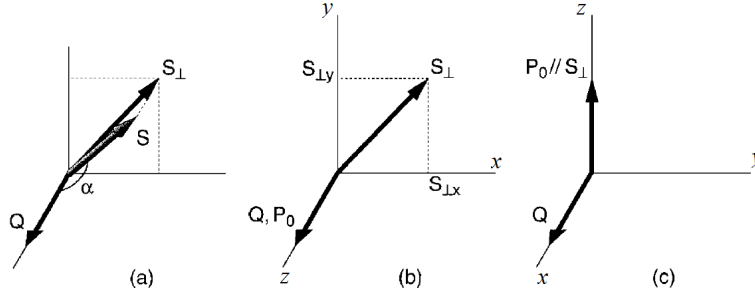


Figure 3.10: a) \mathbf{S}_\perp is the component of the magnetic moment projected onto a plane that is perpendicular to the scattering vector \mathbf{Q} . The angle between \mathbf{Q} and \mathbf{S} is denoted α . b) When $\mathbf{Q} \parallel \mathbf{P}_0$ the $S_{\perp y}$ and $S_{\perp x}$ give rise to spinflip scattering. c) When $\mathbf{Q} \perp \mathbf{P}_0$ and $\mathbf{P} \parallel \mathbf{S}_\perp$ all the scattering is non-spinflip. Adapted from [72].

3.8.3 Coherent and incoherent scattering

By evaluating Eq. (3.45), the four different matrix elements for both nuclear and magnetic scattering $U_{\sigma\sigma}$ are given by [53]:

$$\begin{aligned} U_{\uparrow\uparrow}^{\text{total}} &= b - pS_{z\perp} + BI_z \\ U_{\downarrow\downarrow}^{\text{total}} &= b + pS_{z\perp} - BI_z \\ U_{\uparrow\downarrow}^{\text{total}} &= -p(S_{x\perp} + iS_{y\perp}) + B(I_x + iI_y) \\ U_{\downarrow\uparrow}^{\text{total}} &= -p(S_{x\perp} - iS_{y\perp}) + B(I_x - iI_y) \end{aligned} \quad (3.50)$$

where $p = \gamma r_0/2$. The sum of $U_{\uparrow\uparrow}$ and $U_{\downarrow\downarrow}$ is measured in the non-spinflip channel and the sum of $U_{\uparrow\downarrow}$ and $U_{\downarrow\uparrow}$ is measured in the spinflip channel. All spin-components, both nuclear I_z and magnetic $S_{\perp z}$, that are parallel to the neutron polarization \mathbf{P}_0 give rise to non-spinflip scattering. The other components: $S_{\perp y}$, $S_{\perp x}$, I_y and I_x give rise to spinflip scattering. One can therefore

conclude that when $\mathbf{Q} \parallel \mathbf{P}_0$ all the magnetic scattering is found in the spinflip channel. This statement is true for both elastic, inelastic, coherent and incoherent scattering.

When differentiating between incoherent and coherent scattering, the following expressions for the matrix elements are found [77]:

$$\begin{aligned}
 U_{\uparrow\uparrow}^{\text{total}} &= b_{\text{coherent}} - pS_{z\perp} + b_{\text{isotope incoherent}} + \frac{1}{3}b_{\text{spin incoherent}} \\
 U_{\downarrow\downarrow}^{\text{total}} &= b_{\text{coherent}} - pS_{z\perp} + b_{\text{isotope incoherent}} + \frac{1}{3}b_{\text{spin incoherent}} \\
 U_{\uparrow\downarrow}^{\text{total}} &= -p(S_{x\perp} + iS_{y\perp}) + \frac{2}{3}b_{\text{spin incoherent}} \\
 U_{\downarrow\uparrow}^{\text{total}} &= -p(S_{x\perp} - iS_{y\perp}) + \frac{2}{3}b_{\text{spin incoherent}}
 \end{aligned} \tag{3.51}$$

Here b_{coherent} is the coherent scattering length, $b_{\text{isotope incoherent}}$ is the isotope incoherent scattering length, and $b_{\text{spin incoherent}}$ is the spin-incoherent scattering length. The contribution of the coherent scattering in the spinflip and non-spinflip channels can be found in Table 3.2. Only paramagnetic and nuclear spin scattering give rise to spinflip scattering and they can be distinguished by measuring the spinflip and non-spinflip scattering with a horizontal setup where $\mathbf{P}_0 \parallel \mathbf{Q}$ and a vertical setup where $\mathbf{P}_0 \perp \mathbf{Q}$ Fig. 3.11. The nuclear spin scattering is unchanged while the paramagnetic scattering changes. Horizontal and vertical setup is illustrated in Fig. 3.11.

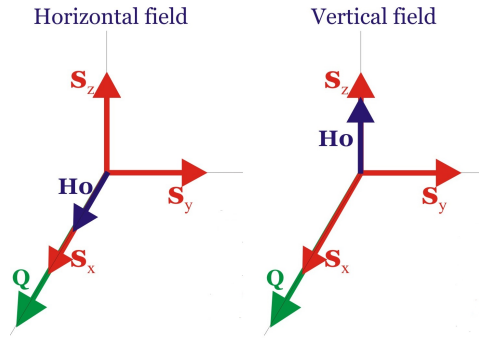


Figure 3.11: Right: When $\mathbf{Q} \parallel \mathbf{H}_0$, the setup is horizontal because the magnetic field determining the polarization direction is horizontal. **Left:** When $\mathbf{Q} \perp \mathbf{H}_0$, the setup is vertical because the magnetic field determining the polarization direction is vertical. The figure was constructed by Zahra Yamani, instrument scientist at the polarizing three-axis spectrometer C5 in Chalk River, Canada.

By measuring the spinflip and the non-spinflip cross sections with both a horizontal field and a vertical field it is possible to determine the direction of the spins and the directions of the spin excitations Table 3.2.

3.8.4 Experimental setup

The following elements must be added to a standard three-axis spectrometer to make it a polarizing instrument.

Polarizers: For polarizing experiments the monochromator often works as a polarizer *i.e.* selects all the neutrons with a given spin. Good polarizer crystals are ferromagnetic single crystals where

Type of scattering	HF:	$\mathbf{P}_0 \parallel \mathbf{Q}$		VF:	$\mathbf{P}_0 \perp \mathbf{Q}$	
	Spinflip	Non-spinflip	Spinflip	Non-spinflip	Non-spinflip	Non-spinflip
Nuclear coherent	0	1	0	1	1	1
Nuclear isotope incoherent	0	1	0	1	1	1
Nuclear spin incoherent	2/3	1/3	2/3	1/3	1/3	1/3
Magnetic	xx+yy	0	xx	yy	yy	yy

Table 3.2: The spinflip and non-spinflip channel cross sections for a horizontal field (HF) and vertical field (VF) at the sample position.

the magnetic structure factor $F_M(\mathbf{Q})$ is equivalent to the nuclear structure factor $F_N(\mathbf{Q})$. The differential cross section for a polarizer is given by:

$$\frac{d\sigma}{d\Omega} = F_N^2(\mathbf{Q}) + 2(\hat{\mathbf{P}} \cdot \hat{\boldsymbol{\mu}})|F_N(\mathbf{Q})||F_M(\mathbf{Q})| + F_M^2(\mathbf{Q}) \quad (3.52)$$

where $\hat{\mathbf{P}}$ is the unit vector along the polarization direction with respect to a magnetic field, $\hat{\boldsymbol{\mu}}$ is the unit vector along the magnetic moments in the polarizing crystal. $\hat{\mathbf{P}} \cdot \hat{\boldsymbol{\mu}} = 1$ if the magnetic moments are parallel to an applied magnetic field and $\hat{\mathbf{P}} \cdot \hat{\boldsymbol{\mu}} = -1$ when the magnetic moments are antiparallel to an applied magnetic field. This is the case for the (111) reflection in the Heusler Alloy Cu_2MnAl , which is a popular polarizer. The analyzer is often made of the same material as the monochromator and works in the same way.

Flippers: The flippers in a polarization experiment can change the direction of the spins. A flipper can work either adiabatically or non-adiabatically. In both cases the precession of the neutron spins around a magnetic field is utilized. The precession rate is given by the Larmor angular frequency ω_L , which is $\omega_L[\text{kHz}] = 2.916 \cdot 10^{-4} B[\text{T}]$ [95]. If the magnetic field rotation ω_B is much smaller than the Larmor frequency, then the component of the polarization parallel to the magnetic field maintains its direction parallel to the field, while the perpendicular component precesses around \mathbf{B} . This is the adiabatic case. If ω_B is much larger than ω_L a guide field switch will leave the polarization unchanged, but it is anti-parallel with the magnetic field \mathbf{B} . This is the non-adiabatic flipping method. Mezei-flippers can both be adiabatic and non-adiabatic flippers. A Mezei-flipper consists of a coil, where a guide field is applied both before, over and after the coil. Before entering the coil the neutron spins are aligned along the guide-field, but entering the coil the neutrons feel a magnetic field in a new direction: the guide field plus the field from the coil. The neutrons start to precess around this new resultant magnetic field and when exiting the coil the neutrons have a new polarization direction. The new polarization direction depends on the resultant field, the thickness of the coil and the neutron velocity.

A sketch of the final three-axis setup, with polarizers (monochromator and analyzer) and flippers, can be seen in Fig. 3.12.

The polarizer only selects one spin state, let us say up, and often the detector can only detect one of the spin states, let us again say up. In order to measure all four spin cross sections, it is necessary to place flippers on both sides of the sample that can change the spin state. These flippers can be turned on and off depending on the desired measurement. If both flippers are off, $\sigma_{\uparrow\uparrow}$ is measured; if the first flipper is on and the second is off, $\sigma_{\downarrow\uparrow}$ is measured, and so on. A more thorough description of the experimental setup for measuring the four cross sections can be found in Fig. 3.13.

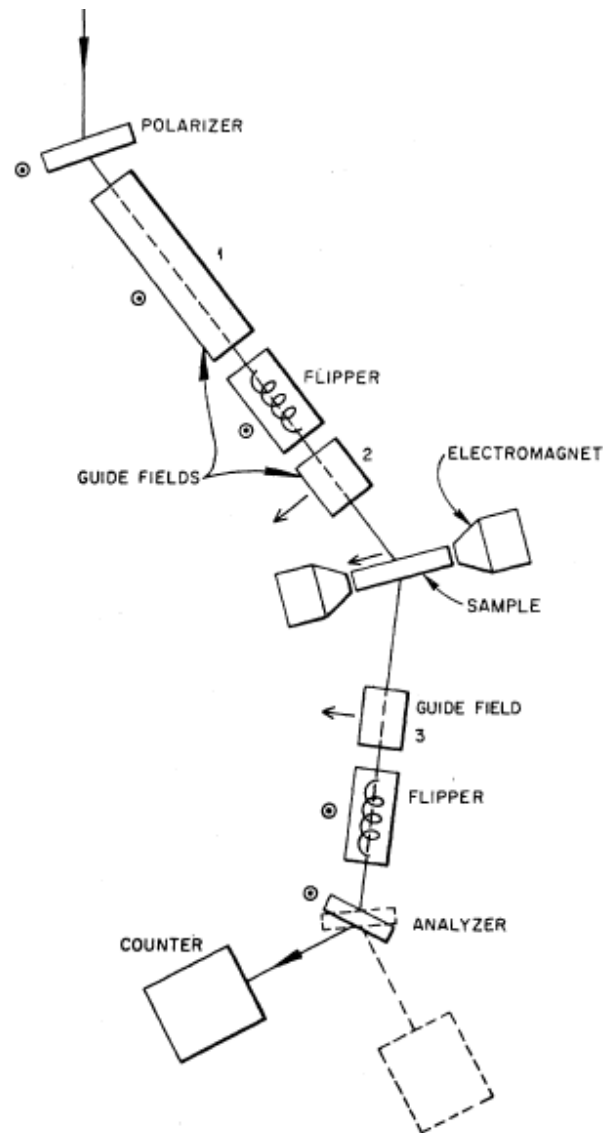


Figure 3.12: A three-axis spectrometer in polarized mode. The 1st axis is the polarizer which is a Co-Fe-crystal situated inside a permanent magnet. On the way to the 2nd axis, where the sample is situated inside an electromagnet, there is a guide field, a flipper and another guide field. On the way to the 3rd axis which is identical to the 1st axis, the neutrons pass through one more guide field and a flipper. The guide fields are marked with a 1 and 2, and the electromagnet containing the sample (at modern instruments the electromagnet is exchanged by two perpendicular Helmholtz coils.), can be in both vertical and horizontal mode. In this setup the arrows, in front of the sample, indicate that the experiment is in horizontal mode *i.e.* the magnetic field and therefore the polarization is parallel to Q . The vertical magnetic fields are indicated with circles and are all pointing out of the paper. From [53].

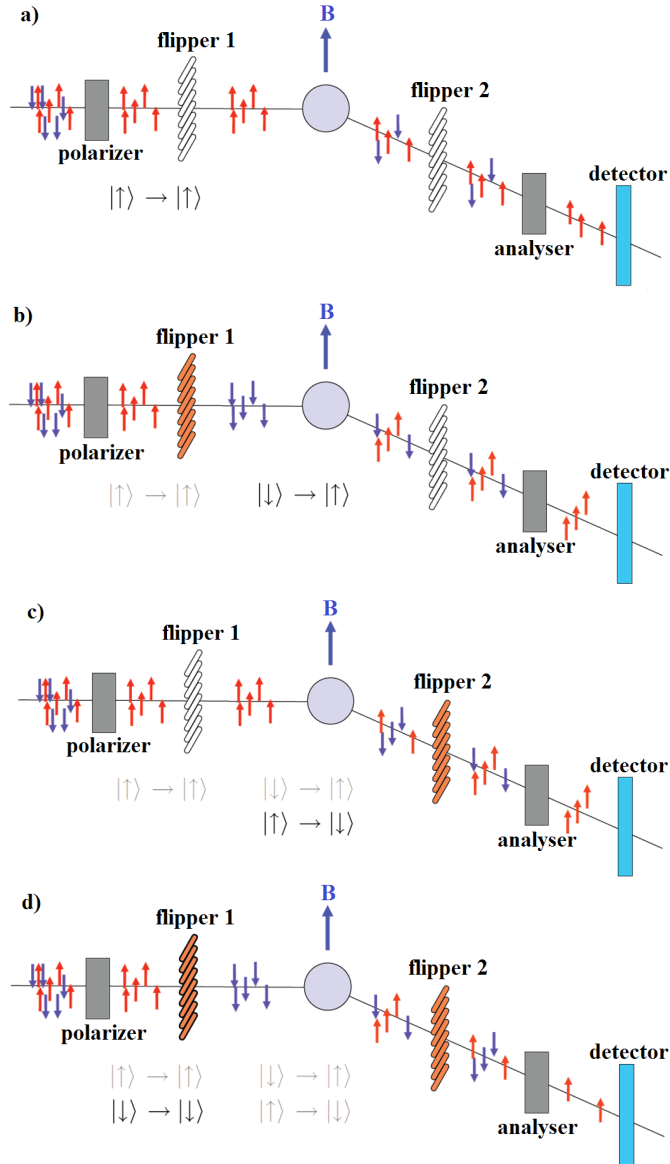


Figure 3.13: The polarizer and the detector can only select neutrons with spin up $|\uparrow\rangle$. Flippers are needed to change the spin-direction, so all the four cross sections can be measured. **a)** When measuring the non-spinflip $|\uparrow\rangle \rightarrow |\uparrow\rangle$ cross section both flippers should be turned off. **b)** When measuring the spinflip $|\downarrow\rangle \rightarrow |\uparrow\rangle$ cross section the first flipper should be on and the second turned off. **c)** When measuring the spinflip $|\uparrow\rangle \rightarrow |\downarrow\rangle$ cross section the first flipper should be off and the second on. **d)** When measuring the non-spinflip $|\downarrow\rangle \rightarrow |\downarrow\rangle$ cross section both flippers should be turned on. Adapted from [78].

3.8.5 Examples of polarization analysis

Polarization analysis can be used to do the following things:

1. Separate isotopic incoherent scattering from coherent scattering (see item 5 a)).
2. Separate nuclear and magnetic Bragg peaks in antiferromagnets.
3. Separate magnon and phonon scattering in both ferromagnets and antiferromagnets (this is what has been in this thesis).
4. Separate coherent and spin-incoherent nuclear signals in solids and liquids (see item 5 b)).
5. Separate paramagnetic scattering from other kinds of incoherent scattering (see item 5 c)).

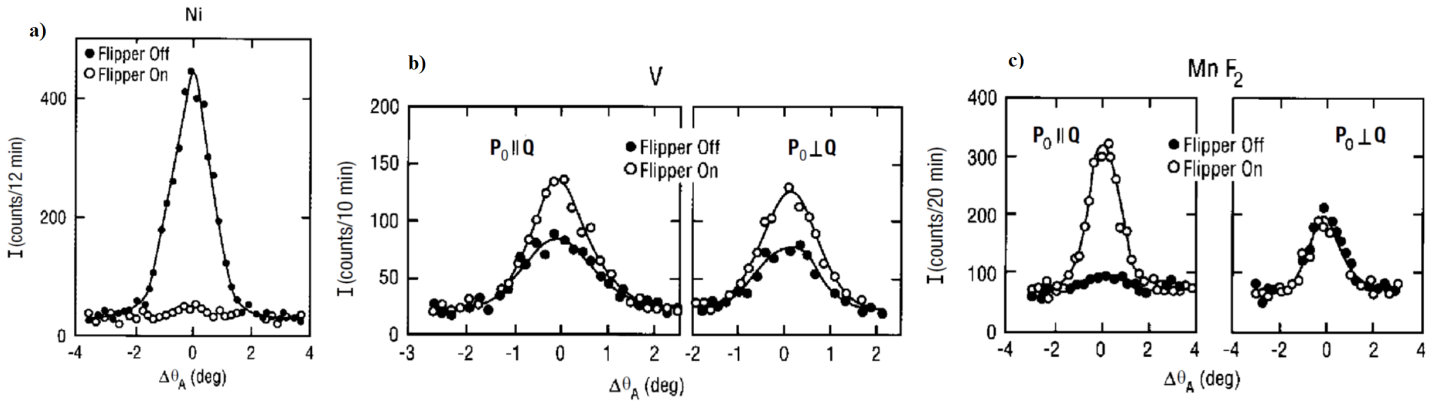


Figure 3.14: The rocking curves^a for different samples around Bragg reflections. **a)** Isotopic incoherent scattering from nickel. All the scattering is in the non-spinflip channel (flipper off). The isotope incoherent scattering is suppressed when the flipper in the scattered beam is turned on. **b)** Nuclear-spin incoherent scattering from a single isotope of vanadium. The spinflip scattering (flipper on) is twice the size of the non-spinflip scattering (flipper off) and independent of the polarization direction. **c)** In manganese-fluoride MnF_2 the paramagnetic scattering can be detected by changing the polarization direction. When measuring in horizontal field all the scattering appears in the spinflip channel (flipper on) and when the polarization is vertical the spinflip and non-spinflip signal is equal. From [72].

^aA rocking curve is the scan one makes of a Bragg peak where the sample is "rocked" around a vertical axis through the Bragg peak position [76].

4 YMnO₃

In this section hexagonal h -YMnO₃ will be presented. h -YMnO₃ has been studied intensively in the last 50 years, but many of its properties are still not understood. YMnO₃ crystallizes naturally in the hexagonal form due to the small R -ion (here Y), but under high pressure it can crystallize in the orthorhombic form o -YMnO₃, which is the natural form of the $RMnO_3$ with a large R -ion radius. Both o -YMnO₃ and h -YMnO₃ are multiferroics, but due to very different mechanisms, they have both been studied closely. One should be aware of the misleading naming of the compounds often found in literature. Systems of the form ABO₃ are called perovskite structures, where the B-ion is in an octahedral environment of O-ions. The orthorhombic form of YMnO₃ is therefore an example of a perovskite structure. Unfortunately many authors refer to the hexagonal structure of YMnO₃ as perovskite YMnO₃, which has confused many groups tricking them to refer to results of the wrong structure. h -YMnO₃ is the only compound considered in this thesis and the h subscript is therefore not used from now on. Even though the compound has been investigated for many years it is still not understood why it is ferroelectric and the magnetic space group is still under great debate. In this section the current knowledge will be presented and discussed, hopefully giving a full picture of what is known and what is merely conjectures.

4.1 Crystal structure and magnetism of Mn³⁺

YMnO₃ is one of the hexagonal compounds of the form $RMnO_3$, where $R = \text{Ho, Er, Tm, Yb, Lu, Sc and Y}$, presented in Sec. 2.5.3.

The lattice parameters are $a = b = 6.14 \text{ \AA}$ and $c = 11.4 \text{ \AA}$ with the angles $\alpha = \beta = 90^\circ$ and $\gamma = 120^\circ$ and belongs to the crystallographic space group $P6_3cm$ at room temperature [87]. The space group specifications can be seen in Fig. B.1 in appendix B.

Manganese is a transition metal in group 7 and occurs with oxidation number Mn³⁺ in hexagonal YMnO₃ and therefore has 4 $3d$ -electrons ($3d^4$). Yttrium is also a transition metal but a period higher in the periodic table with $4d$ -electrons. It is situated in group 3 in the periodic table and has three available d -electrons. In YMnO₃ yttrium occurs as Y³⁺ which shows yttrium's similarity to the rare earth elements that almost always has oxidation number 3+. Because Y³⁺ has no d -electrons (and no f -electrons) the manganese ions are the only magnetic ions in YMnO₃ with $S = 2$, due to Hund's rules, and $L = 0$, due to orbital quenching, as explained in Sec. 2.2.

In Fig. 4.1 the room temperature crystal structure can be seen. The Y³⁺ ions are positioned in a seven-fold oxygen environment and the Mn-ions are in a trigonal bipyramidal environment. The Y³⁺ ions form two-dimensional layers that are separated by the MnO₅ trigonal bipyramids. The bipyramids are corner shared and form an almost perfect triangular lattice of Mn-ions in the basal plane (ab -plane). The unit cell contains six manganese ions and they are positioned at $(a, b, c) = (1/3, 0, 0), (0, 1/3, 0), (2/3, 2/3, 0), (2/3, 0, 1/2), (0, 2/3, 1/2)$ and $(1/3, 1/3, 1/2)$.

The trigonal bipyramidal crystal field splits up the Mn³⁺ d -orbitals and the electrons occupy the low-lying doublets. The $S = 2$ spin configuration above and below the ferroelectric transition is depicted in Fig. 4.2. The ferroelectric transition will be discussed further in Sec. 4.2.

The Mn³⁺ ion is not Jahn-Teller active in this crystal environment [48], *i.e.* it is not favorable for the c -axis to elongate or dis-elongate to lower the energy.

4.2 The structural and magnetic phase transitions

YMnO₃ is an insulator at all temperatures. Above $T_c = 1250 \text{ K}$ the system is both paraelectric and paramagnetic and belongs to the spacegroup $P6_3/mmc$ [27]. Specifications about the

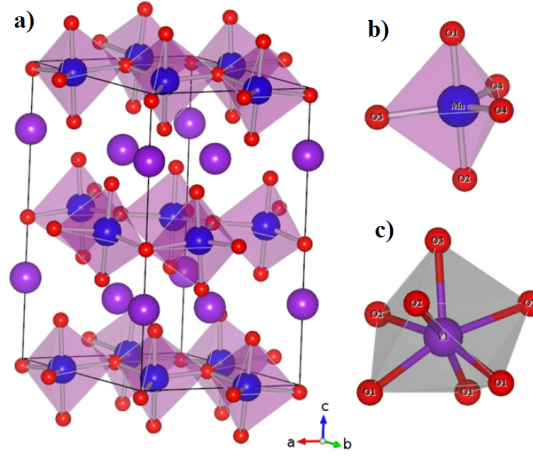


Figure 4.1: a) The room temperature crystal structure of hexagonal YMnO₃ (in the ferroelectric phase). Purple is yttrium, blue is manganese and red is oxygen. The unit cell is indicated with black lines. The unit cell contains two layers of Y³⁺ ions and two layers of MnO₅ bipyramids. b) The MnO₅ trigonal bipyramid. c) The 7-fold coordination of yttrium. From [20].

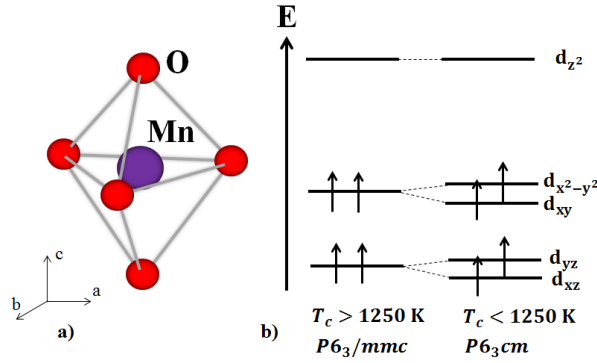


Figure 4.2: a) Visualization of a MnO₅ bipyramid. There is 120° between the oxygen atoms in the *ab*-plane and 90° between the *c*-axis oxygen atoms and oxygen atoms in the *ab*-plane. b) Above the ferroelectric transition temperature T_C the 3d energy levels of manganese are split in three due to the trigonal bipyramidal environment: two low-lying doublets and one singlet at higher energy. Due to the change in structure from $P6_3/mmc$ to $P6_3cm$ when entering the ferroelectric phase at $T_C = 1250$ K the doublets split up. Due to Hund's rules the four *d*-electrons of manganese singly occupy the four low-lying energy levels in both configurations.

$P6_3/mmc$ space group are given in Fig. A.1 in appendix A.

Below $T_c = 1250$ K the MnO₅ bipyramids create close packing by tilting with respect to the *c*-axis and the crystal structure changes from $P6_3/mmc$ to $P6_3cm$ as it enters the ferroelectric phase [1]. The tilting is not random, but is a trimerization of the trigonal bipyramids as seen in Fig. 4.3 a).

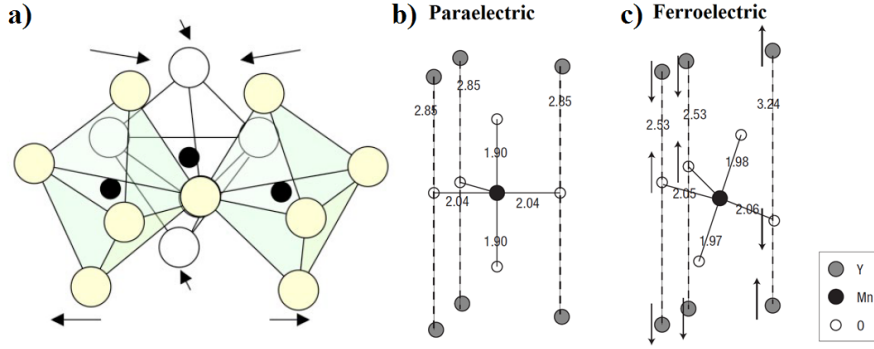


Figure 4.3: a) When entering the ferroelectric phase at $T_c = 1250$ K the trigonal bipyramids tilt and form trimers around the shared oxygen ion in the center. From [1]. b) In the paraelectric phase YMnO_3 is centrosymmetric with an ab mirrorplane. The bond lengths are in Å c) When YMnO_3 enters the ferroelectric phase the centrosymmetry is broken and the bond lengths change. From [88].

The tilting of the trigonal bipyramids breaks the ab mirror plane and inversion symmetry which triples the unit cell and pushes two Y^{3+} -ions up along the c -axis and one down by around 0.5 Å [88]. The movement of the yttrium ions create a spontaneous polarization with the size $P = 5 \mu\text{C}/\text{cm}^2$ [74].

The polarization is created by the hybridization between the empty d -orbitals in the Y^{3+} with the p -orbitals of oxygen along the c -direction [97]. No hybridization or change in chemical bonding between the Mn^{3+} and the surrounding ligands is observed which makes YMnO_3 different from other ferroelectrics¹⁶ and it is therefore referred to as a geometrically (and electrostatically) driven ferroelectric [88] as presented in Sec. 2.4.2. The Y^{3+} ions are too small to naturally crystallize in the orthorhombic form, which is more close packed than the hexagonal form, and the distortion of the bipyramids lower the energy by filling out the extra space around the Y^{3+} atoms [32]. The influence of the tilting on the bond-lengths is illustrated in Fig. 4.3 b) and c).

When cooled further down, YMnO_3 orders antiferromagnetically at $T_N \sim 70$ K. The transition temperature has been determined by numerous groups and two examples can be seen in Fig. 4.4. The intensity of the (100) magnetic Bragg peak has been measured from base to around 80 K. As the temperature is ramped up the intensity of the peak decreases and vanishes at T_N . The points close to, but not at the transition temperature, can be fitted to a power law, thereby determining the transition temperature and the critical exponent β , Eq. (2.16). The transition temperatures and critical exponents measured by Chatterji *et al.* [12] and Roessli *et al.* [65] gave a $T_N = 69.89 \pm 0.05$ K with $\beta = 0.295 \pm 0.008$ and $T_N = 72.1 \pm 0.05$ K and $\beta = 0.187 \pm 0.002$, respectively. The β -value for YMnO_3 shows that the system cannot be described by a single model, but needs a combination of different models Sec. 2.6. For a two-dimensional XY -antiferromagnet the theoretical critical exponent is $\beta = 0.23$. For a three-dimensional triangular Ising antiferromagnet $\beta = 0.19$ [65].

Before discussing the multiferroic couplings and the magnetic structure bulk measurements and other important experimental discoveries will be presented. With the knowledge of all the different (sometimes inconsistent) measurements it is easier to understand the problems addressed in this MSc thesis.

¹⁶It was presumed at first that movements of the Mn-ions with respect to the center of the bipyramide was the origin of ferroelectricity in the compound, but it is the general opinion now that it is only the yttrium ions that contribute to the polarization and that the Mn-ions are stationary in the process.

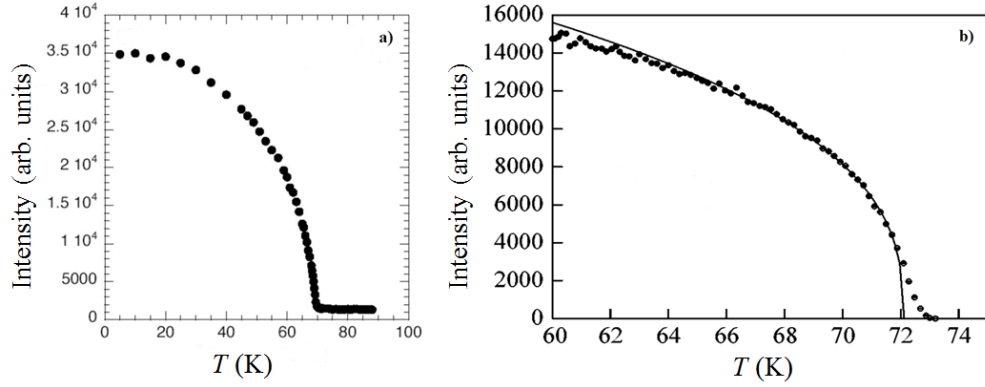


Figure 4.4: **a)** The intensity of the magnetic Bragg peak (100) as a function of temperature finding a transition temperature of $T_N = 69.9$ K and critical exponent $\beta = 0.295$. From Chatterji *et al.* [12]. **b)** The intensity of the magnetic Bragg peak (100) as a function of temperature finding a transition temperature of $T_N = 72.1$ K and critical exponent $\beta = 0.187$. There is a great amount of critical scattering within 1-2 K around T_N . From Roessli *et al.* [65].

4.3 Bulk Measurements

Magnetic susceptibility measurements done in refs. [71] and [44] showed a strong anisotropy between the c -direction and the ab -direction, below the antiferromagnetic transition temperature T_N , as seen in Fig. 4.5 a). From the susceptibility measurements the Curie-Weiss temperature Θ_{CW} was also determined, Fig. 4.5 b).

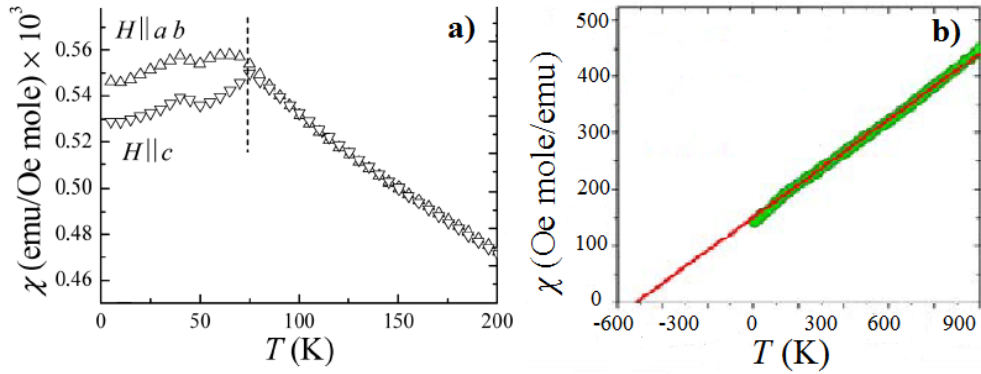


Figure 4.5: **a)** The susceptibility as a function of temperature. It is clear that YMnO_3 orders antiferromagnetically because the susceptibility does not go to zero at zero temperature. [71]. **b)** The Curie-Weiss temperature Θ_{CW} is determined by extrapolating the $1/\chi$ data as a function of temperature to zero. $\Theta_{CW} = -500$ for YMnO_3 which is very far from the Néel temperature $T_N \sim 70\text{K}$ due to frustration. From [44].

The large frustration due to the triangular lattice with antiferromagnetic exchange couplings,

makes it difficult for the magnetic moments of the manganese ions to order until the system is cooled well below the Curie-Weiss temperature $\Theta_{CW} = -500$ K. This results in a high frustration parameter for YMnO_3 given by the ratio between the Curie-Weiss temperature and the Néel temperature $T_N \sim 70$ K [59]:

$$\frac{|\Theta_{CW}|}{T_N} = \frac{|-500\text{K}|}{70\text{K}} \approx 7 \quad (4.1)$$

Because the manganese ions are $S = 2$ ions the magnetic moment per site should be $4\mu_B$, but it turns out that the effective moment per site is only $2.9\mu_B$ at $T = 1.7$ K [54].

Measurements of the heat capacity C_p by refs. [83], [79], and [73] shows a clear anomaly at the magnetic transition temperature.

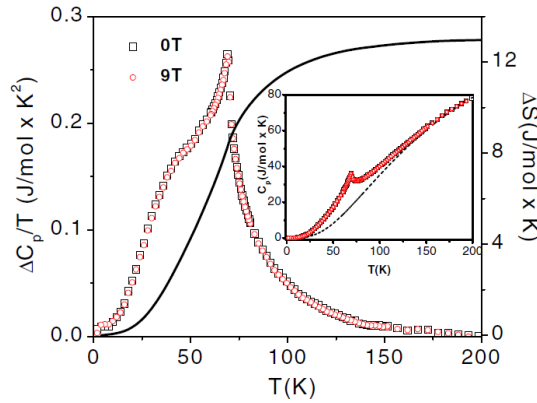


Figure 4.6: The heat capacity at zero field (open black squares) and 9 T (open red circles) and the entropy (black line) as a function of temperature in zero field of a powder sample. At T_N the heat capacity shows an anomaly. The inset shows the raw heat capacity data (red dots) and the modeled phonon contribution (the dotted line). The main graph is the heat capacity measurements with the phonon contribution subtracted. From [83].

The magnetic entropy in Fig. 4.6 at $T = 200$ K is close to the maximal entropy for a $S = 2$ system:

$$\Delta S(200\text{K}) \approx S_{\max} = R \ln(2S + 1) = 13.38 \text{ J mol}^{-1}\text{K}^{-1} \quad (4.2)$$

The thermal conductivity κ_c was measured along the c -direction and the ab -direction in ref. [71] and can be seen in Fig. 4.7. κ_c is constant in both directions from $T = 200$ K to T_N where both curves increase rapidly.

The suppression of the thermal conductivity in the range $20 \text{ K} < T < T_N$ cannot be explained by phonon-only-interactions, as seen in Fig. 4.8. Above T_N the thermal conductivity can be fitted to a model where spin fluctuations are taken into account [71].

Measurements of the dielectric constant ϵ on a powder sample showed an anomaly around the magnetic ordering temperature, Fig. 4.9, indicating a coupling between the polarizations and magnetic degrees of freedom [73].

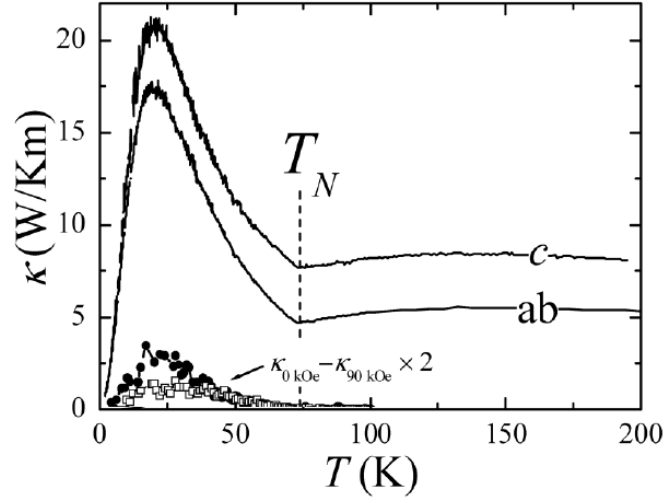


Figure 4.7: The thermal conductivity κ measured along c and ab in a single crystal. Both curves change appearance at T_N . The filled circles represent the difference in the c -direction between measurements done at zero field and at 90 kOe and the open squares show the difference in the ab -direction. The H-field dependence is therefore negligible. Adapted from [71].

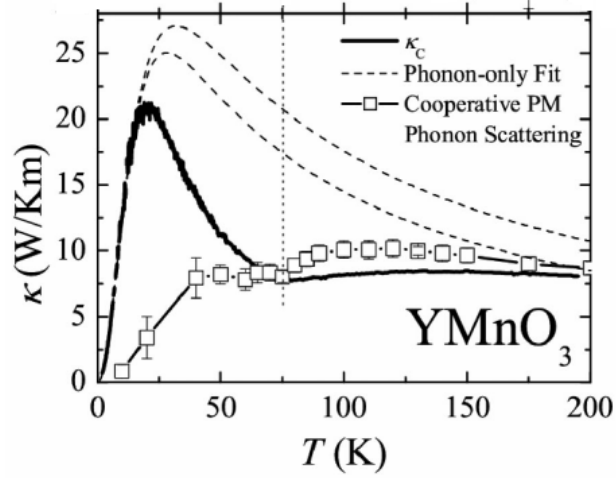


Figure 4.8: Thermal conductivity κ (full black line) as a function of temperature. The dashed lines correspond to two different fits to κ assuming phonon only interactions. The open squares correspond to a model where the effect of spin fluctuations on κ is taken into account. The model is scaled to match the size of the thermal conductivity measurements at T_N . T_N is indicated with the vertical dotted line. Adapted from [71].

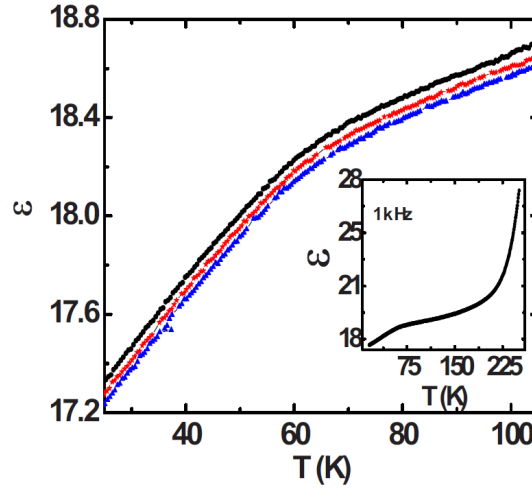


Figure 4.9: The dielectric constant as a function of temperature at different magnetic fields. The black curve was taken with $\mu_0 H = 0$ T, the red curve was taken with $\mu_0 H = 3$ T and the blue curve was measured with $\mu_0 H = 5$ T on a powder sample. The inset shows the dielectric constant in a larger temperature range. The change in the slope around T_N reflects antiferromagnetic ordering. The From [73].

4.4 The magnetic structure and space group

The crystallographic unit cell and the magnetic unit cell are identical and the propagation vector of the magnetic cell is $\mathbf{k} = 0$ which means that the magnetic and nuclear peaks occur at the same positions. This makes the determination of the magnetic structure difficult. Twelve different magnetic structures are allowed in the space group with propagation vector $\mathbf{k} = 0$ [57].

The most recent articles about YMnO_3 states that the magnetic space group is $P6'_3$ [91], $P6'_3 cm'$ [27] and $P6_3 cm$ [84], respectively. Singh *et al.* [74] has compared neutron scattering data, magnetization data, polarization data, dielectric constant data and second harmonic generation concluding that only one magnetic group can explain everything: the $P6'_3$ group. This group was already proposed by ref. [7], but with a magnetic structure that is not compatible with experiments.

Singh *et al.* argue that the polarization and the antiferromagnetic order parameter cannot be in the same irreducible representation because the magneto-elastic coupling is non-linear. In Fig. 4.10 the evolution of the (100) antiferromagnetic Bragg peak and the ab -component of the dielectric constant is shown. There is a clear anomaly at the magnetic ordering temperature indicating a magnetoelectric coupling, but if the coupling were to be linear the anomaly at T_N for the dielectric constant should be divergent [74]. The c -component of the dielectric constant shows no anomaly.

Since the polarization belongs to the totally symmetric Γ_1 representation the antiferromagnetic order cannot belong to the Γ_1 representation of the magnetic space group. The structure proposed by Brown and Chatterji [7] is the Γ_1 of the $P6'_3$ group, Fig. 4.11 b). However, Brown and Chatterji only considered the Γ_1 representation of the magnetic space groups. Instead Singh *et al.* assume that the structure by Muñoz *et al.* [54] is correct (they did a full symmetry analysis) and this structure is the Γ_4 representation of the $P6'_3$ magnetic group, Fig. 4.11 a). This space group allows for a ferromagnetic signal induced by the DM-interaction, seen by [56]

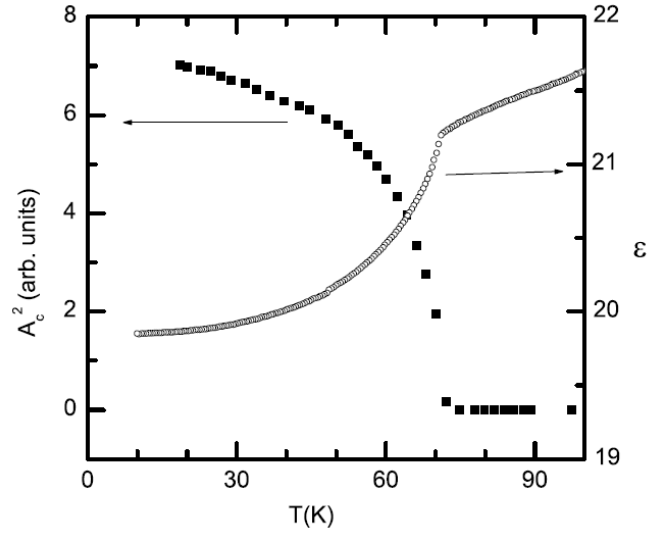


Figure 4.10: Dependence of the (100) magnetic Bragg reflection representing the antiferromagnetic order parameter (filled squares, left scale). The ab -component of the dielectric constant, representing the ferroelectric order parameter, as a function of temperature (open circles, right scale). From [74].

and discussed in Sec. 4.5. With the Γ_4 representation of the $P6'_3$ magnetic group the exchange interaction between the Mn-layers is antiferromagnetic, while the Γ_1 representation results in a ferromagnetic interaction between the manganese layers.

If the small ferromagnetic signal is an artifact there are three other possible magnetic groups that can explain all data: $P6'_3c'm$, $P6'_3cm'$ and $P6_3c'm'$ [74].

4.5 Ferromagnetic signal

Based on the theory on orthorhombic $RMnO_3$ Pailhès *et al.* [56] propose that the system can benefit energetically from the DM-interaction presented in Sec. 2.2. The DM-interaction induces a small ferromagnetic signal due to the movement of the interlayer oxygen atom along the c -direction, see Fig. 4.12 b). The $(2\bar{1}1)$ Bragg reflection was examined, because it is a forbidden antiferromagnetic reflections in the $P6_3cm$ group and a weak nuclear reflection. The intensity as a function of temperature is depicted in Fig. 4.12 a). The $(2\bar{1}1)$ Bragg peak intensity is zero at T_N .

The DM-interaction can be the explanation for the hybridization of the spin and the lattice, but the interaction is three orders of magnitude weaker than the electrostrictive interaction [91].

The magnetic space group of $YMnO_3$ is under debate, and whether the measured signal implies a ferromagnetic moment in $YMnO_3$ or not, is important for determining the magnetic space group. Fiebig *et al.* [21] claims that the ferromagnetic signal appears because of Mn_3O_4 impurities in the crystals despite the similarities in critical temperature.

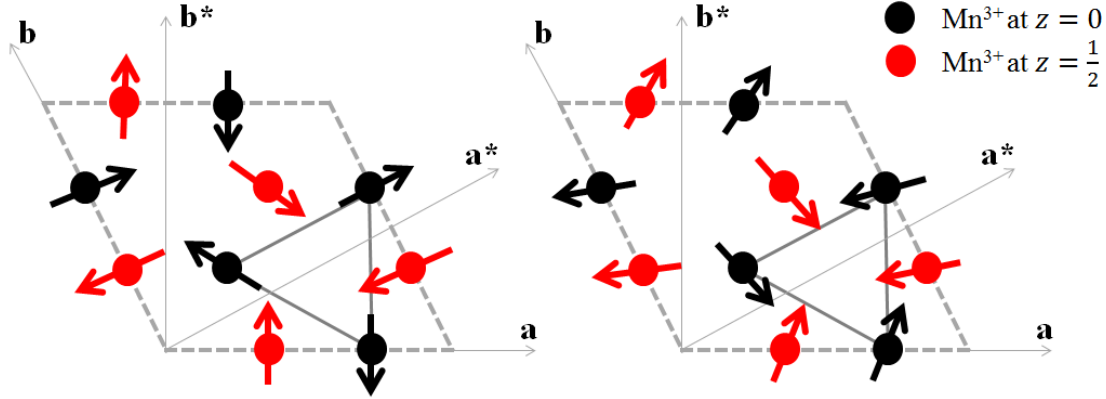


Figure 4.11: Two magnetic structures belonging to the space group $P6'_3$. Black represents the manganese ions in the $z = 0$ layer and red represents the manganese ions in the $z = 1/2$ layer. **Right:** The Γ_4 representation proposed by [74]. **Left:** The Γ_1 representation. This structure was proposed by [12].

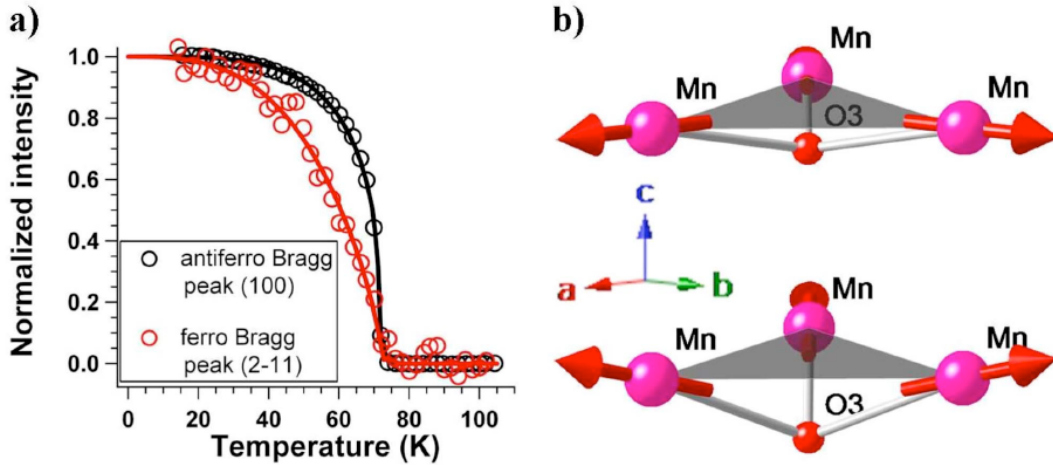


Figure 4.12: **a)** The intensity of the (100) antiferromagnetic Bragg peak and the $(2\bar{1}0)$ ferromagnetic Bragg peak intensity as a function of temperature. **b)** The effect of the DM-interaction on the Mn-spins. In the top picture the spins point along the ab -plane and in the lower picture the spins tilt upwards with respect to the ab -plane creating a small magnetic moment along the c -axis. From [56].

4.6 The magnetoelastic coupling

In 2008 Lee *et al.* [43] observed a giant magneto-elastic coupling in YMnO_3 . This effect is a contraction of the manganese ion lattice sites in the ab -plane when entering the magnetic phase. These measurements were done on a powder sample with neutron diffraction. The direction of

the displacements can be seen in Fig. 4.13 b). The ligands and the yttrium ions also move as indicated in Fig. 4.13 a), but as they are not magnetic ions, the focus is on the movement of the Mn^{3+} ions which is up to 0.1 Å, see Fig. 4.14. The displacements of the atoms do not change the space group of the crystal.

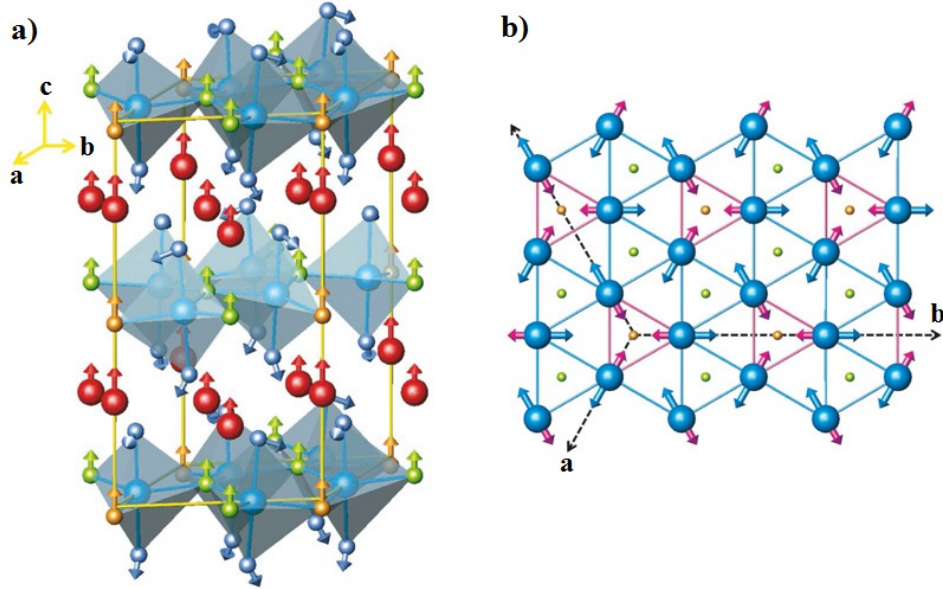


Figure 4.13: a) The unit cell of YMnO_3 indicating the displacements of the atoms during the magnetic phase transition. Red is yttrium, cyan is manganese, green and orange are the ab -plane oxygen atoms and blue is the out of plane c -axis oxygen atoms b) The simplified structure looking along the c -axis. Only atoms in the a - b -plane are shown. The blue arrows indicate the displacement of the manganese ions in YMnO_3 when entering the magnetic phase. The pink arrows show the displacement of the manganese ions in the sister compound LuMnO_3 , which is not relevant here. The displacements are largest in YMnO_3 . From [43].

These results, however, are under debate. Thomson *et al.* [82] question the validity of the measurements. The displacements of around 0.1 Å are within the spread of reported positions at room temperature.

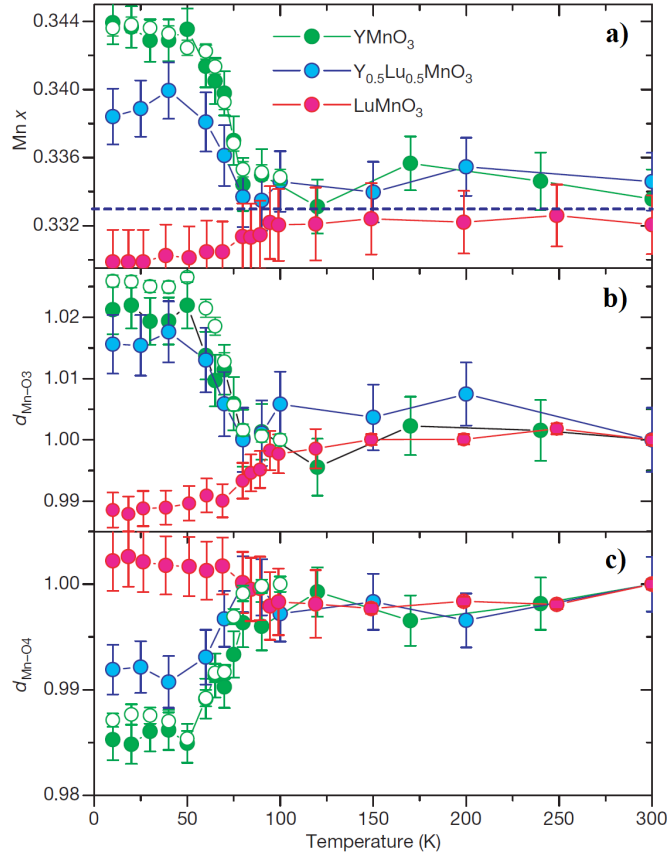


Figure 4.14: The Mn-ion position in Å as a function of temperature determined with high-resolution neutron (filled green circles) and X-ray synchrotron (open green circles) powder diffraction experiments. The errorbars are the standard deviation obtained from Rietveld refinement and Fullprof. **a)** The Mn-ion positions distorted away from the ideal $x = 1/3$ position. **b)** The distance between the Mn-ions and the O3 atom as a function of temperature. **c)** The distance between the Mn and the O4 atom as a function of temperature. From [43].

4.7 Diffuse magnetic scattering

Above the magnetic transition temperature, T_N , scattering is diffuse, representing short-range magnetic order. The correlation length ξ can be derived from the width of diffuse scattering peaks, while the normalized intensity can be determined by the area of the diffuse scattering peaks [59]. The correlation length gives an idea about the nature of spin fluctuations above T_N . The correlation length as a function of temperature can be seen in Fig. 4.15, where a typical scan of the diffuse scattering around the magnetic Bragg peak above the transition temperature is also shown.

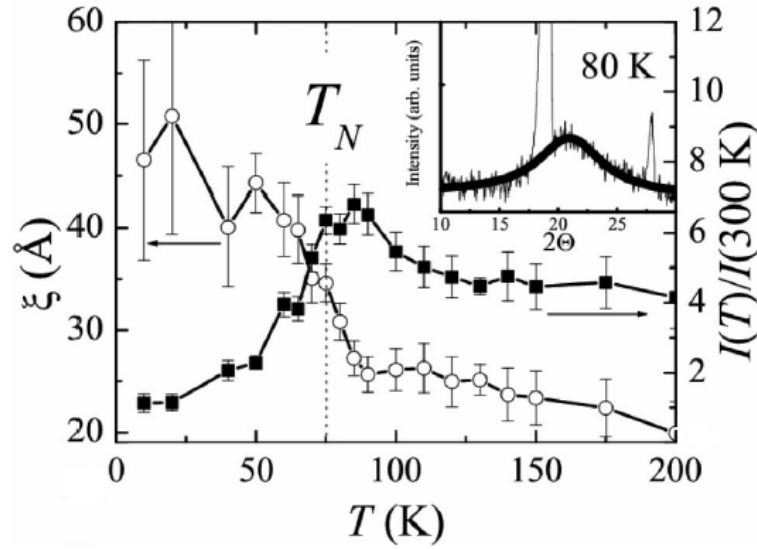


Figure 4.15: The correlation length (circles) and the normalized intensity (black squares) around the magnetic transition temperature T_N derived from diffuse scattering measurements. The inset shows a typical 2θ scan with the sharp nuclear Bragg peak and the broad diffuse magnetic scattering. From [71].

4.8 Excitations in YMnO₃

The phonon dispersions from $\Gamma \rightarrow M \rightarrow L \rightarrow A \rightarrow \Gamma \rightarrow K \rightarrow H \rightarrow A$ have been calculated [67] for YMnO₃ and can be seen in Fig. 4.16. To be reminded of the directions see the Brillouin zone in Fig. 2.4. The only direction in the ab -plane that has not been calculated is $M \rightarrow K$.

The spin wave dispersions of the three modes around (000) have been calculated and measured by Sato *et al.* [68] and Petit *et al.* [63] and can be seen for different directions in reciprocal space in Fig. 4.17 and in the $(h00)$ direction in Fig. 4.18. The mode that goes to zero was not detectable at (100) and was therefore measured at (101) in both refs. [68] and [63]. Sato *et al.* explains this with a better resolution along l at their particular experiment and Petit *et al.* concludes that, it the same mode, but that the gap closes at the (101) position due to the exchange between the Mn-layers.

The spin wave dispersions in Fig. 4.18 can be described by the spin Hamiltonian [62]:

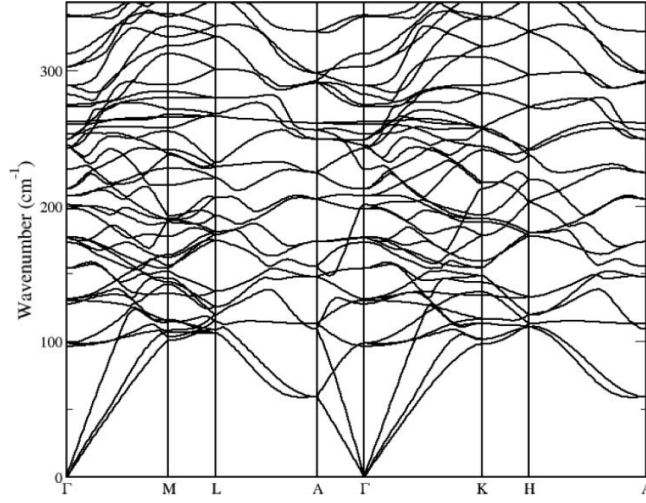


Figure 4.16: The phonon dispersions along different directions in reciprocal space calculated with ab-initio calculations. A wavenumber of 100 cm⁻¹ corresponds to an energy of 12.5 meV. From [67].

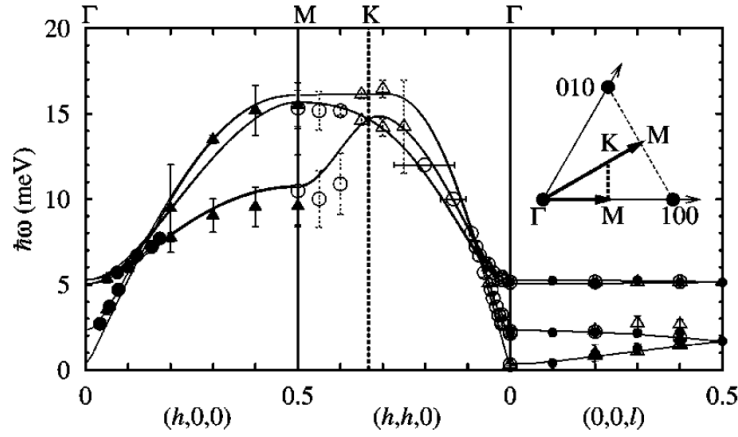


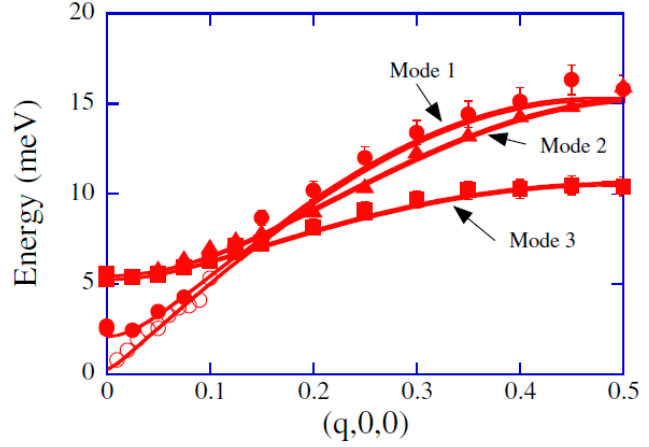
Figure 4.17: Spin wave dispersions derived from data taken at $T = 50$ K (black circles) and a few points measured at $T = 75$ K around the $(h00)$ magnetic Bragg peak. The solid lines are calculated from a nearest neighbor Heisenberg model with two anisotropies. The inset shows the directions in reciprocal space. From [68].

$$H = \sum_{R,R',i,j} \left(J_{R,i,R',j} \vec{S}_{R,i} \cdot \vec{S}_{R',j} + H \vec{S}_{R,i} \cdot \vec{n}_i + D S_{R,i}^z S_{R,i} \right) \quad (4.3)$$

where \vec{S}_{Ri} is the spin at site i in the cell R , $\vec{n}_i = \frac{\langle \vec{S}_{Ri} \rangle}{|\langle \vec{S}_{Ri} \rangle|}$ where $\langle \vec{S}_{Ri} \rangle$ is the mean spin, H and D are the easy axis and easy plane anisotropies, respectively, and $J_{R,i,R',j}$ describes the exchange interactions (both in-plane and out-of-plane). The fitting gives a nearest neighbor

antiferromagnetic exchange interaction of $J = 2.3$ meV, an easy-plane anisotropy of $D = 0.33$ meV and a very small easy-axis anisotropy of $H = 0.0008$ meV.

Figure 4.18: Magnon dispersions along $(h\ 0\ 0)$. Mode 1 was measured around $(1\ 0\ 0)$ and corresponds to out-of-plane fluctuations. The open circles is Mode 1, but measured around $(1\ 0\ 1)$ *i.e.* also measuring the inter-plane interactions and thereby closing the gap. Modes 2 and 3 were measured around $(0\ 0\ 6)$ and correspond to in-plane-fluctuations. From [62].



The dispersions in Fig. 4.18 are derived from the neutron scattering measurements in Fig. 4.19.

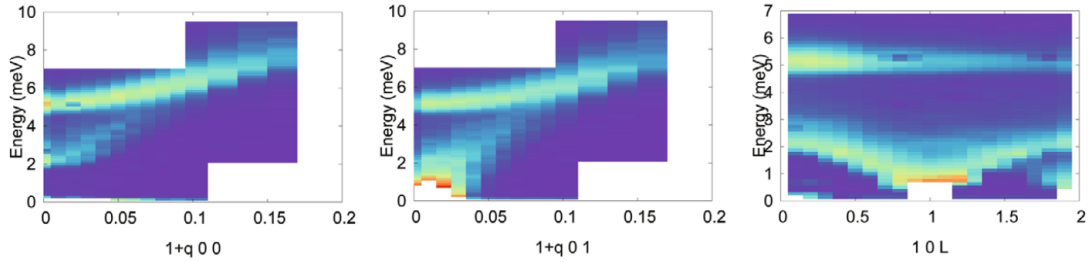


Figure 4.19: Inelastic neutron scattering measurements of the spin wave gap at the zone center. The gap closes when going out along l due to the exchange between the Mn-layers. From [63].

Only a few phonon dispersions have been measured in YMnO₃ and can be seen in Fig. 4.20. In Fig. 4.20 a) the data was taken around $(h\ 0\ 6)$. A spin wave is clearly seen and the phonon signals are weak. The phonon position is marked with a dotted line, while the magnon data is marked with a solid line. The lines are not calculated, but merely guides to the eye. When moving out in \mathbf{Q} the phonon signal intensifies and the magnon signal disappears, as seen in the data taken around $(h\ 0\ 1\ 2)$, Fig. 4.20 b). The solid lines now correspond to the phonon dispersions. At around $h = 0.18$ there is a gap in the phonon dispersion at $T = 18$ K.

When plotting the phonon and the magnon dispersions together, Fig. 4.21, one sees that the magnon and phonon dispersions cross each other at around $h = 0.28$.

Pailhès *et al.* [56] performed experiments with polarized neutrons in 2009. Their measurements revealed a hybrid mode (HM) in the $(h\ 0\ 6)$ direction appearing at low temperatures (below $T = 25$ K). The data for four different h -values can be seen in Fig. 4.22. The hybrid mode is largest at small Q 's. At $h = -0.325$ the signal from the hybrid mode is comparable with the leak from the spinflip channel and is therefore not significant.

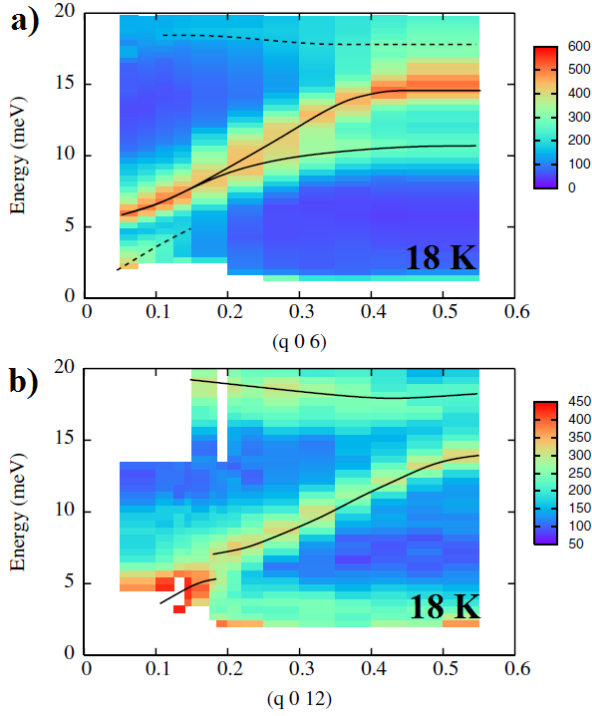


Figure 4.20: Dispersions measured at $T = 18$ K with inelastic neutron scattering. The lines are guides to the eye. **a)** Dispersions around $(0 + q 0 6)$. **b)** Dispersions measured further out in \mathbf{Q} at $(0 + q 0 1 2)$. From [62].

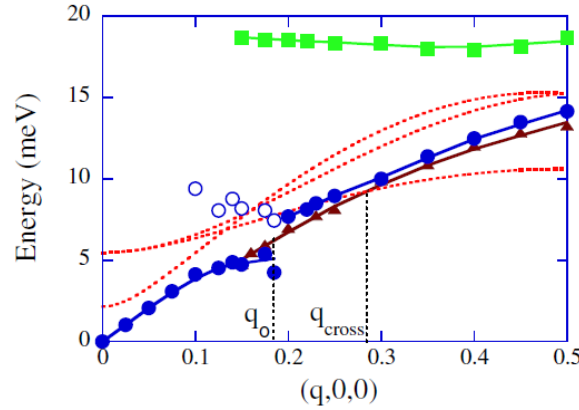


Figure 4.21: Phonon and magnon dispersions in the $(q 0 0)$ direction in YMnO₃. The green boxes correspond the measurements of the optical phonon at $T = 18$ K. The red triangles correspond the measurements at $T = 200$ K of the acoustic phonon, while the filled blue circles is the same dispersion measured at $T = 18$ K. The open blue circles correspond to small intensity measurements of the acoustic phonon, also at $T = 18$ K. The red dotted lines are the calculated magnon dispersions. The gap in the $T = 18$ K data is marked with q_0 and the crossing between the $T = 200$ K acoustic phonon dispersion is marked with q_{cross} . From [62].

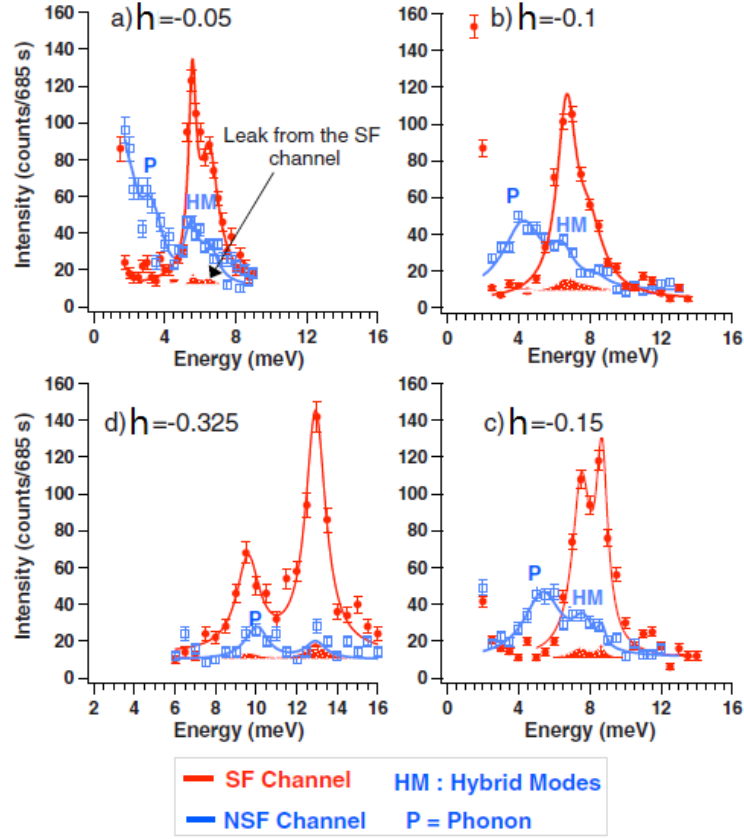


Figure 4.22: Polarized inelastic neutron measurements of excitations in YMnO_3 at $Q=(h\ 0\ 6)$ for four different h -values at $T = 1.5$. Red denotes the spinflip channel and blue denotes the non-spinflip channel. The phonon (P) and the hybrid mode (HM) both occur in the non-spinflip channel. The leak from the spinflip channel is indicated on all the figures with red dots. a) $h = -0.05$. a) $h = -0.1$. a) $h = -0.15$. a) $h = -0.325$. Adapted from [56].

The dispersion relation of the hybrid mode can be seen together with the other low energy modes in Fig. 4.23. When measuring at $(h\ 0\ 6)$ in Q the longitudinal part of the lattice vibrations are seen while it is the transverse component of the spin waves that contribute to the inelastic neutron scattering intensity.

When comparing Fig. 4.21 with Fig. 4.23 it is clear that what Petit *et al.* [62] thought was the acoustic phonon at $T = 18$ K (the blue open circles in Fig. 4.21) is actually the hybrid mode measured by Pailhès *et al.* [56].

4.9 Coupling of the order parameters

Assuming that the symmetry analysis performed by Singh *et al.* [74] is correct, and the magnetic structure is the Γ_4 representation of the $P6_3'$ magnetic space group, the exchange couplings between the layers are antiferromagnetic *i.e.* $J < 0$ with the definition in Eq. (2.10). There is a

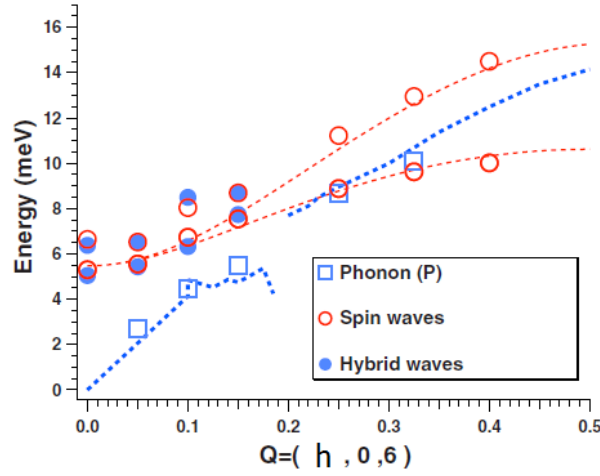


Figure 4.23: Dispersion relations for the low energy modes. Red open circles denote the measured magnon points and the red dotted lines indicate calculations. The open blue squares denote the phonon measurements and the blue dotted line are calculations borrowed from [63]. The filled blue circles denote the data from the hybrid mode. Adapted from [56].

strong Mn-O-Mn nearest neighbor intra layer antiferromagnetic superexchange interaction and weak Mn-O-O-Mn next nearest neighbor interlayer antiferromagnetic superexchange interactions. The average nearest neighbor coupling has the size $J_1 = 2.45$ meV and the couplings between two manganese layers (Mn-ions at $z = 0$ and $z = 1/2$) J_{z_1} and J_{z_2} has the difference $J_{z_1} - J_{z_2} = 0.018$ meV [84]. The superexchange interaction between the layers are two orders of magnitude smaller than the superexchange interaction between nearest neighbor Mn-ions.

The magnetoelectric effect is symmetry forbidden because the polarization is along the c -axis and the magnetic moments are in the ab -plane *i.e.* $\mathbf{P} \cdot \mathbf{M} = 0$. But there is a non-linear coupling between the dielectric constant in the ab -plane and the magnetization as explained in Sec. 4.4.

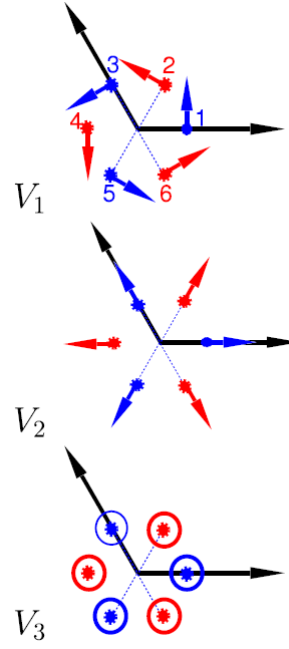
YMnO₃ has three order parameters. The primary one is the antiferromagnetic ordering parameter. The second most important one is the polarization along the c -direction and finally there is the ferromagnetic ordering parameter along c created by the DM-interaction [74]. The magnetic orderings belonging to the Γ_4 representation are shown in Fig. 4.24 and should all be included in a Landau theory analysis.

Following Singh *et al.* a Landau theory containing all the order parameters to the fourth order can be expressed:

$$\begin{aligned}
 F = & \alpha_2(T - T_N)(A^2 + B^2) + \alpha_4(A^2 + B^2)^2 - \beta_2(P - P_0^2) + \beta_4(P^4 - P_0^4) \\
 & + \gamma_2 M^2 + \gamma_4 M^4 + c_4(A^2 + B^2)(P^2 - P_0^2) + d_4 M^2(P^2 - P_0^2) \\
 & + e_4(A^2 + B^2)M^2 + z_4(P^2 - P_0^2)\vec{A} \cdot \vec{M}
 \end{aligned} \tag{4.4}$$

where $\delta P = P - P_0$ is the change in polarization. \vec{A} , B and \vec{M} are the order parameters of the V_1 , V_2 and V_3 magnetic orders, respectively, given by (for one unit cell with $i = 6$ Mn-ions):

Figure 4.24: The magnetic structures belonging to the Γ_4 representation of the magnetic space group $P6'_3$. The V_1 structure can be described by the toroidal component of the in-plane spin component and V_2 by the divergence of the in-plane spin components. V_3 is the out-of-plane component. From [74].



$$\vec{A} = \frac{1}{6r} \sum_i \vec{r}_i \times \vec{S}_i = \frac{1}{6r} \sum_i \vec{r}_i \times \vec{S}_{ab,i} \quad (4.5)$$

$$B = \frac{1}{6r} \sum_i \vec{r}_i \cdot \vec{S}_i = \frac{1}{6r} \sum_i \vec{r}_i \cdot \vec{S}_{ab,i} \quad (4.6)$$

$$\vec{M} = \frac{1}{6} \sum_i \vec{S}_i = \frac{1}{6} \sum_i \vec{S}_{c,i} \quad (4.7)$$

where $\vec{S}_i = \vec{S}_{ab,i} + \vec{S}_{c,i}$ is the spin of the i th manganese ion. \vec{A} and \vec{M} are vectors in the c -direction and B is a scalar. In Eq. (4.4) the first two terms, α_2 and α_4 , correspond to the antiferromagnetic energies, the third and fourth term, β_2 and β_4 , are the changes in the ferroelectric energies and the fifth and sixth term, γ_2 and γ_4 , are the ferromagnetic energies. The four last terms are the coupling terms: the ferroelectric and antiferromagnetic coupling c_4 , the ferromagnetic and ferroelectric coupling d_4 , the antiferromagnetic and the ferromagnetic coupling e_4 , and finally the DM-interaction z_4 . If $A = S_{ab} \cos \phi$ and $B = S_{ab} \sin \phi$ then the intensity of the (100) Bragg peak is proportional to S_{ab}^2 for all values of ϕ . Differentiating Eq. (4.4) with respect to antiferromagnetic order parameter S_{ab} , the polarization P , the magnetization M and the angle ϕ the following results are obtained:

1. V_1 spin arrangement is obtained, *i.e.* $\phi = 0$.
2. Below the antiferromagnetic ordering temperature T_N the polarization decreases.
3. The ferromagnetic order parameter is much weaker than both the antiferromagnetic order parameter and the change in polarization δP .

4. The ferromagnetic and antiferromagnetic ordering parameters M and S_{ab} , respectively, are not linearly related at T_N .
5. The behavior of the dielectric constant corresponds to the measured one in Fig. 4.10.
6. It is not possible to switch the direction of any of the magnetic orders by switching the polarization because $P = P_0 \left(1 - \frac{c_4}{4\beta_4} A^2\right)$ and $M = -\frac{z_4}{\gamma_2} A P_0 \delta P$. A change in P will leave M and A unchanged, but if M is switched A will follow.

Point no. 6. is important when thinking about applications for data storage. The general goal of multiferroics is to be able to switch the magnetization with an electric field as mentioned in Sec. 1.2, but with the analysis above, this does not seem possible. However, the antiferromagnetic order can be switched with a strong magnetic field, thereby making YMnO_3 a material useful for data storage that is not sensitive to small magnetic fields [74].

The coupling between the lattice and spin degrees of freedom, which make the magnetoelectric coupling possible, is not yet fully understood. Other research groups have concentrated on \mathbf{Q} 's close to the zone center and only looked at zones far out in the l -direction, where it is possible to measure phonons and magnons at the same time, hoping to receive information about the microscopic interactions. No one has examined reciprocal space further out in the ab -plane. That is, however, one of the measurements that were performed in this thesis. Before the results are presented a short introduction to the instruments and the settings at the different experiments is reviewed.

5 Instruments

In this section the three-axis instruments used for collecting data for this thesis are described. All instruments are different and they all have their forces and weaknesses. It should be possible to reproduce all the experiments presented in this thesis with the technical details that are given. Hopefully this section can also help with planning future experiments regarding the instrument selection. A conversion table relating important relationships between wavelength, frequency and velocity of neutrons can be found in appendix E.

5.1 RITA II - cold instrument

RITA II is a three-axis instrument situated at SINQ at the Paul Scherrer Institute (PSI) in Switzerland [61]. SINQ is a continuous spallation neutron source. The flux is 10^{14} neutrons/cm²/s. There is a cold moderator of liquid deuterium which provides the neutrons for RITA II which is positioned 42 m away from the moderator at the end of a curved neutron guide. The energy range available at RITA II is from 2.5 meV-20 meV selected by a vertically focusing PG monochromator. The flux at the sample position is of the order 10^6 neutrons/cm²/s and varies with the wavelength of the neutrons. At RITA II the flux is largest at the neutron wavelength $\lambda = 3.5 \text{ \AA}$ (6.7 meV). The resolution also changes with wavelength. The resolution is best for large wavelengths. At RITA II there is an optional Be or BeO-filter removing 2nd order neutrons. The Be-filter works for wavelengths larger than 4 \AA .

RITA II is a special three-axis spectrometer because there are nine PG analyzer blades. It is therefore possible to measure nine ($\mathbf{Q}, \hbar\omega$) points simultaneously. The detector is a position sensitive ³He detector. A sketch of the RITA II instrument can be seen in Fig. 5.1.

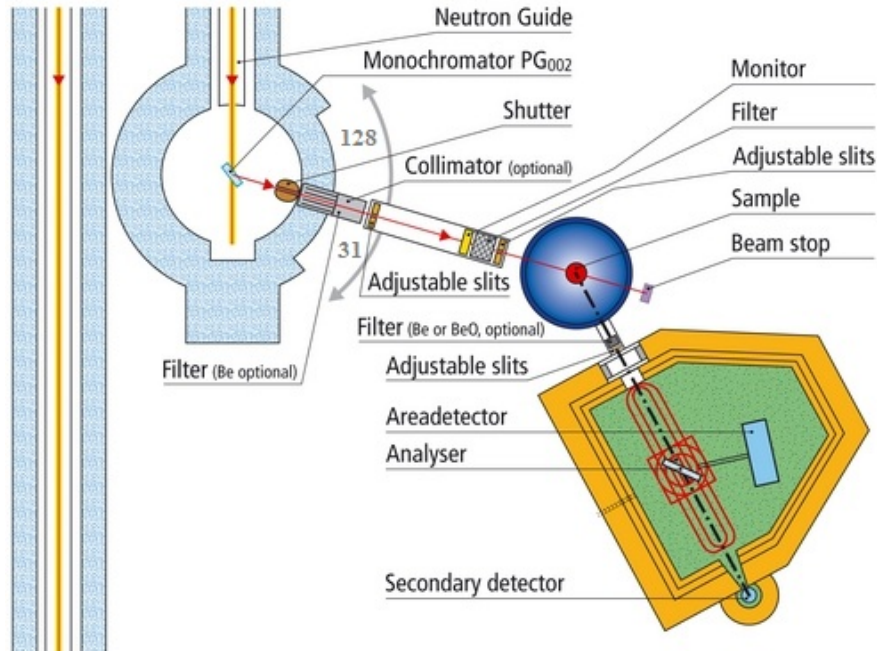


Figure 5.1: Sketch of RITA II. From [61].

RITA II was used for two experiments: one experiment in November 2012 and one experiment

in August 2013. In November 2012 the ordering temperature of YMnO_3 was determined. In addition to that the magnon-dispersion around $(0\bar{1}0)$ was measured. In August 2013 the temperature dependence of the magnon dispersion around (100) was measured. Both experiments concentrated on measuring magnon dispersions and both experiments were executed with a fixed final energy $E_f = 5\text{meV}$. The settings for the two experiments can be found in Table 5.1.

Component	November 2012	August 2013
E_f	5 meV	5 meV
Cryostat	Orange	Orange
Analyzer	Multiple PG Analyzer	Multiple PG Analyzer
Collimation mono-sample	80'	80'
Filters	Be	Be
Distance	monochromator to sample	1.54 m
Distance	sample to analyzer	1.2 m
Distance	analyzer to detector	0.38 m

Table 5.1: Settings at the RITA II experiments executed in November 2012 and August 2013.

The YMnO_3 sample was cylindrical (21 mm long and 10 mm in diameter) and had a mass of $m = 5250\text{ mg}$. The crystal mounted on the crystal holder for both RITA II experiments can be seen in Fig. 5.2. The scattering plane was the ab -plane for all the experiments.

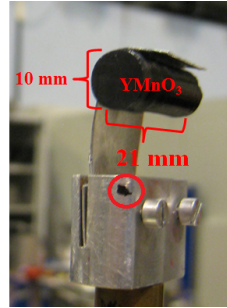


Figure 5.2: Picture of the crystal mounted on the sample holder for both the RITA II experiments and the EIGER experiment. The a/b axis is marked with a black dot on the aluminum holder.

With the formulas in Sec. 3.6 the $(\mathbf{Q}, \hbar\omega)$ range for the final energy $E_f = 5\text{ meV}$ and maximal scattering angle $2\theta = 120^\circ$ can be calculated. The range is plotted in Fig. 5.3.

5.2 EIGER - thermal instrument

EIGER is a three-axis spectrometer also situated at SINQ at PSI [60]. A sketch of EIGER can be seen in Sec. 5.2. It is a thermal instrument with a PG monochromator and a range of energy transfers of -10 meV to 45 meV at a fixed final energy of $E_f = 14.7\text{ meV}$. The detector is a single ^3He -tube detector. A PG-filter removes higher order neutrons.

The experiment on EIGER was executed in December 2012 where the transverse phonon around (030) was measured both below and above the magnetic transition temperature and the settings can be seen in Table 5.2. The sample holder and sample was the same as in the RITA II experiments and a picture of the setup can be seen in Fig. 5.2.

With the formulas in Sec. 3.6 the $(\mathbf{Q}, \hbar\omega)$ range for the fixed final energy $E_f = 14.7\text{ meV}$ and maximal scattering angle $2\theta = 90^\circ$ can be calculated. The range is plotted in Fig. 5.3.

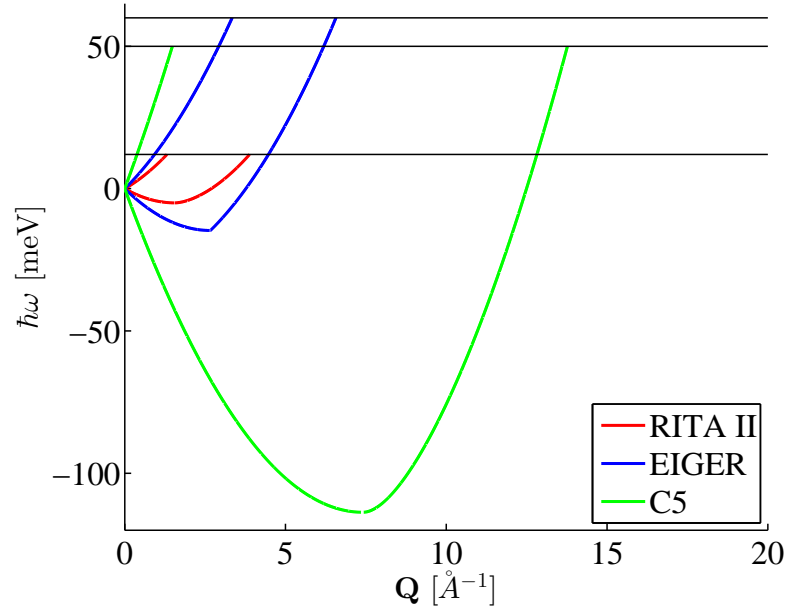


Figure 5.3: $(Q, \hbar\omega)$ -range at RITA II (red) with $E_f = 5$ meV and $2\theta = 120^\circ$ and maximal energy transfer of $\hbar\omega = 12$ meV, EIGER (blue) with $E_f = 14.7$ meV and $2\theta = 90^\circ$ and maximal energy transfer of $\hbar\omega = 60$ meV, and C5 (green) with $E_f = 113.7$ meV and $2\theta = 115^\circ$ and maximal energy transfer of $\hbar\omega = 50$ meV. The black lines indicate the maximal energy transfers.

Component		
E_f	14.7 meV	2.66 \AA^{-1}
Cryostat	Orange	
Monochromator	Double focusing PG	
Analyzer	Horizontally focusing PG	
Filters	Sapphire filter ingoing	37 mm PG outgoing
Distance	monochromator to opening	60 mm
Distance	monochromator to sample	2150 mm
Distance	sample to analyzer	1150 mm
Distance	analyzer to detector	1150 mm

Table 5.2: Settings at the EIGER experiment.

5.3 C5 - thermal polarized instrument

The last experiment, in connection with this work, was executed in Canada at Chalk River National Laboratory in February 2014. The three-axis spectrometer C5 is a polarized thermal instrument with a light water moderator with $T = 300$ K and a flux of 10^9 neutrons/cm²/s at the sample position. Both the monochromator and analyzer is of the polarizing Heusler type, see Sec. 3.8.4. The detector is a cylindrical ³He with a 1.5 inch diameter and 5 inches high. The conversion between inches and centimeters can be found in Table E.2 in appendix E. The settings for the experiment on YMnO₃ can be found in Table 5.3. The sample on the sample holder can be seen in Fig. 5.5.

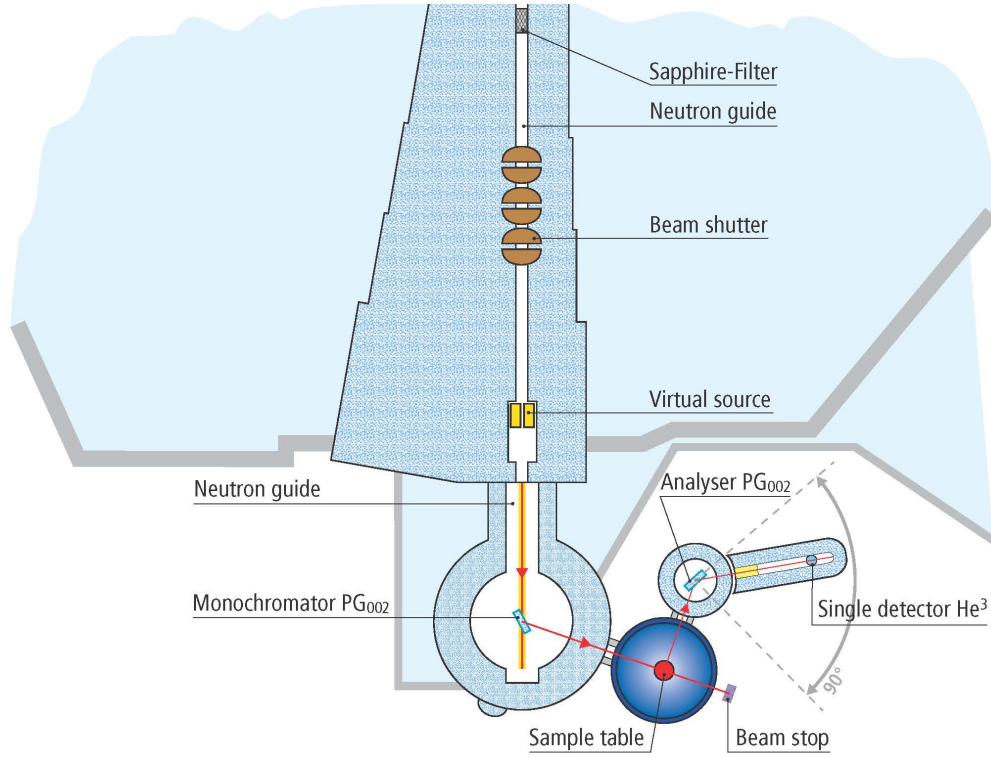


Figure 5.4: Sketch of EIGER. From [60].

Component			
E_f		113.7 meV	7.41 \AA^{-1}
Monochromater	Single crystals of Cu_2MnAl Heusler alloy		
Analyzer	Single crystals of Cu_2MnAl Heusler alloy		
Cryostat	Lemon		
collimators soller	none (0.6°), 0.799°		0.855° 2.4°
Filters			2 PG outgoing
Flippers	Mezei-type ingoing	Mezei-type outgoing	
Guide fields	HF 10 gauss	VF 30 gauss	
Distance	Source to monochromator	6604 mm	
Distance	Monochromator to sample	1784-2159 mm	
Distance	Sample to analyzer	1016-1422 mm	
Distance	Analyzer to detector	267 mm	

Table 5.3: Settings at the C5 experiment. For a neutron wave vector of 2.37 \AA^{-1} the flipping ratio is 24:1, see Eq. (3.43) in Sec. 3.8, the Heusler polarization efficiency is 96.5 % and the flipper efficiency is 99.5%.

With the formulas in Sec. 3.6 the $(\mathbf{Q}, \hbar\omega)$ range for the final energy $E_f = 14.7 \text{ meV}$ and maximal scattering angle $2\theta = 115^\circ$ can be calculated. The range is plotted in Fig. 5.3.

At the C5 instrument the scattering plane is defined by the perpendicular coordinates ζ (zeta) and η (eta). The connection between (ζ, η) and the Miller indices (hkl) are in our setup:

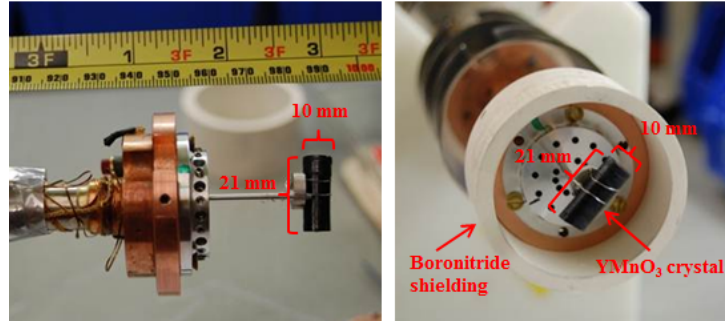


Figure 5.5: Picture of the crystal mounted on the sample stick for the C5 experiment. The boronitride shielding was there to minimize the background. Before the sample was inserted into the cryostat a thin aluminum can was put around the sample and boronitride shielding so prevent the sample from ending up in the bottom of the cryostat if it fell off. A picture of the setup with the aluminum can can be seen in Fig. 5.6.

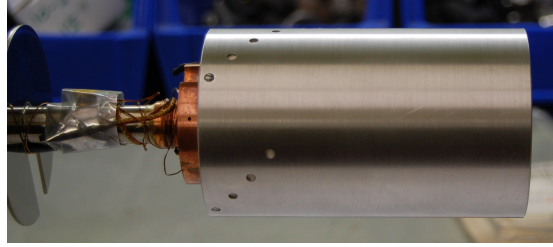


Figure 5.6: An aluminum can encapsulated the crystal on the sample stick preventing it from ending up in the bottom of the cryostat in case the crystal fell off during the experiment.

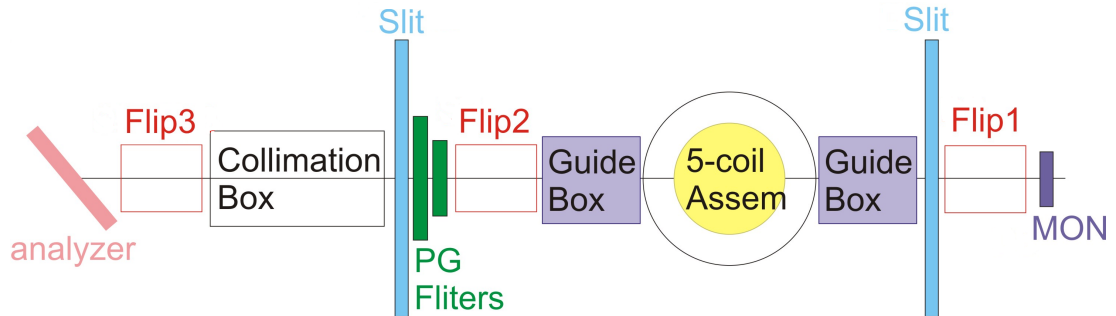


Figure 5.7: Sketch of the polarized setup at C5 with the position of a monitor (MON), three flippers (Flip 1, Flip 2 and Flip 3), two slits, two guide boxes for keeping the polarization, the 5-coil assembly that determines the polarization at the sample position, two PG filters, a collimation box and the analyzer. The sketch is provided by Zahra Yamani, the instrument scientist at C5.

$$\begin{aligned}\zeta &= \frac{h+k}{2} \\ \eta &= \frac{h-k}{2}\end{aligned}\tag{5.1}$$

The scattering plane was spanned by the perpendicular lattice vectors passing through $(1\ 1\ 0)$ and $(1\ \bar{1}\ 0)$ (a larger region of reciprocal space can be seen in Fig. 6.1):

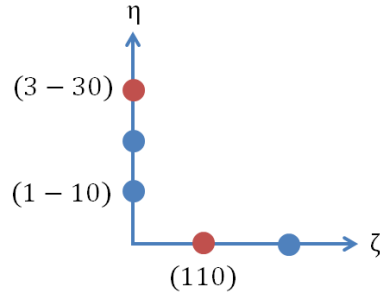


Figure 5.8: The scattering plane at the C5 experiment spanned by the perpendicular axes ζ and η . ζ passes through $(1\ 1\ 0)$ and η passes through $(1\ \bar{1}\ 0)$.

In addition to the (ζ, η) coordinate system, the instrument software works with energies in THz.

6 Non-polarized data

In this section, results from the non-polarized neutron scattering experiments will be presented. The RITA II experiments were performed by S. Holm, K. Lefmann, A. Poole and students of the neutron scattering course at University of Copenhagen. The EIGER experiment was performed by S. Holm, K. Lefmann and A. Bakke in connection with the bachelor's thesis of A. Bakke. I present an accumulated and complete data analysis of all the above mentioned experiments. The data from the polarized neutron scattering experiment, that I have performed in collaboration with S. Holm, K. Lefmann and A. Poole, will be presented in the next section, Sec. 7, and compared to the non-polarized data.

This section begins with a map of reciprocal space where the different data was taken. A discussion of the models used for fitting and general thoughts about how to treat data are included at the beginning of the section before actual results are shown. These considerations, as well as, the map of reciprocal space, should be consulted when reading the subsequent polarized data section.

6.1 Orientation in reciprocal space

Before the results are presented, an overview of the locations in reciprocal space where the measurements were made appears in Fig. 6.1. The symmetry points in the first Brillouin zone annotated as (000) are marked with Γ , K and M as is also shown in Fig. 2.4. All measurements were done in the ab -plane, but in different the Brillouin zones (100), (200) and (300). The green circles indicate the Bragg peaks that have been examined and the red lines indicate the inelastic neutron constant- \mathbf{Q} scans, Fig. 3.9. The (100), (010), ($\bar{1}$ 10), ($\bar{1}$ 00), (0 $\bar{1}$ 0) and (1 $\bar{1}$ 0) (which are all equivalent due to the hexagonal symmetry) are strong magnetic peaks, while the (300), (030), ($\bar{3}$ 30), ($\bar{3}$ 00), (0 $\bar{3}$ 0) and (3 $\bar{3}$ 0) peaks are strong nuclear peaks that were used for alignment of the crystal prior to all experiments.

6.2 Experimental practice and data analysis

Bragg peaks are delta functions in \mathbf{Q} at $\hbar\omega = 0$, but because of the finite resolution of the instrument and the mosaicity of the sample the peak is broadened and often has the form of a Gaussian function given by:

$$f(x) = \frac{1}{\sigma\sqrt{2\pi}} \exp\left(-\frac{(x-\mu)^2}{2\sigma^2}\right) + b \quad (6.1)$$

where $\frac{1}{\sigma\sqrt{2\pi}}$ is the amplitude, σ is the standard deviation, μ is the position of the center of the peak called the mean value and b is the background. The curve looks like a bell that quickly falls off to the value b ; the background. The standard deviation is connected to the Full Width Half Maximum (FWHM) Γ in the following way:

$$\text{FWHM} = \Gamma = 2\sqrt{2\ln 2}\sigma = 2.354\sigma \quad (6.2)$$

Both the Bragg peaks and the inelastic peaks were fitted with Gaussian functions and the errors on the fitting parameters are calculated by the least squares method. A sloping background is sometimes required to account for experimental variations in temperature, scattering angle, and other parameters.

Prior to all experiments, alignment scans were performed to ensure that the orientation of the sample in reciprocal space was correct. The alignment scans are elastic scans, where the Bragg peak is scanned and fitted to a Gaussian function, thereby revealing the exact position of the

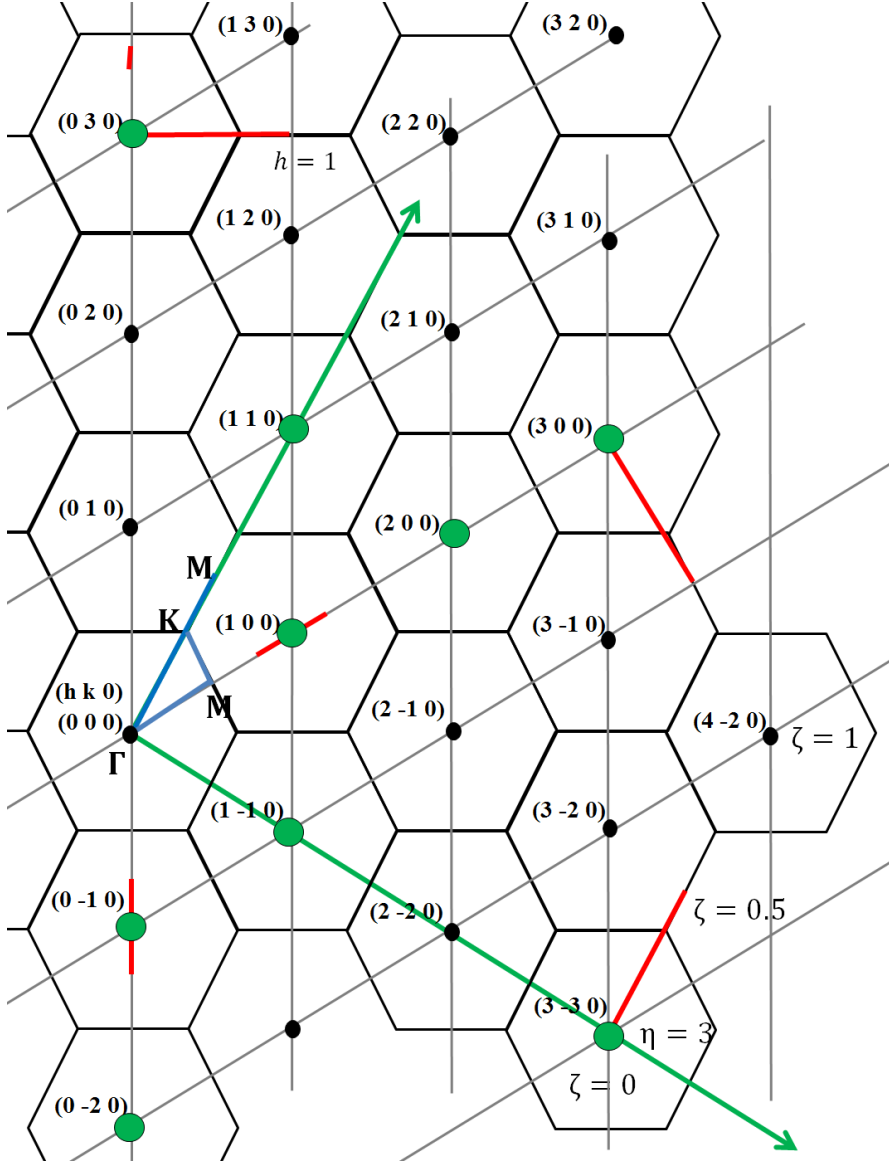


Figure 6.1: An overview of measurements on YMnO_3 in reciprocal space within the (a^*, b^*) -plane. The blue lines are scans made by other groups. Additionally, they have measured along the l -direction *i.e.* out of the plane. Red lines indicate scans performed by our group which are only in the (h, k) -plane. The green circles indicate which Bragg peaks have been used for alignment, determination of transition temperature, and so forth. The scans around $(0\bar{1}0)$ and (100) were performed at RITA II. The scans around (030) were performed at EIGER (no phonons were detectable around $(0\bar{2}0)$). The scans at C5 were done around $(3\bar{3}0)$. The scattering plane spanned by the orthogonal vectors ζ and η is marked with green arrows.

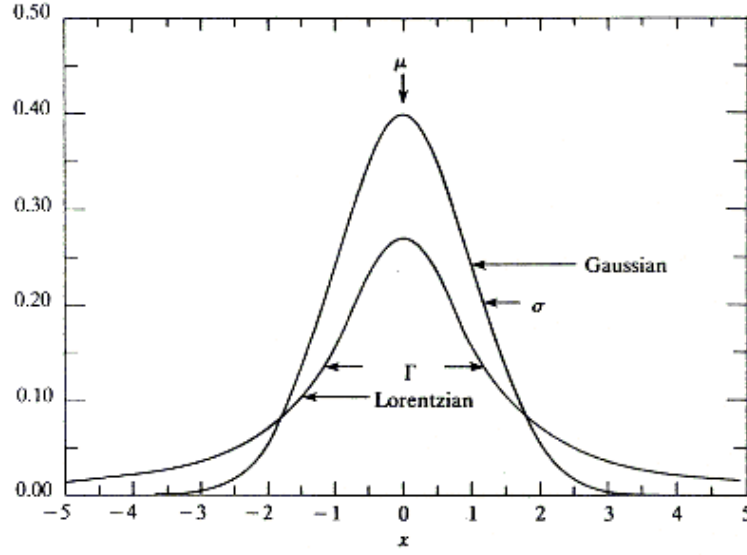


Figure 6.2: The Gaussian distribution with the mean μ and the position of the standard deviation σ . The Lorentzian distribution is also shown with the FWHM Γ . From [8].

peak. The coarse alignment of the sample was performed with a Laue camera, the fine tuning with a four-circle instrument and the remaining fractional degrees were done at the three-axis instrument.

The diffuse scattering around a Bragg Peak is fitted with a Lorentzian because the correlations fall off exponentially in real space. A scattering cross section is the Fourier transform of an exponential function, a Lorentzian function. The Lorentzian function is given by:

$$f(x) = \frac{1}{\pi} \frac{\frac{\Gamma}{2}}{(x - \mu)^2 + \left(\frac{\Gamma}{2}\right)^2} + b \quad (6.3)$$

where μ is the position of the peak, Γ is the FWHM and b is the background. The Lorentzian and the Gaussian distributions are plotted together in Fig. 6.2, where the differences in shape are clear.

The error bars of the counts are given by $1/\sqrt{N}$ [25]. All zero-counts were fixed at 1, to make the fitting routines possible. Changing counts is a problem, but it is a way of making a zero count weigh as little as possible in the statistics. All spurious signals were removed.

The program Spec1d [29] for MatLab was used for fitting the data. Spec1d is written by Henrik Rønnow and Des McMorow. The data were fitted with different fitting-routines written for the fits.m function for Spec1d; when the data are presented the exact fitting-routine will be elaborated.

The intensity of the polarized data is much smaller than the intensity of the non-polarized data. When the polarized data and the non-polarized data are plotted together, the intensities of the non-polarized data is divided by a factor 540. It is normal to lose a factor of 20-40 in intensity when going from a non-polarized to a polarized experiment. One loses a factor 2 because only one spin state out of two is chosen, another factor of 2 is lost because Heusler monochromators are used instead of PG crystals, and finally, a factor of at least 5 is lost due to

the difficulties of focusing the beam from a Heusler polarizer [72].

The last factor accounting for the difference between the non-polarized data and the polarized data is the difference in monitors. The data being compared was normalized to the monitor and not to counts per time. The non-polarized data points were measured for 1-2 minutes per point, whereas the polarized data were measured for around 50 minutes per point.

6.3 The magnetic phase transition

At RITA II the intensity of the $(0\bar{1}0)$ magnetic Bragg Peak was measured from base to just above the critical temperature. To see specifications on the experimental setup see Sec. 5.1. The intensity of the magnetic Bragg peak is proportional to the square of the staggered magnetization $I = (M_{\uparrow} - M_{\downarrow})^2 = M^2$, *i.e.* the squared order parameter for the antiferromagnetic system. The amplitude of each peak was determined by curve-fitting the data using a Gaussian function with a sloping background¹⁷ the amplitude of the peak was determined. By plotting intensity as a function of temperature, Fig. 6.3, and fitting the points closest to the transition temperature to Eq. (6.4), the transition temperature and the critical exponent were found to be $T_N = 71.96$ K and $\beta = 0.1959$, respectively.

$$I \propto \left(\frac{T_N - T}{T_N} \right)^{2\beta} \quad (6.4)$$

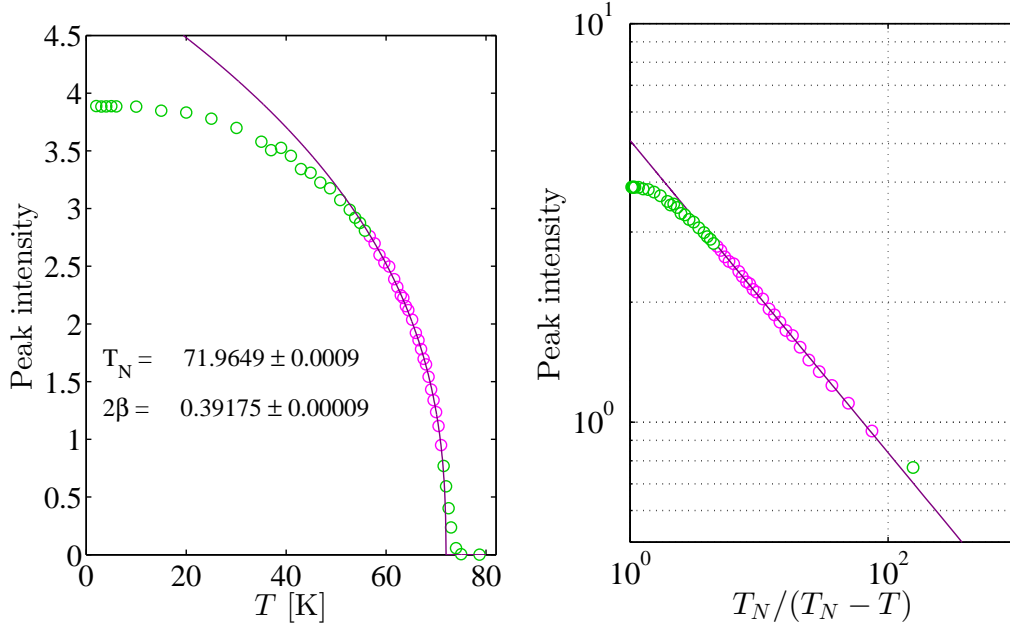


Figure 6.3: **Left:** The intensity of the $(0\bar{1}0)$ magnetic Bragg peak was followed from base to around 80 K (green and purple). The Néel temperature was determined to be $T_N = 71.96$ K and the critical exponent was determined to be $\beta = 0.1959$ in good agreement with previous experiments [65]. The points included in the fit of Eq. (6.4) are purple. **Right:** By plotting the data on a logarithmic scale as a function of $T_N / (T_N - T)$ it is easier to see, which points should be included in the fit.

¹⁷The fitting function sgauss.m for fits.m was utilized.

There is a small amount of critical scattering around T_N in agreement with Roessli *et al.* [65] but not in agreement with Chatterji *et al.* [12]. This was anticipated because both our measurements and the measurements by Roessli *et al.* were performed in three-axis mode, while Chatterji *et al.* worked in two-axis mode; see Fig. 4.4 for comparison. Our values of T_N and β best resembles the data by Roessli *et al.*. Their critical exponent was determined to be $\beta = 0.187$.

6.4 Diffuse scattering around $(0\bar{1}0)$

The $(0\bar{1}0)$ Bragg peak was mapped at several temperatures. Selected color maps are seen in Fig. 6.4.

Scans of the $(0\bar{1}0)$ Bragg peak at selected temperatures, fitted with a Gaussian plus a Lorentzian function¹⁸, can be seen in Fig. 6.5. All of the scans including the fitting parameters to the Lorentzian function are in Fig. G.1, Fig. G.2 and Fig. G.3 in appendix G. The center and background fitting parameters were zero within error bars. The width and the intensity contain information about the system and can be extracted from the fitting procedure. The intensity of the peak is proportional to the magnetic susceptibility $\chi(T)$ and related to the critical exponent γ by the reduced temperature. The width of the diffuse scattering peak is proportional to the inverse correlation length $\xi(T)$ with the critical exponent ν .

If the width and intensity is plotted against the reduced temperature, T_R , a simple power law reveals the critical exponents. T_R is given by:

$$T_R = \frac{T - T_N}{T_N} \quad (6.5)$$

where T_N is the ordering temperature. The relations connecting the intensity I and the width Γ with the critical exponents, for $T > T_N$, are given by [12]:

$$I \propto \chi(T_R) \propto T_R^{-\gamma} \quad (6.6)$$

$$\Gamma = \frac{1}{\xi} \propto T_R^\nu \quad (6.7)$$

The width and the intensity of the diffuse peak as a function of temperature is shown in Fig. 6.6. The width increases with increasing temperature, whereas the intensity decreases.

The width and the intensity of the Lorentzian peak as a function of the reduced temperature on a logarithmic scale¹⁹, used to obtain the critical exponents, can be seen in Fig. 6.7. The data clearly follows a linear trend. Only the data from $T = 72.5$ K to $T = 100$ K was used for the fitting. At $T = 200$ K the diffuse scattering was not visible in the data.

The critical exponents were determined to be $\gamma = 1.55$ and $\nu = 0.614$ from the fits in Fig. 6.7. If the $T = 100$ K data is discarded the critical exponents become $\gamma = 1.510$ and $\nu = 0.569$.

¹⁸The gausslor.m function was utilized

¹⁹The logfit.m routine was used. Uncertainties of the data are not taken into account when using this routine.

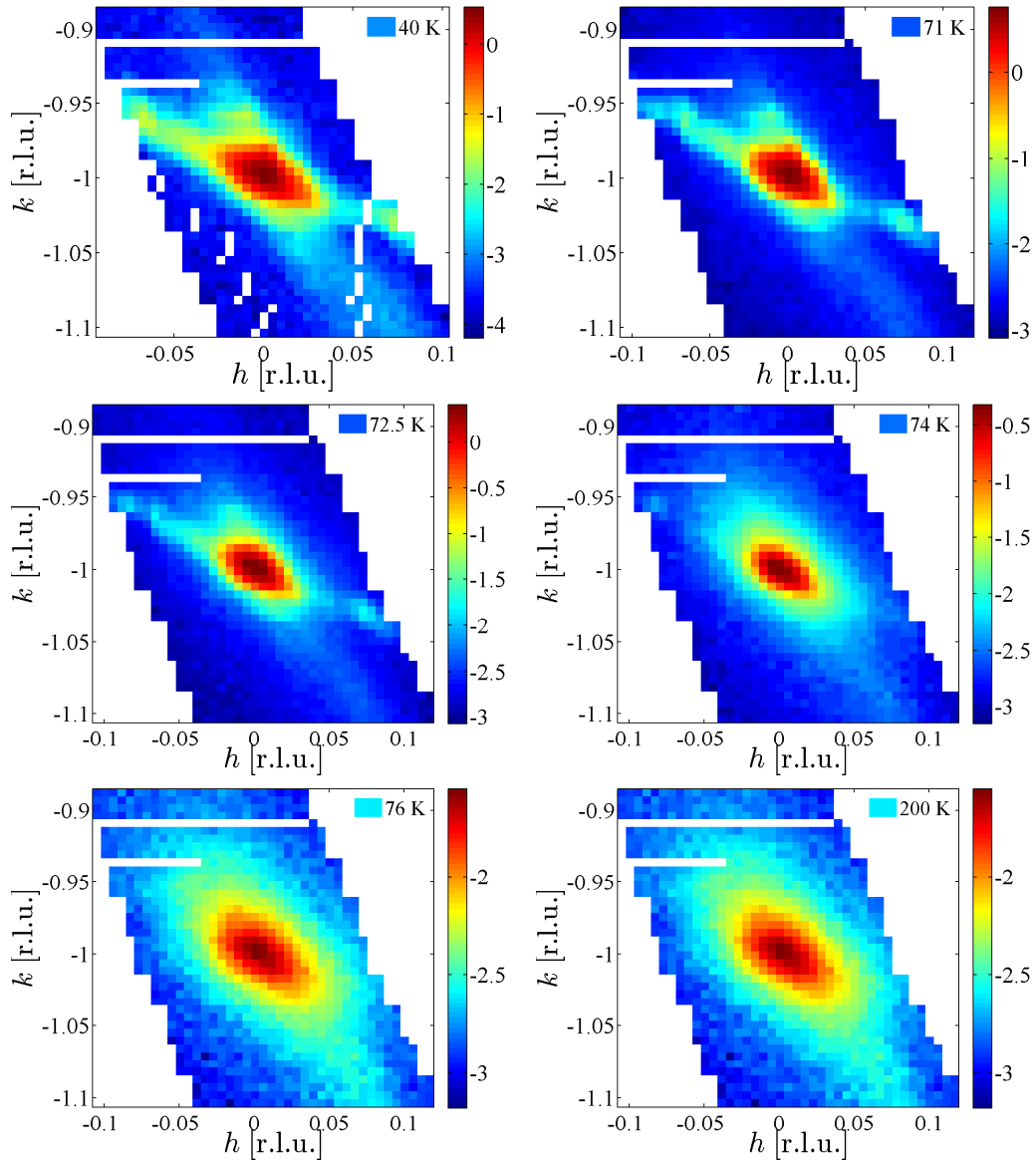


Figure 6.4: Diffuse scattering around $(0\bar{1}0)$ at high and low temperature and at four temperatures close to T_N . The color indicates the logarithm to the number of counts per monitor. Notice that the color scale varies from plot to plot.

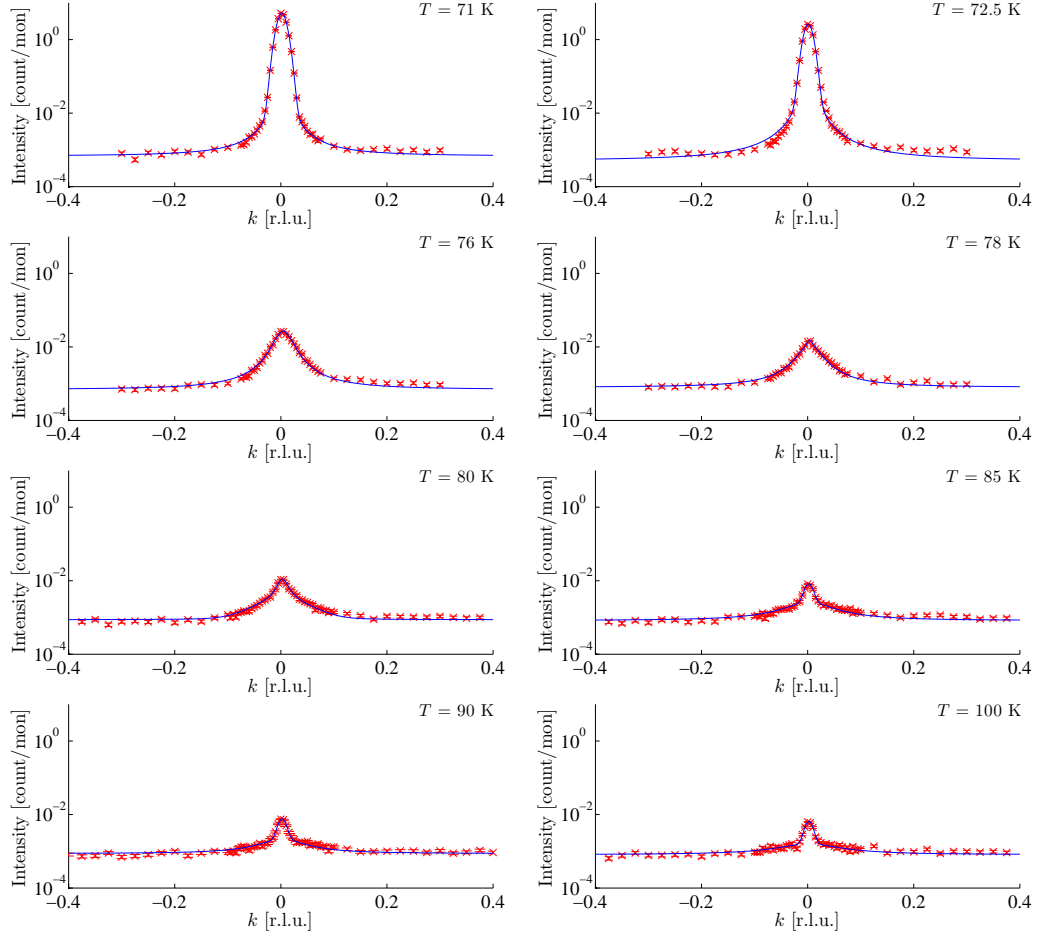


Figure 6.5: Scans of the $(0\bar{1}0)$ Bragg Peak revealing diffuse scattering at high temperatures. Red corresponds to data points and blue is the fit of a Gaussian plus a Lorentzian function. The y -axis is logarithmic.

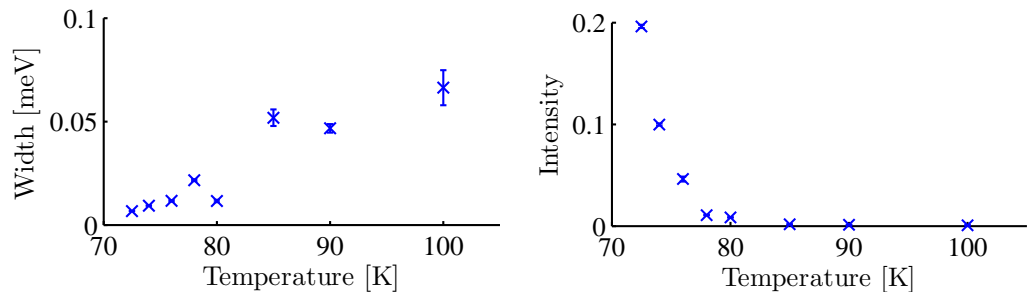


Figure 6.6: **Left:** The Lorentzian peak width as a function of temperature. **Right:** The Lorentzian peak amplitude as a function of temperature.

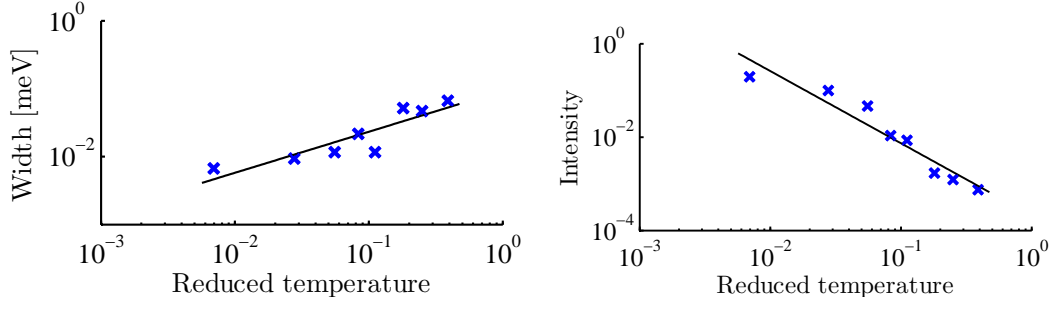


Figure 6.7: **Left:** The Lorentzian peak width as a function of reduced temperature $T_R = (T - T_N)/T_N$. **Right:** The Lorentzian peak amplitude as a function of reduced temperature $T_R = (T - T_N)/T_N$. Both axis are logarithmic.

6.5 Magnon dispersions around $(0\bar{1}0)$

The next step was to measure the magnon dispersion branches around the magnetic Bragg peak. Our data will serve as a supplement to and as a comparison to the data reported by other groups [62], [63], [10], [17], [59], [68]. The magnon map around $(0\bar{1}0)$, Fig. 6.8, was measured with two scans in imaging mode, where all nine analyzer blades were used. The dispersions are in good agreement with the magnon dispersion calculated and measured by the other groups [68] and [63]; see Fig. 4.18 and Fig. 4.19 for comparison.

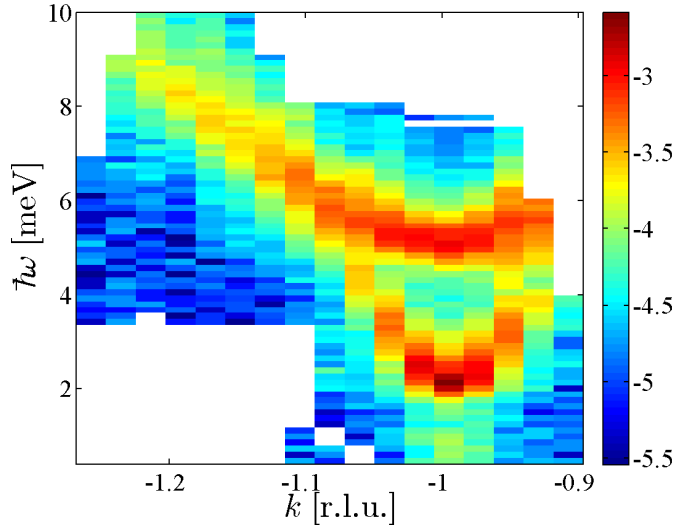


Figure 6.8: The magnon dispersions measured at $T = 40$ K around $(0\bar{1}0)$. The color plot is composed from 18 scans, corresponding to two scans in imaging mode, where the nine analyzer blades on RITA II are positioned to measure at 9 different $(\mathbf{Q}), \hbar\omega$ -points. The color indicates the logarithm to the number of counts per monitor.

The temperature dependence of the magnon branch was measured from $k = -1.26$ [r.l.u.] to $k = 1.1$ [r.l.u.] in Q and 3-10 meV in energy, corresponding to one imaging mode scan. The

energy scans at $k = -1.18$ [r.l.u.] at different temperatures are fitted with Gaussian functions²⁰ and can be seen in Fig. 6.9. The energy width, σ , of the magnon increases with increasing temperature from around $\sigma = 1$ meV at 18 K to around $\sigma = 1.5$ meV at 60 K.

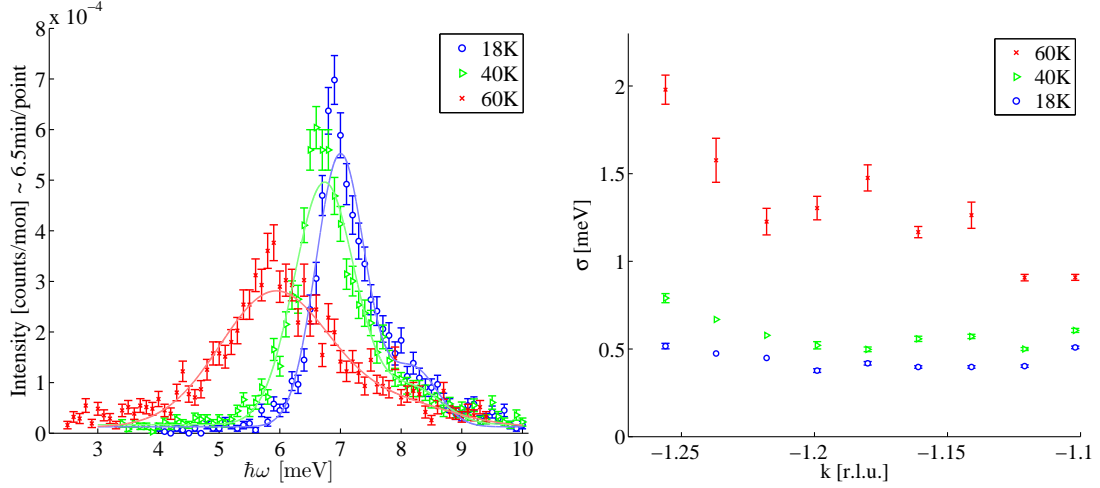


Figure 6.9: **Left:** Energy scans at $(0\ 1.18\ 0)$ with Gaussian fits. Blue corresponds to 18 K measurements, green corresponds to 40 K measurements and red corresponds to 60 K measurements. **Right:** The width as a function of k for the three temperatures: 18 K (blue), 40 K (green) and 60 K (red).

6.6 Spin wave gaps around (100)

At the second RITA II experiment the temperature dependence of the two magnon branches at (100) was measured. The data were fitted with two Gaussian functions and a Lorentzian function²¹ function; and in Fig. 6.10 energy scans at $T = 1.5$ K, $T = 40$ K, $T = 60$ K and $T = 70$ are shown. As temperature increases, both branches move down in energy and the energy gap between them becomes smaller. At low temperatures the two branches are similar in intensity. The intensity of the lower branch increases while the intensity of the high energy branch decreases with increasing temperature.

The four scans in Fig. 6.10 are plotted together in Fig. 6.11. The energy scans for all Q -values can be found in Fig. G.4 in appendix G.

The gap of the low and high energy branches closes as the temperature increases; the size of the gap (the energy of the spin wave) is directly proportional to the order parameter $M = M_{\uparrow} - M_{\downarrow}$ [45]. A plot of the position of the lower energy peak as a function of temperature can be seen in Fig. 6.12 Top Left. The ordering temperature T_N and the critical exponent β can be found by the method described in Sec. 6.3. The values obtained are $T_N = 72.32$ K and $\beta = 0.268$, in good agreement with the previous measurements. More points around the ordering temperature are needed to determine the critical temperature and the critical exponent more precisely. The intensity and the width of both branches are plotted as a function of temperature in Fig. 6.12 (Top Right) and Fig. 6.12 (Bottom Left), respectively. In Fig. 6.12 (Bottom Right) the imaginary

²⁰The function gauss.m was utilized in the fitting procedure.

²¹The gaussSkewx2lorz.m function for fits.m was utilized.

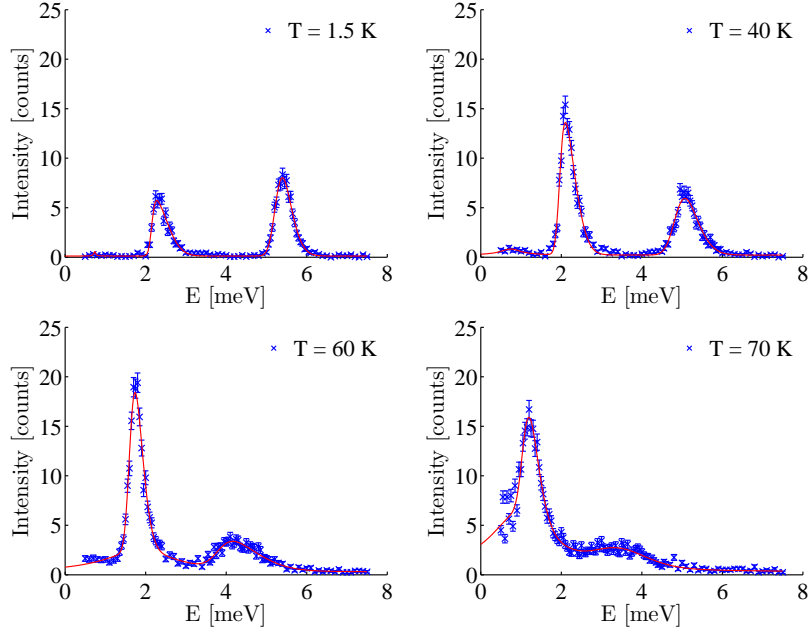


Figure 6.10: Energy scans around (100) at different temperatures.

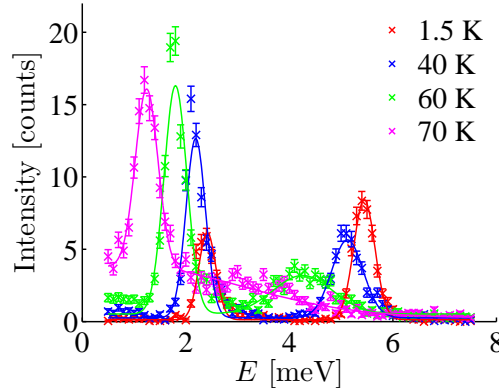


Figure 6.11: Energy scans at (100) at 1.5 K (red), 40 K (blue), 60 K (green) and 70 K (pink).

susceptibility χ'' is plotted as a function of temperature. The connection between the intensity I of the peaks and χ'' is given by:

$$I \propto S(\mathbf{Q}, \omega) = (n_B + 1)\chi'' \quad (6.8)$$

where n_B is the Bose factor given in Eq. (2.21).

Now that the magnons at the zone center has been well examined, the next step is to search for phonons. The intensities of phonons scale with \mathbf{Q} [45] so higher \mathbf{Q} -values are needed in order to detect any phonons. We speculate that the reason why no phonons were observed at the RITA

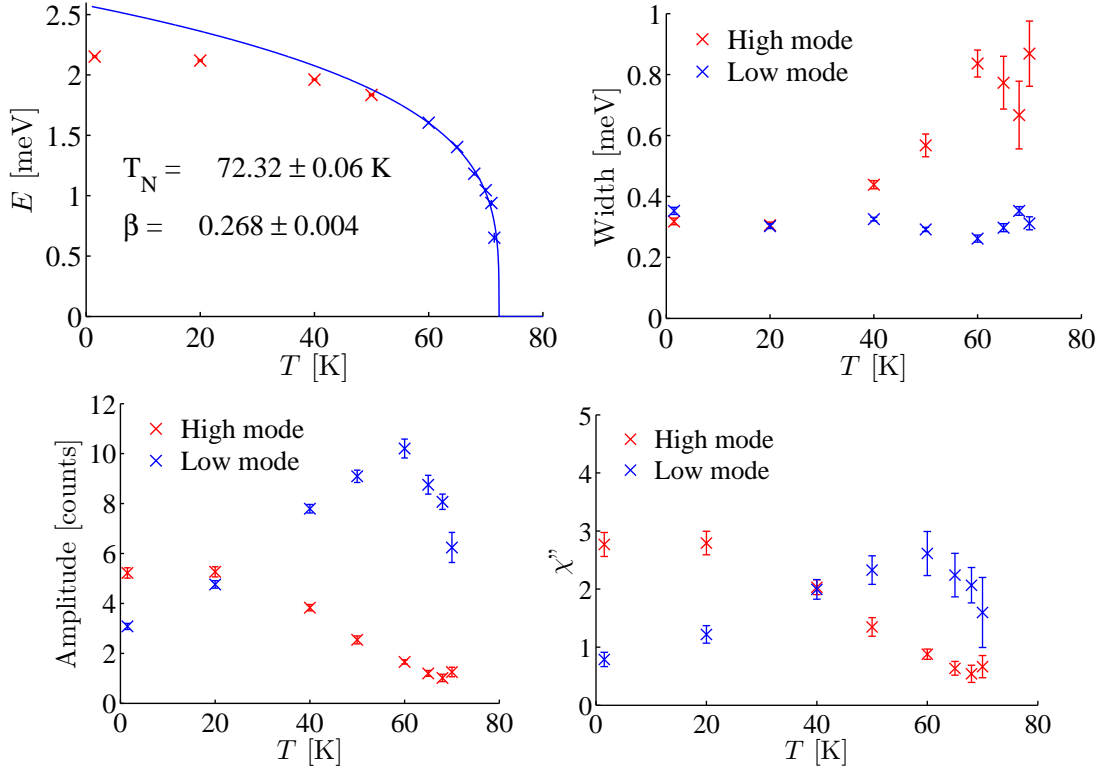


Figure 6.12: Values extracted from the energy scans in Fig. G.4 in appendix G measured at (100). The temperatures closest to T_N are not included, due to large fitting uncertainties. **Top Left:** Peak position of the low energy branch as a function of temperature. Blue points were included in the fit to a power law $\left(\frac{T-T_N}{T_N}\right)^\beta$. **Top Right:** The width of the high energy branch (red) and the low energy branch (blue). **Bottom Left:** The intensity of the high energy branch (red) and the low energy branch (blue). **Bottom Right:** The imaginary susceptibility χ'' of the high energy branch (red) and the low energy branch (blue).

II experiment was the limitations in Q -range. Measurements were done at $T = 100$ K around the $(0\bar{2}0)$ Bragg Peak, but no phonons were detectable. Instead phonons were searched for at a thermal instrument, in this case EIGER.

6.7 Magnon and transverse phonon around (030)

At the thermal instrument EIGER, it is possible to measure higher energy transfers. Details about the experimental setup can be found in Sec. 5.2. All other groups have measured dispersions in the l -direction, close to the zone center. Our measurements were higher in Q in the h, k -plane around (030). There, a clear transverse phonon was detected.

A color plot of the dispersion, from the (030) zone center almost half-way to the next zone center, (220), can be seen on the left of Fig. 6.13. In a hexagonal lattice, it can be a bit tricky to figure out where to perform the scan in order to observe the transverse phonon. With a bit of geometrical insight and a look at Fig. 6.1 it is clear that the transverse component of the phonon is measured along $(h(3 - h/2) 0)$.

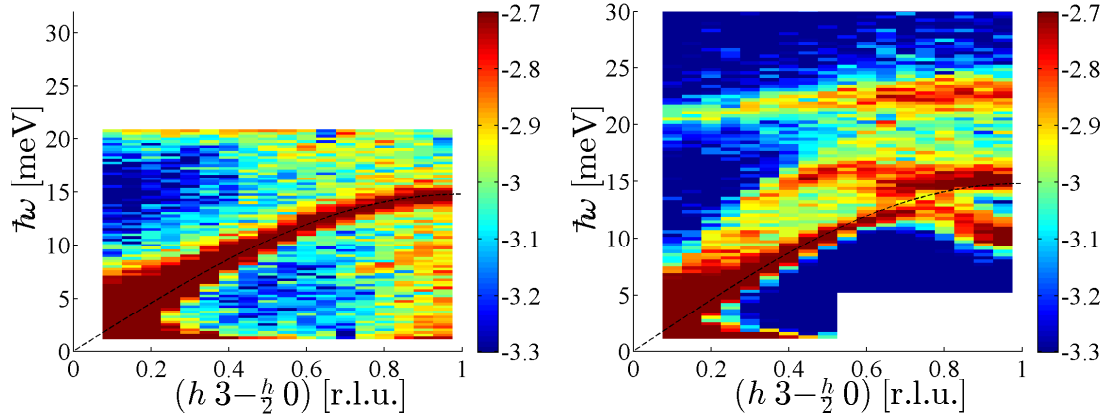


Figure 6.13: **Left:** Transverse acoustic phonon dispersion measured at $T = 100$ K (above T_N). **Right:** Transverse acoustic phonon, optical phonon, and magnon dispersion measured at $T = 40$ K (below T_N). To measure the transverse phonon the scan needed to be of the form $(h \ 3 - \frac{h}{2} \ 0)$. The dotted black line is a plot of the function $y = 14.8 \sin(x\pi/2)$ as a guide to the eye. The color indicates the logarithm to the number of counts per monitor.

Below the magnetic ordering temperature T_N , the same scan geometry was used, but a wider range of energies was recorded, in order to measure the optical phonon dispersion. The color plot can be seen on the right of Fig. 6.13. A magnon appears and either crosses or anti-crosses with the phonon close to $h = 0.75$. The background is much larger at $T = 100$ K than at $T = 40$ K, especially for larger h 's, which could be due to a higher Debye-Waller factor. But because the scan is transverse and \mathbf{Q} is essentially constant, it seems strange that the background is not more regular. Polarized neutrons made it possible to more closely examine the background for $T = 100$ K; see Sec. 7.3. The raw energy scans can be found in Fig. G.5 and Fig. G.6 in appendix G.

6.7.1 Temperature dependence of the transverse phonon

The temperature dependence of the phonon width at $h = 0.35$ was measured for a wide range of temperatures. The energy scans fitted to Gaussian functions²² are shown in Fig. 6.14. Q-scans at $\hbar\omega = 7.9$ meV were also performed and the raw Q-scans can be seen in Fig. G.7 in appendix G.

A plot of phonon width, in terms of energy, σ_E , and in terms of Q , σ_Q , as a function of temperature, is shown in Fig. 6.15. From both plots, it is clear, that the width reaches a minimum close to the transition temperature.

At EIGER, two energy scans at the longitudinal position were performed, at $k = 3.25$ and $k = 3.35$ for both 40 K and 100 K. These measurements, however, were not investigated further. The position in reciprocal space can be seen in Fig. 6.1 and the four scans can be found in Fig. G.8 in appendix G but will not be discussed further in this thesis.

Whether the dispersions in Fig. 6.13, are structural or magnetic, is unknown, and one can only guess what happens at the crossing/anti-crossing at $h = 0.75$. The only way to determine this is with polarized neutrons and the next section describes the data taken on the polarized three-axis spectrometer C5 in Canada to that end.

²²The `ngauss.m` function for `fits.m` was utilized.

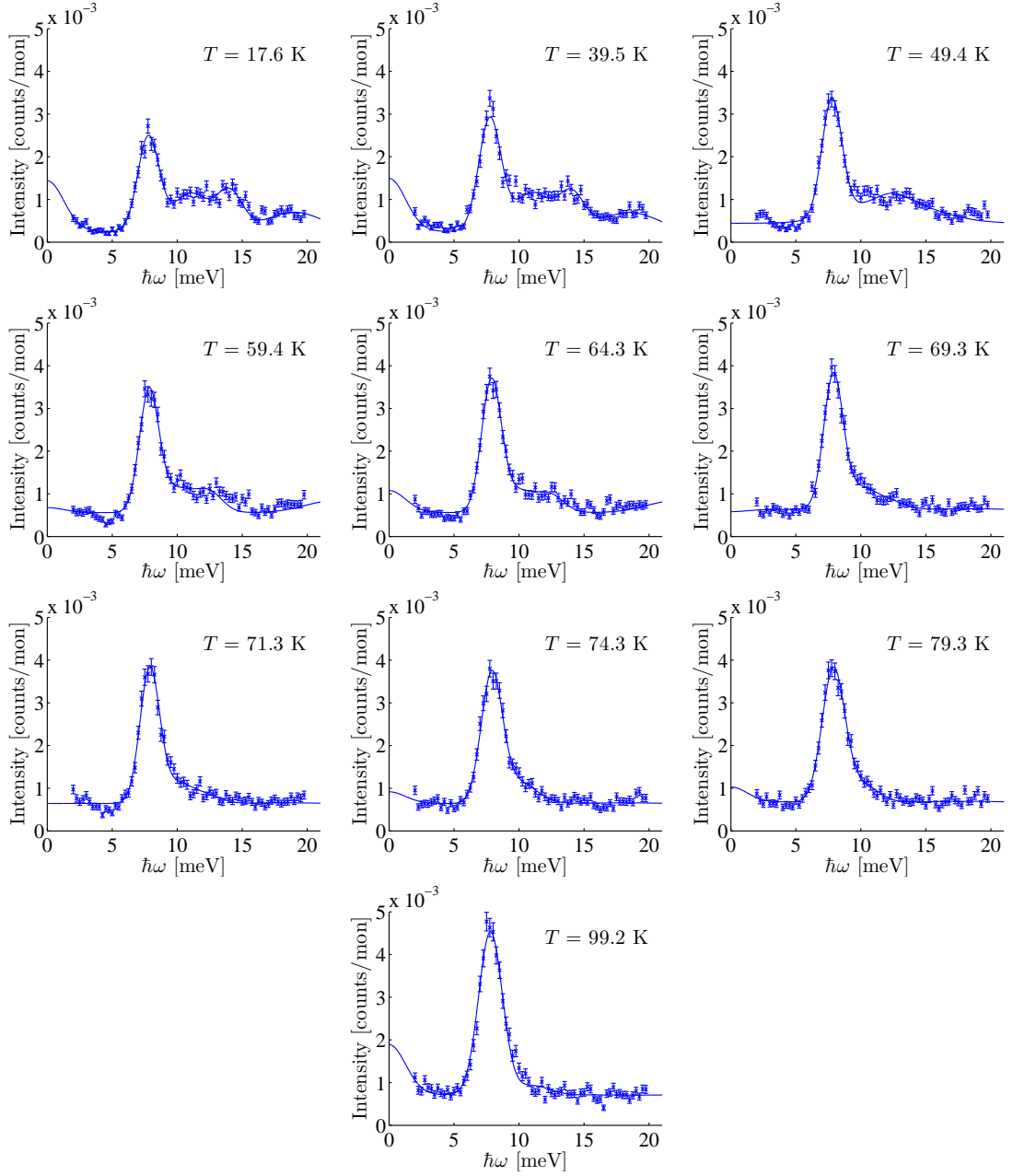


Figure 6.14: Energy scans of the transverse phonon at different temperatures at $h = 0.35$.

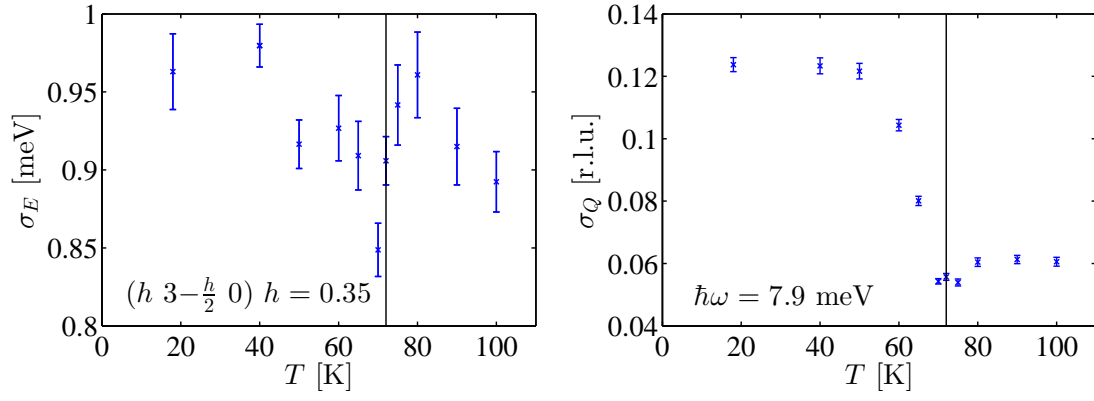


Figure 6.15: Left: Phonon width in energy as a function of temperature ($h = 0.35$). **Right:** The phonon width in Q as a function of temperature $\hbar\omega = 7.9$ meV. T_N is marked with a black line.

7 Polarized data

In this chapter the results from the polarized neutron scattering experiments at C5 will be presented and compared to the non-polarized data taken at EIGER.

7.1 Strategy

When doing polarized neutron experiments the flux is much lower than when doing non-polarized neutron experiments. Therefore it would take a very long time to measure energy scans for all the Q -values that were measured on EIGER. Four Q -values were thus selected: two scans overlapping with the EIGER constant- Q scans and two new Q -values, see Fig. 7.1.

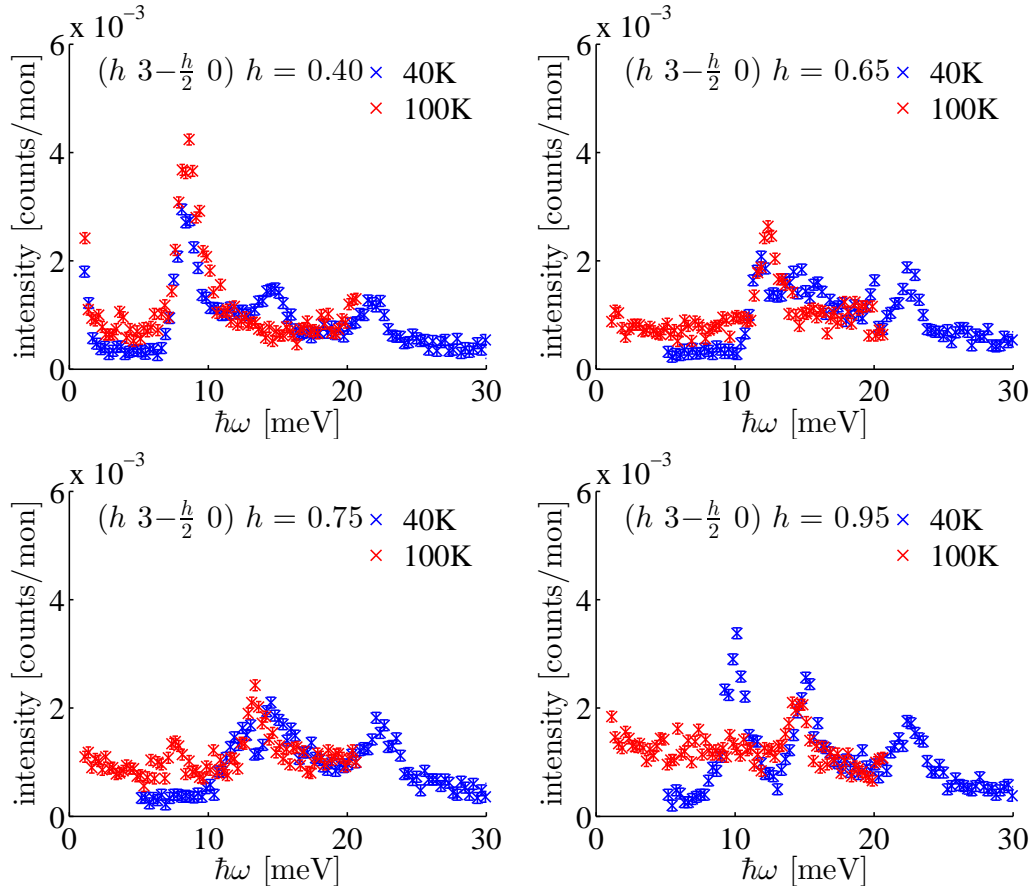


Figure 7.1: Based on the non-polarized EIGER data, the following four scans were selected as the best cuts for the polarized experiment. The first cut, $h = 0.4$, is between the zone center and the zone boundary. The next cut, $h = 0.65$, is very close to the zone boundary at $h = 0.667$. The third cut is at the phonon-magnon crossing at $h = 0.75$ and the last cut, $h = 0.95$, is almost half-way ($h = 1.00$) in between two zone centers.

The position of the C5 scans with respect to the EIGER data can be seen in Fig. 7.2.

All energy scans, unless anything else is specified, were measured with a horizontal field at the sample position. This was chosen so that all the magnetic scattering was measured in the

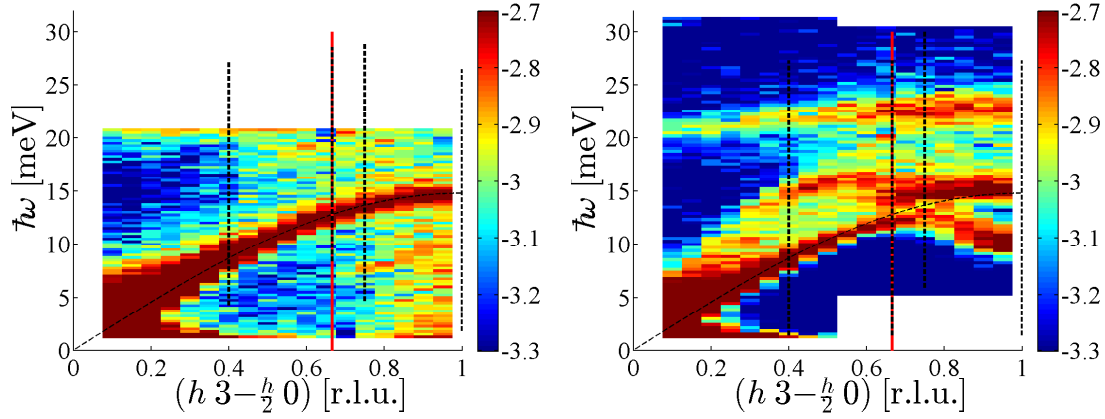


Figure 7.2: **Left:** Color plot at 100 K with the scans done at C5 marked with black dotted lines. **Right:** Color plot at 40 K with the scans done at C5 marked with dotted black lines. Two of the scans are overlapping with the EIGER data ($h = 0.4$ and $h = 0.75$) and the two other do not (the one at the zone boundary at $h = 0.67$ and the one at $h = 1$). The zone boundary is marked with a red line. Notice that the scan range is different for each Q -value and temperature. The dotted black line is a plot of the function $y = 14.8 \sin(x\pi/2)$. The color indicates the logarithm to the number of counts per monitor.

spinflip channel, as explained in Sec. 3.8. One measuring point in the inelastic data corresponds to a measuring time of approximately one hour and all of the data corresponds to around 20 days of beam time.

7.2 Flipping ratio

While aligning the crystal before the actual experiment begins the flipping ratio R should be calculated. As stated in Sec. 3.8 the polarization of the beam is given by:

$$P = \frac{N_+ - N_-}{N_+ + N_-} = \frac{R - 1}{R + 1} \quad (7.1)$$

where R is the flipping ratio that can be measured during an experiment. The flipping ratio is the ratio between the neutron intensity when the flipper is turned off, $I^{\uparrow\uparrow}$, and turned on, $I^{\uparrow\downarrow}$, after the background has been subtracted:

$$R = \frac{I^{\uparrow\uparrow}}{I^{\uparrow\downarrow}} \quad (7.2)$$

The (110) and the ($3\bar{3}0$) peaks, spanning the (ζ, η) scattering plane were used as alignment peaks; see Fig. 6.1. Based on the scans of these peaks the flipping ratio and polarization was calculated. The scans of the (110) peak ($\zeta = 1$ and $\eta = 0$) and the ($3\bar{3}0$) peak ($\zeta = 0$ and $\eta = 3$) at $T = 100$ K fitted to a Gaussian²³ function is shown in Fig. 7.3.

The flipping ratio was calculated as the average of the ζ and η -scan in Fig. 7.3:

$$R = \frac{I^{\uparrow\uparrow}}{I^{\uparrow\downarrow}} = 13.8 \quad (7.3)$$

²³The gauss.m routine for fits.m was utilized.

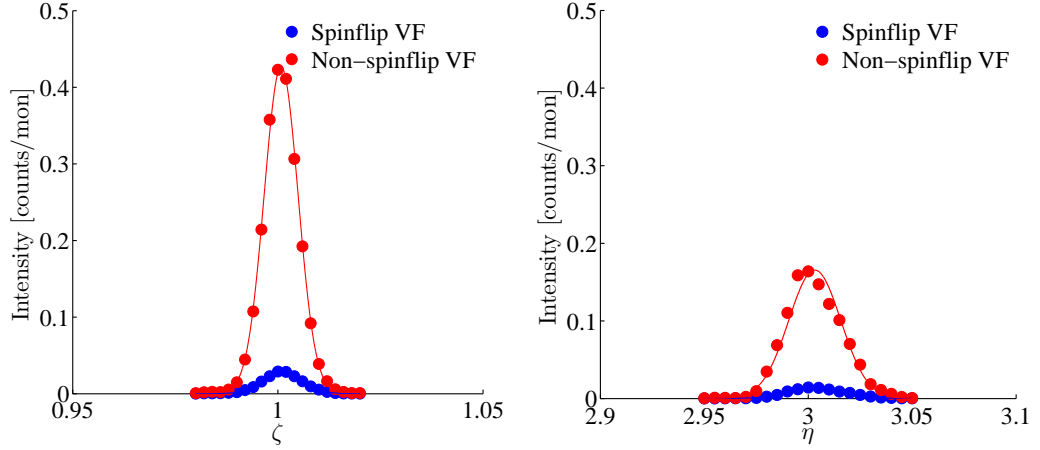


Figure 7.3: **Left:** The scan of the (110) ($(\zeta, \eta) = (1, 0)$) Bragg peak with a vertical field (VF) setting. **Right:** The scan of the (330) ($(\zeta, \eta) = (0, 3)$) Bragg peak with a vertical field (VF) setting. Both scans are longitudinal scans. Blue points correspond to the spinflip channel and red points to the non-spinflip channel.

giving a polarization of:

$$P = \frac{N_+ - N_-}{N_+ + N_-} = \frac{R - 1}{R + 1} = 0.86 \quad (7.4)$$

The normal flipping ratio at C5 is around 1:24 for a wave vector of 2.37\AA^{-1} ; see Sec. 5.3. The flipping ratio obtained for our experiment is quite large and the data are therefore not corrected.

While cooling down to $T = 40$ K (or heating up to $T = 100$ K) the (110) and the (330) Bragg peaks were measured to make sure that the sample was intact (and no intensity was lost).

7.3 Measurements above T_N

The energy scans at $T = 100$ K for the four different Q -values can be seen in Fig. 7.4. All the scans are fitted with multiple Gaussian functions²⁴. Notice that the intensity scale is different on all graphs. The four plots are given with identical intensity scaling in Fig. G.9 in appendix G.

For $h = -0.4$ (Fig. 7.4 upper left) the acoustic phonon is clearly observed in the non-spinflip channel peaking at $\hbar\omega = 8.8$ meV. At higher energies the optical phonon emerges with a peak energy of $\hbar\omega = 22$ meV. At the zone boundary, at $h = -0.67$ (Fig. 7.4 upper right), only the energy range for the acoustic phonon is scanned. The peak is at $\hbar\omega = 13$ meV.

Crossing the zone boundary the intensity of the phonon signal decreases, but the phonon peak is still clear in the non-spinflip channel at $h = -0.75$ (Fig. 7.4 bottom left) with a peak at $\hbar\omega = 14$ meV. The optical phonon at $\hbar\omega = 23$ meV is purely structural.

At $h = -1$ (Fig. 7.4 bottom right) the acoustic phonon signal at $\hbar\omega = 15$ meV appears in both the spinflip and the non-spinflip channel and is therefore a mix between a magnon and a phonon. It is not clear whether the optical phonon signal is structural or magnetic, there seems to be intensity in both channels, so the optical phonon is also a mixed state. What is very interesting in the $h = -1$ scan is the peak in the spinflip-channel at $\hbar\omega = 11$ meV, which must be a magnetic signal. However, the measurements are taken at $T = 100$ K which is ~ 30

²⁴The ngauss.m function was utilized.

K above the magnetic transition temperature. A peak is a token of coherent excitations from long-range order, and long-range magnetic order should not be present so far away from the ordering temperature.

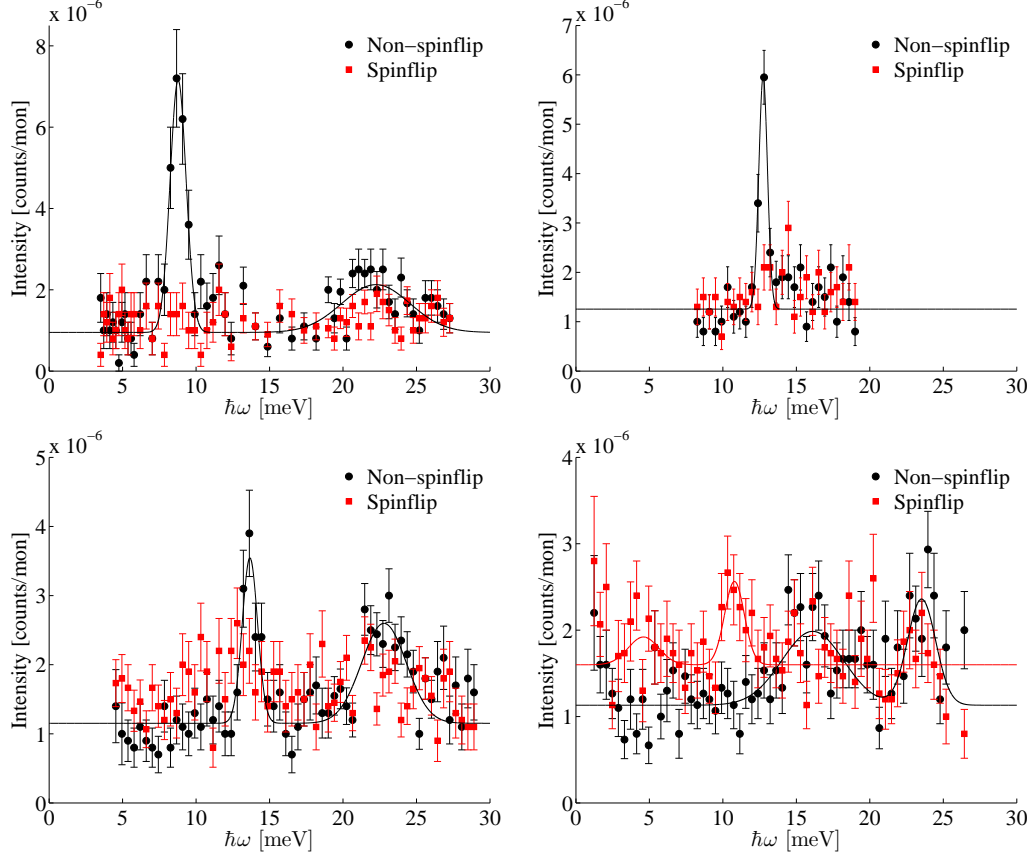


Figure 7.4: The $T = 100$ K data taken at C5. Red is the horizontal field spinflip channel (magnetic) and black is the horizontal field non-spinflip channel (nuclear). **Upper left:** Energy scan at $h = -0.4$, between the zone center and the zone boundary. **Upper right:** Energy scan at $h = -0.67$, at the zone boundary. **Bottom left:** Energy scan at $h = -0.75$ at the crossing. **Bottom right:** Energy scan at $h = -1$, between the (030) and the (220) zone.

In Fig. 7.5, the energy scans are plotted together with the non-polarized EIGER data. For $h = -0.4$ (Fig. 7.5 upper left) the data correspond very well to each other and the acoustic phonon peak is positioned at the same energy (the EIGER peak is positioned at $\hbar\omega = 8.9$ meV and the polarized peak is at $\hbar\omega = 8.8$ meV). The EIGER energy scan was terminated before reaching the optical phonon, but it is possible to see the beginning of a shoulder in the data that fits well with the polarized data. At the zone boundary, at $h = -0.67$ (Fig. 7.5 upper right), the EIGER data was taken at $h = 0.65$. The acoustic phonon peak in the EIGER data should be positioned very close to the polarized data peak, because the difference in Q is very small. Both peaks are positioned at $\hbar\omega = 13$ meV. The EIGER peak is much broader, with a width of $\Delta E = 0.77$ meV whereas the polarized peak has a width of $\Delta E = 0.29$ meV.

At $h = -0.75$ (Fig. 7.5 bottom left) the phonon data corresponds very well with the acoustic

phonon peak positioned at $\hbar\omega = 14$ meV for the polarized data and at $\hbar\omega = 14$ meV for the non-polarized data. However, at $\hbar\omega = 8$ meV there is a clear peak in the EIGER data, which is not observed in the polarized data. On the other hand the $\hbar\omega = 11$ meV peak in the spinflip data is not seen in the EIGER data.

The polarized data measured at $h = -1$ is compared with the EIGER data measured at $h = -0.95$ in (Fig. 7.5 bottom right). The data is quite different, which is probably due to the difference in \mathbf{q} . The acoustic phonon peak in the EIGER data at $\hbar\omega = 15$ meV has gone down in intensity and has moved about 2 meV, with a peak in $\hbar\omega = 16$ in the polarized data. The peak is also much wider in the polarized data. The width of the phonon peak in the EIGER data is $\Delta E = 0.57$ and the analogues peak width in the polarized data is $\Delta E = 2.1$ meV. This is the only scan where the EIGER peak has been sharper than the polarized data peaks. The broadening may be due to the mixed nature of the phonon at $h = -1$, and an energy scan at EIGER at that position could reveal a broad peak as well.

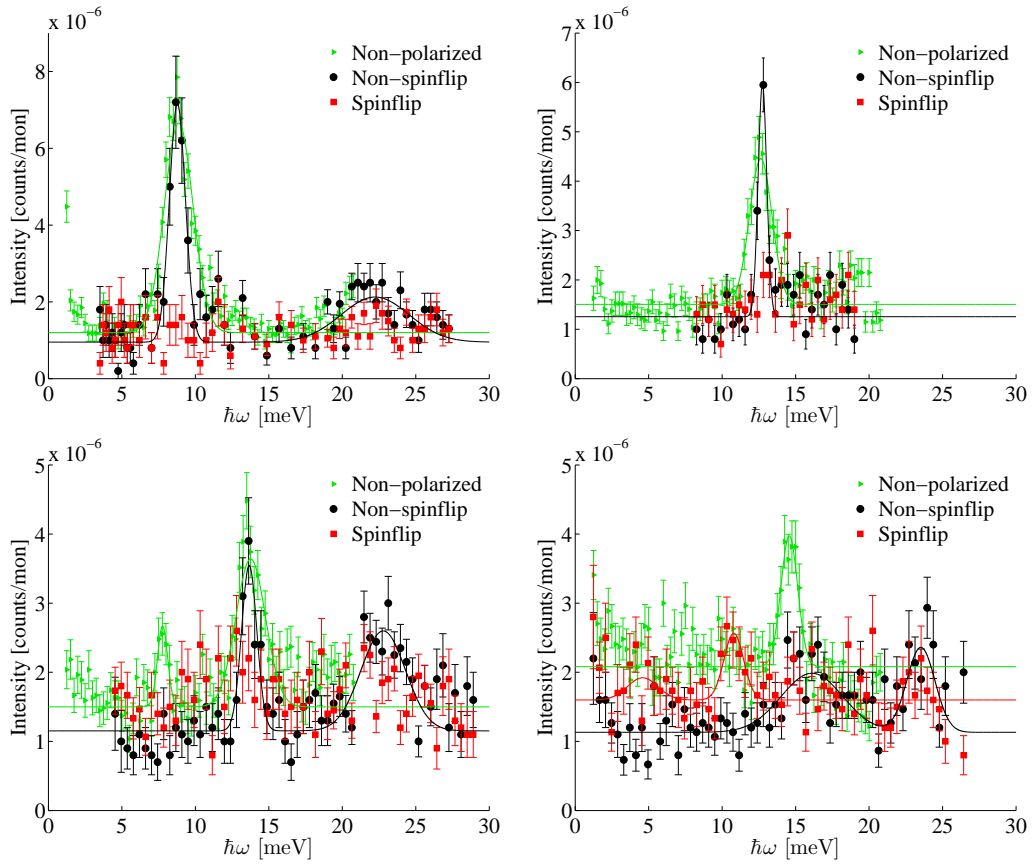


Figure 7.5: The $T = 100$ K data taken at C5 plotted together with the non-polarized EIGER-data. Red is the horizontal field spinflip channel (magnetic), black is the horizontal field non-spinflip channel (nuclear) and green is the scaled non-polarized EIGER data. **Upper left:** Energy scan at $h = -0.4$, between the zone center and the zone boundary. **Upper right:** Polarized energy scan at $h = -0.67$, at the zone boundary and non-polarized data taken at $h = 0.65$. **Bottom left:** Energy scan at $h = -0.75$ at the mode crossing. **Bottom right:** Polarized energy scan at $h = -1$, between the (030) and the (220) zone and non-polarized data at $h = 0.95$.

7.4 Measurements below T_N

The energy scans at $T = 40$ K for the four different Q -values can be seen in Fig. 7.6. The intensity scales are different for the different Q -values. The four $T = 40$ K plots with identical intensity scaling can be found in Fig. G.11 in appendix G.

For $h = -0.4$ (Fig. 7.6 upper left) the acoustic phonon peak is clearly observed in the non-spinflip channel peaking at $\hbar\omega = 8.6$ meV. The magnon signal is weak with a peak at $\hbar\omega = 15$ meV. At this energy the non-spinflip points are generally lower than the spinflip points. At higher energies the optical phonon emerges with a peak energy of $\hbar\omega = 23$ meV. Both the magnon peak and the optical phonon peak are broad.

At the zone boundary, at $h = -0.67$ (Fig. 7.6 upper right), the acoustic phonon peak is not very intense with a peak position at $\hbar\omega = 12$ meV. At this h -value it is observed that the peak at higher energies ($\hbar\omega = 16$ meV) than the phonon is in fact magnetic. The optical phonon on the other hand is mixed *i.e.* there is a peak in both the spinflip and non-spinflip channels.

Crossing the zone boundary, hitting the point of crossing of the two modes at $h = -0.75$ (Fig. 7.6 bottom left) both the acoustic phonon, the magnon and the optical phonon is mixed. It is generally not possible to distinguish between the spinflip and the non-spinflip channel over the whole scan.

At $h = -1$ (Fig. 7.6 bottom right) the spinflip and the non-spinflip channel signals are separated and an intense magnetic peak is observed at $\hbar\omega = 11$ meV. This peak corresponds to the lower branch in Fig. 7.2. At $\hbar\omega = 16$ meV and $\hbar\omega = 23$ meV both the spinflip and non-spinflip channels show broad peaks corresponding to the upper branches in Fig. 7.2.

The polarized data plotted together with the non-polarized EIGER data at $T = 40$ K can be seen in Fig. 7.7. The plots given with identical intensity scaling can be found in Fig. G.12 in appendix G.

For $h = -0.4$ (Fig. 7.7 upper left) the acoustic phonon peak is positioned at $\hbar\omega = 8.6$ meV in the polarized data and at $\hbar\omega = 8.8$ meV in the EIGER data. The width is larger in the EIGER data. The magnon signal is much clearer in the EIGER data and the peaks are positioned at the same energy, near $\hbar\omega = 15$ meV. The optical phonon peak is also much sharper in the EIGER data, with a peak position at $\hbar\omega = 22$ meV and a width of $\Delta E = 0.86$ meV. The intensities of the scattering resemble each other from $\hbar\omega = 17$ meV to around $\hbar\omega = 24$ meV. The background at high energies is largest for the EIGER data.

At the zone boundary, at $h = -0.67$ (Fig. 7.7 upper right), the EIGER data which was taken at $h = -0.65$ is quite different than the polarized data. The peaks in the polarized data are shifted towards higher energies, *e.g.* the optical phonon peak position is at $\hbar\omega = 24$ meV in the polarized data and at $\hbar\omega = 23$ meV in the EIGER data. The background in the EIGER data is lower for both small and large energies and the intensity is larger around the peaks. The EIGER data seems to show an extra peak at around $\hbar\omega = 20$ meV which is not observed in the polarized data (It is only two points so it might be a spurious signal).

Crossing the zone boundary, hitting the point of crossing of the two modes at $h = -0.75$ (Fig. 7.7 bottom left) the EIGER data has three distinct peaks, while the polarized data only reveal two broad features.

At $h = -1$ (Fig. 7.7 bottom right) (and $h = 0.95$ for the EIGER data) both data sets have three peaks. The positions of the peaks in the polarized data are moved toward higher energies compared to the EIGER data, probably due to the difference in Q . The background at low and high energies is lower in the EIGER data.

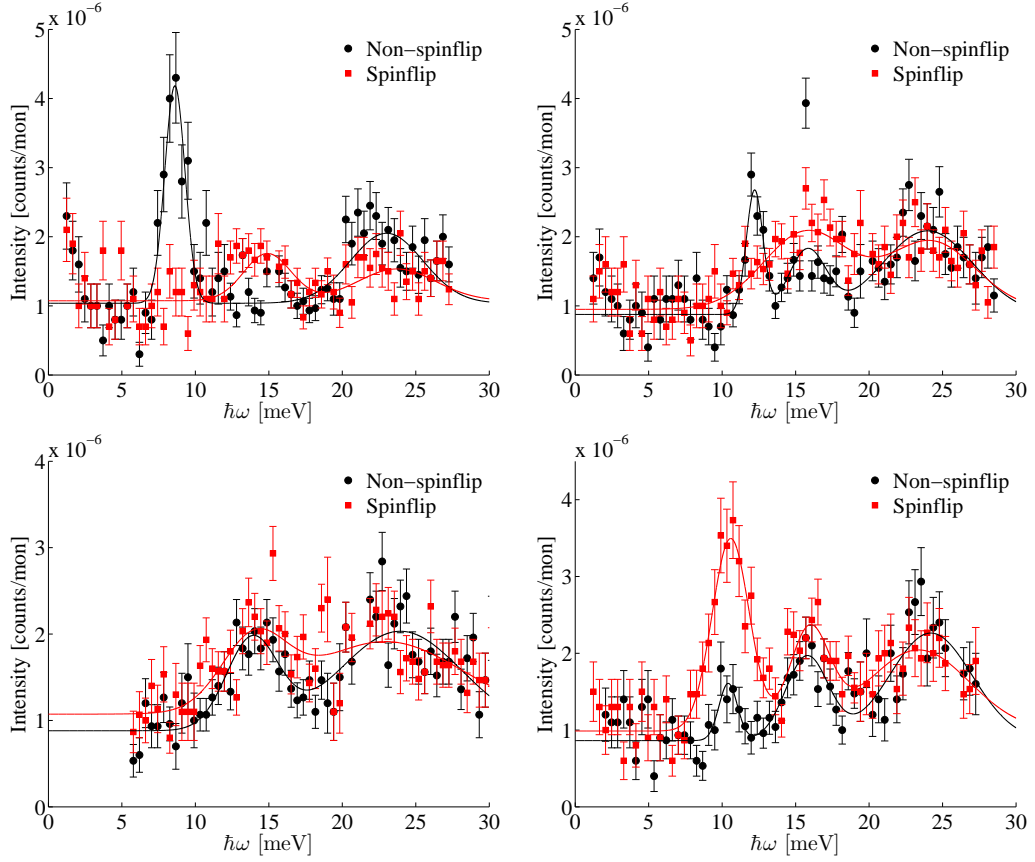


Figure 7.6: The $T = 40$ K data taken at C5. Red is the horizontal field spinflip channel (magnetic) and black is the horizontal field non-spinflip channel (nuclear). **Upper left:** Energy scan at $h = -0.4$, between the zone center and the zone boundary. **Upper right:** Energy scan at $h = -0.67$, at the zone boundary. **Bottom left:** Energy scan at $h = -0.75$ at the crossing. **Bottom right:** Energy scan at $h = -1$, between the (030) and the (220) zone centers.

7.4.1 Horizontal vs vertical field measurements

The energy scan at $h = -1$ was measured both with the field horizontal ($\mathbf{P}_0 \parallel \mathbf{Q}$) at the sample position and with the field vertical ($\mathbf{P}_0 \perp \mathbf{Q}$) at the sample position. These scans can be seen in Fig. 7.8. With \mathbf{Q} along x the horizontal field measurements keeps all the magnetic scattering in the spinflip-channel, while a vertical field measurement can reveal if the scattering is an in-plane y or out-of-plane z movement as explained in Sec. 3.8 and shown in Fig. 3.11.

The horizontal and vertical spinflip data, Fig. 7.8 (Left) reveals that nearly all the intensity is found in the horizontal field channel. The y -component of the spin is therefore zero, according to Table 3.2. In Fig. 7.8 (Right) the horizontal and vertical non-spinflip data are plotted and most of the scattering appears in the vertical field channel. All the magnetic scattering is in the z -direction, out of the scattering plane. The two plots with identical intensity scaling can be seen in Fig. G.13 in appendix G.

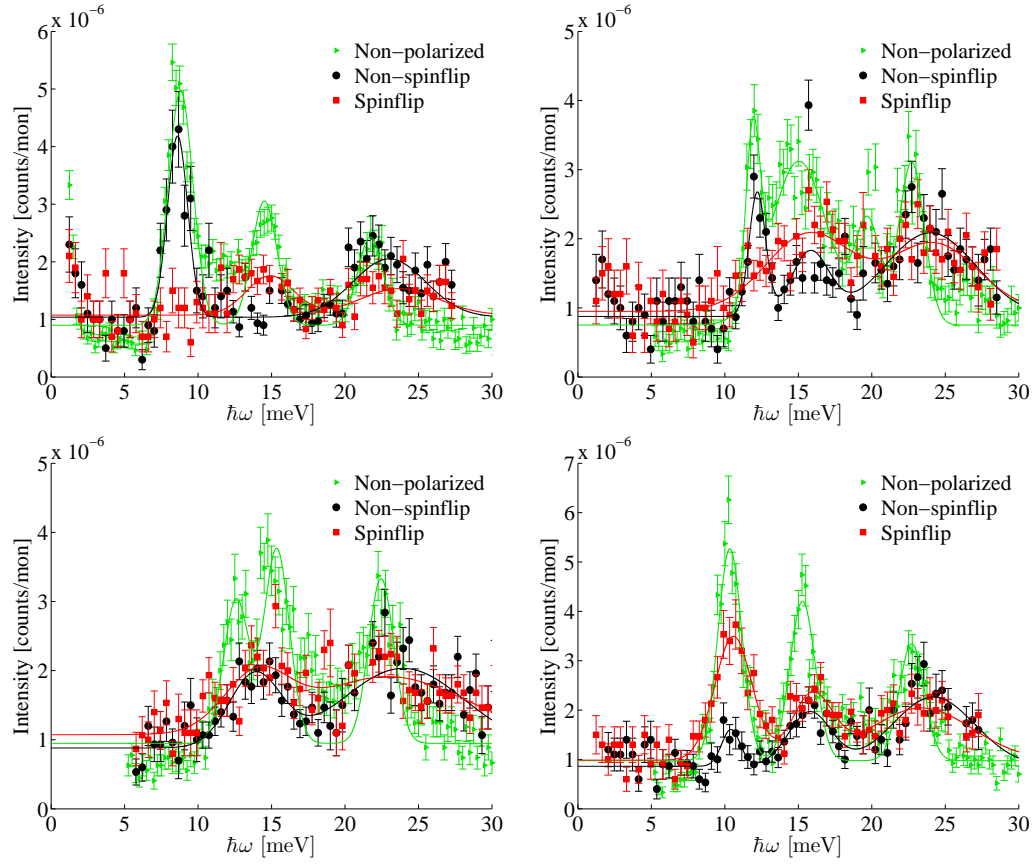


Figure 7.7: The $T = 40$ K data taken at C5 plotted together with the non-polarized EIGER-data. Red is the horizontal field spinflip channel (magnetic), black is the horizontal field non-spinflip channel (nuclear) and green is the non-polarized EIGER data. **Upper left:** Energy scan at $h = -0.4$, between the zone center and the zone boundary. **Upper right:** Polarized energy scan at $h = -0.67$, at the zone boundary and non-polarized data taken at $h = 0.65$. **Bottom left:** Energy scan at $h = -0.75$ at the crossing. **Bottom right:** Polarized energy scan at $h = -1$, between the (030) and the (220) zone and non-polarized data at $h = 0.95$.

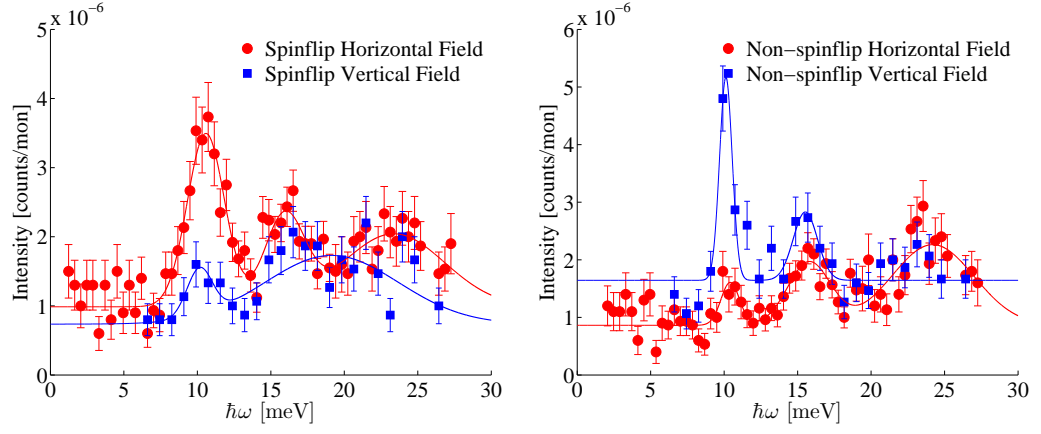


Figure 7.8: Polarized scattering data for two different directions of the incoming polarization. **Left:** Constant- \mathbf{Q} scan at $h = -1$ at 40 K spinflip channel. **Right:** Constant- \mathbf{Q} scan at $h = -1$ at 40 K non-spinflip channel.

8 Discussion

In this section the results will be discussed and compared to similar data collected by others or to measurements on other low-dimensional systems. The discussion of the data is given in the same order as it was presented in Sec. 6 and Sec. 7 and is divided into three parts: critical phenomena (most of the non-polarized data), the phonon-magnon coupling (the non-polarized color plots from EIGER and the polarized data), and a section discussing the magnetic dispersion-like signal observed above the magnetic ordering temperature.

8.1 Critical phenomena

The critical exponent β was determined in two separate ways. The intensity of the magnetic Bragg peak was followed from base to just above the ordering temperature giving $\beta = 0.19$. The size of the spin wave gap of the magnon dispersion from base to T_N gave the critical exponent $\beta = 0.27$, quite different from the Bragg peak determination. The measurements of the magnetic Bragg peak are the most reliable, with many data points close to the transition temperature, while the spin gap data lacked data points close to the critical temperature due to difficulties with fitting the peaks close to the elastic peak when reaching T_N .

The critical exponents $\gamma = 1.55$ and $\nu = 0.614$ were determined by the diffuse scattering around the magnetic Bragg peak for $T > T_N$. If the $T = 100$ K data point was not used in the fitting routine, the exponents had the values $\gamma = 1.51$ and $\nu = 0.569$. This data point had a large impact on ν , which is connected to the width of the Lorentzian peak and the magnetic correlation length.

The critical exponents, except for μ , are quite different from the measurements by Chatterji *et al.* ($\beta = 0.295$, $\gamma = 0.97$ and $\nu = 0.45$) and Roessli *et al.* ($\beta = 0.187$ and $\nu = 0.57$). When measuring critical exponents, one has to integrate over all the fluctuation energies to be able to fit the data in the critical region as well. When using an analyzer, as when doing experiments on a three-axis spectrometer, only the energies inside the resolution function are measured (≈ 2 meV). Chatterji *et al.* worked in two-axis mode *i.e.* integrated over all energies, unlike both Roessli *et al.* and the experiments presented in this thesis. Therefore the Chatterji *et al.* data and the critical exponents $\beta = 0.295$, $\gamma = 0.97$ and $\nu = 0.45$ determined from it should be the most reliable. It should be noted that the critical exponent extracted from the spin wave gap data, $\beta = 0.27$, is close to the beta value determined by Chatterji *et al.* $\beta = 0.295$. Even though the data set lacked points close to the ordering temperature, the experiment was performed in the correct way to obtain the real critical exponent.

The prediction by Kawamura [33] that the critical exponents of the two-dimensional triangular antiferromagnets form a new universality class might be true. With Monte-Carlo simulations Kawamura predicts the critical exponents of the new universality class to be $\beta = 0.25$, $\gamma = 1.1$ and $\nu = 0.53$. In Table 8.1 the critical exponents for different models and the experiments are summarized for an easier comparison. The experimentally determined critical exponents, even though they differ from experiment to experiment, are in quite good agreement with the new universality class. None of the other models fit the experimental values better.

More correct measurements, *i.e.* measurements in two-axis mode, and more precise measurements, *i.e.* many points close to the transition temperature, are needed to determine the critical exponents and thereby determine if the quasi-two-dimensional triangular systems, like YMnO₃ belong to a new universality class.

Model/Experiment	β	γ	ν
2D 3d XY	0.345	1.316	0.669
1D 3d Ising	0.326	1.2378	0.6312
1D 2d Ising	0.125	1.75	1
3D 3d Heisenberg	0.367	1.388	0.707
Mean field	0.5	1	0.5
Chatterji <i>et al.</i> [12]	0.295	0.97	0.45
Roessli <i>et al.</i> [65]	0.187	–	0.57
Kawamura [33]	0.25	1.1	0.53
Our measurements (Bragg peak)	0.19	1.55 (1.51)	0.614 (0.569)
Our measurements (Spin wave gap)	0.27	–	–

Table 8.1: The critical exponents associated with models and critical exponents determined from experiments. β is related to the magnetization, γ is related to the magnetic correlation length and ν is related to the magnetic susceptibility. From [15]. The numbers in parenthesis are the ones obtained without the $T = 100$ K data point.

8.2 The magnetoelastic coupling

Transverse energy scans around the (300) Bragg peak at $T = 100$ K revealed an acoustic phonon dispersion with an energy of $\hbar\omega = 12$ meV at the zone boundary. However, polarized neutron scattering that can separate structural and magnetic signals, revealed the nature of the dispersion. In Fig. 8.1 the color map at $T = 100$ K of the data taken at EIGER is plotted, using labels to show whether the polarized data gave a structural, magnetic or mixed signal. The nature of both the acoustic and the optical (only measured with polarized neutrons) phonon is structural until the zone boundary $h = 0.67$ and a little beyond ($h = 0.75$), but between the (030) and (220) zone centers the signals are mixed, *i.e.* both the spinflip and the non-spinflip channels show a peak of equal size. It is strange that there is a magnetic contribution to the dispersion above T_N at $h = 1$. The energy scan at $h = 1$ also revealed a magnetic signal at $\hbar\omega = 11$ meV. This peak is discussed further later, see Sec. 8.3.

Measurements at EIGER at $T = 40$ K of the dispersions revealed a crossing between a transverse acoustic phonon and a magnon; a feature we had not anticipated. In Fig. 8.3 the color map at $T = 40$ K of the data taken at EIGER is plotted, with labels showing what the polarized data revealed about the nature of the dispersions. Inside the (030) zone, the dispersions are characterized as anticipated *i.e.* both the acoustic and the optical phonon are purely structural while the magnon is purely magnetic. At the (030) zone boundary and at the crossing between the acoustic phonon and the magnon dispersion, on the other hand, all the dispersions are mixed. At $h = 1$, between the (030) and (220) zone centers, the two low-energy dispersions are separable again and the low-energy mode is of magnetic nature, while the high-energy mode is mixed, and not structural as one would expect from Fig. 8.5. The optical phonon is still mixed at this h -value.

Group theoretical analysis of magnetoelastic couplings have shown that interactions will not occur between a magnon and a phonon branch for a line of symmetry passing through Γ in the Brillouin zone if they belong to different irreducible space group representations [16]. Modes with the same symmetry will result in an avoided crossing, while modes with different symmetry can cross unperturbed, therefore the interacting magnon and phonon that we have observed must have the same symmetry. In Fig. 8.5 the phonon and magnon modes cross and return to their original nature after the crossing point. The magnon is magnetic after the crossing, while the phonon is mixed from the zone boundary up to $h = 1$. Theoretical calculations are needed to understand why the modes are mixed this far from their crossing regions between two zone centers.

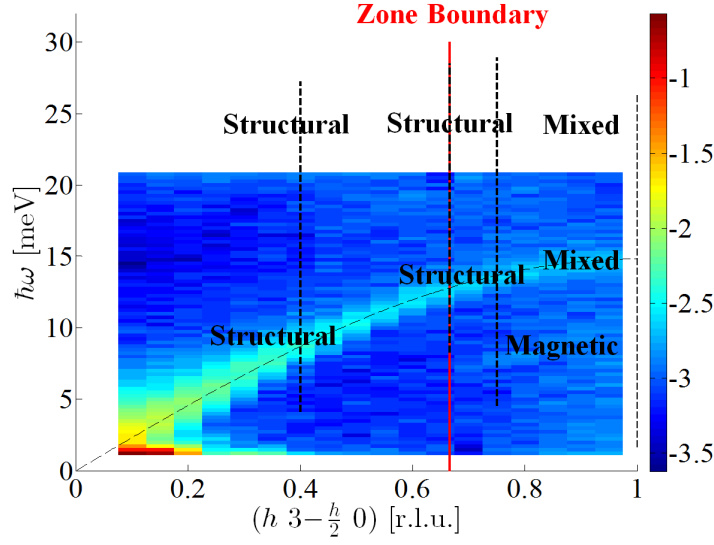


Figure 8.1: Transverse acoustic phonon dispersion measured at $T = 100$ K (above T_N) with labels indicating the nature of the dispersions determined with polarized inelastic neutron scattering. The zone boundary is marked with a red line. The color indicates the logarithm to the number of counts per monitor.

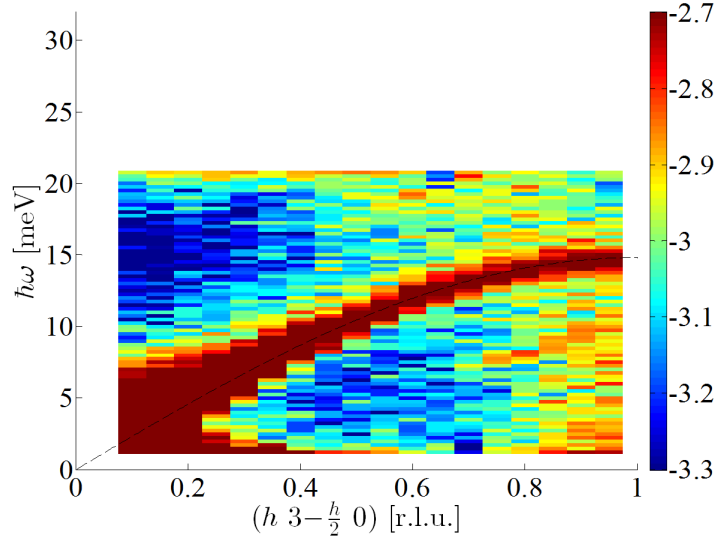


Figure 8.2: Transverse acoustic phonon dispersion measured at $T = 100$ K (above T_N) with a color scaling so it is easier to see the increased background the zone boundary, which is marked with a red line. The color indicates the logarithm to the number of counts per monitor.

Pailhès *et al.* observed a hybrid mode at low temperatures $T < 25$ K (at $T = 40$ K the mode was hard to distinguish from the background and very strong at $T = 1.5$ K) close to the zone

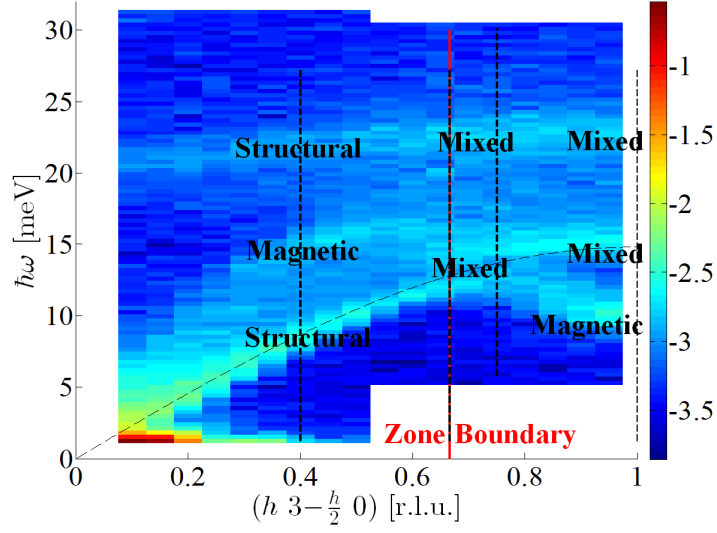


Figure 8.3: Transverse acoustic phonon, optical phonon and magnon dispersion measured at $T = 40$ K (below T_N) with labels indicating the nature of the dispersions determined with polarized inelastic neutron scattering. The zone boundary is marked with a red line. The color indicates the logarithm to the number of counts per monitor.

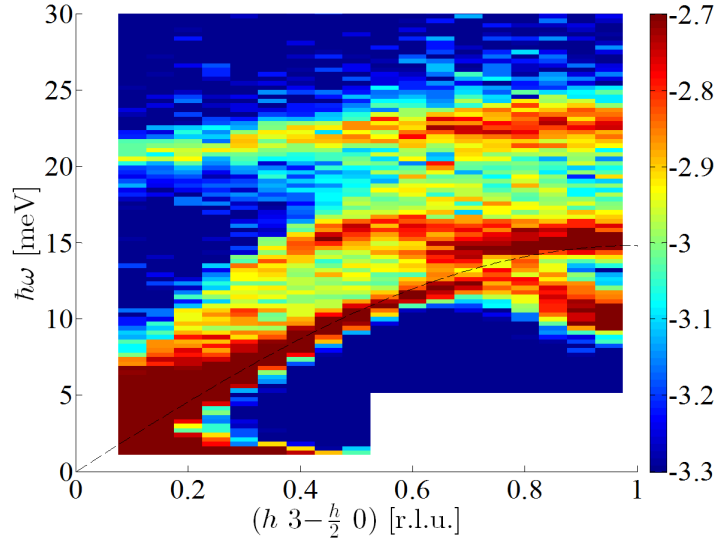


Figure 8.4: Transverse acoustic phonon, optical phonon and magnon dispersion measured at $T = 40$ K (below T_N) with a color scaling making it easier to see less intense, but important part of the dispersions. The zone boundary is marked with a red line. The color indicates the logarithm to the number of counts per monitor.

center as shown in Sec. 4.8. The mixed modes observed in Fig. 8.3 are quite similar to the mode observed by Pailhès *et al.*, but occur at the zone boundary instead of the zone center and are

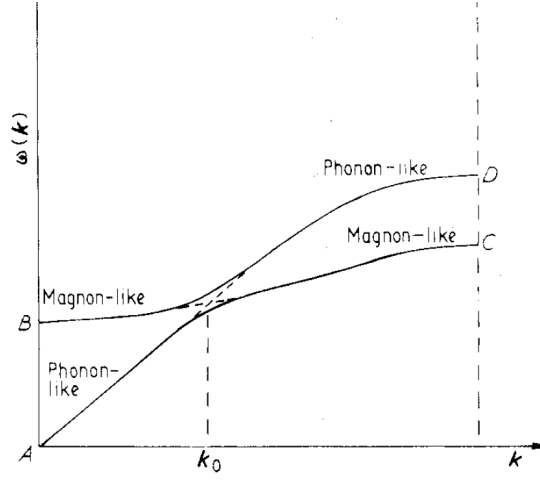


Figure 8.5: Crossing, at k_0 between a magnon and a phonon-mode. The dotted lines indicate the form the dispersion would have had, had the modes not crossed each other. From [16].

not hard to distinguish from the background at higher temperatures, ($T = 40$ K and not $T < 25$ K). An interesting experiment would be to measure the dispersion (analogous to Fig. 8.4) at $T = 1.5$ K in order to see whether the signal intensifies, indicating a hybrid mode similar to the one reported by Pailhès *et al.*. Mixed modes are perhaps some of the most common excitations of multiferroic systems, and our measurements show the first example of observing them far from the zone center.

8.3 Magnetic signal above T_N

The energy scan at $h = -1$ at $T = 100$ K, plotted again in Fig. 8.6, shows a clear magnetic peak at $\hbar\omega = 11$ meV. When looking at the data in Fig. 8.1 it is clear that the peak at $\hbar\omega = 11$ meV is part of a dispersion decreasing in energy for smaller h , and it is therefore necessary to measure at another h -value in that region to be certain that the peak is part of a dispersion. Looking at the polarized data for $h = 0.75$ at $\hbar\omega = 7$ meV in Fig. 7.4 (Bottom Left) the magnetic signal is stronger than the structural signal. A dispersion suggests long range order, but there is no long range order above the magnetic ordering temperature and the peak probably originates from the paramagnetic fluctuations that occur in this frustrated system.

Spin waves above the magnetic ordering temperature were observed in iron up to $1.5T_C$ with neutron scattering by Lynn *et al.* [49]. In this system the effect was called persistent spin waves. The measurements were questioned for many years but recent simulations by Tao *et al.* [80] confirmed the data. The spin waves were measured in the (110) directions as seen in Fig. 8.8 with the zone boundary at $q = 1.55 \text{ \AA}^{-1}$. The energy of the spin waves is lowered as the temperature is increased. At the zone center the spin waves are not detectable.

In many ways our dispersion resembles the persistent spin wave observed by Lynn *et al.* in that they are only visible at finite energies and q away from the zone center and are not visible at the zone center.

Demmel *et al.* [17], on the other hand, saw persistent spin waves above the Néel temperature in YMnO_3 in a powder sample close to the zone center. Two broad peaks occurred in their

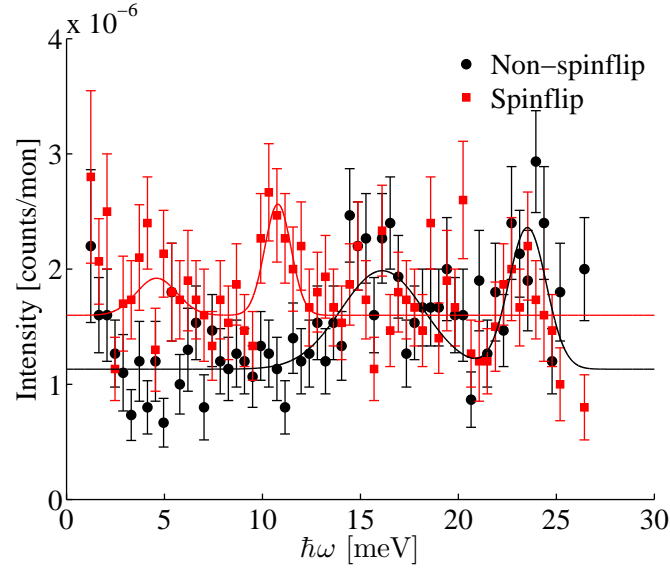


Figure 8.6: Energy scan at $h = -1$ and $T = 100$ K right in between the (030) and the (220) zone centers, revealing a magnetic peak at $\hbar\omega = 11$ meV.

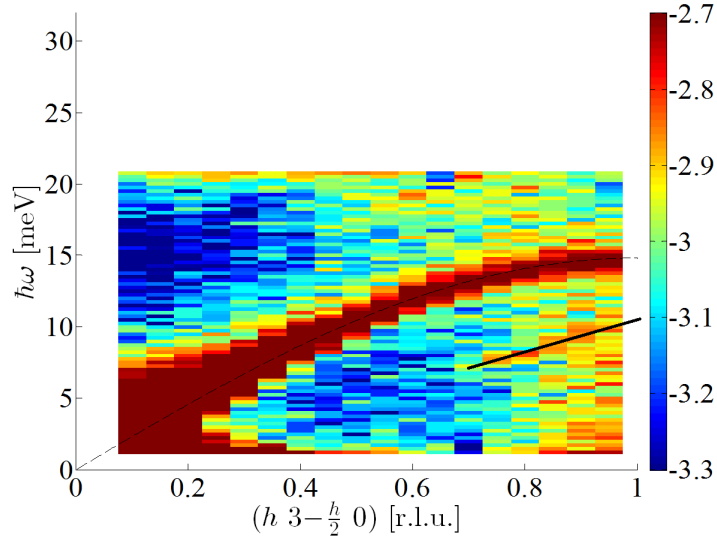


Figure 8.7: Transverse acoustic phonon dispersion measured at $T = 100$ K (above T_N). The magnetic dispersion is emphasized with a black line. The color indicates the logarithm to the number of counts.

energy scans at small q and Demmel *et al.* argue that the short life time and two dispersions close together in energy made it impossible to see them for $q > 1$.

Persistent spin waves are often seen in low-dimensional systems, like YMnO_3 , due to the fact that two-dimensional spin waves are not dependent on three-dimensional long range order. Chat-

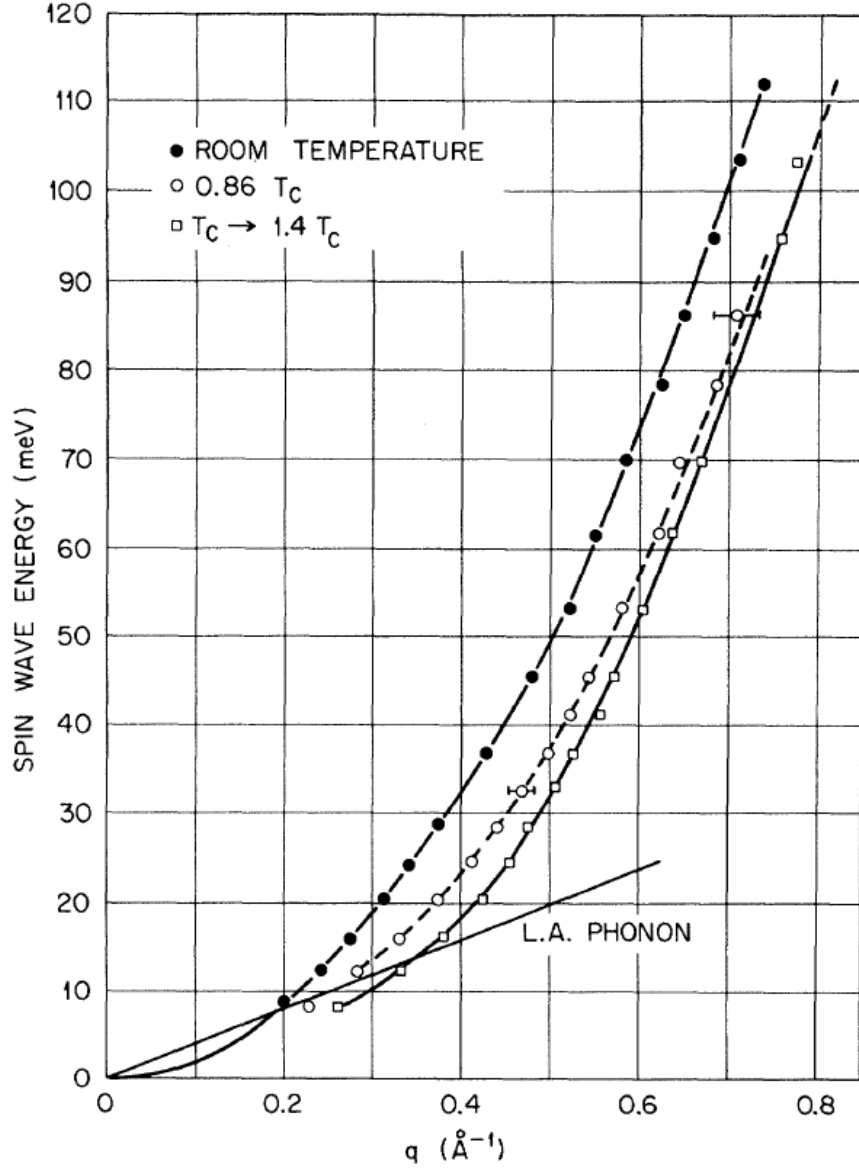


Figure 8.8: Spin wave dispersions in iron measured at different temperatures. The filled black circles are room temperature measurements, open circles are measurements at $0.86T_C$ and the open squares are measurements at $T_C \rightarrow 1.4T_C$. The solid black line indicates the longitudinal acoustic phonon. From [49].

terji *et al.* [11] observed unusual spin responses above T_N in the two-dimensional ferromagnet $\text{La}_{1.2}\text{Sr}_{1.8}\text{Mn}_2\text{O}_7$ with inelastic neutron scattering. Inelastic peaks were seen in constant-energy scans, but not in constant Q -scans. Birgeneau *et al.* [3] observed persistent magnons in the two-dimensional antiferromagnet K_2NiF_4 and Skalyo *et al.* [75] observed short-wavelength excitations along the chain at $2T_N$ in the one-dimensional antiferromagnet $\text{CsMnCl}_3 \cdot 2\text{D}_2\text{O}$. The

low-dimensionality systems present new aspects of understanding spin dynamics also above the ordering temperature.

As a last comment, the magnetic peak (or, hopefully, dispersion) observed in YMnO_3 at temperatures higher than T_N could be the reason for the paramagnetic scattering reducing the thermal conductivity as proposed by Sharma *et al.* [71] at temperatures larger than T_N . A plot of the thermal conductivity data and the models fitted to the data can be seen in Fig. 8.9. The suppression at lower temperatures (down to $T = 20$ K) could be a result of the phonon-magnon coupling observed at $T = 40$ K. For $T < 20$ K, the temperature might be too low for the coupling energy at $\hbar\omega = 15$ meV to be populated, eliminating the suppression of the thermal conductivity at low temperatures.

Our measurements together with theoretical calculations, both above and below the critical temperature, may contribute to the solution of the mystery of the suppressed thermal conductivity in YMnO_3 .

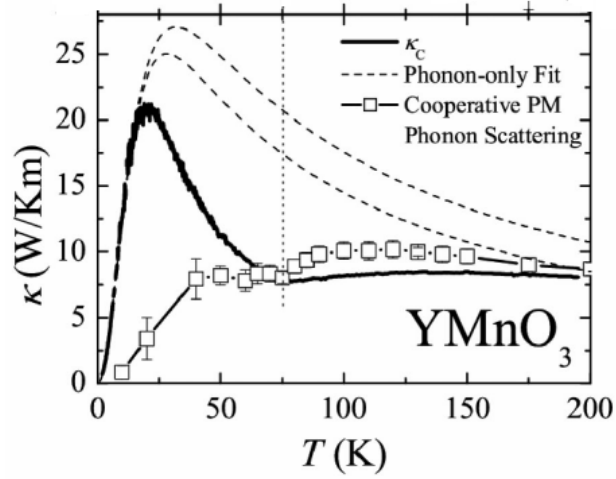


Figure 8.9: Thermal conductivity κ (black line) as a function of temperature. The dashed lines correspond to two different fits to κ assuming phonon only interactions. The open squares correspond to a model where the effect of spin fluctuations, possibly caused by the magnetic dispersion above T_N (as measured in this thesis project), on κ is taken into account. The model is scaled to match the size of the thermal conductivity measurements at T_N . T_N is indicated with the vertical dotted line. Adapted from [71].

9 Conclusion

The frustrated and multiferroic material h -YMnO₃, which is both ferroelectric and antiferromagnetic below $T_N \sim 70$ K has been investigated with both elastic and inelastic neutron scattering. The magnetic ordering temperature was determined by following the intensity of the (1 0 0) magnetic Bragg peak from base to 80 K, revealing a critical temperature of $T_N = 72$ K and a critical exponent $\beta = 0.19$. The elastic data also revealed a great amount of diffuse scattering around the (100) due to spin fluctuations, giving critical exponents of $\gamma = 1.5$ and $\nu = 0.72$. The critical exponents cannot be associated with standard model systems, but are closer to a new universality class proposed for two-dimensional triangular antiferromagnets to which YMnO₃ belongs. Improved measurements are needed to confirm or reject this theory.

The magnon branches around (100), measured with inelastic neutron scattering, show a dispersion broadening as the temperature is increased, giving the spin waves a shorter life time for temperatures near T_N . The gap closes as T_N is approached and reveals a critical exponent of $\beta = 0.27$, which fits well with the new two-dimensional model.

The transverse component of the acoustic phonon at (0 3 0) was measured and the temperature dependence determined. The line-width of the transverse phonon dips down at T_N for reasons that are still unknown.

The nature of the acoustic and optical phonon dispersions at $T = 100$ K was determined with polarized neutron scattering. Even though the measurements were done at $T \gg T_N$, the polarized measurements revealed a magnetic contribution to both the optical and acoustic phonon between the (0 3 0) and (2 2 0) zone centers. In addition to that, the $T = 100$ K data revealed at magnetic signal at $\hbar\omega = 11$ meV and $\mathbf{Q} = (1 \ 3 - \frac{1}{2} \ 0)$. From the non-polarized data, it seems that the signal is part of a dispersion and can, therefore, be associated with persistent spin waves, *i.e.* spin waves above the magnetic ordering temperature, due to the frustration of the system. Persistent spin waves may be the link between the microscopic and macroscopic properties of YMnO₃ *i.e.* the unexplained suppressed thermal conductivity at temperatures higher than the ordering temperature.

Below the magnetic ordering temperature at $T = 40$ K, an acoustic phonon branch and a magnon branch cross at the transverse position $\mathbf{Q} = (0.75 \ 3 - \frac{0.75}{2} \ 0)$. Polarized neutron data from the zone center and out to the zone boundary show that the acoustic phonon and magnon are purely structural and magnetic, respectively. At the crossing point the nature of the modes changes to a mixed state. Between the two zone centers, on the other side of the crossing, the lower branch is purely magnetic, while the higher branch is still mixed. The optical phonon is mixed from the zone boundary and out to $\mathbf{Q} = (1 \ 3 - \frac{1}{2} \ 0)$. The phonon-magnon coupling at $\hbar\omega = 15$ meV and $\mathbf{Q} = (1 \ 3 - \frac{1}{2} \ 0)$ may be the reason for the suppressed thermal conductivity at low temperatures. Theoretical calculations are needed to support this hypothesis.

Our measurement of mixed modes, *i.e.* excitations associated with multiferroic systems, is the first example of mixed modes at the zone boundary in YMnO₃.

10 Outlook

In this section future experiments are proposed. Experiments that are a continuation of the experiments presented in this thesis, as well as experiments that take completely different directions are considered.

10.1 Completion of present data

The following suggestions for measurements can all be made on EIGER or a similar thermal three-axis instrument. All the measurements are quick and would make it easier to draw conclusions about the data taken so far. Some of the measurements are merely aesthetic and would make the data more beautiful for publishing.

10.1.1 Color maps at $T = 40$ K and $T = 100$ K

First the $(\hbar\omega, \mathbf{Q})$ maps, Fig. 6.13, should be completed so the optical phonon is measured at $T = 100$ K to compare with the polarized data. More data would improve the statistics in the crossing at $T = 40$ K, and finally scans at $h = 1$ are needed. The $(\hbar\omega, \mathbf{Q})$ area below the acoustic phonon and beyond the zone boundary would be useful to get more statistics on, because the polarized data show that the higher background seems related to a persistent spin wave mode. Since one point at EIGER takes about 1 minute to measure, the data could be collected over a prolonged weekend.

If any beam time is left, data at $T = 40$ K at large \mathbf{Q} and low energy could be collected so the maps are the same size (aesthetic reasons) although the maps look as if there is only a flat background in that area.

10.1.2 Temperature dependence

At EIGER it would also be interesting to measure the temperature dependence and the \mathbf{Q} -dependence of the magnetic peak at $T = 100$ K at $\hbar\omega = 11$ meV at $h = 1$, Fig. 7.4 (Lower right)²⁵. The peak in the EIGER data at $T = 100$ K at $\hbar\omega = 8$ meV at $h = 0.75$, Fig. 7.5 (Lower left), which is not seen in the polarized data, would be interesting to measure again and determine the \mathbf{Q} -dependence. Measurements of the width in energy as a function of temperature of the transverse phonon and magnon branches at three different \mathbf{Q} -values: at $h = 0.4$ where they are completely distinguishable, at $h = 0.75$ right at the crossing and at $h = 1$ after the crossing.

Finally the temperature dependence of the optical phonon should be measured in order to test Pailhès *et al.*'s [56] prediction that the optical phonon spectrum should exhibit anomalies at T_N .

10.1.3 Other directions in reciprocal space

Until now only the transverse components of the mode has been measured apart from the two longitudinal scans at $k = 3.25$ and $k = 3.35$. It would be interesting to measure along other directions in reciprocal space *i.e.* investigating both the longitudinal and transverse components 60° away or only the longitudinal components 90° away from the current transverse position. A model for determining the influence of the persistent spin wave on the acoustic phonon might be the key in explaining the suppressed thermal conductivity in YMnO_3 .

²⁵Four days at the cold three-axis spectrometer PANDA at Forschungsreaktor München II in Germany has been provided for this exact experiment.

10.1.4 Line-widths with spin-echo

In January 2014 we performed an experiment at a thermal three-axis spectrometer called TRISP situated at Forschungsreaktor München II (FRM II) in Garching in Germany. The instrument uses neutron resonance spin echo, to determine energy widths of elementary excitations. For a broad range of momentum and energy transfers the widths can be determined with a μeV precision [52], which is one or two orders of magnitude better than normal three-axis experiments. The experiment probably failed because that the counting time was much longer than anticipated. A second attempt at measuring the energy width of the phonon with high resolution when crossing the magnetic ordering temperature, should be made in order to obtain a complete graph, as the one in Fig. 6.15 (Left) with more points, to see if the width really dips down at the ordering temperature.

10.2 Theoretical calculations

Calculations of the spin modes including the spin-lattice coupling and the phonon modes needs to be done and is currently being executed by theorists at the Niels Bohr Institute supervised by Brian M. Andersen. The coupled spin-phonon modes should hopefully explain the nature of the dispersions at the crossing and beyond the crossing point. We also anticipate that the result of these calculations can help explain why the dispersions are mixed when crossing the zone boundary, and possibly predict new features of the modes in *e.g.* the presence of an external magnetic field or applied pressure.

10.3 Pressure experiments

Due to the large magnetoelastic coupling in YMnO_3 applying pressure to the system, changing the lattice parameters and thereby changing the magnetic couplings in the system could be attempted.

Many groups have done pressure experiments on powder samples, but pressure experiments on single crystals are yet to be performed. Kozlenko *et al.* [39] [40] and Janoschek *et al.* [31] measured the angle between the magnetic moments and the hexagonal axes and the size of the magnetic moment as a function of pressure, see Fig. 10.1 a). The angle between the Mn-spins and the hexagonal axes is reduced from 90° at ambient pressure to around 38° at 6.7 GPa. The magnetic moment is suppressed at high pressure ($1.6 \mu_B$ at 6.7 GPa), Fig. 10.1 b). The higher pressure induces a larger frustration thereby making it more difficult for the system to order, which results in a smaller magnetic moment. Also the bond lengths between the two different Mn-O bonds, Mn-O3 and Mn-O4 change as a function of pressure (Fig. 10.1 c)), making them more alike at thereby closer to a perfect triangular network of spins. The perfect triangular network of spin creates a larger frustration with enhanced spin fluctuations and thereby a reduction in magnetic moment.

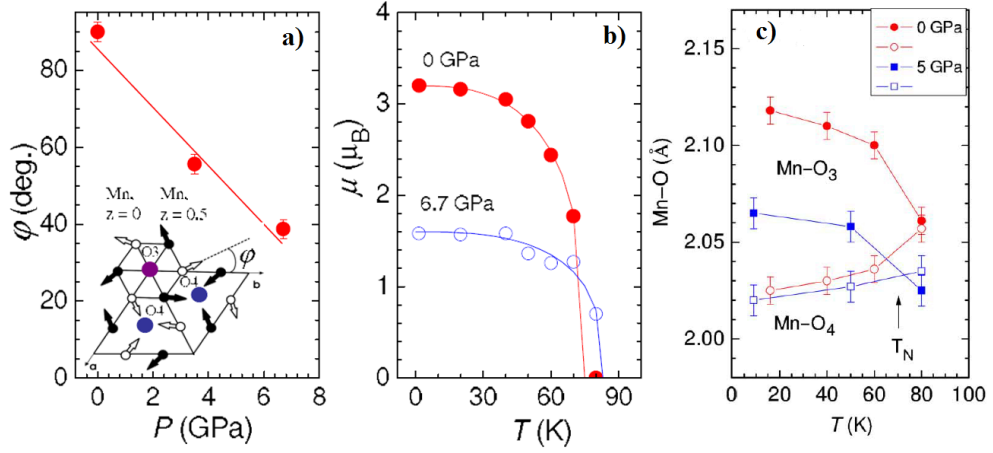


Figure 10.1: **a)** The change in the angle ϕ between the Mn-ions and the ab -axes as a function of pressure. At ambient pressure the angle is 90° . **b)** The total magnetic moment as a function of pressure. From [39]. **c)** The Mn-O3 and Mn-O4 bond lengths as a function of pressure. From [40].

Lancaster *et al.* [41] studied the ordering temperature as a function of pressure with Muon Spin Relaxation and found that the ordering temperature increases with increasing pressure, see Fig. 10.2. This is striking because the magnetic moment is suppressed when the pressure is applied. In addition, the exchange couplings change as a function of pressure, enhancing the ordering temperature. Competing interactions are present in YMnO_3 .

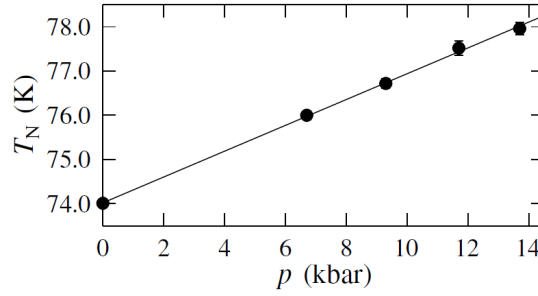


Figure 10.2: The ordering temperature T_N increases with increasing pressure p . From [41].

Finally Gao *et al.* [22] measured the unit cell volume and the compressibility along c and in the ab -plane with powder synchrotron X-ray diffraction, Fig. 10.3. The cell volume decreases with increasing pressure Fig. 10.3 a). The compressibility is largest in the ab and smallest along the hexagonal axis c Fig. 10.3 b).

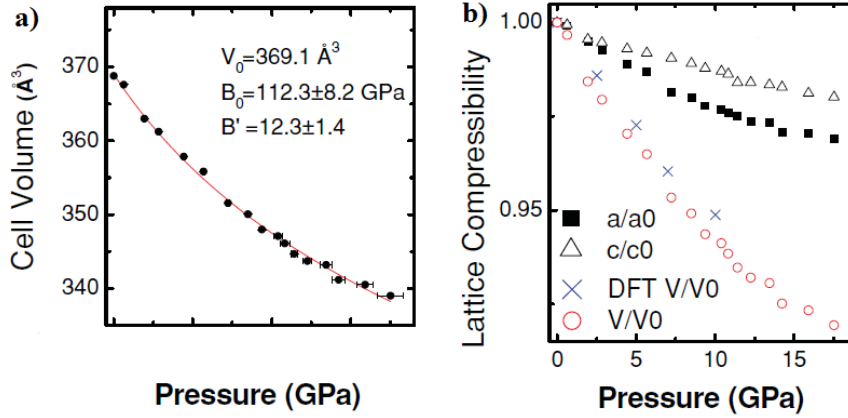


Figure 10.3: a) The unit cell volume as a function of pressure. The data is fitted to a Murnaghan equation of state: $V(P) = V_0[1 + B'_0(P/B_0)]^{-1/B'_0}$. b) The a/b and c lattice constants as a function of pressure. It is easiest to compress the ab -plane. From [22].

Elastic and inelastic neutron experiments under pressure would be interesting to perform. First one could follow the intensity of the (100) Bragg peak across the phase transition for different pressures reproducing, hopefully the experiments by Lancaster *et al.* at a cold three-axis experiment²⁶. Inelastic neutron scattering experiments could provide the pressure dependence of the spin wave dispersions. At a thermal experiment it would be interesting to see the development of the phonon-magnon crossing as a function of pressure.

10.4 Magnetic field experiments

Magnetic fields have been applied numerous times to the type II multiferroics, *i.e.* the multiferroics where the ferroelectricity is induced because of the magnetic order, and where the magnetoelectric coupling is large [42] [37] [28]. In the type II multiferroics, the magnetic fields can switch and control the polarization.

In h -YMnO₃ the direct magnetoelectric coupling is forbidden and therefore small. However, the magnetoelectric coupling that is present is mediated by the magnetoelastic coupling and magnetic fields can therefore enhance or change the magnetoelastic coupling and thereby the electrostatic properties. A field of $\mu_0 H = 5 \text{ T}$ is enough to change atomic positions and change the dielectric constant [73], so the fields needed for these magnetoelastic experiments can be reached at many facilities with standard magnets. The different measurements that could be done are

1. Field variations along the c -direction, enhancing the DM-interaction that is mediating the magnetoelectric effect.
2. Intensity of the (100) Bragg peak as a function of field.
3. Spin wave positions both at the zone center and zone boundary and both along $(h\ 0\ 0)$ and $(h\ h\ 0)$ at different temperatures and fields.
4. Field effect of avoided crossing at zone boundary and the temperature dependence.

²⁶In August 2014 a week of beam time has been provided for a pressure experiment at the cold three-axis instrument RITA II at Paul Scherrer Institut in Switzerland.

10.5 Electric field experiments

Electric field control of magnetic ordering has been obtained for type II multiferroics [66] [34] [5], but also in the type I multiferroic h -HoMnO₃ [85] and [47]. HoMnO₃ is closely related to YMnO₃ with the only difference being the magnetic rare earth ion Ho³⁺. Polarized neutron scattering experiments while applying an electric field of size $E = 25$ kV/cm show that the electric field couples to the antiferromagnetic domain walls, *i.e.* that electric field induced magnetization arises from uncompensated spins in antiferromagnetic domain walls [85].

Electric field experiments would be interesting to perform on YMnO₃ as well, but may be difficult to perform due to the large electric fields needed. The displacements of the atoms cannot be seen with experimentally accessible fields [91].

Even though the first neutron scattering experiments on YMnO₃ were performed in 1963 [2] many more are yet to be done.

References

- [1] AIKAWA, Y., KATSUFUJI, T., ARIMA, T., AND KATO, K. Effect of Mn trimerization on the magnetic and dielectric properties of hexagonal YMnO₃. *Phys. Rev. B* **71**, 18 (May 2005), 184418.
- [2] BERTAUT, E. F., AND MERCIER, M. Structure Magnétique de MnYO₃. *Phys. Lett.* **5**, 1 (1963), 27–29.
- [3] BIRGENEAU, R. J., SKALYO, J. J., AND SHIRANE, G. Critical Magnetic Scattering in K₂NiF₄. *Phys. Rev. B* **3**, 5 (1971), 1736–1749.
- [4] BLUNDELL, S. *Magnetism in Condensed Matter*. Oxford Master Series in Condensed Matter Physics, 2001.
- [5] BODENTHIN, Y., STAUB, U., GARCÍA-FERNÁNDEZ, M., JANOSCHEK, M., SCHLAPPA, J., GOLOVENCHITS, E., SANINA, V., AND LUSHNIKOV, S. Manipulating the Magnetic Structure with Electric Fields in Multiferroic ErMn₂O₅. *Phys. Rev. Lett.* **100**, 2 (Jan. 2008), 027201.
- [6] BREWTON-PARKER COLLEGE. http://www.bpc.edu/mathscience/chemistry/history_of_the_periodic_table.html.
- [7] BROWN, P. J., AND CHATTERJI, T. Neutron diffraction and polarimetric study of the magnetic and crystal structures of HoMnO₃ and YMnO₃. *J. Phys. Condens. Matter* **18**, 44 (Nov. 2006), 10085–10096.
- [8] BURTON, M. http://newt.phys.unsw.edu.au/~mgb/pg_mod3 lec5/node16.html.
- [9] CHATTERJI, T. *Neutron Scattering from Magnetic Materials*, 1 ed. Elsevier, 2006.
- [10] CHATTERJI, T. Neutron scattering investigations of multiferroic YMnO₃. *PRAMANA - J. Phys.* **71**, 4 (2008), 847–858.
- [11] CHATTERJI, T., DEMMEL, F., DHALENNE, G., DROUIN, M.-A., REVCOLEVSCHI, A., AND SURYANARAYANAN, R. Spin dynamics of the quasi-two-dimensional ferromagnetic bilayer manganite La_{1.2}Sr_{1.8}Mn₂O₇. *Phys. Rev. B* **72**, 1 (July 2005), 014439.
- [12] CHATTERJI, T., GHOSH, S., SINGH, A., REGNAULT, L. P., AND RHEINSTÄDTER, M. Spin dynamics of YMnO₃ studied via inelastic neutron scattering and the anisotropic Hubbard model. *Phys. Rev. B* **76**, 144406 (2007), 1–10.
- [13] CHEONG, S.-W., AND MOSTOVOY, M. Multiferroics: a magnetic twist for ferroelectricity. *Nat. Mater.* **6**, 1 (Jan. 2007), 13–20.
- [14] CHOI, Y., YI, H., LEE, S., HUANG, Q., KIRYUKHIN, V., AND CHEONG, S.-W. Ferroelectricity in an Ising Chain Magnet. *Phys. Rev. Lett.* **100**, 4 (Jan. 2008), 047601.
- [15] COLLINS, M. F. *Magnetic Critical Scattering*. Oxford University Press, 1989.
- [16] CRACKNELL, A. Selection rules for inelastic neutron scattering by magnetic crystals : I . The symmetries of magnetoelastic waves and the determination of selection rules for magnon-phonon interactions , with an application to antiferromagnetic FeF₂. *J. Phys. C Solid State Phys.* **6** (1973), 1054–1062.

REFERENCES

- [17] DEMMEL, F., AND CHATTERJI, T. Persistent spin waves above the Néel temperature in YMnO₃. *Phys. Rev. B* 76, 21 (Dec. 2007), 212402.
- [18] EERENSTEIN, W., MATHUR, N. D., AND SCOTT, J. F. Multiferroic and magnetoelectric materials. *Nature* 442, 7104 (Aug. 2006), 759–65.
- [19] EFREMOV, D. V., VAN DEN BRINK, J., AND KHOMSKII, D. I. Bond- versus site-centred ordering and possible ferroelectricity in manganites. *Nat. Mater.* 3, 12 (Dec. 2004), 853–6.
- [20] EL AMRANI, M., TA PHUOC, V., AMMAR, M., ZAGHRIQUI, M., AND GERVAIS, F. Structural modifications of disordered YMn_{1-x}In_xO₃ solid solutions evidenced by infrared and Raman spectroscopies. *Solid State Sci.* 14, 9 (Sept. 2012), 1315–1320.
- [21] FIEBIG, M., FROHLICH, D., KOHN, K., LEUTE, S., LOTTERMOSER, T., PAVLOV, V., AND PISAREV, R. Determination of the magnetic symmetry of hexagonal manganites by second harmonic generation. *Phys. Rev. Lett.* 84, 24 (June 2000), 5620–3.
- [22] GAO, P., CHEN, Z., TYSON, T. A., WU, T., AHN, K. H., LIU, Z., TAPPERO, R., KIM, S. B., AND CHEONG, S.-W. High-pressure structural stability of multiferroic hexagonal RMnO₃ (R=Y, Ho, Lu). *Phys. Rev. B* 83, 22 (June 2011), 224113.
- [23] GRIFFITHS, D. J. *Introduction to electrodynamics*, 3 ed. Pearson Prentice Hall, 1999.
- [24] GRIFFITHS, D. J. *Introduction to quantum mechanics Second edition David J. Griffiths Pearson Prentice Hall*, 2 ed. Pearson Prentice Hall, 2005.
- [25] HEDEGÅRD, P. *Statistisk fysik*. University of Copenhagen, 2008.
- [26] HILL, N. A. Why Are There so Few Magnetic Ferroelectrics? *J. Phys. Chem. B* 104 (2000), 6694–6709.
- [27] HOWARD, C. J., CAMPBELL, B. J., STOKES, H. T., CARPENTER, M. A., AND THOMSON, R. I. Crystal and magnetic structures of hexagonal YMnO₃. *Acta Crystallogr. B. Struct. Sci. Cryst. Eng. Mater.* 69, Pt 6 (Dec. 2013), 534–40.
- [28] HUR, N., PARK, S., SHARMA, P. A., AHN, J. S., GUHA, S., AND CHEONG, S.-W. Electric polarization reversal and memory in a multiferroic material induced by magnetic fields. *Nature* 429, May (2004), 392–395.
- [29] INSTITUT LAUE-LANGEVIN. <http://www.ill.eu/instruments-support/computing-for-science/cs-software/all-software/matlab-ill/spec1d/>.
- [30] JACOBSON, D., ARIF, M., HUFFMAN, P., AND SATIJA, R. A New Neutron Imaging Facility at BT-6 for the Non-Destructive Analysis of Working Fuel Cells. *NCNR Annu. Rep. 2003 1006* (2003), 8–9.
- [31] JANOSCHEK, M., ROESSLI, B., KELLER, L., GVASALIYA, S. N., CONDER, K., AND POM-JAKUSHINA, E. Reduction of the ordered magnetic moment in YMnO₃ with hydrostatic pressure. *J. Phys. Condens. Matter* 17, 42 (Oct. 2005), L425–L430.
- [32] KATSUFUJI, T., MASAKI, M., MACHIDA, A., MORITOMO, M., KATO, K., NISHIBORI, E., TAKATA, M., SAKATA, M., OHYAMA, K., KITAZAWA, K., AND TAKAGI, H. Crystal structure and magnetic properties of hexagonal RMnO₃ (R=Y, Lu, and Sc) and the effect of doping. *Phys. Rev. B* 66, 13 (Oct. 2002), 134434.

REFERENCES

- [33] KAWAMURA, H. Universality of phase transitions of frustrated antiferromagnets. *J. Phys. Condens. Matter* **10** (1998), 4707–4754.
- [34] KHAREL, P., SUDAKAR, C., DIXIT, A., HARRIS, A. B., NAIK, R., AND LAWES, G. Electric-field control of a magnetic phase transition in $\text{Ni}_3\text{V}_2\text{O}_8$. *EPL (Europhysics Lett.)* **86**, 1 (Apr. 2009), 17007.
- [35] KHOMSKII, D. Multiferroics: Different ways to combine magnetism and ferroelectricity. *J. Magn. Magn. Mater.* **306**, 1 (Nov. 2006), 1–8.
- [36] KHOMSKII, D. Classifying multiferroics: Mechanisms and effects. *Physics (College. Park. Md.)* **2** (Mar. 2009), 20.
- [37] KIMURA, T., GOTO, T., SHINTANI, H., ISHIZAKA, K., ARIMA, T., AND TOKURA, Y. Magnetic control of ferroelectric polarization. *Lett. to Nat.* **426**, 6962 (Nov. 2003), 55–8.
- [38] KITTEL, C. *Introduction to Solid State Physics*. John Wiley & Sons, Inc, 2005.
- [39] KOZLENKO, D., MIREBEAU, I., PARK, J.-G., GONCHARENKO, I., LEE, S., PARK, J., AND SAVENKO, B. High-pressure-induced spin-liquid phase of multiferroic YMnO_3 . *Phys. Rev. B* **78**, 5 (Aug. 2008), 054401.
- [40] KOZLENKO, D. P., KICHANOV, S. E., LUKIN, E. V., LEE, S., PARK, J.-G., AND SAVENKO, B. N. Spin fluctuations and structural modifications in frustrated multiferroics RMnO_3 ($\text{R}=\text{Y}, \text{Lu}$) at high pressure. *High Press. Res.* **30**, 2 (June 2010), 252–257.
- [41] LANCASTER, T., BLUNDELL, S., ANDREICA, D., JANOSCHEK, M., ROESSLI, B., GVASALIYA, S., CONDER, K., POMJAKUSHINA, E., BROOKS, M., BAKER, P., PRABHAKARAN, D., HAYES, W., AND PRATT, F. Magnetism in Geometrically Frustrated YMnO_3 under Hydrostatic Pressure Studied with Muon Spin Relaxation. *Phys. Rev. Lett.* **98**, 19 (May 2007), 197203.
- [42] LAWES, G., HARRIS, A., KIMURA, T., ROGADO, N., CAVA, R., AHARONY, A., ENTIN-WOHLMAN, O., YILDIRIM, T., KENZELMANN, M., BROHOLM, C., AND RAMIREZ, A. Magnetically Driven Ferroelectric Order in $\text{Ni}_3\text{V}_2\text{O}_8$. *Phys. Rev. Lett.* **95**, 8 (Aug. 2005), 087205.
- [43] LEE, S., PIROGOV, A., KANG, M., JANG, K.-H., YONEMURA, M., KAMIYAMA, T., CHEONG, S.-W., GOZZO, F., SHIN, N., KIMURA, H., NODA, Y., AND PARK, J.-G. Giant magneto-elastic coupling in multiferroic hexagonal manganites. *Nature* **451**, 7180 (Feb. 2008), 805–808.
- [44] LEE, S., PIROGOV, A., KANG, M., JANG, K.-H., YONEMURA, M., KAMIYAMA, T., CHEONG, S.-W., GOZZO, F., SHIN, N., KIMURA, H., NODA, Y., AND PARK, J.-G. Supplementary information. *Nature* **451**, Supplemenatry Information (2008), 1–10.
- [45] LEFMANN, K., WILDES, A., AND LEBECH, B. *Neutron Scattering: Theory, Instrumentation, and Simulation*. Lecture Notes, 2013.
- [46] LORENZ, B., WANG, Y.-Q., AND CHU, C.-W. Ferroelectricity in perovskite HoMnO_3 and YMnO_3 . *Phys. Rev. B* **76**, 10 (Sept. 2007), 104405.
- [47] LOTTERMOSER, T., LONKAI, T., AMANN, U., AND FIEBIG, M. Magnetic phase control by an electric field. *Lett. to Nat.* **193**, May (2004), 541–544.

REFERENCES

- [48] LUEKEN, H. A magnetoelectric effect in YMnO₃ and HoMnO₃. *Angew. Chem. Int. Ed. Engl.* **47**, 45 (Jan. 2008), 8562–4.
- [49] LYNN, J. W. Temperature dependence of the magnetic excitations in iron. *Phys. Rev. B* **11**, 7 (1975), 2624–2637.
- [50] MARTIN, L. W., CRANE, S. P., CHU, Y.-H., HOLCOMB, M. B., GAJEK, M., HUIJBEN, M., YANG, C.-H., BALKE, N., AND RAMESH, R. Multiferroics and magnetoelectrics: thin films and nanostructures. *J. Phys. Condens. Matter* **20**, 43 (Oct. 2008), 434220.
- [51] MASSA, W. *Crystal Structure Determination*. Springer, 2004.
- [52] MAX-PLANCK-GESELLSCHAFT. <http://www.mlz-garching.de/trisp>.
- [53] MOON, R. M., RISTE, T., AND KOEHLER, W. C. Polarization Analysis of Thermal-Neutron Scattering. *Phys. Rev.* **181**, 2 (1968), 920–931.
- [54] MUÑOZ, A., ALONSO, J. A., MARTÍNEZ-LOPE, M., CASÁIS, M., MARTÍNEZ, J., AND FERNÁNDEZ-DÍAZ, M. T. Magnetic structure of hexagonal RMnO₃ (R=Y, Sc): Thermal evolution from neutron powder diffraction data. *Phys. Rev. B* **62**, 14 (2000), 9498–9510.
- [55] NOBEL MEDIA AB. <http://www.nobelprize.org/nobel-prizes/physics/laureates/1994/>.
- [56] PAILHÈS, S., FABRÈGES, X., RÉGNAULT, L., PINSARD-GODART, L., MIREBEAU, I., MOUSSA, F., HENNION, M., AND PETIT, S. Hybrid Goldstone modes in multiferroic YMnO₃ studied by polarized inelastic neutron scattering. *Phys. Rev. B* **79**, 13 (Apr. 2009), 134409.
- [57] PARK, J., KONG, U., PIROGOV, A., CHOI, S. I., CHOI, Y. N., LEE, C., AND JO, W. Neutron-diffraction studies of YMnO₃. *Appl. Phys. A* **74** (2002), 796–798.
- [58] PARK, J., LEE, S., KANG, M., JANG, K.-H., LEE, C., STRELTSOV, S. V., MAZURENKO, V. V., VALENTYUK, M. V., MEDVEDEVA, J. E., KAMIYAMA, T., AND PARK, J.-G. Doping dependence of spin-lattice coupling and two-dimensional ordering in multiferroic hexagonal Y(1x)LuxMnO₃(0x1). *Phys. Rev. B* **82**, 5 (Aug. 2010), 054428.
- [59] PARK, J., PARK, J.-G., JEON, G., CHOI, H.-Y., LEE, C., JO, W., BEWLEY, R., MCEWEN, K., AND PERRING, T. Magnetic ordering and spin-liquid state of YMnO₃. *Phys. Rev. B* **68**, 10 (Sept. 2003), 104426.
- [60] PAUL SCHERRER INSTITUT. <http://www.psi.ch/sinq/eiger/description>.
- [61] PAUL SCHERRER INSTITUT. <http://www.psi.ch/sinq/ritaii/description>.
- [62] PETIT, S., MOUSSA, F., HENNION, M., PAILHÈS, S., PINSARD-GAUDART, L., AND IVANOV, A. Spin Phonon Coupling in Hexagonal Multiferroic YMnO₃. *Phys. Rev. Lett.* **99**, 26 (Dec. 2007), 266604.
- [63] PETIT, S., PAILHÈS, S., FABRÈGES, X., HENNION, M., MOUSSA, F., PINSARD, L., RÉGNAULT, L.-P., AND IVANOV, A. Spin lattice coupling in multiferroic hexagonal YMnO₃. *PRAMANA - J. Phys.* **71**, 4 (2008), 869–876.
- [64] PYATAKOV, A. P., AND ZVEZDIN, A. K. Magnetoelectric and multiferroic media. *Physics-Uspekh* **55**, 6 (June 2012), 557–581.

REFERENCES

- [65] ROESSLI, B., GVASALIYA, S. N., POMJAKUSHINA, E., AND CONDER, K. Spin fluctuations in the stacked-triangular antiferromagnet YMnO₃. *JETP Lett.* **81**, 6 (2005), 1–5.
- [66] ROVILLAIN, P., SOUSA, R. D., GALLAIS, Y., SACUTO, A., MÉASSON, M. A., COLSON, D., FORGET, A., BIBES, M., BARTHÉLÉMY, A., AND CAZAYOUS, M. Electric-field control of spin waves at room temperature in multiferroic BiFeO₃. *Nat. Mater.* **9**, December (2010), 975–979.
- [67] RUSHCHANSKII, K. Z., AND LEŽAIĆ, M. Ab Initio Phonon Structure of h-YMnO₃ in Low-Symmetry Ferroelectric Phase. *Ferroelectrics* **426**, 1 (Jan. 2012), 90–96.
- [68] SATO, T. J., LEE, S., KATSUFUJI, T., MASAKI, M., PARK, S., COPLEY, J., AND TAKAGI, H. Unconventional spin fluctuations in the hexagonal antiferromagnet YMnO₃. *Phys. Rev. B* **68**, 1 (July 2003), 014432.
- [69] SENFF, D., LINK, P., HRADIL, K., HIESS, A., REGNAULT, L. P., SIDIS, Y., ALIOUANE, N., ARGYRIOU, D. N., AND BRADEN, M. Magnetic Excitations in Multiferroic TbMnO₃: Evidence for a Hybridized Soft Mode. *Phys. Rev. Lett.* **98**, 13 (Mar. 2007), 137206.
- [70] SETYAWAN, W., AND CURTAROLO, S. High-throughput electronic band structure calculations: Challenges and tools. *Comput. Mater. Sci.* **49**, 2 (Aug. 2010), 299–312.
- [71] SHARMA, P., AHN, J., HUR, N., PARK, S., KIM, S. B., LEE, S., PARK, J.-G., GUHA, S., AND CHEONG, S.-W. Thermal Conductivity of Geometrically Frustrated, Ferroelectric YMnO₃: Extraordinary Spin-Phonon Interactions. *Phys. Rev. Lett.* **93**, 17 (Oct. 2004), 177202.
- [72] SHIRANE, G., SHAPIRO, S. M., AND TRANQUADA, J. M. *Neutron Scattering with a Triple-Axis Spectrometer*. Cambridge University Press, Cambridge, 2004.
- [73] SINGH, A. K., PATNAIK, S., KAUSHIK, S. D., AND SIRUGURI, V. Dominance of magnetoelastic coupling in multiferroic hexagonal YMnO₃. *Phys. Rev. B* **81**, 18 (May 2010), 184406.
- [74] SINGH, K., LEPETIT, M.-B., SIMON, C., BELLIDO, N., PAILHÈS, S., VARIGNON, J., AND DE MUER, A. Analysis of the multiferroicity in the hexagonal manganite YMnO₃. *J. Phys. Condens. Matter* **25**, 41 (Oct. 2013), 416002.
- [75] SKALYO, J. J., SHIRANE, G., FRIEDBERG, S. A., AND KOBAYASHI, H. Magnons in the Linear-Chain Antiferromagnet CsMnCl₂·2D₂O. *Phys. Rev. B* **2**, 11 (1970), 4632–4635.
- [76] SQUIRES, G. L. *Introduction to the Theory of Thermal Neutron Scattering*, 3rd ed. Cambridge University Press, 1978.
- [77] STEWART, J. R., DEEN, P. P., ANDERSEN, K. H., SCHÖBER, H., BARTHÉLÉMY, J.-F., HILLIER, J. M., MURANI, A. P., HAYES, T., AND LINDENAU, B. Disordered materials studied using neutron polarization analysis on the multi-detector spectrometer, D7. *J. Appl. Crystallogr.* **42**, 1 (Dec. 2008), 69–84.
- [78] STEWART, R. *Polarized Neutrons - Lecture Notes*. ISIS - Science and Technology Facilities Council, 2013.
- [79] TACHIBANA, M., YAMAZAKI, J., KAWAJI, H., AND ATAKE, T. Heat capacity and critical behavior of hexagonal YMnO₃. *Phys. Rev. B* **72**, 6 (Aug. 2005), 064434.

REFERENCES

- [80] TAO, X., LANDAU, D., SCHULTHESS, T., AND STOCKS, G. Spin Waves in Paramagnetic bcc Iron: Spin Dynamics Simulations. *Phys. Rev. Lett.* **95**, 8 (Aug. 2005), 087207.
- [81] TAUXE, L. *Essentials of Pelamagnetism*, third web ed. Scripps Institution of Oceanography, 2014.
- [82] THOMSON, R. I., CHATTERJI, T., HOWARD, C. J., PALSTRA, T. T. M., AND CARPENTER, M. A. Elastic anomalies associated with structural and magnetic phase transitions in single crystal hexagonal YMnO₃. *J. Phys. Condens. Matter* **26**, 4 (Jan. 2014), 045901.
- [83] TOMUTA, D. G., RAMAKRISHNAN, S., NIEUWENHUYTS, G. J., AND MYDOSH, J. A. The magnetic susceptibility, specific heat and dielectric constant of hexagonal YMnO₃, LuMnO₃ and ScMnO₃. *J. Phys. Condens. Matter* **13** (2001), 4543–4552.
- [84] TOULOUSE, C., LIU, J., GALLAIS, Y., MEASSON, M., SACUTO, A., CAZAYOUS, M., CHAIX, L., SIMONET, V., DE BRION, S., PINSARD-GODART, L., WILLAERT, F., BRUBACH, J. B., ROY, P., AND PETIT, S. Lattice and spin excitations in multiferroic h-YMnO₃. *Phys. Rev. B* **89**, 094415 (2014), 1–8.
- [85] UELAND, B. G., LYNN, J. W., LAVER, M., CHOI, Y. J., AND CHEONG, S.-W. Origin of Electric-Field-Induced Magnetization in Multiferroic HoMnO₃. *Phys. Rev. Lett.* **104**, 14 (Apr. 2010), 147204.
- [86] VALASEK, J. Piezo-Electric and Allied Phenomena in Rochelle Salt. *Phys. Rev.* **17**, 4 (1921), 475–481.
- [87] VAN AKEN, B. B., MEETSMA, A., AND PALSTRA, T. T. M. Hexagonal YMnO₃. *Acta Crystallogr. Sect. C Cryst. Struct. Commun.* **57**, 3 (Mar. 2001), 230–232.
- [88] VAN AKEN, B. B., PALSTRA, T. T. M., FILIPPETTI, A., AND SPALDIN, N. A. The origin of ferroelectricity in magnetoelectric YMnO₃. *Nat. Mater.* **3**, 3 (Mar. 2004), 164–70.
- [89] VAN AKEN, B. B., RIVERA, J.-P., SCHMID, H., AND FIEBIG, M. Observation of ferrotoroidic domains. *Nature* **449**, 7163 (Oct. 2007), 702–5.
- [90] VAN HOVE, L. Correlations in Space and Time and Born Approximation Scattering in Systems of Interacting Particles. *Phys. Rev.* **95**, 1 (1954), 249–262.
- [91] VARIGNON, J., PETIT, S., GELLÉ, A., AND LEPETIT, M. B. An ab initio study of magneto-electric coupling of YMnO₃. *J. Phys. Condens. Matter* **25**, 49 (Dec. 2013), 496004.
- [92] WANG, K., LIU, J.-M., AND REN, Z. Multiferroicity: the coupling between magnetic and polarization orders. *Adv. Phys.* **58**, 4 (July 2009), 321–448.
- [93] WEB OF SCIENCE. <http://apps.webofknowledge.com/>.
- [94] WIKIPEDIA. http://en.wikipedia.org/wiki/Brillouin_zone.
- [95] WILLIS, B. T. M., AND CARLILE, C. J. *Experimental Neutron Scattering*. Oxford University Press, 2009.
- [96] YAMANI, Z., TUN, Z., AND RYAN, D. H. Neutron scattering study of the classical antiferromagnet MnF₂: a perfect hands-on neutron scattering teaching course. *Can. J. Phys.* **88**, 10 (Oct. 2010), 771–797.

REFERENCES

- [97] ZHONG, C., JIANG, Q., ZHANG, H., AND JIANG, X. Effect of spin frustration and spin-orbit coupling on the ferroelectric polarization in multiferroic YMnO₃. *Appl. Phys. Lett.* *94*, 22 (2009), 224107.

A Space Group $P6_3/mmc$

$P6_3/mmc$

D_{6h}^4

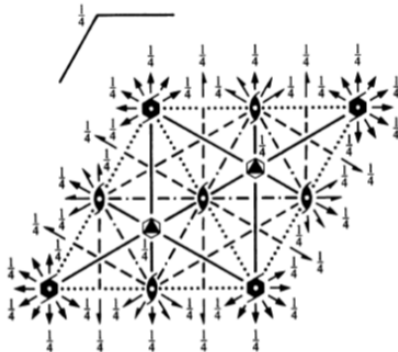
$6/mmm$

Hexagonal

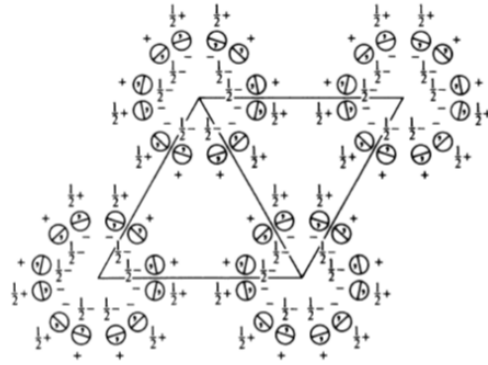
No. 194

$P 6_3/m 2/m 2/c$

Patterson symmetry $P6/mmm$



For $\bar{1}$ and $\bar{6}$ see $P6_3/m$ (No. 176)



Origin at centre ($\bar{3}m1$) at $\bar{3}2/mc$

Asymmetric unit $0 \leq x \leq \frac{2}{3}; 0 \leq y \leq \frac{2}{3}; 0 \leq z \leq \frac{1}{2}; x \leq 2y; y \leq \min(1-x, 2x)$
 Vertices $0, 0, 0$ $\frac{2}{3}, \frac{1}{3}, 0$ $\frac{1}{3}, \frac{2}{3}, 0$
 $0, 0, \frac{1}{2}$ $\frac{2}{3}, \frac{1}{3}, \frac{1}{2}$ $\frac{1}{3}, \frac{2}{3}, \frac{1}{2}$

Figure A.1: In the paraelectric (and paramagnetic) phase YMnO_3 belongs to the space group $P6_3mmc$ (No. 194).

Symmetry operations

(1) 1	(2) $3^+ 0,0,z$	(3) $3^- 0,0,z$
(4) $2(0,0,\frac{1}{2}) 0,0,z$	(5) $6^-(0,0,\frac{1}{2}) 0,0,z$	(6) $6^+(0,0,\frac{1}{2}) 0,0,z$
(7) $2 x,x,0$	(8) $2 x,0,0$	(9) $2 0,y,0$
(10) $2 x,\bar{x},\frac{1}{4}$	(11) $2 x,2x,\frac{1}{4}$	(12) $2 2x,x,\frac{1}{4}$
(13) $\bar{1} 0,0,0$	(14) $\bar{3}^+ 0,0,z; 0,0,0$	(15) $\bar{3}^- 0,0,z; 0,0,0$
(16) $m x,y,\frac{1}{4}$	(17) $\bar{6}^- 0,0,z; 0,0,\frac{1}{4}$	(18) $\bar{6}^+ 0,0,z; 0,0,\frac{1}{4}$
(19) $m x,\bar{x},z$	(20) $m x,2x,z$	(21) $m 2x,x,z$
(22) $c x,x,z$	(23) $c x,0,z$	(24) $c 0,y,z$

Maximal non-isomorphic subgroups

I	[2] $P\bar{6}2c$ (190)	1; 2; 3; 7; 8; 9; 16; 17; 18; 22; 23; 24
	[2] $P\bar{6}m2$ (187)	1; 2; 3; 10; 11; 12; 16; 17; 18; 19; 20; 21
	[2] $P6_3mc$ (186)	1; 2; 3; 4; 5; 6; 19; 20; 21; 22; 23; 24
	[2] $P6_322$ (182)	1; 2; 3; 4; 5; 6; 7; 8; 9; 10; 11; 12
	[2] $P6_3/m11$ ($P6_3/m$, 176)	1; 2; 3; 4; 5; 6; 13; 14; 15; 16; 17; 18
	[2] $P\bar{3}m1$ (164)	1; 2; 3; 7; 8; 9; 13; 14; 15; 19; 20; 21
	[2] $P\bar{3}1c$ (163)	1; 2; 3; 10; 11; 12; 13; 14; 15; 22; 23; 24
	{ [3] $Pmmc$ ($Cmcm$, 63)	1; 4; 7; 10; 13; 16; 19; 22
	{ [3] $Pmmc$ ($Cmcm$, 63)	1; 4; 8; 11; 13; 16; 20; 23
	{ [3] $Pmmc$ ($Cmcm$, 63)	1; 4; 9; 12; 13; 16; 21; 24

IIa none

IIb [3] $H6_3/mmc$ ($a' = 3a, b' = 3b$) ($P6_3/mcm$, 193)

Maximal isomorphic subgroups of lowest index

IIc [3] $P6_3/mmc$ ($c' = 3c$) (194); [4] $P6_3/mmc$ ($a' = 2a, b' = 2b$) (194)

Minimal non-isomorphic supergroups

I none

II [3] $H6_3/mmc$ ($P6_3/mcm$, 193); [2] $P6/mmm$ ($c' = \frac{1}{2}c$) (191)

Generators selected (1); $t(1,0,0)$; $t(0,1,0)$; $t(0,0,1)$; (2); (4); (7); (13)

Figure A.2: In the paraelectric (and paramagnetic) phase $YMnO_3$ belongs to the space group $P6_3mmc$ (No. 194).

Positions		Coordinates				Reflection conditions
Multiplicity, Wyckoff letter, Site symmetry						General:
24	<i>l</i> 1	(1) <i>x, y, z</i> (4) $\bar{x}, \bar{y}, z + \frac{1}{2}$ (7) <i>y, x, z</i> (10) $\bar{y}, \bar{x}, z + \frac{1}{2}$ (13) \bar{x}, \bar{y}, z (16) <i>x, y, z</i> + $\frac{1}{2}$ (19) \bar{y}, \bar{x}, z (22) <i>y, x, z</i> + $\frac{1}{2}$	(2) $\bar{y}, x - y, z$ (5) <i>y, x</i> + <i>y, z</i> + $\frac{1}{2}$ (8) <i>x - y, y, z</i> (11) $\bar{x} + y, y, z + \frac{1}{2}$ (14) <i>y, x</i> + <i>y, z</i> (17) $\bar{y}, x - y, z + \frac{1}{2}$ (20) $\bar{x} + y, y, z$ (23) <i>x - y, y, z</i> + $\frac{1}{2}$	(3) $\bar{x} + y, \bar{x}, z$ (6) <i>x - y, x, z</i> + $\frac{1}{2}$ (9) $\bar{x}, \bar{x} + y, z$ (12) <i>x, x - y, z</i> + $\frac{1}{2}$ (15) <i>x - y, x, z</i> (18) $\bar{x} + y, \bar{x}, z + \frac{1}{2}$ (21) <i>x, x - y, z</i> (24) $\bar{x}, \bar{x} + y, z + \frac{1}{2}$	<i>hh2hl</i> : <i>l</i> = 2 <i>n</i> <i>000l</i> : <i>l</i> = 2 <i>n</i>	
						Special: as above, plus
12	<i>k</i> . <i>m</i> .	<i>x, 2x, z</i> <i>2x, x, z</i> + $\frac{1}{2}$ \bar{x}, x, \bar{z}	$2\bar{x}, \bar{x}, z$ $\bar{x}, x, z + \frac{1}{2}$ $2\bar{x}, \bar{x}, z + \frac{1}{2}$	<i>x, x, z</i> <i>2x, x, z</i> <i>x, 2x, z</i> + $\frac{1}{2}$	$\bar{x}, 2\bar{x}, z + \frac{1}{2}$ $\bar{x}, 2\bar{x}, z$ <i>x, x, z</i> + $\frac{1}{2}$	no extra conditions
12	<i>j</i> <i>m</i> . .	<i>x, y, $\frac{1}{4}$</i> <i>y, x, $\frac{3}{4}$</i>	$\bar{y}, x - y, \frac{1}{4}$ <i>x - y, y, $\frac{3}{4}$</i>	$\bar{x} + y, \bar{x}, \frac{1}{4}$ $\bar{x}, \bar{x} + y, \frac{3}{4}$	$\bar{x}, \bar{y}, \frac{3}{4}$ <i>y, x</i> + <i>y, $\frac{3}{4}$</i> $\bar{x} + y, y, \frac{1}{4}$	<i>x - y, x, $\frac{3}{4}$</i> <i>x, x - y, $\frac{1}{4}$</i> no extra conditions
12	<i>i</i> . 2 .	<i>x, 0, 0</i> $\bar{x}, 0, 0$	<i>0, x, 0</i> $0, \bar{x}, 0$	$\bar{x}, \bar{x}, 0$ <i>x, x, 0</i>	$\bar{x}, 0, \frac{1}{2}$ <i>x, 0, $\frac{1}{2}$</i> $0, \bar{x}, \frac{1}{2}$ $\bar{x}, \bar{x}, \frac{1}{2}$	<i>hkil</i> : <i>l</i> = 2 <i>n</i>
6	<i>h</i> <i>mm</i> 2	<i>x, 2x, $\frac{1}{4}$</i>	$2\bar{x}, \bar{x}, \frac{1}{4}$	<i>x, x, $\frac{1}{4}$</i>	$\bar{x}, 2\bar{x}, \frac{3}{4}$ <i>2x, x, $\frac{3}{4}$</i> $\bar{x}, x, \frac{3}{4}$	no extra conditions
6	<i>g</i> . 2/ <i>m</i> .	$\frac{1}{2}, 0, 0$	$0, \frac{1}{2}, 0$	$\frac{1}{2}, \frac{1}{2}, 0$	$\frac{1}{2}, 0, \frac{1}{2}$ $0, \frac{1}{2}, \frac{1}{2}$ $\frac{1}{2}, \frac{1}{2}, \frac{1}{2}$	<i>hkil</i> : <i>l</i> = 2 <i>n</i>
4	<i>f</i> 3 <i>m</i> .	$\frac{1}{3}, \frac{2}{3}, z$	$\frac{2}{3}, \frac{1}{3}, z + \frac{1}{2}$	$\frac{2}{3}, \frac{1}{3}, \bar{z}$	$\frac{1}{3}, \frac{2}{3}, \bar{z} + \frac{1}{2}$	<i>hkil</i> : <i>l</i> = 2 <i>n</i> or <i>h - k</i> = 3 <i>n</i> + 1 or <i>h - k</i> = 3 <i>n</i> + 2
4	<i>e</i> 3 <i>m</i> .	<i>0, 0, z</i>	<i>0, 0, z</i> + $\frac{1}{2}$	<i>0, 0, z</i>	<i>0, 0, z</i> + $\frac{1}{2}$	<i>hkil</i> : <i>l</i> = 2 <i>n</i>
2	<i>d</i> $\bar{6}$ <i>m</i> 2	$\frac{1}{3}, \frac{2}{3}, \frac{1}{4}$	$\frac{2}{3}, \frac{1}{3}, \frac{1}{4}$	$\left. \begin{array}{l} \frac{2}{3}, \frac{1}{3}, \frac{1}{4} \\ \frac{2}{3}, \frac{1}{3}, \frac{3}{4} \end{array} \right\}$	<i>hkil</i> : <i>l</i> = 2 <i>n</i> or <i>h - k</i> = 3 <i>n</i> + 1 or <i>h - k</i> = 3 <i>n</i> + 2	
2	<i>c</i> $\bar{6}$ <i>m</i> 2	$\frac{1}{3}, \frac{2}{3}, \frac{1}{4}$	$\frac{2}{3}, \frac{1}{3}, \frac{3}{4}$			
2	<i>b</i> $\bar{6}$ <i>m</i> 2	<i>0, 0, $\frac{1}{4}$</i>	<i>0, 0, $\frac{3}{4}$</i>	<i>hkil</i> : <i>l</i> = 2 <i>n</i>		
2	<i>a</i> $\bar{3}$ <i>m</i> .	<i>0, 0, 0</i>	<i>0, 0, $\frac{1}{2}$</i>	<i>hkil</i> : <i>l</i> = 2 <i>n</i>		
Symmetry of special projections						
Along [001] <i>p6mm</i> a' = a b' = b Origin at 0, 0, <i>z</i>		Along [100] <i>p2gm</i> a' = $\frac{1}{2}(\mathbf{a} + 2\mathbf{b})$ b' = c Origin at <i>x, 0, 0</i>		Along [210] <i>p2mm</i> a' = $\frac{1}{2}\mathbf{b}$ b' = $\frac{1}{2}\mathbf{c}$ Origin at <i>x, $\frac{1}{2}x, 0$</i>		

Figure A.3: In the paraelectric (and paramagnetic) phase YMnO_3 belongs to the space group $P6_3mmc$ (No. 194).

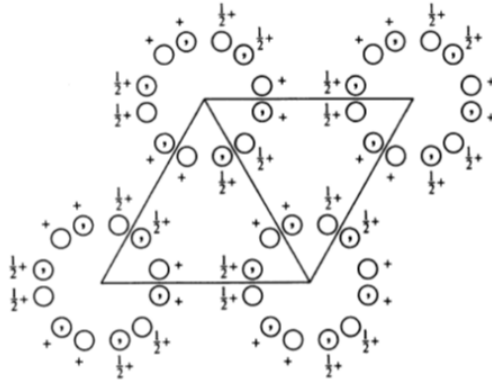
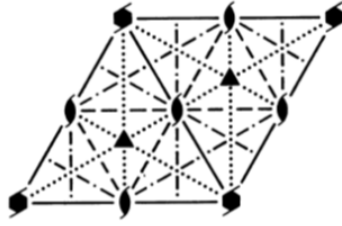
B Space Group $P6_3cm$

 $P6_3cm$
 C_{6v}^3
 $6mm$

Hexagonal

No. 185

 $P6_3cm$

 Patterson symmetry $P6/mmm$

 Origin on $31m$ on 6_3cm

 Asymmetric unit $0 \leq x \leq \frac{2}{3}; 0 \leq y \leq \frac{1}{3}; 0 \leq z \leq \frac{1}{2}; x \leq (1+y)/2; y \leq \min(1-x, x)$

 Vertices $0,0,0 \quad \frac{1}{2},0,0 \quad \frac{2}{3},\frac{1}{3},0 \quad \frac{1}{2},\frac{1}{2},0$
 $0,0,\frac{1}{2} \quad \frac{1}{2},0,\frac{1}{2} \quad \frac{2}{3},\frac{1}{3},\frac{1}{2} \quad \frac{1}{2},\frac{1}{2},\frac{1}{2}$

Symmetry operations

- | | | |
|--------------------------------|----------------------------------|----------------------------------|
| (1) 1 | (2) $3^+ 0,0,z$ | (3) $3^- 0,0,z$ |
| (4) $2(0,0,\frac{1}{2}) 0,0,z$ | (5) $6^-(0,0,\frac{1}{2}) 0,0,z$ | (6) $6^+(0,0,\frac{1}{2}) 0,0,z$ |
| (7) $c x,\bar{x},z$ | (8) $c x,2x,z$ | (9) $c 2x,x,z$ |
| (10) $m x,x,z$ | (11) $m x,0,z$ | (12) $m 0,y,z$ |

 Generators selected (1); $t(1,0,0); t(0,1,0); t(0,0,1); (2); (4); (7)$

Figure B.1: In the ferroelectric (and paramagnetic) phase YMnO_3 belongs to the $P6_3cm$ space group (No. 185).

Positions				Coordinates				Reflection conditions					
Multiplicity, Wyckoff letter, Site symmetry								General:					
12	d	1	(1) x, y, z (4) $\bar{x}, \bar{y}, z + \frac{1}{2}$ (7) $\bar{y}, \bar{x}, z + \frac{1}{2}$ (10) y, x, z	(2) $\bar{y}, x - y, z$ (5) $y, \bar{x} + y, z + \frac{1}{2}$ (8) $\bar{x} + y, y, z + \frac{1}{2}$ (11) $x - y, \bar{y}, z$	(3) $\bar{x} + y, \bar{x}, z$ (6) $x - y, x, z + \frac{1}{2}$ (9) $x, x - y, z + \frac{1}{2}$ (12) $\bar{x}, \bar{x} + y, z$	$h\bar{h}0l : l = 2n$ $000l : l = 2n$							
										Special: as above, plus			
6	c	. . m	$x, 0, z$	$0, x, z$	\bar{x}, \bar{x}, z	$\bar{x}, 0, z + \frac{1}{2}$	$0, \bar{x}, z + \frac{1}{2}$	$x, x, z + \frac{1}{2}$	no extra conditions				
4	b	3 . .	$\frac{1}{3}, \frac{2}{3}, z$	$\frac{2}{3}, \frac{1}{3}, z + \frac{1}{2}$	$\frac{1}{3}, \frac{2}{3}, z + \frac{1}{2}$	$\frac{2}{3}, \frac{1}{3}, z$	$hkil : l = 2n$						
2	a	3 . m	$0, 0, z$	$0, 0, z + \frac{1}{2}$	$hkil : l = 2n$								
Symmetry of special projections													
Along $[001]$ $p6mm$ $\mathbf{a}' = \mathbf{a} \quad \mathbf{b}' = \mathbf{b}$ Origin at $0, 0, z$				Along $[100]$ $p1m1$ $\mathbf{a}' = \frac{1}{2}(\mathbf{a} + 2\mathbf{b}) \quad \mathbf{b}' = \frac{1}{2}\mathbf{c}$ Origin at $x, 0, 0$				Along $[210]$ $p1g1$ $\mathbf{a}' = \frac{1}{2}\mathbf{b} \quad \mathbf{b}' = \mathbf{c}$ Origin at $x, \frac{1}{2}x, 0$					
Maximal non-isomorphic subgroups													
I	[2] $P6_311$ ($P6_3$, 173)			1; 2; 3; 4; 5; 6									
	[2] $P3c1$ (158)			1; 2; 3; 7; 8; 9									
	[2] $P31m$ (157)			1; 2; 3; 10; 11; 12									
	{	[3] $P2_1cm$ ($Cmc2_1$, 36)		1; 4; 7; 10									
[3] $P2_1cm$ ($Cmc2_1$, 36)		1; 4; 8; 11											
[3] $P2_1cm$ ($Cmc2_1$, 36)		1; 4; 9; 12											
IIa	none												
IIb	[3] $H6_3cm$ ($\mathbf{a}' = 3\mathbf{a}, \mathbf{b}' = 3\mathbf{b}$) ($P6_3mc$, 186)												
Maximal isomorphic subgroups of lowest index													
IIc	[3] $P6_3cm$ ($\mathbf{c}' = 3\mathbf{c}$) (185); [4] $P6_3cm$ ($\mathbf{a}' = 2\mathbf{a}, \mathbf{b}' = 2\mathbf{b}$) (185)												
Minimal non-isomorphic supergroups													
I	[2] $P6_3/mcm$ (193)												
II	[3] $H6_3cm$ ($P6_3mc$, 186); [2] $P6mm$ ($\mathbf{c}' = \frac{1}{2}\mathbf{c}$) (183)												

Figure B.2: In the ferroelectric (and paramagnetic) phase YMnO_3 belongs to the $P6_3cm$ space group (No. 185).

C Space Group $P6_3$

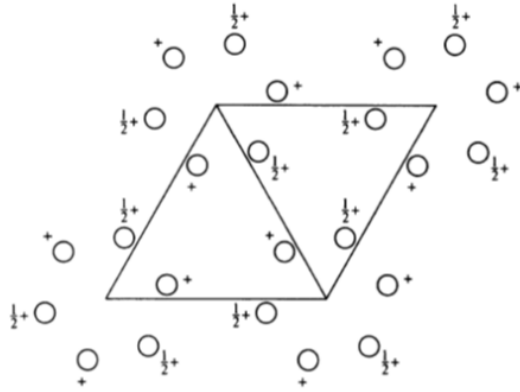
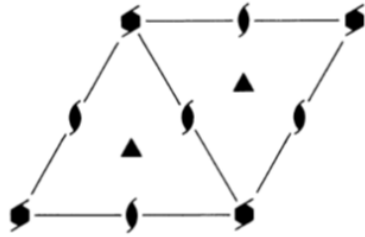
 $P6_3$

No. 173

 C_6^6
 $P6_3$

6

Hexagonal

 Patterson symmetry $P6/m$

 Origin on 3 on 6₃

 Asymmetric unit $0 \leq x \leq \frac{1}{3}; 0 \leq y \leq \frac{2}{3}; 0 \leq z \leq \frac{1}{2}; x \leq (1+y)/2; y \leq \min(1-x, (1+x)/2)$

 Vertices $0, 0, 0 \quad \frac{1}{2}, 0, 0 \quad \frac{2}{3}, \frac{1}{3}, 0 \quad \frac{1}{3}, \frac{2}{3}, 0 \quad 0, \frac{1}{2}, 0$
 $0, 0, \frac{1}{2} \quad \frac{1}{2}, 0, \frac{1}{2} \quad \frac{2}{3}, \frac{1}{3}, \frac{1}{2} \quad \frac{1}{3}, \frac{2}{3}, \frac{1}{2} \quad 0, \frac{1}{2}, \frac{1}{2}$

Symmetry operations

 (1) 1 (2) $3^+ 0, 0, z$ (3) $3^- 0, 0, z$
 (4) $2(0, 0, \frac{1}{2}) 0, 0, z$ (5) $6^-(0, 0, \frac{1}{2}) 0, 0, z$ (6) $6^+(0, 0, \frac{1}{2}) 0, 0, z$

 Generators selected (1); $t(1, 0, 0); t(0, 1, 0); t(0, 0, 1); (2); (4)$

Figure C.1: In the antiferromagnetic (and ferroelectric) phase YMnO_3 belongs to the $P6_3'$ magnetic space group (No. 173).

Positions			Coordinates	Reflection conditions		
Multiplicity, Wyckoff letter, Site symmetry						
6	<i>c</i>	1	(1) x, y, z (4) $\bar{x}, \bar{y}, z + \frac{1}{2}$	(2) $\bar{y}, x - y, z$ (5) $y, \bar{x} + y, z + \frac{1}{2}$	(3) $\bar{x} + y, \bar{x}, z$ (6) $x - y, x, z + \frac{1}{2}$	General: $000l : l = 2n$ Special: as above, plus $hkil : l = 2n$ or $h - k = 3n + 1$ or $h - k = 3n + 2$ $hkil : l = 2n$
2	<i>b</i>	3	$\frac{1}{3}, \frac{2}{3}, z$	$\frac{2}{3}, \frac{1}{3}, z + \frac{1}{2}$		
2	<i>a</i>	3	$0, 0, z$	$0, 0, z + \frac{1}{2}$		
Symmetry of special projections						
Along $[001]$ $p6$ $\mathbf{a}' = \mathbf{a}$ $\mathbf{b}' = \mathbf{b}$ Origin at $0, 0, z$			Along $[100]$ $p1g1$ $\mathbf{a}' = \frac{1}{2}(\mathbf{a} + 2\mathbf{b})$ $\mathbf{b}' = \mathbf{c}$ Origin at $x, 0, 0$			Along $[210]$ $p1g1$ $\mathbf{a}' = \frac{1}{2}\mathbf{b}$ $\mathbf{b}' = \mathbf{c}$ Origin at $x, \frac{1}{2}x, 0$
Maximal non-isomorphic subgroups						
I	$[2] P3 (143)$ 1; 2; 3 $[3] P2_1 (4)$ 1; 4					
IIa	none					
IIb	$[3] P6_3 (c' = 3c) (170); [3] P6_1 (c' = 3c) (169)$					
Maximal isomorphic subgroups of lowest index						
IIc	$[3] P6_3 (c' = 3c) (173); [3] H6_3 (a' = 3a, b' = 3b) (P6_3, 173)$					

Figure C.2: In the antiferromagnetic (and ferroelectric) phase YMnO_3 belongs to the $P6_3'$ magnetic space group (No. 173).

E Conversion Tables

Quantity	Relationship	Value at $E = 10\text{meV}$
Energy	$E[\text{meV}] = 2.072k^2[\text{\AA}^{-1}]$	10 meV
Wavelength	$\lambda = 9.044/\sqrt{E[\text{meV}]}$	2.86 \AA
Wave vector	$k[\text{\AA}^{-1}] = 2\pi/\lambda[\text{\AA}]$	2.20 \AA ⁻¹
Frequency	$\nu[\text{THz}] = 0.24818E[\text{meV}]$	2.418 THz
Wavenumber	$\nu[\text{cm}^{-1}] = \nu[\text{Hz}]/(2.998 \cdot 10^{10}\text{cm/s})$	80.65 cm ⁻¹
Velocity	$v[\text{km/s}] = 0.6302k[\text{\AA}^{-1}]$	1.38 km/s
Temperature	$T[\text{K}] = 11.605E[\text{meV}]$	116.05 K

Table E.1: The relationships between wavelength, frequency, velocity are important when doing neutron scattering.

Quantity	Relationship	Relationship
Pressure	1 Pa = 10 ⁻⁵ bar	1 bar = 10 ⁵ Pa
Length	1 inch = 2.54 cm	1 cm = 0.394 inches
Magnetic field (B-field)	1 gauss = 0.0001 T	1 T = 10.000 gauss
Magnetic field (H-field)	1 oersted = 79.6 A/m	1 A/m = 0.0126 oersted

Table E.2: Other relationships that are useful, when planning and executing experiments.

G Plots

G.1 Diffuse scattering around $(0\bar{1}0)$

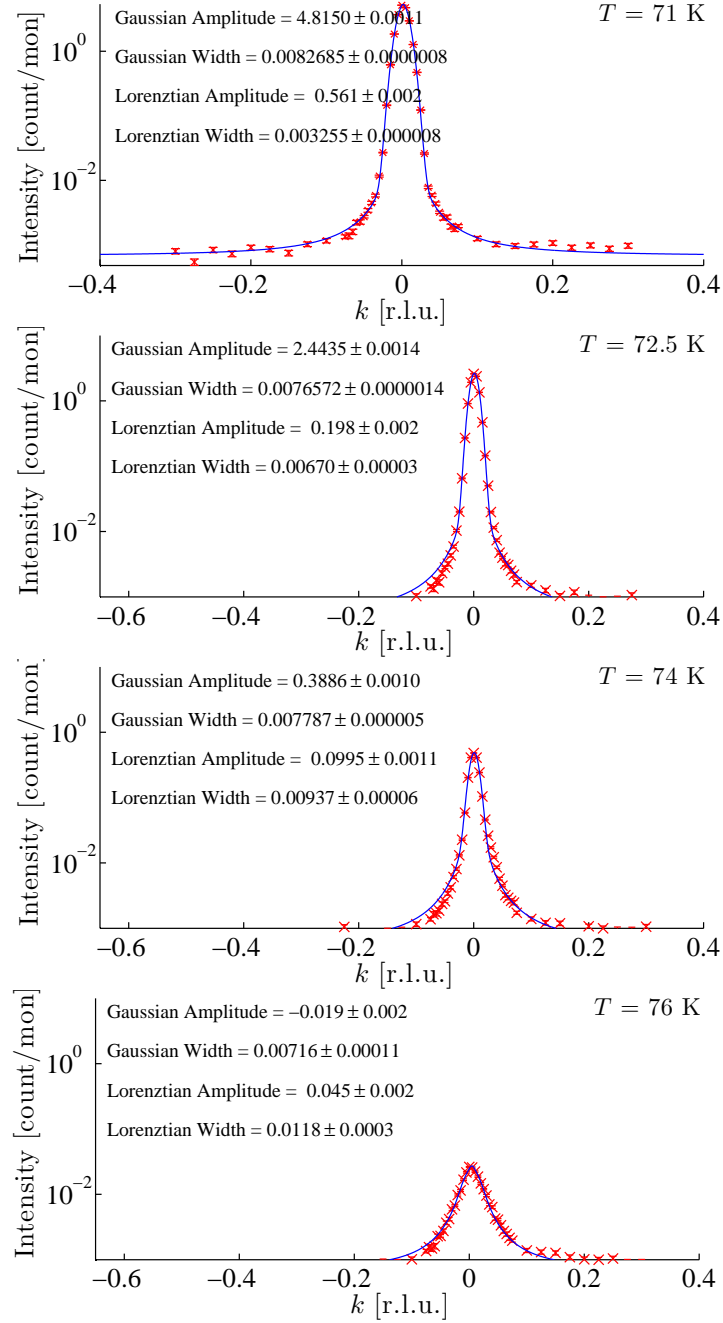


Figure G.1: Diffuse scattering around $(0\bar{1}0)$ at $T = 71$ K, $T = 72.5$ K, $T = 74$ K and $T = 76$ K.

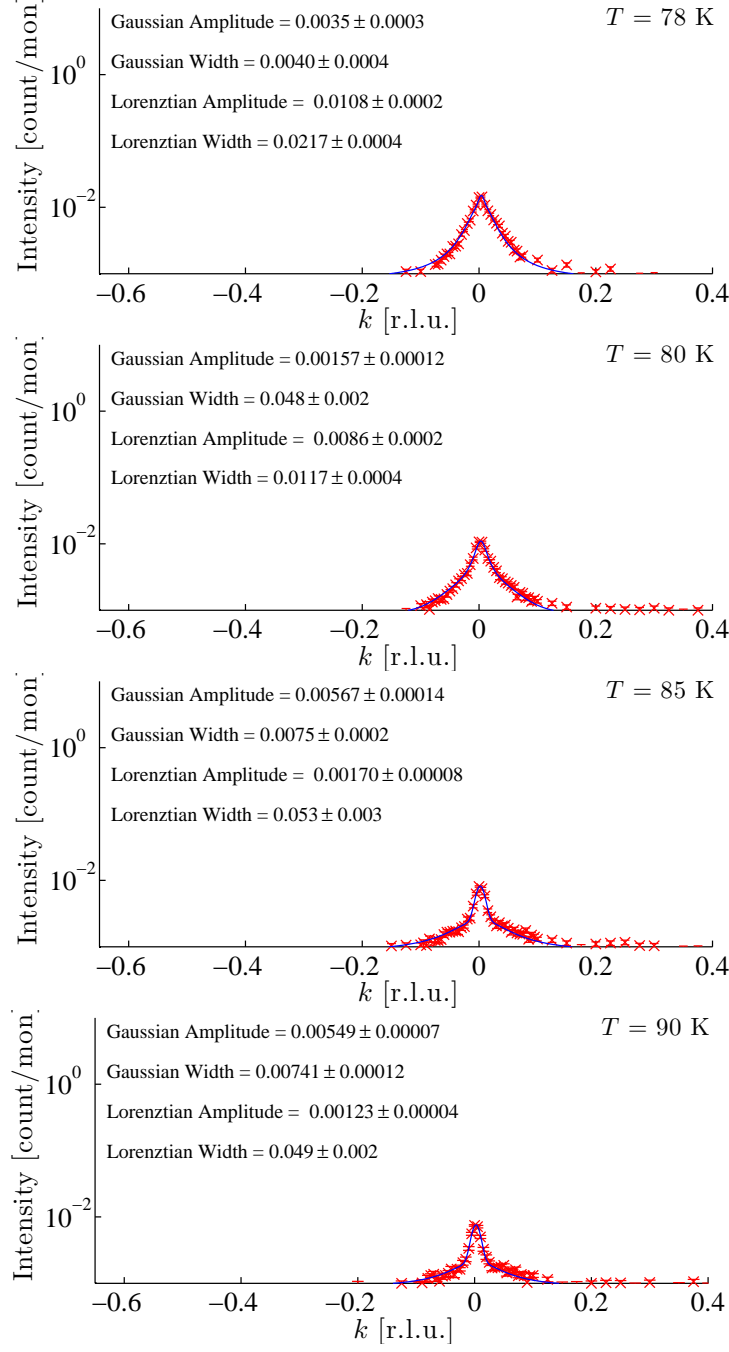


Figure G.2: Diffuse scattering around $(0\bar{1}0)$ at $T = 78$ K, $T = 80$ K, $T = 85$ K and $T = 90$ K.

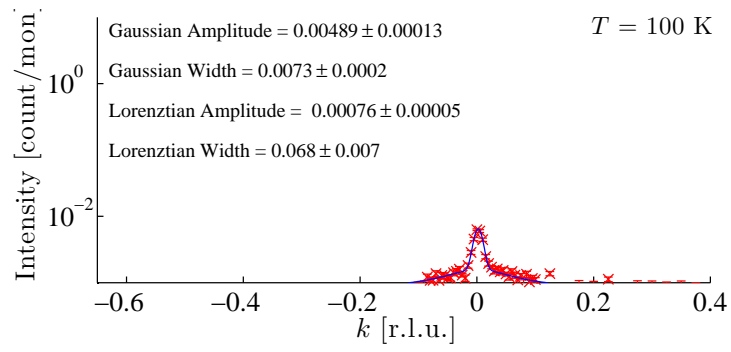


Figure G.3: Diffuse scattering around $(0\bar{1}0)$ at $T = 100 \text{ K}$.

G.2 Energy scans around the (100) magnon dispersions

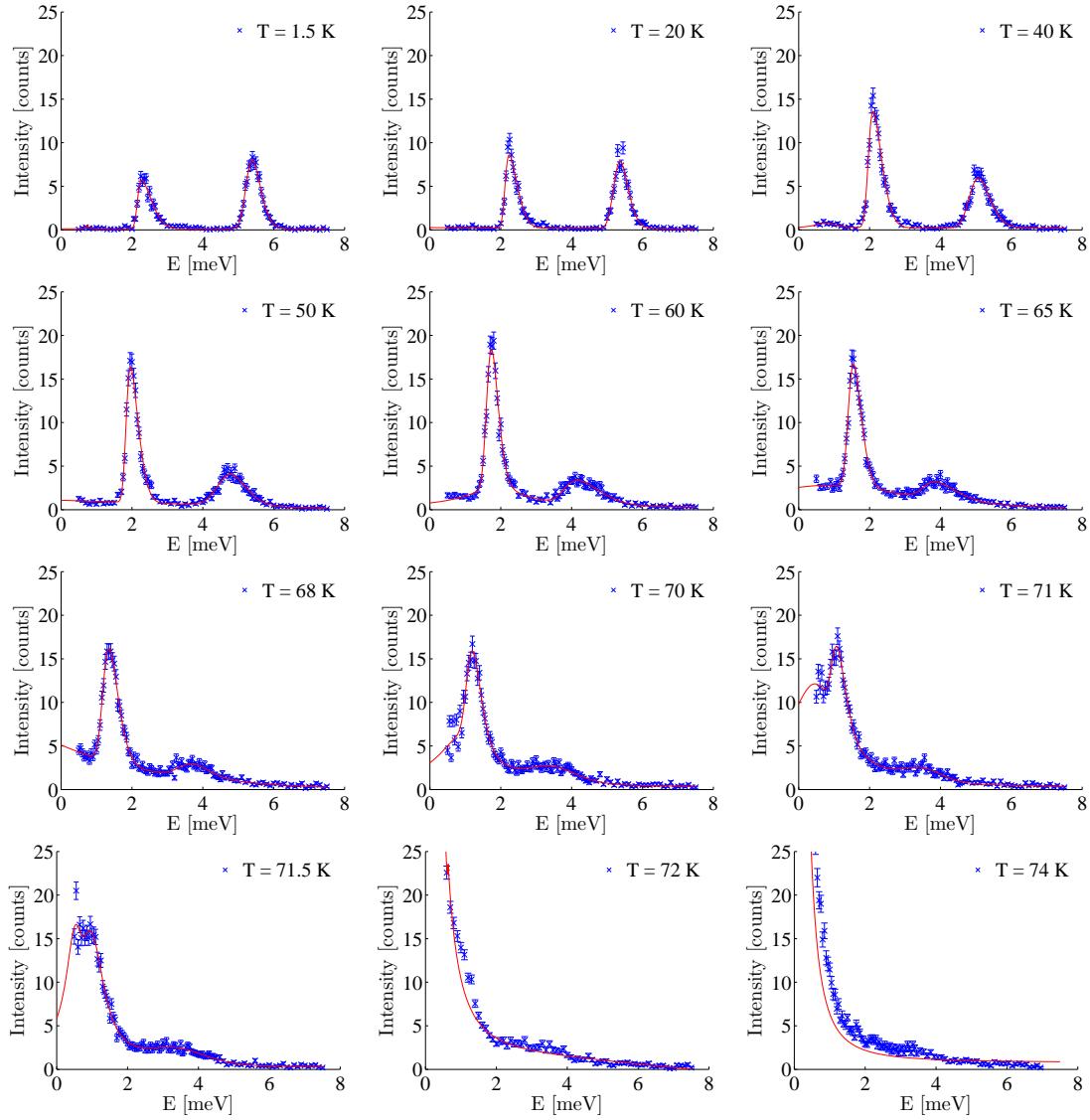


Figure G.4: Energy scan at (100) for different temperatures. Fitting parameters from the four scans: 71 K, 71.5 K, 72 K and 74 K, were not included in rest of the data analysis due to the bad fits.

G.3 Energy scans around (300) at $T = 40$ K and $T = 100$ K

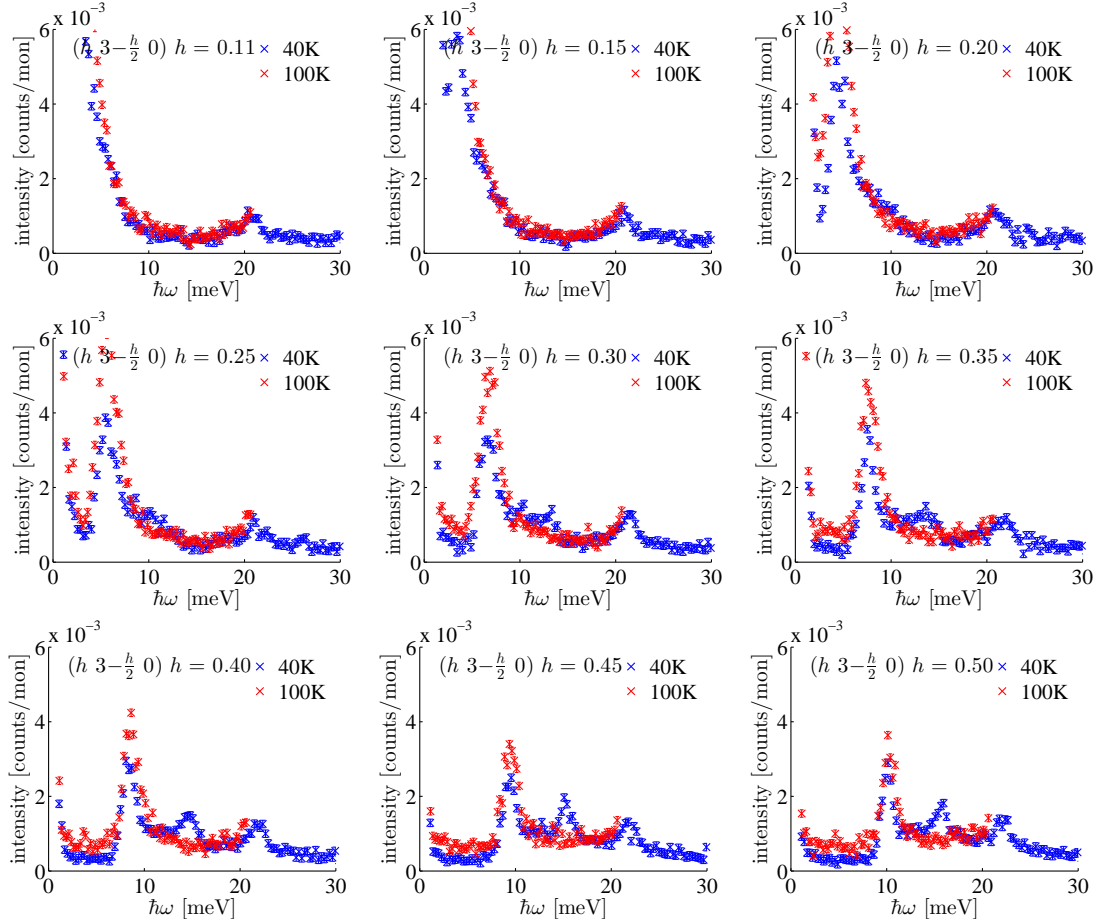


Figure G.5: Energy scans of the transverse phonon and magnon at (300).

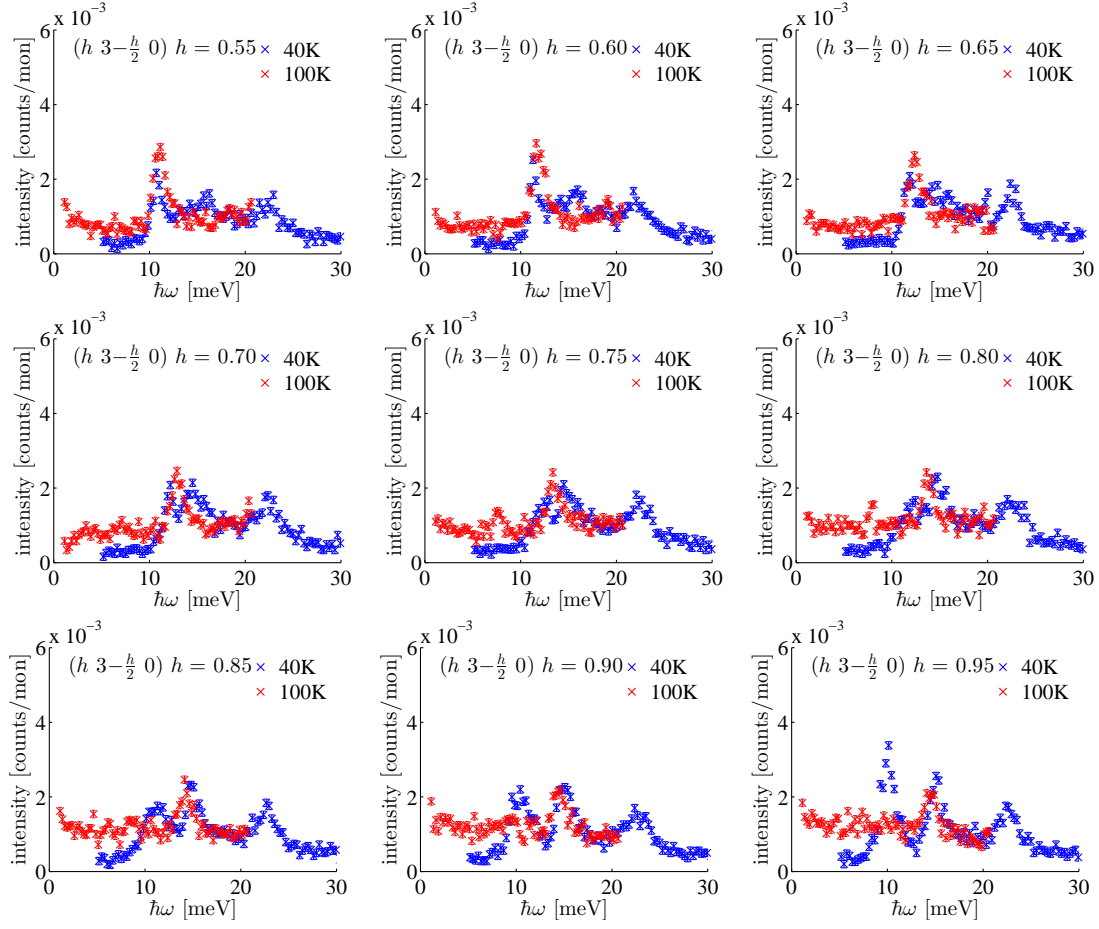


Figure G.6: Energy scans of the transverse phonon and magnon at (300).

G.4 Q-scans of transverse phonon around (300)

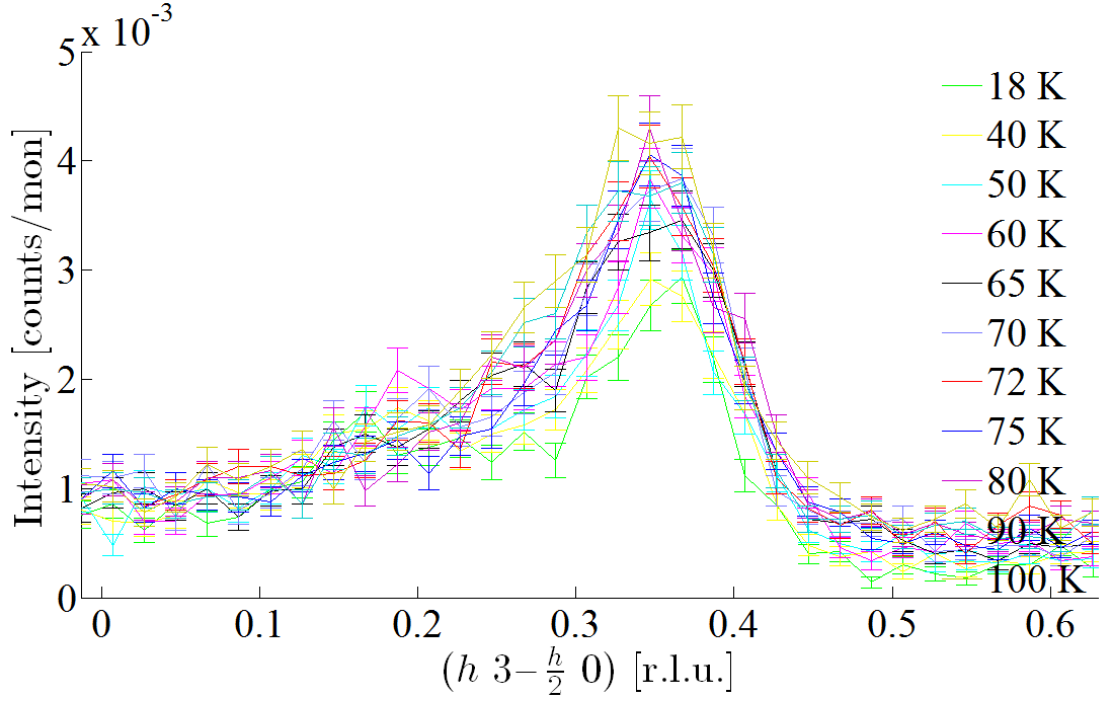


Figure G.7: Q-scans of transverse phonon at different temperatures at (300). The energy transfer was $\hbar\omega = 7.9 \text{ meV}$ for all temperatures.

G.5 Longitudinal phonon measured at $k = 3.25$ and $k = 3.35$

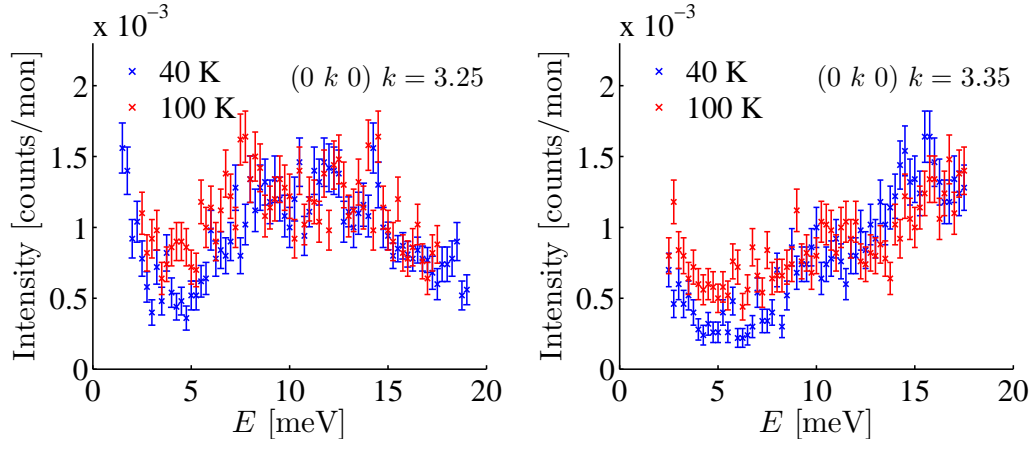


Figure G.8: Longitudinal energy scans at $k = 3.25$ and $k = 3.35$.

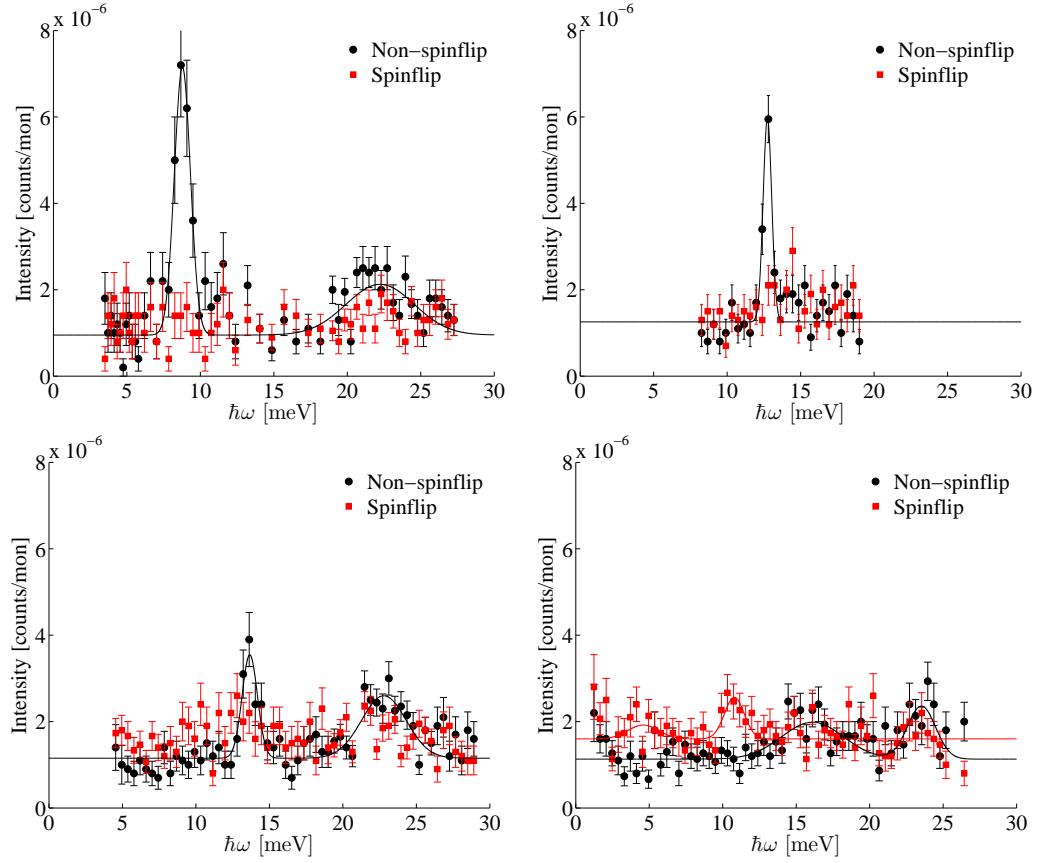
G.6 Measurements above T_N 

Figure G.9: The $T = 100$ K data taken at C5. Red is the horizontal field spinflip channel (magnetic) and black is the horizontal field non-spinflip channel (nuclear). **Upper left:** Energy scan at $h = -0.4$ right between the zone center and the zone boundary. **Upper right:** Energy scan at $h = -0.67$ right at the zone boundary. **Bottom left:** Energy scan at $h = -0.75$ at the crossing. **Bottom right:** Energy scan at $h = -1$ right in between the (030) and the (220) zone.

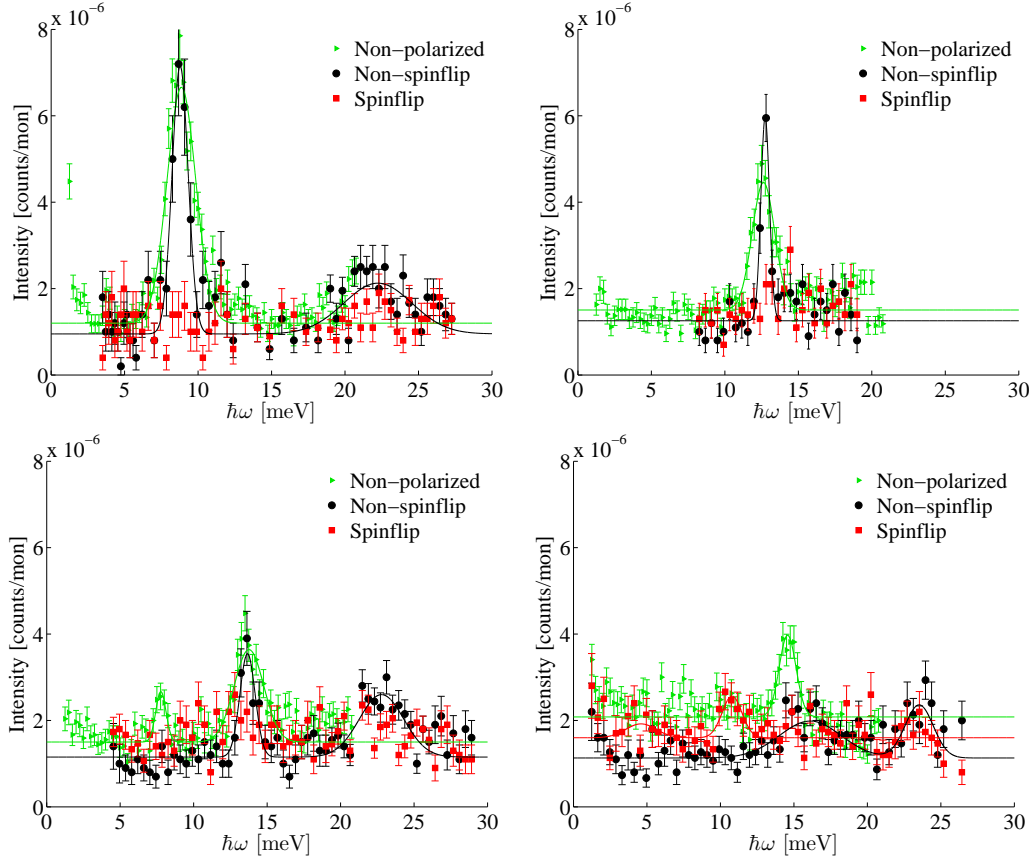


Figure G.10: The $T = 100$ K data taken at C5 plotted with the non-polarized EIGER-data. Red is the horizontal field spinflip channel (magnetic), black is the horizontal field non-spinflip channel (nuclear) and green is the non-polarized EIGER data. **Upper left:** Energy scan at $h = -0.4$ right between the zone center and the zone boundary. **Upper right:** Polarized energy scan at $h = -0.67$ right at the zone boundary and non-polarized data taken at $h = 0.65$. **Bottom left:** Energy scan at $h = -0.75$ at the crossing. **Bottom right:** Polarized energy scan at $h = -1$ right in between the (030) and the (220) zone and non-polarized data at $h = 0.95$.

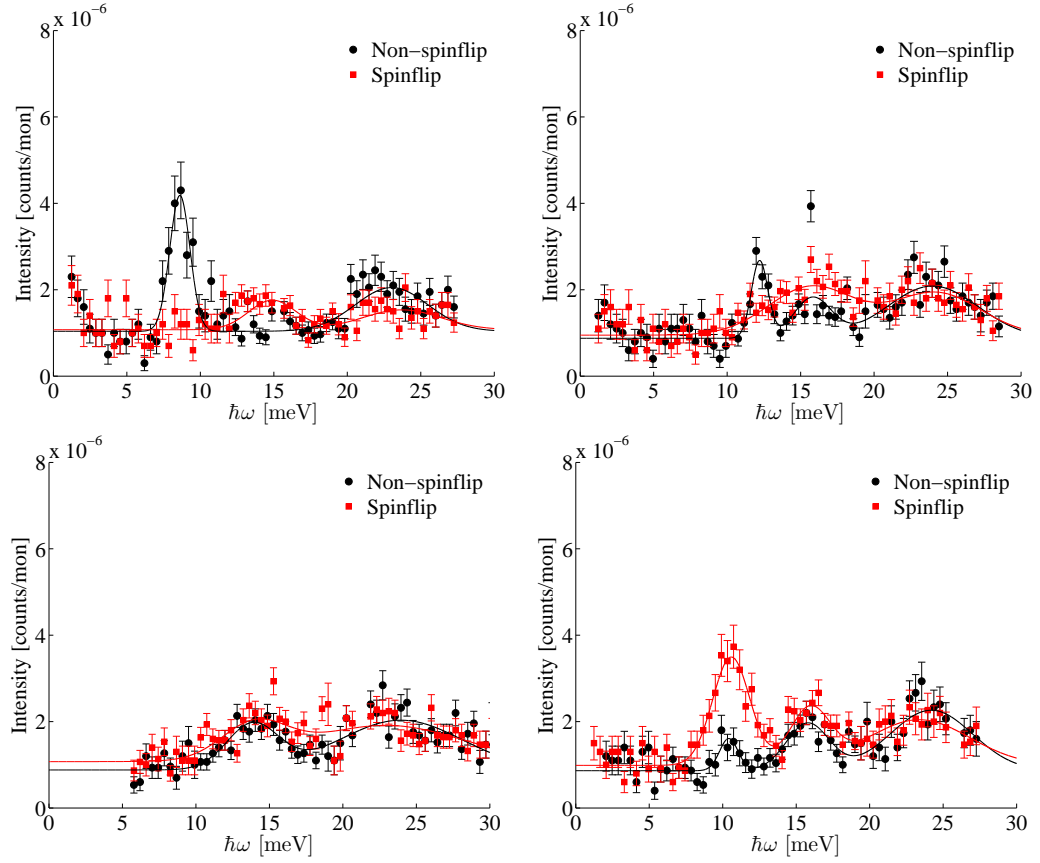
G.7 Measurements below T_N 

Figure G.11: The $T = 40$ K data taken at C5. Red is the horizontal field spinflip channel (magnetic) and black is the horizontal field non-spinflip channel (nuclear). **Upper left:** Energy scan at $h = -0.4$ right between the zone center and the zone boundary. **Upper right:** Energy scan at $h = -0.67$ right at the zone boundary. **Bottom left:** Energy scan at $h = -0.75$ at the crossing. **Bottom right:** Energy scan at $h = -1$ right in between the (030) and the (220) zone.

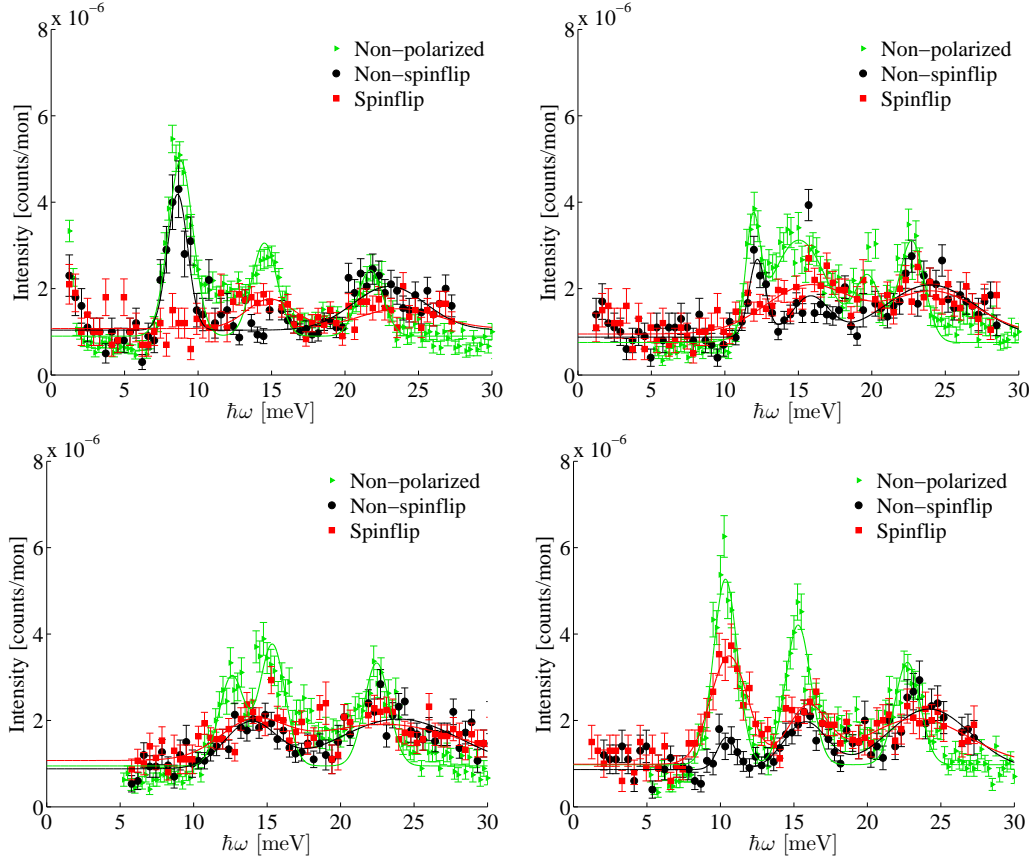


Figure G.12: The $T = 40$ K data taken at C5 plotted with the non-polarized EIGER-data. Red is the horizontal field spinflip channel (magnetic), black is the horizontal field non-spinflip channel (nuclear) and green is the non-polarized EIGER data. **Upper left:** Energy scan at $h = -0.4$ right between the zone center and the zone boundary. **Upper right:** Polarized energy scan at $h = -0.67$ right at the zone boundary and non-polarized data taken at $h = 0.65$. **Bottom left:** Energy scan at $h = -0.75$ at the crossing. **Bottom right:** Polarized energy scan at $h = -1$ right in between the (0 3 0) and the (2 2 0) zone and non-polarized data at $h = 0.95$.

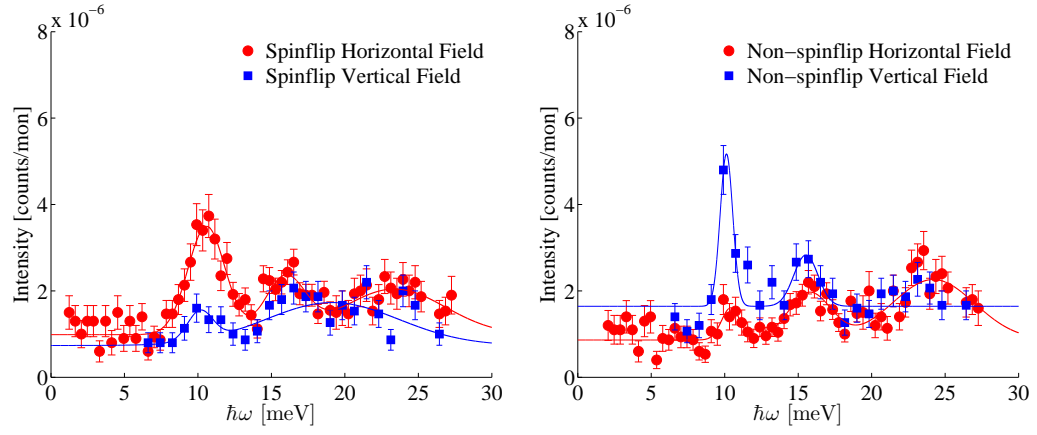
G.7.1 Horizontal field versus vertical field at $T = 40$ K

Figure G.13: Left: Constant- Q scan at $h = 1$ at 40 K spinflip channel. **Right:** Constant- Q scan at $h = 1$ at 40 K non-spinflip channel.

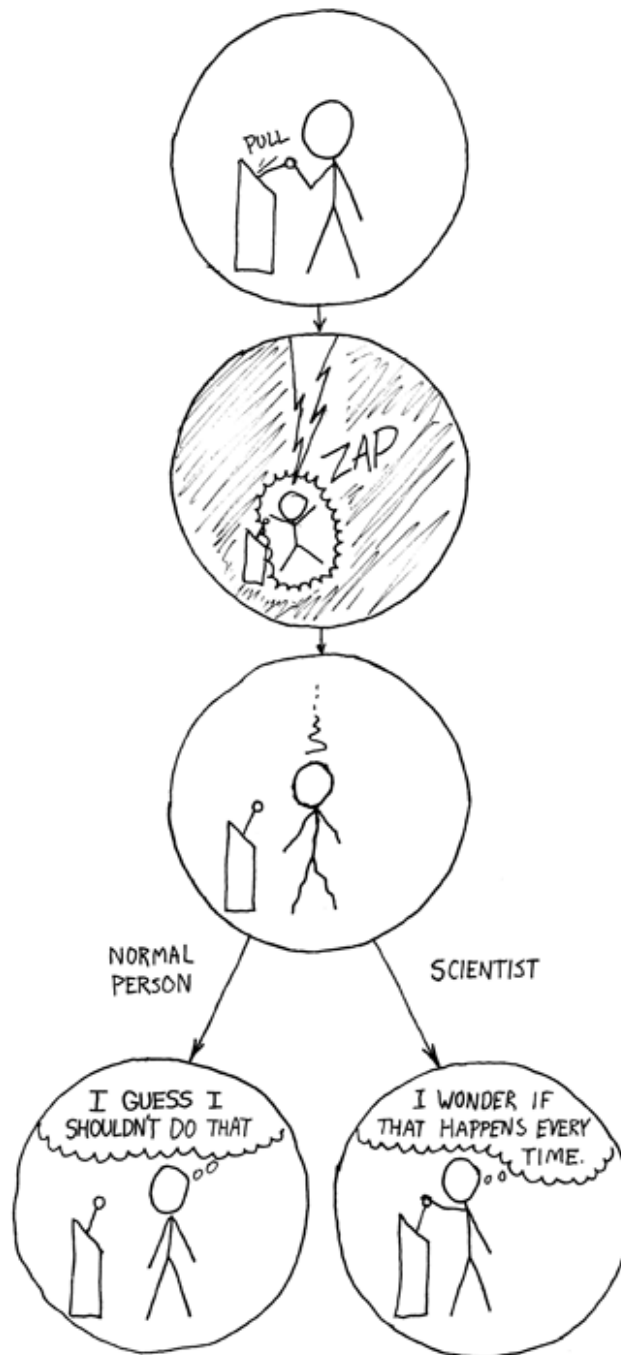


Figure G.14: xkcd - The difference